Plasma Physics Reports, Vol. 29, No. 3, 2003, pp. 187–189. Translated from Fizika Plazmy, Vol. 29, No. 3, 2003, pp. 211–213.

CENTENNIAL OF ACADEMICIAN M.A. LEONTOVICH

Founder of a Scientific School on Plasma Physics

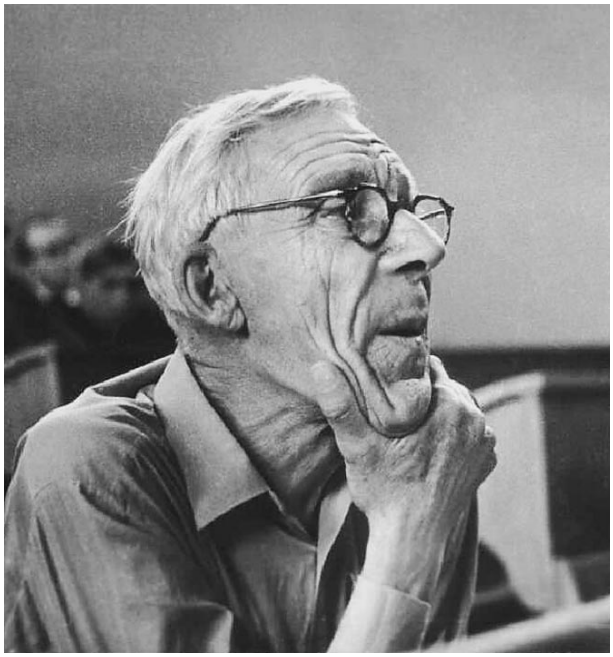

Academician Mikhail Aleksandrovich Leontovich, a multidisciplinary theoretical physicist, who worked in the fields of physical optics, theory of oscillations, acoustics, statistical physics, and thermodynamics, was a founder of the greatest scientific schools on radiophysics and plasma physics. It is due to the successful development of plasma theory under the leadership of Leontovich that theoretical research on the problem of controlled nuclear fusion (CNF) in the USSR achieved a very high level and promoted the successful development of experimental studies.

Mikhail Aleksandrovich Leontovich was born on March 7, 1903, in St. Petersburg to the family of Aleksandr Vasil'evich Leontovich (1869–1943), a lecturer at Kiev University; a prominent physiologist and neurohistologist; and, later (since 1929), academician of the Academy of Sciences of the Ukrainian SSR. The mother of Mikhail Aleksandrovich, Vera Viktorovna Kirpicheva, was an oculist. Because of his sympathy and help to revolutionaries, Aleksandr Vasil'evich had problems with his work at the university. However, he won a competition for the position of the head of the Department of Physiology at the Moscow Petrovsko-Razumovsky Agricultural Institute (now, the Timiryazev Agricultural Academy). Thus, in 1913, Leontovich's family moved to Moscow.

When he was 12 or 13 years old, M.A. Leontovich showed interest in natural sciences, such as geology and chemistry (his father admitted him in a chemical laboratory). From his father, he inherited a lifelong love of nature and of the vegetable and animal world. However, he was also interested in exact science. As early as in high school, he had begun studying higher mathematics. In 1919, he entered the Department of Physics and Mathematics at Moscow State University. This hungry year, his mother died. After his father got married for a second time, M.A. Leontovich started his independent life, having taken under his trusteeship his sister Evgeniya (born in 1906). In 1921, he helped her enter the Department of Physics and Mathematics at Moscow State University. Being a student, he worked as a laboratory assistant at the Institute of Biological Physics, founded by P.P. Lazarev, and, later, at the Laboratory of the Kursk Magnetic Anomaly (till 1925). During summer vacations and, sometimes, in winter, he traveled the length and breadth of the Kursk Province with a magnetometer in his hands. In 1925, Leontovich and his university friends A.A. Andronov, A.A. Vitt, and S.É. Khaĭkin became the first postgraduate students of the eminent soviet physicist L.I. Mandelstam. In connection with experiments on light scattering in liquids that were conducted at Moscow State University and, then, at the Lebedev Physical Institute under the guidance of Mandelstam, Leontovich's interest was mainly concentrated on molecular optics. He participated in the development of the classical theory of combination light scattering in crystals. Very soon, the originality, depth, and universality of theoretical investigations by Leontovich made him one of the leading physicists at the institute.

After finishing his postgraduate study in 1928, Leontovich began to work at the Research Institute of Physics at Moscow State University. He became an assistant professor and, then, a professor at the Physics Department of Moscow University. Besides reading lectures, he conducted a practical work on general physics and, together with S.I. Vavilov, the future President of the USSR Academy of Sciences (1945–1951), in 1931, organized a special practical work on optics.

In 1928–1929, Leontovich carried out three experimental studies on light scattering on surfaces with inhomogeneities smaller than the light wavelength (the results of these studies were published in Ztschr. Phys.). When conducting these experiments, he himself had, e.g., to perform very laborious work on polishing and etching glass to achieve such feeble inhomogeneities. As I.L. Fabelinskiĭ remembered, Leontovich suc-

1063-780X/03/2903-0187$24.00 © 2003 MAIK "Nauka/Interperiodica"

cessfully managed with experimental work and could foresee "where the experimentalist could be trapped by the insidiousness of nature or make an error or, possibly, a false step."

At the end of 1934, Leontovich joined the Lebedev Physical Institute, where he began to work as a senior scientist at the Laboratory of Oscillations, headed by N.D. Papaleksi. Somewhat later, the future Nobel Prize winner I.E. Tamm (who at that time had become the corresponding member of the USSR Academy of Sciences and the Head of the Theoretical Department at the Lebedev Physical Institute) wrote the following in the recommendation given to Leontovich in connection with awarding him with a doctoral degree in physics and mathematics in 1935 without defending a thesis: "Mikhail Alekcandrovich Leontovich is one of the prominent theoretical physicists. His distinguishing features are an excellent intellect, a critical mind, depth of physical thought, exceptional erudition, and perfect knowledge of the mathematical apparatus. At the same time, he presents a rare example of combining in one person both a theoretical physicist and an experimentalist, because, along with theoretical studies, he has performed a series of experimental works. Some of his papers are concerned with very different fields of physics, such as the theory of oscillations, quantum theory, and the theory of relativity. However, the most important are his works on optics and statistical physics." L.I. Mandelstam also noted that Leontovich was the best expert in statistical physics in our country.

In 1939, Leontovich was elected a corresponding member of the USSR Academy of Sciences. In his scientific testimonial signed by S.I. Vavilov, it was, in particular, written: "M.A. Leontovich, the closest assistant and pupil of Academician L.I. Mandelstam, is a prominent and versatile theoretical physicist. He freely operates with the methods of very different branches of physics. The scientific interests of M.A. Leontovich embrace statistical physics, thermodynamics, hydrodynamics, theory of electromagnetism, and physical optics.

The scientific publications by Leontovich are not so numerous; however, each of them contributes greatly to the problem to which it is devoted."

In the beginning of the Great Patriotic War, Leontovich was evacuated in Kazan together with the Lebedev Physical Institute; however, in March 1942, he returned to Moscow. Here, he began to work at a defense factory, where, by the proposal of his friend S.É. Khaĭkin, he took part in the studies on radiolocation and the creation of a system for detecting enemy bombers and determining their coordinates, as well as a system of radio guidance for blind bombing. In 1944, Academician A.I. Berg, the head of the NII-108 research institute, related to the above defense factory, invited Leontovich to work at his institute. Here, along with solving express defense problems, Leontovich carried out important theoretical studies in the field of radiophysics. When working at the Laboratory of Oscillations of the Lebedev Physical Institute, he formulated very efficient approximate boundary conditions for an electromagnetic field on the surface of highly conducting bodies (he published these results only ten years later, in 1948). These "Leontovich's boundary conditions," which made it possible to solve a wide class of radiophysical problems, are widely used in radiophysics and radio engineering. In 1944, Leontovich proposed a powerful method of a parabolic equation for the complex wave amplitude for studying radiowave propagation along the Earth's surface. Another fundamental study that was carried out in this period and also initiated a new line of investigations was his work (together with M.L. Levin) on the general theory of thin-wire antennas. For these studies and other works in the field of radiophysics and defence applications, Leontovich was awarded Popov's Grand Gold Medal in 1952.

Until 1946, Leontovich read lectures at Moscow State University. In 1944, his remarkable course *Statistical Physics* came out, and seven years later, his book *Introduction to Thermodynamics* was published.

In 1945, Leontovich returned to the Lebedev Physical Institute, where, after N.D. Papaleksi died in 1947, he became the Head of the Laboratory of Oscillations. In 1946, at the first postwar elections to the Academy of Sciences, Leontovich was elected a full member of the USSR Academy of Sciences. When working at the Lebedev Physical Institute, he continued his pedagogical activity, which was very important for the education of a new generation of Soviet physicists. From 1946 to 1954, he taught at the Moscow Engineering Physics Institute (MEPI), where, since 1949, he headed the Department of Theoretical Physics. Simultaneously, in 1947–1950, he was the Head of the Department of Physics at the Inostrannaya Literatura Publishing House (ILPH) (this department was founded on the initiative of S.I. Vavilov, the President of the USSR Academy of Sciences, in order to accelerate the post-war training of scientists and engineers). A.A. Gusev, the Vice-President of the Scientific–Editorial Council of the Sovetskaya Éntsiklopediya Publishing House, who worked that time at the ILPH, remembered that Leontovich was the first to clearly formulate the rules for the selection of translators and scientific editors, as well as for the choice of books to be translated and new important papers to be included in the collections of articles.

In 1951, a new thirty-year period of Leontovich's activity opened: by the proposal of I.E. Tamm, he was charged with the supervision of theoretical research on the CNF problem at the Institute of Atomic Energy. This appointment had played a very important role in the successful development of high-temperature plasma physics in the USSR. Leontovich got down to this new work with great enthusiasm. His first works on the calculation of electrodynamic forces arising when a current channel shifts with respect to the conducting

casing, on the dynamics of a pinch discharge, and on the stabilizing effect of a strong longitudinal magnetic field on the discharge became a basis for subsequent extensive investigations of his pupils. He took part in the organization of new experiments and in the analysis and discussion of their results. For the entire collective of physicists whose task was to solve an exclusively difficult problem of producing thermonuclear plasma, Leontovich became the higher authority not only in scientific problems, but also in humanitarian and everyday life problems. The moral principles of Leontovich, his direct and open sight on life, and his sharp interest in all new scientific results over long years promoted a healthy climate in the collective that was in the sphere of his influence and attention. Many tens of physicists, both those who worked immediately with Leontovich and those who participated his famous Theoretical Physics Seminar, experienced his wholesome influence.

Clearly understanding the extreme complexity and diversity of the problems of the creation and confinement of high-temperature plasmas, Leontovich devoted much time to the education of young theoretical physicists. When reading lectures at MEPI and, then, at Moscow State University (from 1954 to 1971), he selected talented students for working in the field of plasma physics. His deep knowledge of different fields of theoretical physics (electrodynamics, hydrodynamics, statistical physics, quantum theory, and the theory of oscillations and fluctuations) turned out to be very useful for the development of the new branch of science. Under the leadership of Leontovich, the theory of plasma equilibrium, the theory of magnetohydrodynamic and numerous kinetic instabilities of a magnetized plasma, the theory of classical and anomalous turbulent processes in plasma, and the theory of atomic processes and radiation in high-temperature plasma (i.e., all of those that form a basis of modern plasma physics) were developed. Since that time, Leontovich's theoretical school became a leader in the theory of high-temperature plasma for long years.

Along with scientific and educational activity, Leontovich conducted important organizing work. For more than 30 years, he was a member of the Bureau of the Department of General Physics and Astronomy of the USSR Academy of Sciences and headed the publishing work at this Department. Being the Deputy Editor-in-Chief of the Journal of Theoretical and Experimental Physics, he significantly contributed to the success of this outstanding journal. Along with his very fruitful professional activity, Leontovich was always deeply interested in the social aspects of science and, more generally, in the social atmosphere in our country. The name of Leontovich was well known not only in the Academy, but generally to everyone who had any relation to science, by his active resistance to the "contamination" of the Academy by the people promoted for reasons other than their personal outstanding contribution to science. At all the stages of our postwar history, he, among few intellectuals, did everything possible to support the progressive and democratic tendencies in science and society and actively withstood retrograde attempts of rehabilitating and, to a certain extent, acquitting Stalinism.

Leontovich died on March 30, 1981. He is buried in Moscow, at the Kuntsevo cemetery.

Plasma Physics Reports, Vol. 29, No. 3, 2003, pp. 190–202. Translated from Fizika Plazmy, Vol. 29, No. 3, 2003, pp. 214–226.

DUSTY PLASMAS

Development of a Self-Consistent Model of Dust Grain Charging at Elevated Pressures Using the Method of Moments

A. V. Filippov, N. A. Dyatko, A. F. Pal', and A. N. Starostin

Troitsk Institute for Innovation and Fusion Research, Troitsk, Moscow oblast, 142092 Russia

Received August 21, 2002

Abstract—A model of dust grain charging is constructed using the method of moments. The dust grain charging process in a weakly ionized helium plasma produced by a 100-keV electron beam at atmospheric pressure is studied theoretically. In simulations, the beam current density was varied from 1 to 10^6 μA/cm^2. It is shown that, in a He plasma, dust grains of radius 5 μm and larger perturb the electron temperature only slightly, although the reduced electric field near the grain reaches 8 Td, the beam current density being 10^6 μA/cm^2. It is found that, at distances from the grain that are up to several tens or hundreds of times larger than its radius, the electron and ion densities are lower than their equilibrium values. Conditions are determined under which the charging process may be described by a model with constant electron transport coefficients. The dust grain charge is shown to be weakly affected by secondary electron emission. In a beam-produced helium plasma, the dust grain potential calculated in the drift–diffusion model is shown to be close to that calculated in the orbit motion limited model. It is found that, in the vicinity of a body perturbing the plasma, there may be no quasineutral plasma presheath with an ambipolar diffusion of charged particles. The conditions for the onset of this presheath in a beam-produced plasma are determined. © *2003 MAIK "Nauka/Interperiodica".*

1. INTRODUCTION

At present, there is increased interest in the study of a dusty plasma, which stems from its unique properties [1–3] and various technological applications [4]. A study of the grain charging process is one of the key problems in the physics of dusty plasma, because it provides information about the charge of the grains and the potential of the interaction between them. Such information is needed to develop a theory of dusty plasma capable of describing, on the one hand, the formation, existence, evolution, and destruction of ordered plasma–dust structures and, on the other, the dynamic processes occurring in a dusty plasma, which have recently attracted increased attention [1, 2].

The charging of dust grains is now commonly described in the orbit motion limited (OML) model [3, 5], which is based on a probe theory [6–8] and which is valid in the low-pressure limit, when the collisions of electrons and ions with neutral plasma particles can be neglected. We do not yet have an analytic theory of probes at elevated pressures [7–9]; solutions have been obtained only for some specific modes of the probe operation at particular boundary and initial conditions. Since these solutions are not of interest for the theory of dusty plasma, its properties at elevated pressures are usually studied by numerical methods. It should be noted that different theoretical papers in which the grain charging processes at elevated pressures are studied numerically and transport processes are described in the drift–diffusion model are based on different assumptions concerning the transport and kinetic coefficients of the electrons near the dust grain, where the electric field gradients, as well as the electron and ion density gradients, are large. Thus, in [10], in calculating the dust grain charge in a helium plasma at atmospheric pressure, these coefficients were assumed to be constant and were determined from the plasma parameters far from the grain. In [11, 12], in studying dusty plasmas in molecular gases at elevated pressures, the electron coefficients were determined from the local value of the reduced electric field. In the general case, however, the electron energy distribution function (EEDF) near a charged dust grain (as well as the related transport and kinetic electron coefficients) is nonlocal in character. That is why, in order to describe the charging process correctly (especially in a dusty plasma of atomic gases), it is necessary to take into account nonlocal effects.

In this paper, we study the effect of the nonlocal nature of the EEDF on the charging of dust grains in a He plasma at elevated pressures. The nonlocal nature of the distribution function is modeled by the so-called nonlocal method of moments [13, 14], which differs from the standard method of moments in that the transport and kinetic electron coefficients are determined from the mean electron energy, rather than from the local values of the electric field. The local values of the electron energy are obtained using an additional integral equation that relates the mean electron energy at each point to the values of the plasma parameters at the neighboring points. That is why this method may be called "nonlocal." Our model of dust grain charging is constructed based on this integral equation and includes

1063-780X/03/2903-0190$24.00

the electron and ion continuity equations, Poisson's equation, and the balance equation for the mean electron energy. The nonlocal method of moments was used to analyze the results from experiments with drift tubes [13, 15] and to study nonequilibrium electron transport in glow discharges [14, 16, 17]. A comparison of our results with experiment and with more precise theories (such as the one in which transport processes are modeled by a particle-in-cell method and the EEDF is calculated by the Monte Carlo method) shows that the nonlocal method of moments is potentially promising and can give a high degree of accuracy [13–17]. A similar method was successfully used to study instabilities in glow discharges [18, 19], model RF discharges [20, 21], and develop a theory of probes at elevated pressures [7–9, 22].

Our analysis is concerned with a beam-produced plasma in helium at atmospheric pressure. In simulations, the radius of the dust grains was varied from 5 to 20 μm; the dust density was taken in the range from 10^2 to 10^6 cm^{-3}; and the current density of a 120-keV electron beam was changed from 1 to 10^6 μA/cm^2, which corresponds approximately to ionization rates of 10^{14}–10^{22} cm^{-3} s^{-1}. On the whole, these parameter values are close to those in experiments carried out by Ivanov *et al.* [10], who reported the results of theoretical and experimental investigation of the plasma of a non-self-sustained helium discharge at atmospheric pressure, into which dust grains with a mean radius of 12 μm were injected.

2. MODEL OF DUST GRAIN CHARGING BASED ON THE NONLOCAL METHOD OF MOMENTS

We consider the charging of a spherical dust grain of radius r_0, placed at the center of a spherically symmetric cell whose radius a_d is determined by the relationship

$$a_d = \left(\frac{4}{3}\pi n_d\right)^{-1/3}, \quad (1)$$

where n_d is the dust particle density. We assume that the plasma is dominated by one species of positive ions. The charging of dust grains with a radius of 10 μm and larger in the plasma of noble gases at atmospheric pressure can be described in the hydrodynamic approximation, which is valid under the conditions [23–28]

$$l_e \ll r_0 + d, \quad l_i \ll r_0 + d, \quad (2)$$

where l_e and l_i are the electron and ion mean free paths, r_0 is the grain radius, and d is the characteristic spatial scale on which the plasma is nonquasineutral. Under these conditions, we can apply the two-term approximation referring to the expansion of the EEDF in spherical harmonics [23] and can reduce the Boltzmann equation for electrons to the set of two equations [28]

$$\frac{\partial f_0 n_e}{\partial t} + \frac{1}{3}\sqrt{\frac{2\varepsilon}{m_e}}\nabla\cdot(n_e\mathbf{f}_1) - \frac{en_e}{3\varepsilon}\sqrt{\frac{2\varepsilon}{m_e}}\frac{\partial}{\partial\varepsilon}(\varepsilon\mathbf{E}\cdot\mathbf{f}_1) = S_0,$$
$$\frac{\partial\mathbf{f}_1 n_e}{\partial t} + \sqrt{\frac{2\varepsilon}{m_e}}\nabla(n_e f_0) - en_e\mathbf{E}\sqrt{\frac{2\varepsilon}{m_e}}\frac{\partial f_0}{\partial\varepsilon} = \mathbf{S}_1 = -\nu_m n_e\mathbf{f}_1. \quad (3)$$

Here, f_0 and f_1 are the first moments in the expansion of the EEDF in Legendre polynomials:

$$f \approx f_0 + \frac{\mathbf{v}}{v}\mathbf{f}_1 = f_0 + f_1\cos\theta; \quad (4)$$

e is the absolute value of the electron charge; m_e is the mass of an electron; n_e is the electron density; ε is the electron energy; $\mathbf{v}$ is the electron velocity; v is the absolute value of the electron velocity; $\nu_m = N\sigma_m v$ is the elastic collision frequency; N is the density of neutral particles; σ_m is the elastic collision cross section; $\mathbf{E}$ is the electric field; S_0 and S_1 are the moments of the collision integral; and the angle θ is measured from the direction of the vector $\mathbf{E}$. The EEDF is normalized so as to satisfy the condition

$$\frac{1}{2}\int_0^\infty\int_0^\pi f\sqrt{\varepsilon}\sin\theta\,d\theta\,d\varepsilon = \int_0^\infty f_0\sqrt{\varepsilon}\,d\varepsilon = 1. \quad (5)$$

If the plasma parameters vary on a characteristic time scale of $t \gg \nu_m^{-1}$, then the time derivative in the equation for f_1 can be neglected, in which case Eqs. (3) yield the electron continuity equation

$$\frac{\partial n_e}{\partial t} + \nabla\cdot\mathbf{j}_e = Q_{\text{ion}} + \nu_{\text{ion}}n_e - \beta_{ei}n_e n_i \quad (6)$$

with the electron current density

$$\mathbf{j}_e = -\nabla(D_T n_e) - k_e n_e\mathbf{E}, \quad (7)$$

where Q_{ion} is the rate of gas ionization by an external source; ν_{ion} is the rate of ionization by plasma electrons; β_{ei} is the electron–ion recombination rate; and the electron mobility and electron diffusion coefficient are described by the expressions [13]

$$k_e = -\frac{2e}{3m_e}\int\frac{\varepsilon^{3/2}}{\nu_m}\frac{\partial f_0}{\partial\varepsilon}d\varepsilon, \quad D_T = \frac{2}{3m_e}\int\frac{\varepsilon^{3/2}}{\nu_m}f_0\,d\varepsilon. \quad (8)$$

Under condition (2) for the ions, the ion transport can also be described by the ion continuity equation in the drift–diffusion model:

$$\frac{\partial n_i}{\partial t} + \nabla\cdot\mathbf{j}_i = Q_{\text{ion}} + \nu_{\text{ion}}n_e - \beta_{ei}n_e n_i \quad (9)$$

with the ion current density

$$\mathbf{j}_i = n_i k_i\mathbf{E} - D_i\nabla n_i, \quad (10)$$

where n_i is the ion density, k_i is the ion mobility, and D_i is the ion diffusion coefficient. In the drift–diffusion model, the dust grain charging is described by Eqs. (6)–(10) supplemented with Poisson's equation for the electric field,

$$\nabla \cdot \mathbf{E} = 4\pi e(n_i - n_e). \quad (11)$$

In [10], the dust grain charging was described by a set of equations analogous to Eqs. (6)–(11), and the coefficients in the electron continuity equation were assumed to be constant and were determined from the EEDF for a plasma that is free of dust. It should be noted that, under the conditions of [10], the applicability of this approximation is questionable.

Under the applicability condition of the local approximation [23],

$$l_u \ll r_0 + d \quad (12)$$

the EEDF and, accordingly, the transport coefficients and the production and loss rates of the electrons are determined by the local value of the reduced electric field E/N. In condition (12), the electron energy relaxation length l_u is defined by [24]

$$l_u = (N\sqrt{\sigma_m \sigma_u})^{-1}, \quad (13)$$

where σ_u is the effective inelastic collision cross section, which can be approximately represented as $\sigma_u = \delta\sigma_m = \frac{2m_e}{M}\sigma_m$ (with M the mass of a particle of neutral gas) in the case when elastic losses are dominant.

In [24, 25, 28], the theory of electron transport in a weakly inhomogeneous plasma was constructed based on perturbation theory. Accounting for the linear term in the expansion of the EEDF in the electron density gradient led to a renormalization of the electron diffusion coefficient D_T; as a result, the notion of the longitudinal electron diffusion coefficient D_L had to be introduced. The local approximation was used in [11, 12, 29] in modeling the grain charging process in molecular gases, in which case the coefficient D_T in the electron continuity equation (7) was replaced with D_L.

In helium at atmospheric pressure, the mean free path of electrons with energies up to several electronvolts is essentially constant [28] and approximately equal to $l_e \sim 0.5$ μm, the electron energy relaxation length being $l_u \sim 30$ μm. Consequently, for dust grains with a radius of ~10 μm, condition (2) is satisfied under these circumstances, while condition (12) fails to hold. Moreover, this case is most difficult to analyze because the quantities l_u and $r_0 + d$ are comparable; hence, the electron transport should be described by solving the inhomogeneous Boltzmann equation (3), which is a fairly complicated task.

Here, the nonlocal nature of the EEDF is taken into account by the nonlocal method of moments [13, 14], which is based on the assumption that the transport coefficients, the production and loss rates of the electrons, and the electron energy loss rate are determined exclusively by the mean electron energy; in other words, the dependence of these parameters on the coordinates (their nonlocal nature) manifests itself through the coordinate dependence of the mean electron energy. In turn, the coordinate dependence of the mean electron energy is determined by the electron energy balance equation, which can be derived by multiplying the first of Eqs. (3) by the electron energy and by integrating the resulting equation over energy:

$$\frac{\partial n_e \langle \varepsilon_e \rangle}{\partial t} + \nabla \cdot \mathbf{h}_e + e\mathbf{j}_e \cdot \mathbf{E} = (\eta - I)Q_{\text{ion}} - n_e W_S, \quad (14)$$

where the mean electron energy $\langle \varepsilon_e \rangle$ is defined as $\langle \varepsilon_e \rangle = \int_0^\infty f_0 \varepsilon^{3/2} d\varepsilon$, $\mathbf{h}_e$ is the electron energy flux density, η is the energy cost of the production of one electron–ion pair (in a first approximation, it is equal to the doubled ionization energy), and the electron energy loss rate W_S in elastic and inelastic collisions has the form $W_S = \int_0^\infty S_0 f_0 \varepsilon^{3/2} d\varepsilon$. Then, we multiply the second of Eqs. (3) by $\varepsilon^{3/2}$ and integrate over energy to obtain an expression for the electron energy flux density:

$$\mathbf{h}_e = -\nabla(Gn_e) - \beta n_e \mathbf{E}, \quad (15)$$

where the coefficients G and β are defined through the relations [13]

$$\beta = -\frac{2e}{3m_e}\int \frac{\varepsilon^{5/2}}{\nu_m}\frac{\partial f_0}{\partial \varepsilon} d\varepsilon, \quad G = \frac{2}{3m_e}\int \frac{\varepsilon^{5/2}}{\nu_m} f_0 d\varepsilon. \quad (16)$$

As a result, a complete set of equations describing dust grain charging in a nonlocal model based on the nonlocal method of moments takes the form

$$\begin{aligned}
&\frac{\partial n_e}{\partial t} - \frac{1}{r^2}\frac{\partial}{\partial r}\left[r^2\left(\frac{\partial D_T n_e}{\partial r} + k_e n_e E\right)\right] \\
&\quad = Q_{\text{ion}} + \nu_{\text{ion}} n_e - \beta_{ei} n_e n_i, \\
&\frac{\partial n_i}{\partial t} + \frac{1}{r^2}\frac{\partial}{\partial r}\left[r^2\left(-D_i\frac{\partial n_i}{\partial r} + k_i n_i E\right)\right] \\
&\quad = Q_{\text{ion}} + \nu_{\text{ion}} n_e - \beta_{ei} n_e n_i, \quad (17) \\
&\frac{1}{r^2}\frac{\partial (r^2 E)}{\partial r} = 4\pi e(n_i - n_e), \\
&\frac{\partial n_e \langle \varepsilon_e \rangle}{\partial t} - \frac{1}{r^2}\frac{\partial}{\partial r}\left[r^2\left(\frac{\partial G n_e}{\partial r} + \beta n_e E\right)\right] \\
&\quad + e\mathbf{j}_e \cdot \mathbf{E} = (\eta - I)Q_{\text{ion}} - n_e W_S.
\end{aligned}$$

These equations are written in the one-dimensional model in spherical coordinates with their origin at the center of the grain. Note that the model at hand yields

exact results for a Maxwellian EEDF, in which case the electron kinetic coefficients for a given gas are uniquely determined by the electron temperature $T_e = \frac{2}{3}\langle\varepsilon_e\rangle$. The electron distribution function is Maxwellian when, e.g., the collision integral is dominated by the term accounting for electron–electron collisions. When elastic energy losses dominate over inelastic losses, this is the case if the following condition is satisfied [30]:

$$n_e \gg n_{e,M} \approx \frac{m_e}{M}\frac{N\sigma_m T_e^2}{e^4 \ln\Lambda}, \tag{18}$$

where $\ln\Lambda$ is the Coulomb logarithm. For $T_e = 0.025$ eV in helium at atmospheric pressure, the boundary electron density is on the order of $n_{e,M} \sim 10^{10}$ cm^{-3}. In helium at atmospheric pressure, the electron density exceeds this value even for ionization rates higher than 10^{12}–10^{13} cm^{-3} s^{-1}. (Note that, for the degrees of gas ionization that are under investigation here, electron–ion collisions can be neglected.)

In the literature, the electron heat flux is often written in other forms (see, e.g., [7–9, 18–22]); therefore, we briefly analyze this point here. Let us perform simple manipulations with the expression for the electron energy flux density [14]. Expressing the electric field from formula (7) and substituting into formula (15), we obtain

$$\begin{aligned}\mathbf{h}_e &= \frac{\beta}{k_e}\mathbf{j}_e + \frac{\beta}{k_e}\nabla(D_T n_e) - \nabla(G n_e)\\ &= \frac{\beta}{k_e}\mathbf{j}_e + \left(\frac{\beta}{k_e}D_T - G\right)\nabla n_e - \left(\frac{\beta}{k_e}\frac{\partial D_T}{\partial T_e} - \frac{\partial G}{\partial T_e}\right)n_e\nabla T_e.\end{aligned} \tag{19}$$

For a Maxwellian EEDF, the transport coefficients are related by the Einstein relationships

$$D_T/k_e = G/\beta = T_e/e. \tag{20}$$

We thus see that the term with the electron density gradient drops out of formula (19):

$$\mathbf{h}_e = \frac{G}{D_T}\mathbf{j}_e - \chi_e n_e \nabla T_e; \tag{21}$$

where $\chi_e = (\hat{G} - \hat{D}_T)G/T_e$ is the electron thermal conductivity with $\hat{G} = \partial\ln G/\partial\ln T_e$ and $\hat{D}_T = \partial\ln D_T/\partial\ln T_e$. When the electron transport rate is independent of the electron energy, formula (21) yields the following widely used expression for the electron energy flux density [19, 21, 22]:

$$\mathbf{h}_e = \frac{5}{2}T_e\mathbf{j}_e - \frac{5}{2}D_T n_e \nabla T_e. \tag{22}$$

Since the assumption that the transport rate is constant usually fails to hold for real gases, expression (22) is an approximate one; hence, in calculations, it is necessary to use the actual transport cross sections.

3. FORMULATION OF THE BOUNDARY CONDITIONS

The boundary conditions for the electron and ion densities at the grain surface $r = r_0$ were analyzed in detail in [29]. In the present paper, we additionally take into account the secondary electron emission (SEE) induced by beam electrons, which slightly modifies the boundary condition for electrons at the grain boundary. Here, we consider the boundary condition on the electron energy balance equation, because opinion in the literature is divided on this question. Note that the use of effective boundary conditions for the electron density makes it possible to remove the singularity (see, e.g., [9]) in the electron energy balance equation at the grain boundary.

In order to derive the boundary condition for the electron temperature, we must, first, correctly specify the electron energy flux onto the dust grain. To do this, we equate the hydrodynamic electron energy flux to the flux predicted by kinetic theory, as was done in [29] in obtaining effective boundary conditions for the electron and ion densities. For simplicity, we work in plane geometry and consider the case $l_e \ll r_0$:

$$-\nabla(G n_e) - \beta n_e \mathbf{E} = -\frac{1}{2}n_e v_T T_e \mathbf{e}_r - \frac{1}{2}\nabla(G n_e), \tag{23}$$

where $\mathbf{e}_r$ is a vector normal to the boundary and $v_T = \sqrt{8T_e/\pi m_e}$ is the electron thermal velocity. The left-hand side of Eq. (23) is the hydrodynamic flux, and the right-hand side is the kinetic flux, derived on the basis of a two-term expansion of the EEDF (see [14]). If the electron mean free path is energy-independent (which is a good approximation in the case of a helium plasma), the electron transport coefficients are related by the expressions

$$\begin{aligned}D_T &= \frac{l_e v_T}{3}, \quad k_e = \frac{eD_T}{T_e},\\ G &= 2D_T T_e = \frac{2}{3}l_e v_T T_e, \quad \beta = \frac{eG}{T_e} = 2k_e T_e.\end{aligned} \tag{24}$$

Using expressions (24), we transform Eq. (23) into

$$\frac{1}{2}n_e v_T T_e = \frac{1}{3}l_e v_T \frac{\partial(n_e T_e)}{\partial r} + 2k_e E n_e T_e \tag{25}$$

and, taking into account the relationships $v_{dr} = |k_e E| \ll v_T$, we get

$$\frac{1}{2}n_e v_T T_e \approx \frac{1}{3}l_e v_T T_e \frac{\partial n_e}{\partial r} + \frac{1}{3}l_e v_T n_e \frac{\partial T_e}{\partial r}. \tag{26}$$

In the approach used here, the effective boundary condition for the electron density has the form $n_e =$

$\frac{2}{3} l_e \partial n_e/\partial r$ [29]. With allowance for this condition, we finally reduce Eq. (26) to

$$\partial T_e/\partial r = 0. \quad (27)$$

Introducing the new variables $\tilde{n}_e = n_e r$, $\tilde{n}_i = n_i r$, and $\tilde{T}_e = T_e$, we simplify electron energy balance equation (17) to the form corresponding to a planar problem. This indicates that boundary condition (27) does not change when changing into a spherical problem.

As a result, we arrive at the following boundary conditions on Eqs. (17):

$$\left[n_e - \gamma_e \frac{l_e}{r}\frac{\partial(n_e r)}{\partial r}\right]\Bigg|_{r=r_0} = \frac{4 j_{ee}}{v_T},$$

$$\left[n_i - \gamma_i \frac{l_i}{r}\frac{\partial(n_i r)}{\partial r}\right]\Bigg|_{r=r_0} = 0, \quad \left[\frac{\partial T_e}{\partial r}\right]\Bigg|_{r=r_0} = 0, \quad (28)$$

$$\mathbf{j}_e|_{r=a_d} = 0, \quad \mathbf{j}_i|_{r=a_d} = 0, \quad \mathbf{h}_e|_{r=a_d} = 0, \quad \mathbf{E}|_{r=a_d} = 0,$$

where the constants γ_e and γ_i are weakly dependent on the ratios of the electron and ion mean free paths to the grain radius, $j_{ee} = \theta j_b/4e$ is the flux density of the electrons produced from the secondary emission, θ is the SEE coefficient, and j_b is the current density of a beam of fast electrons. In our study, the constants γ_e and γ_i are assumed to depend on the ratios l_e/r_0 and l_i/r_0 according to the relationships

$$\begin{aligned} \gamma_{e(i)} &= \frac{2}{3} + \frac{1}{6}\lambda_{e(i)}^{5/2}, \quad \lambda_{e(i)} \le 1; \\ \gamma_{e(i)} &= \frac{4}{3} - \frac{1}{2}\lambda_{e(i)}^{-1}, \quad \lambda_{e(i)} \ge 1; \end{aligned} \quad (29)$$

where $\lambda_{e(i)} = l_{e(i)}/r_0$. These relationships yield correct values of the fluxes in the collisionless approximation.

4. TRANSPORT AND KINETIC COEFFICIENTS IN THE NUMERICAL MODEL

The difference scheme for numerically solving the nonlinear boundary-value problem as formulated is based on the method of integral identities [31] and is implemented on a nonuniform grid that becomes progressively finer toward the grain surface. At each time step, Eqs. (17) are solved iteratively until the desired accuracy of the solution is reached. At each iteration step, the equations were solved in the order in which they are written in set (17). The balance equations, of which the electron energy balance equation was linearized, were solved by the sweep method [32]. The numerical model also makes use of the unconditionally stable Crank–Nicholson scheme for integration over time.

The electron transport coefficients and electron energy loss rate were calculated for a Maxwellian EEDF (in the electron temperature range from 10^2 to 10^5 K) and for an EEDF obtained by solving the homogeneous Boltzmann equation numerically (for the reduced electric field E/N ranging from 0.001 to 6×10^{-16} V cm^2). The cross sections for the processes under consideration were taken from [28]. In the parameter range in which elastic losses are dominant ($E/N \le 3$ Td, $T_e \le 1.1$ eV), the coefficients calculated by solving the Boltzmann equation are well approximated by the relationships

$$\begin{aligned} T_e &= \frac{2}{3}\langle \varepsilon_e \rangle \approx 0.025 + 0.352 E/N, \\ D_T/k_e &\approx 1.20 T_e^{1.03} \approx 1.158 T_e, \\ D_T &\approx 1347 T_e^{0.444}, \quad k_e \approx 1123 T_e^{-0.584}, \\ G &\approx 2341 T_e^{1.426}, \quad \beta \approx 2639 T_e^{0.447}, \\ W_S &\approx 5.943 \times 10^8 (1 - T/T_e) T_e^{1.604}, \end{aligned} \quad (30)$$

where $\langle \varepsilon_e \rangle$ and T_e are in eV, E/N is in Td, D_T is in cm^2/s, k_e is in cm^2/(V s), G is in cm^2 eV/s, β is in cm^2 eV/(V s), and W_S is in eV/s. For the same range of electron temperatures, calculations with a Maxwellian EEDF yield the relationships

$$\begin{aligned} D_T &\approx 1337.6 T_e^{0.453}, \quad k_e = e D_T/T_e \approx 1337.6 T_e^{-0.547}, \\ G &\approx 2685.3 T_e^{1.46}, \quad \beta = eG/T_e \approx 2685.3 T_e^{0.46}. \\ W_S &\approx 6.108 \times 10^8 (1 - T/T_e) T_e^{1.542}. \end{aligned} \quad (31)$$

A comparison between coefficients (30) and (31) shows that they differ only slightly. In simulations, we used transport coefficients (31), which were obtained for a Maxwellian EEDF.

According to [33], the rate of ionization of helium at atmospheric pressure by a 120-keV electron beam is related to the beam current density by Q_{ion} [cm^{-3} s^{-1}] = $1.1 \times 10^{14} j_b$ [μA/cm^2]. An analysis of the ion conversion processes shows that, in helium at the pressure p = 1 atm, the main plasma ions are diatomic He_2^+ ions. The dissociative recombination coefficient for these ions was modeled by the dependence $\beta_{ei} = 0.9 \times 10^{-8}(T_e/300)^{-1.5}$ cm^3/s [34], and their mobility was determined from the Langevin formula $k_i = 18.7$ cm^2/V s [35].

5. ELECTRON ENERGY DISTRIBUTION FUNCTION IN A BEAM-PRODUCED PLASMA

According to the theory based on the OML model [3, 5] and the analytic theory of dust grain charging at elevated pressures [36, 37], the grain charge in an unperturbed plasma depends almost linearly on the electron temperature. Since, in simulations, the elec-

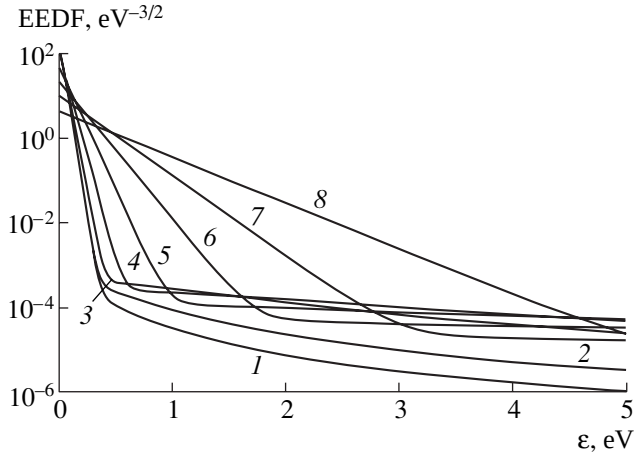

Fig. 1. EEDF in a beam-produced helium plasma at the pressure p = 1 atm and at different gas ionization rates: Q_{ion} = (*1*) 10^{16}, (*2*) 10^{17}, (*3*) 10^{19}, (*4*) 10^{20}, (*5*) 10^{21}, (*6*) 10^{22}, (*7*) 10^{23}, and (*8*) 10^{24} cm^{-3} s^{-1}.

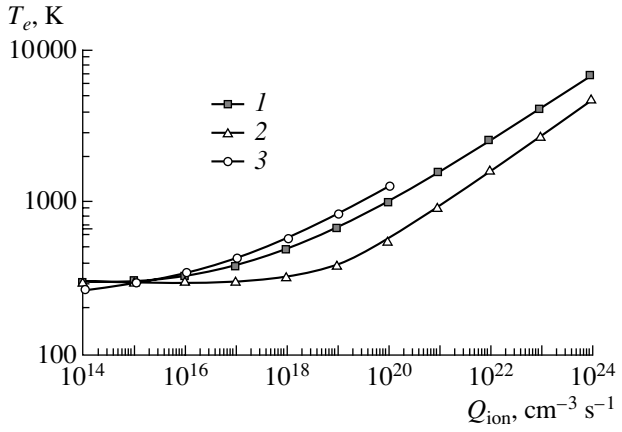

Fig. 2. Electron temperature in a helium plasma at atmospheric pressure as a function of the gas ionization rate. Curve *1* was calculated based on the energy balance equation, curve *2* was obtained by numerically solving the Boltzmann equation for the EEDF, and curve *3* represents the electron temperature near a dust grain.

tron temperature was determined from the electron energy balance equation, we had to convince ourselves that the electron temperature far from the grain was calculated correctly. To do this, we numerically solved the homogeneous Boltzmann equation for the EEDF in a beam-produced plasma with allowance for electron–electron collisions. The simulation technique was described in [38]. The results of calculating the EEDF showed that its low-energy part, describing the majority of electrons, is indeed a Maxwellian function (Fig. 1). Thus, we can conclude that the nonlocal method of moments should provide a good approximation for describing transport processes in a beam-produced helium plasma. The electron temperature was also calculated from the electron energy balance equation at different gas ionization rates. According to Fig. 2, the calculated temperatures are only slightly higher than those obtained when calculating the EEDF. This leads to the conclusion that, in a beam-produced plasma, the electron temperature far from a dust grain can be determined fairly reliably from the electron energy balance equation.

6. DISCUSSION OF THE RESULTS FROM MODELING THE GRAIN CHARGING PROCESS

Figure 3 illustrates the results of calculating the charge of an isolated dust grain of radius 10 μm in a He plasma at atmospheric pressure for different current densities of a 120-keV electron beam. In simulations, the SEE coefficient was taken to be 0.1 and 1. According to Fig. 3, an increase in the SEE coefficient from 0.1 to 1 results in a slightly smaller dust grain charge. This indicates that the SEE process has a weak effect on the charge of glass–carbon dust grains. An analogous conclusion was reached in [29] on the basis of analytic estimates.

For comparison, Fig. 3 also shows the grain charge calculated by the analytic theory of dust grain charging [36, 37] and by the theory based on the OML model [3, 5]. It can be seen that both of these theories underestimate the dust grain charge and predict that it should be directly proportional to the grain radius. For this reason, Fig. 4 shows how the grain charge-to-radius ratio for grains of different radii depends on the beam current density. We again see that these two theories are applicable within a limited range.

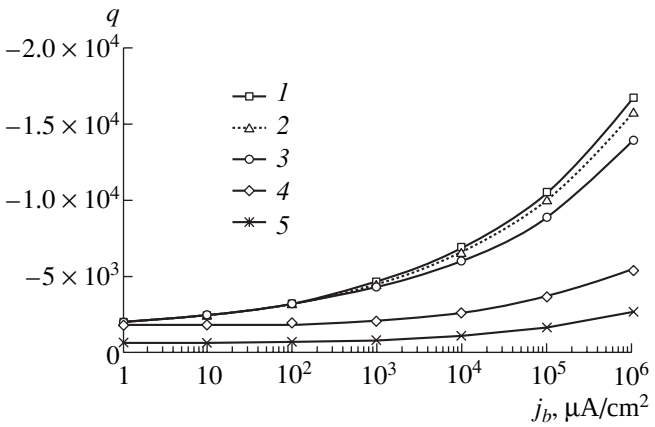

Fig. 3. Dependence of the charge of an isolated dust grain of radius 10 μm in a helium plasma at atmospheric pressure on the current density of a fast electron beam. Curve *1* was calculated with the SEE coefficient θ = 0.1, curve *2* corresponds to θ = 1, curve *3* was calculated for θ = 0.1 under the condition T_e = const, curve *4* was obtained analytically, and curve *5* was calculated in the OML model.

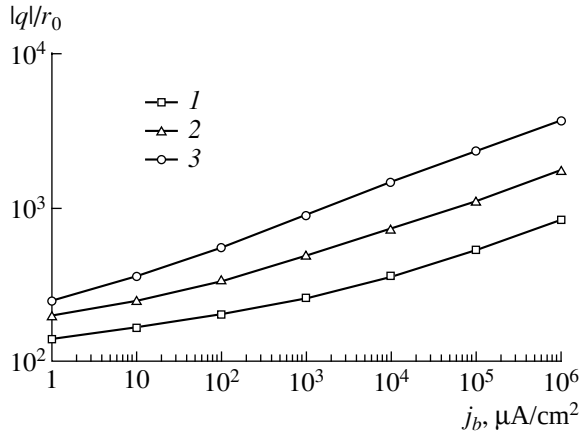

Fig. 4. Dependence of the reduced charge of solitary dust grains with different radii r_0 = (*1*) 5, (*2*) 10, and (*3*) 20 μm in a helium plasma at atmospheric pressure on the current density of a fast electron beam for θ = 0.1.

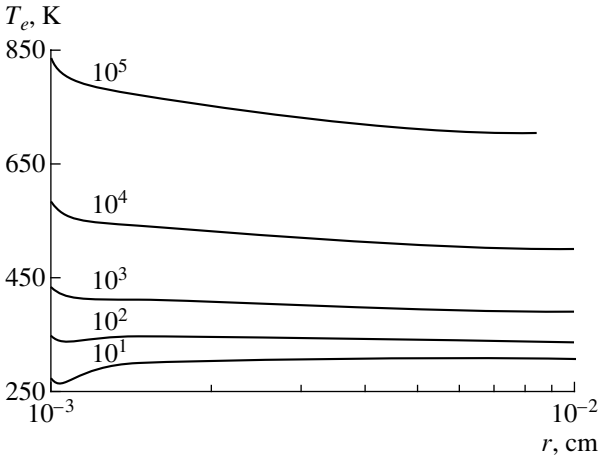

Fig. 5. Steady-state radial electron temperature profiles near a solitary dust grain of radius 10 μm. Numerals near the curves denote the beam current density expressed in μA/cm^2.

Before moving to a description of other numerical results, we give the following definitions. In what follows, we will use the term "ion sheath" for the space charge region [7] and the term "presheath" for the quasineutral plasma region in which the transport of charged plasma particles is ambipolar [39]. The presheath on the side of the grain goes over into the ion sheath, and, on the opposite side, it goes over into the unperturbed plasma.

Figure 5 shows radial profiles of the electron temperature near a dust grain of radius 10 μm in a helium plasma for different current densities of a fast electron beam. We can see that, for all of the gas ionization rates under consideration, the electron temperature changes insignificantly as the dust grain is approached. This result is quite unexpected, because other plasma parameters (such as the electron and ion densities and the electric field) near the grain change substantially, the more so since electron energy balance equation (14) contains the constant term $(\eta - I)Q_{\text{ion}}$, which accounts for plasma heating by the beam, and the term $n_e W_S$, which describes the collisional energy loss, and decreases because of the decrease in the electron density (Fig. 6).

In order to understand the cause for such behavior of T_e, we consider the contribution of individual terms to Eq. (14). The radial profiles of each of the terms are shown in Fig. 7. One can see that, as the dust grain is approached, a decrease in the collisional loss in the presheath is compensated for by the divergence of the heat flux and that, within the ion sheath, this decrease is compensated for by electron cooling in the counteracting electric field; moreover, the term $\nabla \cdot \mathbf{h}_e$ again acts to reduce the deviation of the electron temperature from the equilibrium temperature in an unperturbed plasma.

Let us consider in more detail the divergence of the heat flux. Using formula (21), which is valid in a steady state, and performing simple manipulations, we obtain the following equation for the steady-state electron energy flux density:

$$\nabla \cdot \mathbf{h}_e = \frac{G}{D_T}\nabla \cdot \mathbf{j}_e + \chi_e \frac{j_e}{D_T}\frac{\partial T_e}{\partial r} - \nabla \cdot \left(\chi_e n_e \frac{\partial T_e}{\partial r}\frac{\mathbf{r}}{r}\right). \quad (32)$$

Estimates show that, in a steady state, the ratio of the first term on the right-hand side of Eq. (32) to the collisional energy loss rate is on the order of $4T_e/(\eta - I)$; as a result, under the conditions adopted here, that first term can be neglected. The ratio of the second term to the third term is equal in order of magnitude to the ratio of the ion and electron mobilities.

Let the jump in the electron temperature across a distance equal to the dust grain radius be ΔT_e. Then, the third term in Eq. (32) is estimated as

$$\nabla \cdot \left(\chi_e n_e \frac{\partial T_e}{\partial r}\frac{\mathbf{r}}{r}\right) \sim \chi_e n_e \Delta T_e / r_0^2.$$

Now, we determine the temperature jump at which this term exactly cancels the term describing plasma heating by an electron beam in the presheath:

$$\Delta T_e \sim \frac{Q_{\text{ion}}(\eta - I) r_0^2}{\chi_e n_e} \sim \frac{\tau_D}{\tau_r} I, \quad (33)$$

where $\tau_D = r_0^2/2D_T$ is the characteristic time for electrons to diffuse over a distance equal to the grain radius and $\tau_r = 1/\sqrt{\beta_{ei} Q_{\text{ion}}}$ is the characteristic electron–ion recombination time. For j_b = 100 μA/cm^2, T_e = 0.025 eV, $I \sim 25$ eV, and r_0 = 10 μm, we obtain

$$\tau_D = 10^{-4}\ \text{s}, \quad \tau_r = 2 \times 10^{-9}\ \text{s}, \quad \Delta T_e \sim 5 \times 10^{-4}\ \text{eV} \approx 6\ \text{K}.$$

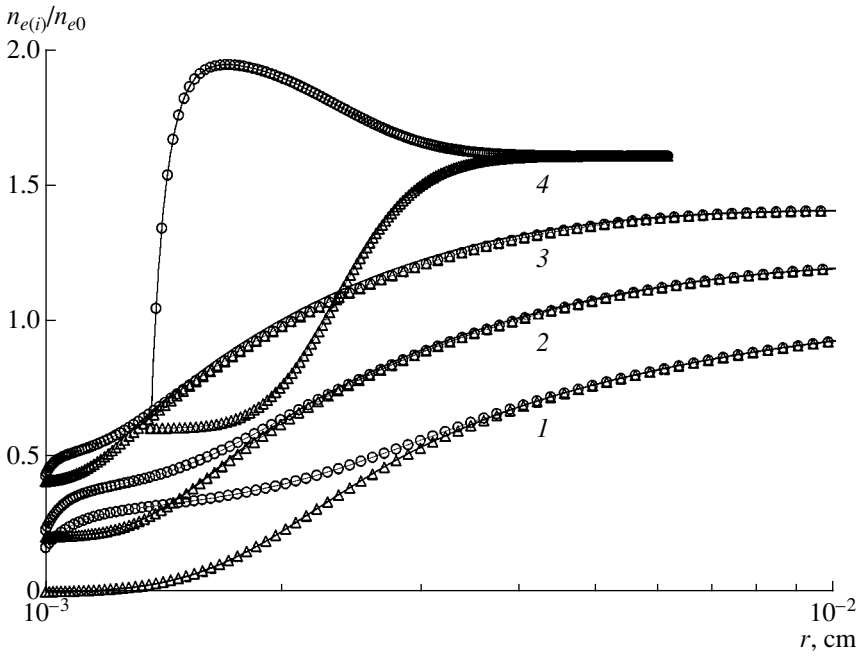

Fig. 6. Steady-state radial profiles of the electron (triangles) and ion (circles) densities and the Boltzmann electron density distribution (solid curves) in a He plasma for dust grains of radius 10 μm and for (*1*) $j_b = 1$ μA/cm^2 and $n_{e0} = 1.03 \times 10^{11}$ cm^{-3}, (*2*) $j_b = 10^2$ μA/cm^2 and $n_{e0} = 1.12 \times 10^{12}$ cm^{-3}, and (*3*) $j_b = 10^4$ μA/cm^2 and $n_{e0} = 1.61 \times 10^{13}$ cm^{-3}. Curves *4* were calculated for a Xe plasma with $Q_{\text{ion}} = 10^{16}$ cm^{-3} s^{-1} and for $r_0 = 13.6$ μm and $n_{e0} = 0.66 \times 10^{11}$ cm^{-3}. For convenience, the curves are shifted relative to each other by 0.2.

According to these estimates, even a slight temperature jump is capable of compensating for the reduction in the collisional energy loss due to a decrease in the electron density as the dust grain is approached. This result is a consequence of the facts that the characteristic dimension of the region where the electron density changes is governed by the ambipolar diffusion of the electrons and that the characteristic spatial scale on which the electron temperature changes is determined by the electron thermal conductivity, which is equal in order of magnitude to the free diffusion coefficient and is thus appreciably greater than the ambipolar diffusion coefficient. Consequently, the electron temperature T_e changes on substantially longer characteristic spatial scales than does the electron density n_e. In other words, due to the high thermal conduction, the electron temperature has enough time to be nearly equalized over the region of ambipolar diffusion near the dust grain. As a result, under the condition

$$\frac{\tau_D}{\tau_r} I \ll T_e \tag{34}$$

the electron temperature in the vicinity of the grain changes insignificantly. In this case, dust grain charging can be modeled under the assumption that the electron transport coefficients are constant, just as was done in [10]. Parenthetically, when the electrons are heated predominantly by an external electric field E_0, the applicability condition of the local method of moments has the form $T_e \gg eE_0 r_0$.

Recall that the OML model underestimates the charge of dust grains in a beam-produced helium plasma (Fig. 3). Note that, in the OML model, the charge of a grain is determined by its potential under the assumption that they are coupled to each other as in a vacuum. In Fig. 8, we plot the dust grain potentials obtained from our simulations and by using the OML model. A comparison of these results shows that they are in an unexpectedly close agreement. This can probably be explained as follows.

Our simulation results show that the electrons near a dust grain closely obey a Boltzmann distribution (Fig. 6). In this case, the effective boundary conditions imply that the steady-state electron flux onto the dust grain becomes Maxwellian:

$$J_e\big|_{r = r_0} \approx 4\pi r_0^2 \cdot \frac{n_e v_{T,e}}{4} = \pi r_0^2 v_{T,e} n_{e,\infty} e^{e\phi/T_e}, \tag{35}$$

which coincides with the electron flux obtained in the OML model [5]. Since the dust grain potential depends logarithmically on the ion flux, the potentials in our simulations are comparable to those in the OML model; moreover, the smaller the grain radius, the closer the agreement.

The relationship between the potential of the grain and its charge is given by the corresponding boundary

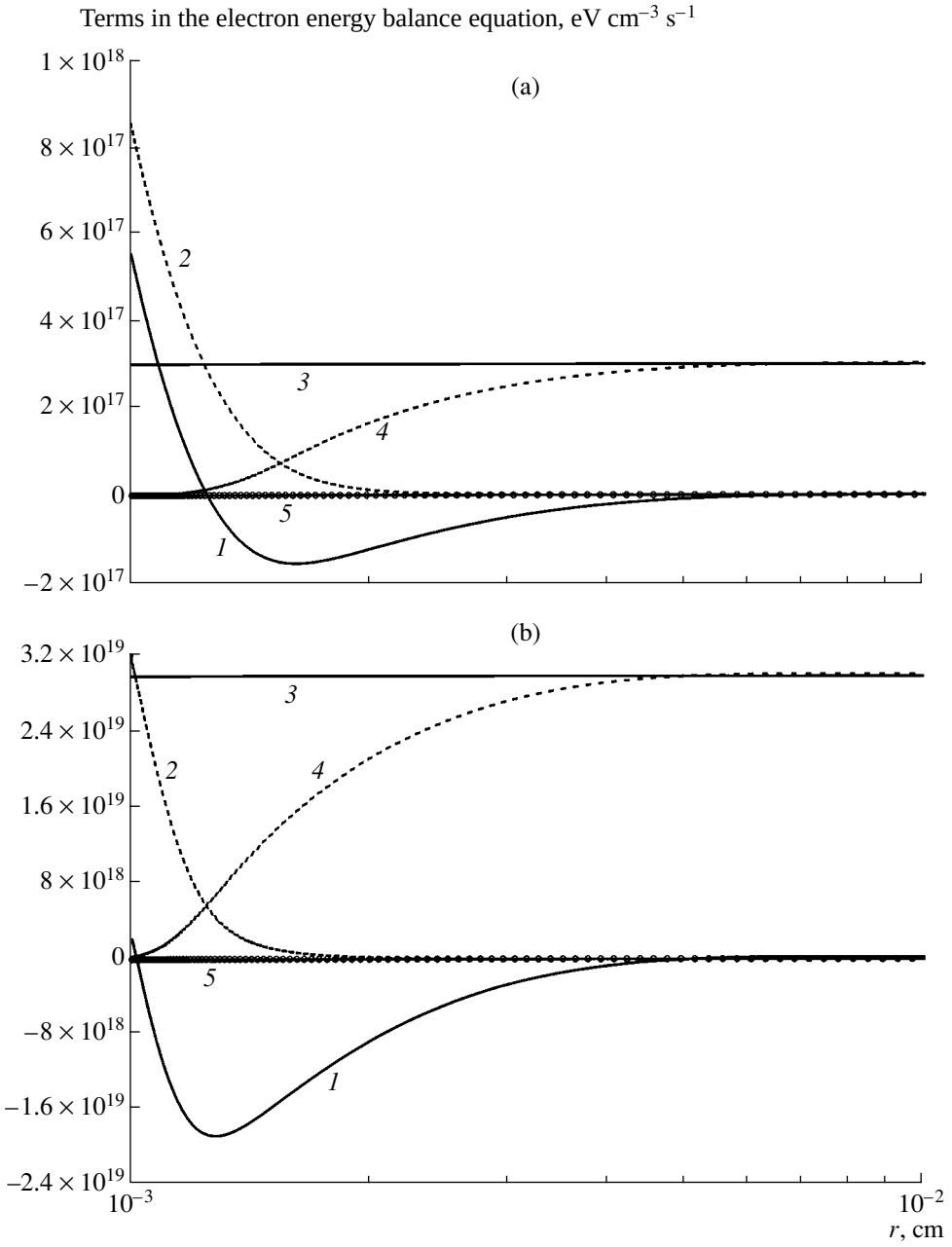

Fig. 7. Steady-state radial profiles of each of the terms, namely, (*1*) $T_1 = \nabla \cdot \mathbf{h}_e$, (*2*) $T_2 = -ej_eE$, (*3*) $T_3 = (\eta - I)Q_{\text{ion}}$, and (*4*) $T_4 = n_eW_S$, in the electron energy balance equation for a He plasma with dust grains with the radius $r_0 = 10$ μm for (a) $n_d = 10^5$ cm^{-3} and $j_b = 10^2$ μA/cm^2 and (b) $n_d = 2 \times 10^5$ cm^{-3} and $j_b = 10^4$ μA/cm^2. Curve *5* reflects the balance of all the terms, $T = T_1 + T_2 + T_3 - T_4$.

condition at the grain surface. In spherical geometry, the boundary condition has the form

$$\phi|_{r = r_0} = \frac{eq}{r_0} + 4\pi e\int_{r_0}^{\infty}(n_i - n_e)r\,dr, \qquad (36)$$

which shows that the dust grain potential is lower in absolute value than that obtained for the same grain charge in a vacuum. When the screening of the dust grain charge is described in the Debye–Hückel theory, we can see that, with allowance for the finite grain radius, the grain potential is a Derjaguin–Landau–Verwey–Overbeek (DLVO) potential [29]:

$$\phi = \frac{eq}{1 + r_0/R_d}\frac{1}{r}\exp[-(r - r_0)/R_D], \qquad (37)$$

where R_D is the Debye screening radius. Formula (37) yields the following relationship between the charge and the potential:

$$\phi|_{r=r_0} = \frac{eq}{r_0}\frac{1}{1+r_0/R_D}. \quad (38)$$

This relationship implies that the charge and the potential are coupled to each other as in vacuum only when $r_0 \ll R_D$. The table compares the dust grain charges calculated numerically, obtained in the OML model under the assumption of the vacuum coupling between the charge of the grain and its potential, and evaluated from relationship (38). The Debye screening length was determined from the parameters of the plasma electrons far from the dust grain. As can be seen, the assumption of vacuum coupling underestimates the charge computed numerically, while relationship (38) overestimates it. However, under the conditions adopted in our numerical simulations, the grain potential cannot be described by the Debye–Hückel linear theory and the relationship between the charge and the potential is far more complicated. It is for this reason that, even when the dust grain potential is known, determining the grain charge requires knowledge of the space charge distribution.

The above agreement between the grain potentials obtained in the hydrodynamic model and the OML model suggests ways in which the theory of dust grain charging can be extended to intermediate pressures such that the electron and ion mean free paths are comparable with the characteristic dimension of the problem. For this purpose, it is necessary to take into account, first of all, the ion and electron inertia, in which case Eqs. (17) should be supplemented with the equations for the directed velocities of charged plasma particles.

Figure 6 illustrates how the length of the ion sheath decreases with increasing ionization rate, which is proportional to the current density of a fast electron beam. This decrease is a consequence of a decrease in the Debye screening radius in a plasma, although the dust grain potential differs from the Debye potential, as can be seen from Fig. 9.

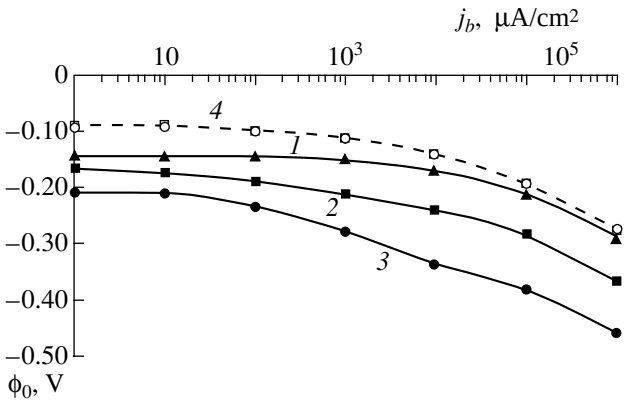

Fig. 8. Comparison between the potentials at the surfaces of dust grains with different radii of (*1*) 5, (*2*) 10, and (*3*) 20 μm as functions of the beam current density. Curve *4* shows the potential calculated in the OML model.

Figure 6 demonstrates an interesting feature of a beam-produced helium plasma: the region where the plasma is perturbed by the dust grain extends far beyond the ion sheath. This feature results from the high mobility of He_2^+ ions and the low rate of their recombination. Consequently, in a helium plasma, even dust grains whose concentration is about 10^3 cm^{-3} have an appreciable influence on the mean electron density, resulting in a decrease in the current density in a non-self-sustained discharge. This effect was observed experimentally in [10].

Figure 6 also presents radial profiles of the electron and ion densities near a dust grain in a xenon plasma at atmospheric pressure [11]. A comparison of profiles *1–3* with profiles *4* shows that, in contrast to a xenon plasma, in which the presheath does not form, in a helium plasma, there is a region far from the grain in which the diffusion of charged particles is ambipolar, which indicates the formation of a presheath [39]. In

Charge q of dust grains with the radius $r_0 = 10$ μm at different electron beam current densities j_b: (I) calculations with a nonlocal model of grain charging; (II) calculations in the OML model under the assumption of vacuum coupling between the grain charge and potential; and (III) calculations in the OML model according to relationship (38)

j_b, μA/cm^2		1	10	10^2	10^3	10^4	10^5	10^6
ϕ_{OML}, V		−0.087	−0.089	−0.095	−0.109	−0.137	−0.188	−0.272
$T_{e,0}$, K		304	311	335	387	497	700	1060
$n_{e,0}$, cm^{-3}		1.03×10^{11}	3.55×10^{11}	1.12×10^{12}	4.18×10^{12}	1.61×10^{13}	6.58×10^{13}	2.81×10^{14}
R_D, μm		2.64	1.44	0.842	0.467	0.270	0.159	0.094
q	I	-1.98×10^3	-2.48×10^3	-3.35×10^3	-4.79×10^3	-7.10×10^3	-1.08×10^4	-1.70×10^4
	II	-7.03×10^2	-7.19×10^2	-7.75×10^2	-8.95×10^2	-1.15×10^3	-1.62×10^3	-2.45×10^3
	III	-3.37×10^3	-5.72×10^3	-9.98×10^3	-2.00×10^4	-4.37×10^4	-1.04×10^5	-2.63×10^5

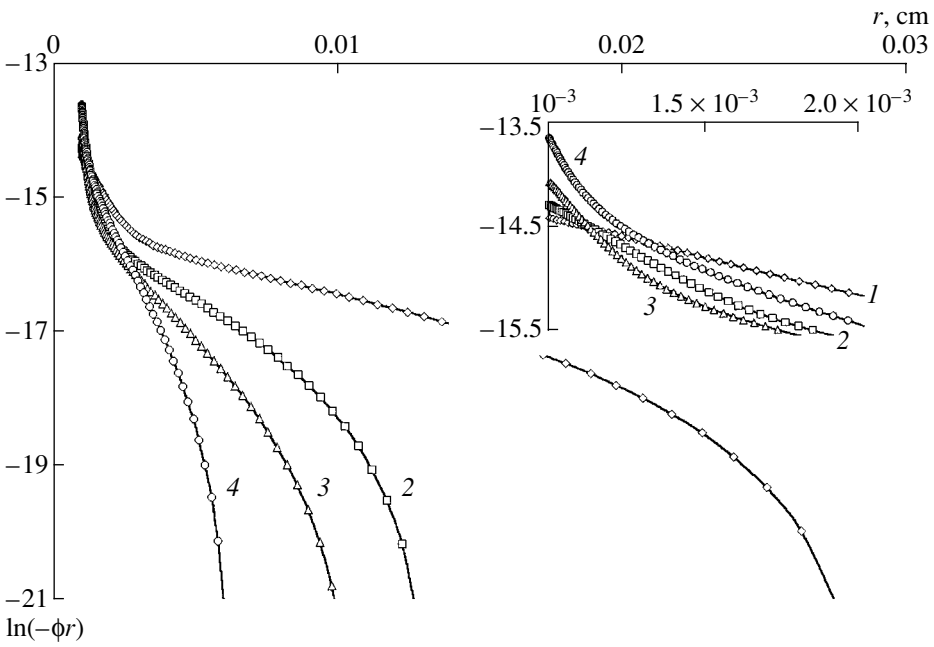

Fig. 9. Steady-state radial profiles of the potential of a solitary dust grain of radius 10 μm for j_b = (*1*) 1, (*2*) 10^2, (*3*) 10^4, and (*4*) 10^6 μA/cm^2.

order to understand such a large difference in behavior of the radial profiles of the charged-particle densities in helium and xenon, we consider Eqs. (6) and (9) in the local approximation in a steady state. In this case, one of the continuity equations becomes unnecessary and can be replaced with the equality

$$j_{e,r} = j_{i,r}. \tag{39}$$

Substituting expressions (7) and (10) for the electron and ion flux densities into equality (39) and neglecting ion diffusion, we obtain the electric field

$$E = -\frac{1}{(k_e n_e + k_i n_i)}\frac{\partial}{\partial r}(D_T n_e). \tag{40}$$

Using expression (40) and Poisson's equation (11), we transform the divergence term in ion continuity equation (9) into

$$-\frac{k_i}{(k_e n_e + k_i n_i)}\frac{\partial n_i}{\partial r}\frac{\partial (D_T n_e)}{\partial r} = Q_{\text{ion}} + \nu_{\text{ion}} n_e - \beta_{ei} n_e n_i - \beta_L n_i (n_i - n_e), \tag{41}$$

where $\beta_L = 4\pi e k_i$ is the Langevin recombination coefficient. Using Eq. (41), we establish whether the radial profile of the ion density has a maximum. Let us assume that the maximum does exist. In this case, the condition $\partial n_i/\partial r|_{r = r_m} = 0$ should be satisfied at the point r_m where the ion density is maximum; hence, for $\nu_{\text{ion}} = 0$, Eq. (41) yields

$$Q_{\text{ion}} - \beta_{ei} n_{e,m} n_{i,m} - \beta_L n_{i,m}(n_{i,m} - n_{e,m}) = 0, \tag{42}$$

where $n_{e,m}$ and $n_{i,m}$ are the electron and ion densities at the point $r = r_m$, respectively; moreover, it is physically clear that the following two conditions should hold: $n_{e,m} < n_{i,m}$ and $n_{i,m} > n_{i,0} = \sqrt{Q_{\text{ion}}/\beta_{ei}}$. The quadratic equation for $n_{i,m}$ has the only physically meaningful solution,

$$n_{i,m} = \sqrt{\frac{\beta_{ei}}{\beta_L} n_{i,0}^2 + \left[\frac{1}{2}\left(1 - \frac{\beta_{ei}}{\beta_L}\right) n_{e,m}\right]^2} + \frac{1}{2}\left(1 - \frac{\beta_{ei}}{\beta_L}\right) n_{e,m}. \tag{43}$$

Under the equality $\beta_{ei} = \beta_L$, solution (43) becomes $n_{i,m} = n_{i,0} = \sqrt{Q_{\text{ion}}/\beta_{ei}}$. In this case, the ion density over almost the entire presheath remains the same as that in an unperturbed plasma: it decreases only near the grain, i.e., in a region where the diffusive ion losses become significant. For $\beta_L > \beta_{ei}$, we find that $n_{i,m} < n_{i,0}$. This indicates that there can be no maximum in the radial profile of the ion density, which is in agreement with the results of our simulations for helium. Under the condition

$$\beta_{ei} > \beta_L \tag{44}$$

the maximum does exist; note that solution (43) gives $\lim_{n_{e,m} \to n_{i,0} - 0} n_{i,m} = n_{i,0} + 0$. In this case, the presheath (or the plasma region in which the transport of charged particles is ambipolar) does not form near the dust grain. In [11], simulations for xenon were carried out assum-

ing Xe_2^+ ions to be the most abundant in the plasma and the electron–ion recombination rate and ion mobility to be $\beta_{ei} = 2.3 \times 10^{-6}$ cm^3/s and $k_i = 0.55$ cm^2/V s, respectively. In this case, $\beta_L = 1.0 \times 10^{-6}$ cm^3/s and condition (44) is satisfied. Consequently, in a xenon plasma, the presheath does not form. According to Fig. 6, at the point at which the ion density is maximum, we have $n_{e,m} \ll n_{i,m}$, and solution (43) yields the estimate $n_{i,m}/n_{i,0} \approx \sqrt{\beta_{e,i}/\beta_L} \approx 1.5$. However, the value of this ratio obtained in simulations is somewhat smaller, $n_{i,m}/n_{i,0} \approx 1.34$, because we neglected ion diffusion, which plays an increasingly important role as the dust grain is approached.

7. CONCLUSION

Our investigations have shown that, in a helium plasma, the electron temperature in the vicinity of a dust grain varies only slightly. Consequently, under condition (34), dust grain charging in a beam-produced plasma can be described by assuming that the transport and kinetic electron coefficients, which should be determined from the parameters of an unperturbed plasma, are constant.

We have established that the dust grain charge is weakly sensitive to the secondary electron emission. We have shown that, because of the high ion mobility, dust grains strongly perturb a helium plasma; as a result, the presheath extends far beyond the ion sheath. This causes a drop in the mean electron density in a plasma even at dust densities of about 100–1000 cm^{-3}.

Our study has also shown that, in a beam-produced helium plasma, the dust grain potential calculated in the drift–diffusion model is close to that obtained in the OML model. We have found that, near a body perturbing the plasma, there may be no quasineutral plasma presheath and have determined the conditions under which this is the case in a beam-produced plasma. The phenomena revealed in our investigations are of interest for both the theory of dusty plasmas and the theory of probes.

ACKNOWLEDGMENTS

This work was supported in part by the Russian Foundation for Basic Research, project nos. 01-02-17726, 02-02-16758, and 00-15-96539.

REFERENCES

1. P. M. Shukla, Phys. Plasmas **8**, 1791 (2001).
2. A. Piel and A. Melzer, Plasma Phys. Controlled Fusion **44**, R1 (2002).
3. V. N. Tsytovich, Usp. Fiz. Nauk **167** (1), 57 (1997) [Phys. Usp. **40**, 53 (1997)].
4. Ch. Hollenstein, Plasma Phys. Controlled Fusion **42**, R93 (2000).
5. M. S. Barnes, J. H. Keller, J. C. Forster, *et al.*, Phys. Rev. Lett. **68**, 313 (1992).
6. O. V. Kozlov, *Electric Probe in Plasma* (Atomizdat, Moscow, 1969).
7. P. Chung, L. Talbot, and K. Touryan, *Electric Probes in Stationary and Flowing Plasmas* (Springer-Verlag, Heidelberg, 1975; Mir, Moscow, 1978).
8. B. V. Alekseev and V. A. Kotel'nikov, *Probe Plasma Diagnostics* (Énergoatomizdat, Moscow, 1988).
9. M. S. Benilov, in *Diagnostics of Low Temperature Plasma*, Ed. by M. F. Zhukov and A. A. Ovsyannikov (Nauka, Novosibirsk, 1994), p. 214.
10. V. V. Ivanov, A. F. Pal', T. V. Rakhimova, *et al.*, Zh. Éksp. Teor. Fiz. **115**, 2020 (1999) [JETP **88**, 1105 (1999)].
11. A. F. Pal', A. N. Starostin, and A. V. Filippov, Fiz. Plazmy **27**, 155 (2001) [Plasma Phys. Rep. **27**, 143 (2001)].
12. A. F. Pal', A. O. Serov, A. N. Starostin, *et al.*, Zh. Éksp. Teor. Fiz. **119**, 272 (2001) [JETP **92**, 235 (2001)].
13. J. H. Ingold, Phys. Rev. A **40**, 7158 (1989).
14. J. H. Ingold, Phys. Rev. E **56**, 5932 (1997).
15. J. H. Ingold, Phys. Rev. A **42**, 950 (1990).
16. J. H. Ingold, Phys. Rev. A **44**, 3822 (1991).
17. E. Kawamura and J. H. Ingold, J. Phys. D **34**, 3150 (2001).
18. A. V. Nedospasov, Usp. Fiz. Nauk **94**, 439 (1968) [Sov. Phys. Usp. **11**, 174 (1968)].
19. R. A. Haas, Phys. Rev. A **8**, 1017 (1973).
20. A. M. Popov, A. T. Rakhimov, and T. V. Rakhimova, Fiz. Plazmy **19**, 1241 (1993) [Plasma Phys. Rep. **19**, 651 (1993)].
21. J. P. Boeuf and L. C. Pitchford, Phys. Rev. E **51**, 1376 (1995).
22. M. S. Benilov, J. Phys. D **33**, 1683 (2000).
23. L. D. Tsendin, Zh. Éksp. Teor. Fiz. **66**, 1638 (1974) [Sov. Phys. JETP **39**, 805 (1974)].
24. N. L. Aleksandrov, A. P. Napartovich, and A. N. Starostin, Fiz. Plazmy **6**, 1123 (1980) [Sov. J. Plasma Phys. **6**, 618 (1980)].
25. N. L. Aleksandrov, A. M. Konchakov, A. P. Napartovich, and A. P. Starostin, *Plasma Chemistry*, Ed. by B. M. Smirnov (Énergoatomizdat, Moscow, 1984), Vol. 11, p. 3.
26. Yu. B. Golubovskiĭ, V. M. Zakharov, V. N. Pasunkin, and L. D. Tsendin, Fiz. Plazmy **7**, 620 (1981) [Sov. J. Plasma Phys. **7**, 340 (1981)].
27. N. A. Gorbunov, N. B. Kolokolov, and A. A. Kudryavtsev, Fiz. Plazmy **15**, 1513 (1989) [Sov. J. Plasma Phys. **15**, 881 (1989)].
28. L. G. H. Huxley and R. W. Crompton, *The Diffusion and Drift of Electrons in Gases* (Wiley-Interscience, New York, 1974).
29. A. F. Pal', D. V. Sivokhin, A. N. Starostin, *et al.*, Fiz. Plazmy **28**, 32 (2002) [Plasma Phys. Rep. **28**, 28 (2002)].

30. B. M. Smirnov, *Physics of Weakly Ionized Gases* (Nauka, Moscow, 1978).
31. G. I. Marchuk, *Methods of Computational Mathematics* (Nauka, Moscow, 1989; Springer-Verlag, New York, 1975).
32. A. A. Samarskiĭ and A. V. Gulin, *Numerical Methods* (Nauka, Moscow, 1989).
33. C. Cason, J. E. Perkins, A. H. Werkheizer, and J. Duderstadt, AIAA J. **15**, 1079 (1977).
34. V. A. Ivanov, Usp. Fiz. Nauk **162**, 35 (1992) [Sov. Phys. Usp. **35**, 17 (1992)].
35. B. M. Smirnov, *Ions and Excited Atoms in Plasma* (Atomizdat, Moscow, 1974).
36. B. M. Smirnov, Usp. Fiz. Nauk **170**, 495 (2000) [Phys. Usp. **43**, 453 (2000)].
37. V. Yu. Baranov, I. A. Belov, A. V. Dem'yanov, *et al.*, in *Izotopy*, Ed. by V. Yu. Baranov (IzdAT, Moscow, 2000), p. 626.
38. N. V. Dyatko, I. V. Kochetov, and A. P. Napartovich, Fiz. Plazmy **19**, 425 (1993) [Plasma Phys. Rep. **19**, 222 (1993)].
39. A. Engel, *Ionized Gases* (Clarendon, Oxford, 1955; Fizmatgiz, Moscow, 1959).

Translated by O.E. Khadin

Plasma Physics Reports, Vol. 29, No. 3, 2003, pp. 203–206. Translated from Fizika Plazmy, Vol. 29, No. 3, 2003, pp. 227–230.

PLASMA INSTABILITY

Dissipative Centrifugal Instability in a Rotating Conducting Atmosphere

S. L. Shalimov

Institute of Physics of the Earth, Russian Academy of Sciences, ul. Bol'shaya Gruzinskaya 10, Moscow, 123810 Russia

Received July 18, 2002

Abstract—It is shown that the earlier revealed dissipative centrifugal instability of large-scale two-dimensional vortex motions of a neutral gas in a rapidly rotating atmosphere may also occur for analogous motions of a weakly ionized gas in a magnetic field in the absence of dissipation, in which case it is necessary to take into account electrodynamic effects, namely, the induction drag and the gyroscopic force due to the Hall current. In a conducting atmosphere, strictly anticyclonic circulations occurring during dissipative centrifugal instability in a neutral atmosphere may not be possible or may even change into cyclonic circulations, depending on the value of the Hall conductivity. © *2003 MAIK "Nauka/Interperiodica".*

1. In generalizing the classical problem of a two-dimensional oscillator performing small oscillations in a rotating frame of reference (a Foucault pendulum [2]), Chefranov [1] revealed a new mechanism by which the oscillation amplitude increases exponentially when the oscillator frequency ω is lower than the rotation rate Ω of the noninertial frame. The origin of the name "dissipative centrifugal instability" (DCI) arises from the fact that, in order for this instability to occur, it is of fundamental importance that there be both a frictional force proportional to the velocity and a centrifugal force [1]. As was shown in [1], the equation for a two-dimensional oscillator models vortex solutions to the hydrodynamic equations for an incompressible fluid in the form of rigid rotations (in particular, on a sphere), which corresponds to the formation of large-scale vortex structures in the atmosphere and oceans. The distinctive feature of the DCI is that it causes vortex motions to become asymmetric, as is the case, e.g., with low-frequency anticyclonic Rossby vortices [3]. On rapidly rotating planets (such as Jupiter, Saturn, and Earth), large-scale vortex motions are observed to occur even in the upper layers of the atmosphere [4, 5]. However, the upper atmosphere of each of these planets is a weakly ionized gas (ionosphere) in the planet's magnetic field. That is why, in describing vortices in the ionosphere, it is necessary to take into account the electrodynamic forces resulting from the effect of the magnetic field on the induced current produced in a conducting medium moving in this field [6, 7]. The objective of the present paper is to investigate the development of a DCI in a rotating conducting atmosphere (ionosphere).

2. We will use a local Cartesian coordinate system associated with a rotating planet. The x and y coordinate axes are in a plane tangential to the planet's surface, the x-axis directed eastward, the y-axis directed northward, and the z-axis pointing to the zenith. In describing the ionospheric plasma, which is a weakly ionized gas, it is necessary to take into account not only Coriolis and centrifugal forces but also the ponderomotive force $[\mathbf{j}\mathbf{B}_0]/c$, associated with the effect of the magnetic field on the induced current produced in a conducting medium moving in this field [6, 7]. The current density is described by the expression [7]

$$\mathbf{j} = \sigma_0(\mathbf{E}'\mathbf{b}_0)\mathbf{b}_0 + \sigma_P[[\mathbf{b}_0\mathbf{E}']\mathbf{b}_0] + \sigma_H[\mathbf{b}_0\mathbf{E}'],$$

where $\mathbf{b}_0$ is a unit vector in the magnetic field direction; σ_0 is the longitudinal (along the magnetic field) conductivity; σ_P and σ_H are the Pedersen and Hall conductivities, respectively; and $\mathbf{E}' = \mathbf{E} + (1/c)[\mathbf{u}\mathbf{B}_0]$. With allowance for the Coriolis, centrifugal, and ponderomotive forces, the x and y components of the equations of motion for the ionospheric plasma in a rotating frame of reference have the form

$$\ddot{x} - \left(2\Omega + \frac{\sigma_H B_0 B_{0z}}{\rho c^2}\right)\dot{y} + \frac{\sigma_P B_0^2}{\rho c^2}\dot{x} + (\omega^2 - \Omega^2)x = -\frac{1}{\rho}\frac{\partial p}{\partial x},$$

$$\ddot{y} + \left(2\Omega + \frac{\sigma_H B_0 B_{0z}}{\rho c^2}\right)\dot{x} + \frac{\sigma_P B_{0z}^2}{\rho c^2}\dot{y} + (\omega^2 - \Omega^2)y = -\frac{1}{\rho}\frac{\partial p}{\partial y}$$

or, in other terms,

$$\ddot{\xi} + 2[\alpha + i(\Omega - \beta)]\dot{\xi} + (\omega^2 - \Omega^2)\xi = P, \qquad (1)$$

where $\xi = x + iy = r\exp(i\phi)$, $\dot{\xi} = \partial\xi/\partial t$, $P = -(1/\rho)(\partial p/\partial x + \partial p/\partial y)$, $\beta = \sigma_H B_0^2/2\rho c^2$, $\alpha = \sigma_P B_0^2/2\rho c^2$, Ω is the angular frequency of a rotating planet, B_0 is the magnetic field induction, and ρ is the density of the medium. In deriving Eq. (1), we used the condition $B_0 \approx B_{0z}$, which holds for middle and high latitudes, and neglected the rotational electric field in comparison with the MHD

1063-780X/03/2903-0203$24.00

dynamo electric field. We also took into account the quasineutrality of the ionospheric plasma, which allowed us to neglect the electrostatic field. Equation (1) differs from Eq. (1) of [1] in that it contains the term $-\beta$ on the left-hand side and the term P on the right-hand side.

The quantities α and β, which contain the conductivities σ_P and σ_H, account for the electrodynamic force. The component of this force that depends on the Pedersen conductivity σ_P determines the inductive deceleration [6], which is proportional to the velocity of the motion. Another component, which depends on the Hall conductivity σ_H, is responsible for the gyroscopic effect, acting as a Coriolis force but in the opposite direction [8]. The degree to which the flow of a conducting fluid is affected by the magnetic field in comparison with the effect of the viscosity can be estimated from the Hartman number G [7], whose square is $G^2 = \sigma_P B_0^2 L^2/\eta c^2$, where L is the scale on which the wind speed varies and $\eta = \nu\rho$ is the dynamic viscosity coefficient. For motions occurring on sufficiently large scales under conditions typical of planetary ionospheres, we have $G^2 \gg 1$; i.e., the neglect of conventional viscosity in the equations of motion is justified (the corresponding estimates will be given below).

In Eq. (1), we set $P = 0$, which corresponds to the so-called inertial wind approximation [9]. In this case, the solution to Eq. (1) has the form

$$\xi = C_1 \exp(\tau\gamma_1) + C_2 \exp(-\tau\gamma_2), \tag{2}$$

where

$$\gamma_{1,2} = \lambda(\bar\alpha, \bar\beta, \bar\omega) \mp \bar\alpha + i(1-\bar\beta)\left(\frac{\bar\alpha}{\lambda(\bar\alpha, \bar\beta, \bar\omega)} \mp 1\right),$$

$$\lambda(\bar\alpha, \bar\beta, \bar\omega) = \left(\frac{(\bar\alpha^2 - \bar\beta^2 - \bar\omega^2 + 2\bar\beta) + \sqrt{(\bar\alpha^2 - \bar\beta^2 - \bar\omega^2 + 2\bar\beta)^2 + 4\bar\alpha^2(1-\bar\beta)^2}}{2}\right)^{1/2},$$

$\bar\alpha = \alpha/\Omega$, $\bar\beta = \beta/\Omega$, $\bar\omega = \omega/\Omega$, $\tau = t\Omega$, and C_1 and C_2 are constants.

For $\bar\beta = 0$, the condition under which the equilibrium position ($x = 0$, $y = 0$) is unstable at $\bar\omega < 1$ was derived in [1]: $\lambda(\bar\alpha, 0, \bar\omega) > \bar\alpha$ (for $\tau \gg 1$, this corresponds to an unstable focal point). The rotation frequency is equal to $\dot\phi = -\Omega[1 - \bar\alpha/\lambda(\bar\alpha, 0, \bar\omega)]$; hence, $\dot\phi$ and Ω have opposite signs (anticyclonic rotation) and $|\dot\phi| < \Omega$. In this case, the most unstable mode is that with the frequency $\omega = 0$, because it is corresponds to the maximum value $\lambda_{max} = \lambda(\bar\alpha, 0, 0)$. It is only when $\bar\alpha \neq 0$ that the instability may occur and that ξ may increase along the trajectories of anticyclonic motion in the (x, y) plane, because, as $\bar\alpha \longrightarrow 0$ (and $\bar\alpha \longrightarrow \infty$), $\lambda(\bar\alpha, 0, 0) - \bar\alpha \longrightarrow 0$.

For $\bar\beta \neq 0$, it is not necessary to impose the condition $\bar\alpha \neq 0$ for the onset of instability. In fact, let us assume that $\bar\alpha = 0$. Then, the condition for the onset of instability has the form $\lambda(0, \bar\beta, \bar\omega) > 0$. For $\bar\omega < 1$, this gives a new range of instability:

$$\frac{1}{2}\bar\omega^2 < \bar\beta < 2 - \frac{1}{2}\bar\omega^2; \tag{3}$$

moreover, from solution (2), we can see that, for $\tau \gg 1$, the rotation frequency is equal to

$$\dot\phi = -\Omega(1-\bar\beta)\left[1 - \frac{\bar\alpha}{\lambda(\bar\alpha, \bar\beta, \bar\omega)}\right]. \tag{4}$$

Therefore, anticyclonic circulations are also possible when $\bar\alpha = 0$, provided that $\bar\beta < 1$, in which case it is necessary to take into account the lower limit of the range of instability (3). For $\bar\beta > 1$, but with allowance for the upper limit of the range of instability (3), the circulations are cyclonic.

For the general case $\bar\alpha \neq 0$ and $\bar\beta \neq 0$ and for the most unstable mode with $\omega = 0$, the dependence of the growth rate $\lambda(\bar\alpha, \bar\beta, 0) - \bar\alpha$ on the parameters $\bar\alpha$ and $\bar\beta$ has the form

$$\lambda(\bar\alpha, \bar\beta, 0) - \bar\alpha = \sqrt{\bar\beta(2-\bar\beta)} - \bar\alpha + O(\bar\alpha^2/\bar\beta^2),$$
$$\bar\alpha \ll \bar\beta;$$

$$\lambda(\bar\alpha, \bar\beta, 0) - \bar\alpha = \bar\alpha\left(\sqrt{\frac{1+s}{2}} - 1\right)\left[1 + \frac{1}{\bar\beta}\left(\frac{1}{s} + \sqrt{\frac{2}{1+s}}\right)\right] + O(\bar\beta^2/\bar\alpha^2),$$
$$\bar\alpha \gg \bar\beta;$$

where $s = \sqrt{1 + 4/\bar\alpha^2}$.

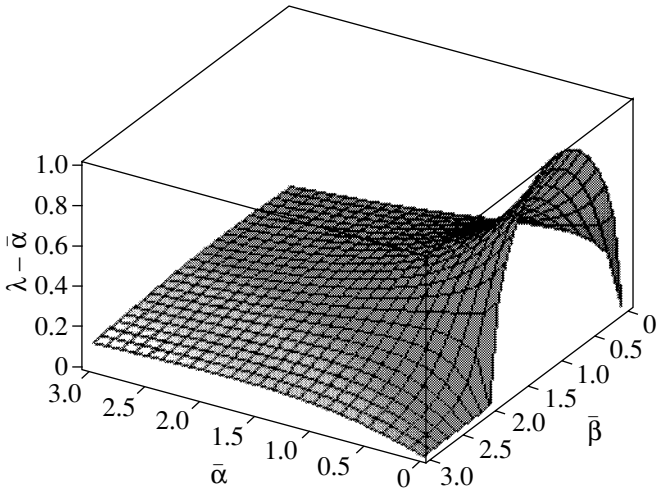

Fig. 1. A graphical illustration of the instability growth rate $\lambda(\bar{\alpha}, \bar{\beta}, 0) - \bar{\alpha}$.

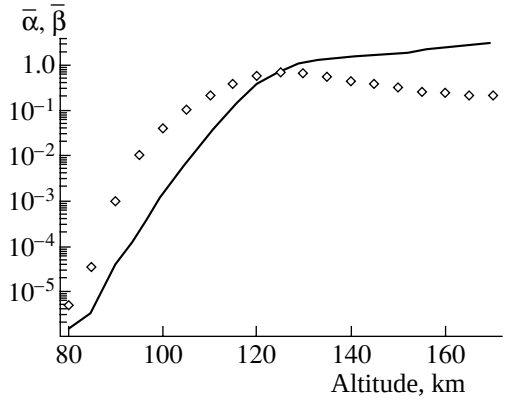

Fig. 2. Variations of the parameters $\bar{\alpha}$ (solid curve) and $\bar{\beta}$ (dotted curve) with altitude in the daytime midlatitude ionosphere (at solar maximum). The plots were calculated using the standard ionosphere and atmosphere models, IRI-90 and CIRA-72, from the World Data Center in Kyoto.

The growth rate of the most unstable mode with $\omega = 0$ in the general case is illustrated graphically in Fig. 1. We can see that the instability originates predominantly in the region ($\bar{\alpha} < 1, 0 < \bar{\beta} < 2$), in accordance with inequalities (3). At $\bar{\alpha} = 0$ and $\bar{\beta} = 1$, the instability growth rate is the fastest: $\lambda(\bar{\alpha}, \bar{\beta}, 0) - \bar{\alpha} = 1$. Hence, in this case, the dissipative term $\bar{\alpha} \neq 0$ reduces the instability growth rate (rather than increases it, as is the case with the DCI of a neutral gas [1]).

Now, we consider the case $\bar{\alpha} \neq 0$ and $\bar{\beta} \neq 0$ and set $\bar{\beta} = 1$. In this case, as follows from Eqs. (2) and (4), the instability can also occur; however, instead of an unstable focal point, Eq. (1) has a saddle-point singularity; i.e., rotations in the (x, y) plane are impossible.

Let us estimate the angular momentum in the (x, y) plane about the z axis. This momentum is equal to $M_z = r^2(\dot{\phi} + \Omega)$, where $r = r_0\exp\{\tau[\lambda(\bar{\alpha}, \bar{\beta}, \bar{\omega}) - \bar{\alpha}]\}$. Accordingly, taking into account expression (4), we obtain

$$\dot{M}_z = 2r^2\Omega\{\operatorname{sgn}\dot{\phi}\bar{\alpha}\dot{\phi} + [\lambda(\bar{\alpha}, \bar{\beta}, \bar{\omega}) - \bar{\alpha}]\Omega\}.$$

This indicates an exponential increase in $\dot{M}_z$ under the instability conditions $\bar{\omega} < 1$ and $\lambda(\bar{\alpha}, \bar{\beta}, \bar{\omega}) > \bar{\alpha}$; i.e., the angular momentum is not an integral of motion. For $\bar{\alpha} = 0$, we have $\dot{M}_z = 2r^2\Omega^2\bar{\beta}\lambda(0, \bar{\beta}, \bar{\omega})$ and the instability is also possible.

3. Here, we analyze DCI in the limiting cases that are of interest for geophysical applications.

Let us consider the case $\bar{\alpha} \neq 0$ and $\bar{\beta} = 0$. Setting $\omega = 0$ in Eq. (1), we immediately see that the physical reason for the instability is associated with the presence of waves with negative energy and, accordingly, with a negative frequency shift (we note that in plasma physics, the possible existence of such waves was pointed out by Kadomtsev *et al.* [10]). For a small frequency shift, we have $\delta\Omega \approx (\alpha\Omega)^{1/2}$. However, the instability can be suppressed by dispersion, which was not taken into account in the above analysis. In the case in question, the dispersion is on the order of $\Omega(k_\perp r_R)^2$ [11], where $k_\perp$ is the horizontal component of the wave vector and r_R is the Rossby–Obukhov radius. The instability can occur for $\delta\Omega > \Omega(k_\perp r_R)^2$. Under this condition, waves with frequencies close to Ω can be generated due to the negative frequency shift. The wavelength of large-scale two-dimensional vortex circulations should satisfy the inequalities $k_\perp H_0 < 1 < k_\perp R$ [11], where H_0 is the atmospheric height scale and R is the planet's radius. For Jupiter, we have $R = 70000$ km and $r_R = 6000$ km (at the latitude at which the Great Red Spot is centered); i.e., $r_R/R \leq 0.1$. For the Earth, we have $r_R \approx 1900$–3000 km (depending on the latitude); hence, at sufficiently high latitudes, $r_R/R \approx 1/3$. Accordingly, for the waves under discussion, the dispersion term $\Omega(k_\perp r_R)^2$ is small in comparison with the frequency Ω in Jupiter's atmosphere and, for the Earth's atmosphere, we have $\Omega(k_\perp r_R)^2 > \Omega/9$. This implies that, in Jupiter's atmosphere, the conditions for wave generation are more favorable. In the Earth's atmosphere, waves can be generated under the condition $\delta\Omega \approx (\alpha\Omega)^{1/2} > \Omega/9$, which gives $\bar{\alpha} > 1/81$. The altitude variations of $\bar{\alpha}$ in the Earth's ionosphere are shown by the solid curve in Fig. 2. We can see that, in the case $\bar{\alpha} \neq 0$ and $\bar{\beta} = 0$, the conditions for the onset of instability in the Earth's lower ionosphere are satisfied at altitudes above about 100 km.

The parameter $\bar{\alpha}$ in Eq. (1) describes the inductive, rather than viscous, drag, because, for large-scale ionospheric circulations with $L \geq 10^2$ km, which we are

interested in here, the viscous forces can be neglected in comparison with the electromagnetic forces. To be specific, for the parameter values $\sigma_P = 5 \times 10^{-5}$ S/m = 4.5×10^5 s^{-1}, $\eta = 3 \times 10^{-4}$ g/(cm s), and $B_0 = 0.5$ G, typical of the altitudes at which the degree of ionization in the E region is maximum, and for $L \approx 10^2$ km, the squared Hartman number turns out to be $G^2 \approx 40$.

At altitudes of about 90 to 125 km, the ionospheric plasma satisfies the inequality $\sigma_H \gg \sigma_P$ [12, 13]. Consequently, for this altitude range, we have $\bar{\alpha} \ll \bar{\beta}$ and the contribution of the Pedersen current to the electromagnetic force can usually be neglected. In this case, in accordance with inequalities (3) and expression (4), the development of the instability is determined by the parameter $\bar{\beta}$.

Now we consider the case $\bar{\beta} \neq 0$ and $\bar{\alpha} = 0$. Setting $\omega = 0$ in Eq. (1), we see that the negative frequency shift is equal to $\delta\Omega = \beta$ and is not associated with the frictional force. The condition $\delta\Omega > \Omega(k_\perp r_R)^2$, which serves to cancel the dispersion effect, changes the lower bound of the range of instability (3) for the fastest growth rate; i.e., for the Earth's ionosphere, we have $\bar{\beta} > 1/9$. The altitude variations of the parameter $\bar{\beta}$ at midlatitudes in the ionosphere are shown by the dotted curve in Fig. 2. One can see that, at altitudes higher than about 105 km, this parameter is $\bar{\beta} > 1/9$ and, in the altitude range 115–125 km, it is close to (but remains less than) unity. Let us estimate the plasma density required to satisfy the condition $\bar{\beta} = 1$. Setting the density of the medium at these altitudes equal to $\rho = (1–3) \times 10^{-11}$ g/cm^3 and the rotation rate equal to $\Omega = 7 \times 10^{-5}$ s^{-1}, we arrive at the following estimate of the plasma density: $n = (1.8–5.3) \times 10^5$ cm^{-3}. At midlatitudes, the density of the ionospheric plasma is usually somewhat lower than even the lowest value in this estimate. However, the estimated density values are typical of high latitudes in the ionosphere [14] and, in the nighttime midlatitude ionosphere, such densities are observed in the so-called sporadic E layers [12, 13], which are in the ionospheric E region, as implied by their name. Since the value $\bar{\beta} = 1$ determines an upper bound on the rate of anticyclonic circulations, the fact that, according to the above estimates, it is possible to exceed this value allows us to conclude that, in the nighttime midlatitude E region of the ionosphere and in the lower ionosphere at high latitudes, anticyclonic wind circulations may, in principle, change into cyclonic winds, which is consistent with observations [15].

Hence, in the equations describing the dynamics of the conducting atmosphere, it is necessary to take into account the $[\mathbf{jB}_0]$ ponderomotive force associated with the effect of the planet's magnetic field on the induced current produced in a conducting medium moving in this field [6]. Under the action of the ponderomotive force, the geostrophic wind changes its nature (due to the Hall currents) and the wind streamlines deviate from those of the geostrophic wind as a result of the inductive deceleration (caused by the Pedersen currents), which plays a more important role in the Earth's ionosphere than the viscous drag [8]. Accordingly, the earlier revealed DCI of large-scale two-dimensional vortex motions of a neutral gas in a rapidly rotating atmosphere [1] also changes its nature: for analogous motions of a weakly ionized gas in a magnetic field, when it is necessary to take into account electrodynamic effects, this DCI may take place even in the absence of dissipation; in a conducting atmosphere, strictly anticyclonic circulations occurring during the DCI in a neutral atmosphere may not be possible or may even change into cyclonic circulations, depending on the value of the Hall conductivity.

ACKNOWLEDGMENTS

I am grateful to the reviewer for valuable remarks.

REFERENCES

1. S. G. Chefranov, Pis'ma Zh. Éksp. Teor. Fiz. **73**, 312 (2001) [JETP Lett. **73**, 274 (2001)].
2. L. D. Landau and E. M. Lifshitz, *Mechanics* (Nauka, Moscow, 1988; Pergamon, New York, 1988).
3. M. V. Nezlin and E. N. Snezhkin, *Rossby Vortices and Spiral Structures* (Nauka, Moscow, 1990).
4. K. H. Baines, R. W. Carlson, and E. C. Newman, BAAS **30**, 64 (1998).
5. A. D. Danilov, E. S. Kazimirovskiĭ, G. V. Vergasova, and G. Ya. Khachikyan, *Meteorological Effects in Ionosphere* (Gidrometeoizdat, Leningrad, 1987).
6. T. G. Cowling, *Magnetohydrodynamics* (Interscience, New York, 1957; Inostrannaya Literatura, Moscow, 1959).
7. L. D. Landau and E. M. Lifshitz, *Electrodynamics of Continuous Media* (Nauka, Moscow, 1982; Pergamon, New York, 1984).
8. V. P. Dokuchaev, Izv. Akad. Nauk SSSR, Ser. Geofiz. **5**, 783 (1959).
9. G. J. Haltiner and F. L. Martin, *Dynamical and Physical Meteorology* (McGraw-Hill, New York, 1957; Inostrannaya Literatura, Moscow, 1960).
10. B. B. Kadomtsev, A. B. Mikhaĭlovskiĭ, and A. V. Timofeev, Zh. Éksp. Teor. Fiz. **47**, 2266 (1964) [Sov. Phys. JETP **20**, 1517 (1965)].
11. V. I. Petviashvili and O. A. Pokhotelov, *Solitary Waves in Plasma and Atmosphere* (Énergoatomizdat, Moscow, 1989).
12. B. N. Gershman, *Ionospheric Plasma Dynamics* (Nauka, Moscow, 1974).
13. M. C. Kelley, *The Earth Ionosphere: Plasma Physics and Electrodynamics* (Academic, San Diego, 1989).
14. P. C. Anderson, A. B. Christinsen, J. H. Hecht, *et al.*, J. Geophys. Res. **100**, 17265 (1995).
15. A. Ivanovskiĭ, A. Repnev, and E. Shvidkovskiĭ, *Kinetic Theory of the Upper Atmosphere* (Nauka, Leningrad, 1967).

Translated by O.E. Khadin

Plasma Physics Reports, Vol. 29, No. 3, 2003, pp. 207–210. From Fizika Plazmy, Vol. 29, No. 3, 2003, pp. 231–235.

NEW TRENDS IN PLASMA PHYSICS

Fundamental Physics with an X-ray Free Electron Laser[1]

T. Tajima

Advanced Photon Research Center, JAERI, Kizu, Kyoto, 619-0215 Japan

Received August 19, 2002

Abstract—Of late, laboratories around the world are considering building X-ray free electron lasers based on high energy electron accelerators (with energies exceeding 10 GeV) to produce bright coherent X rays with wavelengths on the order of 1 Å. Because of the extremely small wavelength and high brilliance of these coherent X rays, there is an unprecedented opportunity to explore new applications of what is sometimes called the fourth generation of light sources. Here, we point out that in addition to the anticipated applications to material science and biology, a number of applications to fundamental physics may become possible in the fields of extreme high-energy accelerating gradients, ultrahot matter creation, coherent γ-ray generation, violent acceleration and "horizon physics," and nonlinear field theory (quantum electrodynamics). Intensive development in technical areas, particularly that of X-ray optics, will be needed, however, in order to achieve ultrahigh intensity X-rays that can allow these applications. *© 2003 MAIK "Nauka/Interperiodica".*

1. X-RAY FREE-ELECTRON LASER

The rapid growth in the demand for synchrotron radiation and the successful employment of wiggler devices in light sources have allowed the development stage often called the "third generation" of accelerator-based light source facilities to be reached, following the first- and second-generation sources that used bending magnets with electron bunches from storage rings. Third-generation X-ray sources are capable of generating radiation in the 1- to 10-nm wavelength range. On the drawing board for X-ray free-electron lasers (FEL) driven by a high energy electron accelerator, however, are devices that will deliver even shorter wavelength X-rays with much higher brightness, often called the fourth-generation sources. These include the plan for the Linac Coherent Light Source (LCLS), being designed by the Stanford Linear Accelerator Center, the Lawrence Livermore National Laboratory, and several other collaborating institutions, as well as the DESY plan of Germany. For example, the LCLS calls for a wavelength of 1.5 Å, pulse duration of 230 fs, peak power of 9 GW, and peak brightness of 10^{33} photons/(s mm^2 mrad^2) in a bandwidth of 0.1%. Clearly, these impressive parameters are orders of magnitude higher in the energy and brightness of X rays than those of existing facilities [1]. As impressive as these are, Chen and Pellegrini [2] have ventured the opinion that an even higher performance might be theoretically possible by increasing the FEL energy extraction (by the tapered undulator technique) and a yet unspecified method of diffraction-limited X-ray focusing. Chen and Pellegrini [2] suggested that X-ray laser intensities of 10^{24}–10^{28} W/cm^2 are theoretically possible. At present, available technology does not allow such fantastic intensities, mostly because the current X-ray optics do not allow diffraction-limited focusing. With some development effort, intensities of 10^{17} W/cm^2 can be reached [3] and, with some major effort, intensities of 10^{23} W/cm^2 might be possible [3, 4]. This prospect, however remote it might be from becoming reality, would represent a major demarcation from the previous generations of light sources. The reason is that, in addition to applications to material sciences and life sciences, an X-ray FEL could be employed to probe some of the questions that touch on fundamental physics issues. These are high-field science applications of the X-ray FEL, taking advantage of not only the high energy and coherency of photons, but also their extreme high fields, which interact with matter in a unique way. In this regard, there has been recent theoretical suggestion of creating intense incoherent petawatt X rays by irradiating intense petawatt laser on a metal [5].

If and when the intensity of FEL X-rays can be increased as some of the above scenarios indicate, there will be unprecedented opportunities to use these intense X-rays in order to explore some of the issues of fundamental physics that have eluded man's grasp so far. In the present article, we list a few examples of these applications. If optical laser physics is any guide, remarkable new phenomena emerge when the laser intensity approaches the relativistic regime. In the optical wavelength range, the so-called "high-field science" regime begins to occur at intensities of 10^{14}–10^{15} W/cm^2, where some new atomic physics and plasma physics phenomena have been observed. At around 10^{18} W/cm^2, relativistic effects fully enter into the dynamics. Since the frequency of the X-ray FEL of LCLS is four orders higher than that of an optical laser, the corresponding intensities would be 10^{22}–10^{23} W/cm^2 and 10^{26} W/cm^2, respectively. These inten-

[1] This article was submitted by the author in English.

1063-780X/03/2903-0207$24.00 © 2003 MAIK "Nauka/Interperiodica"

sities are very high as compared with the prospective high intensity anticipated at LCLS, namely, 10^{17} W/cm^2. We point out that even though progress to achieve such a lofty goal is rather slow and laborious, the rewards that may be derived in this unique regime are so extraordinary that looking into LCLS's extension of X-ray FEL to this regime merits serious consideration.

2. EXTREME HIGH-ENERGY ACCELERATING GRADIENT

For the X rays of LCLS, the X-ray frequency is so high that even the density of metallic electrons is subcritical. As has been pointed out in [6, 7], short X-ray bursts in a metal are capable of exciting a wake field inside the metallic electrons. The wake field may be accentuated by the seeding technique [8]. The wake field strength is proportional to the square root of the electronic density:

$$E = (n/n_{18})^{1/2} a_0^2 \text{ GeV/cm}, \quad (1)$$

where n_{18} is the density in units of 10^{18} cm^{-3}, a_0 is the normalized vector potential $eE_0/m\omega_0 c$ of the X-ray FEL, E_0 and ω_0 are the electric field and frequency of the X-ray laser, e is the electron charge, and m is the electron rest mass. When the laser becomes relativistic, a_0 approaches unity. If the electron density of a metal is $n = 10^{24}$ cm^{-3}, the wake field electric field amounts to

$$E = a_0^2 \text{ TeV/cm}. \quad (2)$$

Let us consider one example of how we can take advantage of this tremendous accelerating gradient induced by LCLS X rays. By creating a nanohole in a metal, the electron density in the nanohole is slightly below the surrounding density. If the metal is chosen such that the electron density is 10^{23} cm^{-3}, then the dephasing length of an electron with the X-ray wake field is on the order of 10 cm, because the plasma wavelength is on the order of 100 nm. If X rays are focused into the nanohole and kept focused either by the self-focusing mechanism or by the geometrical optics of the nanohole itself, then, over the length of a metallic slab of thickness d, the energy gain by this X-ray wake field through the slab nanohole is deE. If we choose the slab thickness to be 10 cm, the electron energy gain can be as great as $3a_0^2$ TeV. If the laser is relativistic, the energy gain is 3 TeV through a 10-cm slab.

One may be able to study beam dynamics under channeling conditions (and dechanneling conditions) [9]. For example, Huang *et al.* [10] suggested the possibility of beam cooling due to radiation channeling. In addition, the longitudinal component of intense X-ray fields can itself be employed as the accelerating gradient [11] if the crystal is appropriately designed with the use of emerging nanotechnology.

3. ULTRAHOT MATTER

The irradiation of relativistic X-rays on a metallic target should exhibit a remarkable phenomenon. As is well known, hard X rays, such as those from the X-ray LCLS, will penetrate any material over a long distance. However, when the X-ray intensity is raised to the extent of becoming relativistic, the absorption of X rays suddenly becomes very efficient. This phenomenon was discovered in the laser–cluster interaction [12–15]. The effective cluster radius for laser absorption is 10 nm–1 μm. We now apply this knowledge from relativistic laser–cluster interaction to the interaction of a relativistic X-ray laser with atoms. For an optical laser interacting with nano- and microclusters, the physics of strong interaction between the electromagnetic (EM) waves and clusters was investigated in [16]. When the applied EM field is sufficiently strong [17], the electron wave function is skewed in the tilted nuclear Coulomb potential and the electron can tunnel through the potential barrier and become ionized. This is Coulomb-barrier suppression ionization. This process creates ionized itinerant electrons instantly (within a femtosecond). These free electrons create a large polarization field, because ions in the cluster are immobile over this short time scale. Due to the combined effects of the large cluster polarization and the strong laser EM fields, the orbits of the itinerant electrons become chaotic (orbital stochasticity) [16]. This stochasticity of the electrons that carry the bulk of the laser energy implies the instantaneous absorption of the laser energy. Particle-in-cell simulations show this process and indicate extraordinarily high laser absorption by clusters [16].

With a four orders of magnitude reduction in the scales, the cluster size of 1 μm transforms into 1 Å, the size of an atom. The size of the inner-shell electron orbitals is a fraction of this. Thus, metallic atoms become very efficient absorbers of X rays, just as clusters are efficient absorbers of optical lasers. Typically, relativistic laser light is absorbed by several layers of clusters. Thus, we expect that relativistic X rays will be absorbed by several atomic layers. The range of high-energy X rays in a metal is quite long (a matter of fractions of mm). However, we expect the range to be a strong function of the X-ray intensity, a_0^2. As a_0 increases and approaches unity, the range rapidly decreases toward nm. The typical absorption rate by several layers exceeds 50%. If 1 J of X-ray energy is suddenly absorbed by a 1-μm^2 square area of thickness 1 nm, this amounts to a typical energy deposition of a couple of GeV per particle (or nucleon). The physics of this regime of X-ray laser–matter interaction may be called a *driven quantum liquid.* The matter so created is extraordinarily hot. Such matter not only generates copious positrons, but perhaps gives rise to exotic matter such as quark–gluon plasma.

4. GAMMA RAYS

Similar irradiation of strong X-rays on a metal target should lead to the copious emission of γ rays. The energy conversion rate from X rays to γ rays is very high, probably in excess of 50%. The X-ray laser-driven quantum liquid, as we mentioned above, gives rise to temporary coherent periodic bremsstrahlung emission of γ photons. With a clever manipulation of the target and the laser frequency, it may be possible to change these γ rays into coherent γ rays. Since X rays are so intense and their conversion efficiency so high, one would expect extremely brilliant γ rays. These γ rays may be utilized to investigate various nuclear physics issues. These issues may include (i) the less trodden paths of (γ, *n*) and (γ, *p*) processes (rather than neutron capture processes) [18], (ii) the excitation of giant resonances of nuclei, (iii) excitation of isomers such as Hf and Ta (and their relevance to the cosmic synthesis of heavier elements) [19–21], (iv) the measurement of cross sections of photonuclear reactions [22], and (v) the possible detection of parity nonconservation [17, 23].

5. NONLINEAR QUANTUM ELECTRODYNAMICS AND THE RECREATION OF ASTROPHYSICAL CONDITIONS

With a sufficiently strong X-ray laser, the electric field of the laser begins to polarize the vacuum, causing the vacuum to "split." This causes spontaneous generation of copious electron positron pairs. Nonlinear field theory may then be studied.

An X-ray FEL in the relativistic regime is able to access astrophysical conditions that, so far, are only dreamt of, such as conditions not so far removed from those at the site of a gamma-ray burst (GRB). The above techniques can give rise to the X-ray irradiance so high that it resembles that of a GRB. In the case of a typical GRB, it is believed that γ rays (about 100-keV energy) have a flux of 10^{30} W/cm^2. This intensity corresponds to the field strength of the Schwinger field, $E_S = mc^2/\lambda_C$, where λ_C is the Compton wavelength h/mc. At or near the Schwinger field, the fluctuating vacuum polarization may be ripped open, so that the copious production of electron–positron pairs occurs. The fact that the most intense astronomical emitter of energy, GRB, has this field intensity is therefore not a coincidence. Also, γ rays are just about relativistic at this energy, yielding an a_0 of about unity for 100-keV γ rays. The intensity of FEL X rays (10 keV for LCLS), if relativistic, also has an a_0 of on the order of unity. Thus, the nonlinearity of photons in a GRB and that of FEL X rays are in the same ballpark. There are other astrophysical extreme conditions that may be recreated by X-ray FELs, such as LCLS. See more examples in [24].

6. VIOLENT ACCELERATION, GRAVITY, AND HORIZON PHYSICS

The acceleration by the electric field of a relativistic laser is so enormous that an electron may be accelerated sideways with a gradient similar to that near the surface of a black hole horizon. As was demonstrated in [25], proper setup of a standing X-ray laser will cause such a large acceleration that the electron in the accelerated frame of reference feels a tremendous equivalent gravity. This causes the horizon of the electron to emerge at a finite distance. This is the fundamental reason why Unruh radiation arises, which is a sister phenomenon to Hawking radiation from a black hole horizon. Perhaps, we could peek into the physics at a horizon, just like that at a black hole horizon. Some of the interesting questions to ask include the following: (i) Can we confirm the predicted existence of Unruh radiation? (ii) What is the spectrum of Unruh radiation? Is it blackbody radiation or that of Chen–Tajima [25]? Is there a deficit of radiation due to new physics such as the leakage into extra dimensions [26]? Because a violently accelerated electron sees the horizon shrink to a finite distance in the direction opposite to that of the acceleration, the gravitational (or equivalent accelerating) field within the distance to the horizon may obey a law different from that of our daily Gauss's law. This different law may be manifested in the spectrum of Unruh radiation.

7. CONCLUSION

In conclusion, we have speculated about various possibilities for applying the upcoming X-ray FELs to high-field science. If and when the technology of X-ray optics and other associated X-ray FEL systems is advanced to make the intensity of X rays to become nearly relativistic, there will be a new class of applications that can investigate fundamental physics issues from a novel perspective. In addition, a similar deployment of undulators for a future high energy electron accelerator such as an NLC (Next Linear Collider) can stretch the X-ray (or γ-ray) energy up to ~100 keV. A technique for generating ultrashort electron bunches will facilitate such a deployment in the future. Although we have focused on high-energy X-ray FELs in the regime of keV (or beyond), most of the applications mentioned here also are relevant for FELs with photon energies in the 10- to 100-eV range (with the appropriate parameters adjusted accordingly).

ACKNOWLEDGMENTS

This paper was originally presented as a plenary talk at the Mini-Workshop on High-Field, High-Intensity Physics with LCLS organized by C. Pellegrini and P. Chen (SLAC, Stanford, CA, 2000). Since then, papers [27–29] have appeared on similar subjects. Discussions with Drs. P. Chen, A. Toor, R. Tatchyn, R. Ruth, and C. Pellegrini are appreciated.

REFERENCES

1. LCLS Design Study Group, LCLS Design Study Report No. SLAC-R–521 (SLAC, Stanford, CA, 1998).
2. P. S. Chen and C. Pellegrini, in *Quantum Aspects of Beam Physics* (World Scientific, Singapore, 1999).
3. A. Toor, *Paper Presented at the Mini-Workshop on High-Field, High-Intensity Physics with LCLS* (SLAC, Stanford, CA, 2000).
4. R. Tatchyn, *Paper Presented at the Mini-Workshop on High-Field, High-Intensity Physics with LCLS* (SLAC, Stanford, CA, 2000).
5. A. Zhidkov, J. Koga, A. Sasaki, and M. Uesaka, Phys. Rev. Lett. **88**, 185002 (2002).
6. T. Tajima and J. M. Dawson, Phys. Rev. Lett. **43**, 267 (1979).
7. P. Chen and R. J. Noble, in *Advanced Accelerator Concepts*, Ed. by F. E. Mills (AIP, New York, 1986).
8. D. F. Fisher and T. Tajima, Phys. Rev. E **53**, 1844 (1996).
9. B. S. Newberger and T. Tajima, Phys. Rev. A **40**, 6897 (1989).
10. Z. Huang, P. Chen, and R. D. Ruth, Phys. Rev. Lett. **74**, 1759 (1995).
11. T. Tajima and M. Cavenago, Phys. Rev. Lett. **59**, 1440 (1987).
12. T. Ditmire, T. Donnelly, R. W. Falcone, and M. D. Perry, Phys. Rev. Lett. **75**, 3122 (1995).
13. T. Ditmire, J. W. J. Tish, E. Springate, *et al.*, Nature (London) **386**, 54 (1997).
14. T. Ditmire, J. Zweiback, V. D. Yanovsky, *et al.*, Nature (London) **398**, 489 (1999).
15. T. Ditmire, T. Donnelly, A. M. Rubenchik, *et al.*, Phys. Rev. A **53**, 3379 (1996).
16. Y. Kishimoto, L. Hillman, and T. Tajima, in *High Field Science*, Ed. by T. Tajima, K. Mima, and H. Baldis (Kluwer-Plenum, New York, 2000), p. 85.
17. M. V. Ammosov, N. B. Delone, and V. P. Kraĭnov, Zh. Éksp. Teor. Fiz. **91**, 2008 (1986) [Sov. Phys. JETP **64**, 1191 (1986)].
18. *Proceedings of the International Workshop on Nuclear Physics with Different Degrees of Freedom*, Ed. by H. Bhang, S. W. Hong, and H. Shimizu (Sungkyunkwan Univ., Seoul, 2002).
19. D. Belic, C. Arlandini, J. Besserer, *et al.*, Phys. Rev. Lett. **83**, 5242 (1999).
20. P. Walker and G. Draconllis, Nature (London) **399**, 35 (1999).
21. T. Shizuma, P. D. Strvenson, P. M. Walker, *et al.*, Phys. Rev. C **65**, 064310 (2002).
22. K. Vogt, P. Mohr, M. Babilon, *et al.*, Phys. Rev. C **63**, 055802 (2001).
23. M. Fujiwara, in *Proceedings of the International Workshop on Nuclear Physics with Different Degrees of Freedom*, Ed. by H. Bhang, S. W. Hong, and H. Shimizu (Sungkyunkwan University, Seoul, 2002).
24. P. Chen, T. Tajima, and Y. Takahashi, Phys. Rev. Lett. **89**, 161101 (2002).
25. P. Chen and T. Tajima, Phys. Rev. Lett. **83**, 256 (1999).
26. N. Arkani-Hamed, S. Dimopoulos, and G. Dvali, Phys. Lett. B **429**, 263 (1998).
27. A. Ringwald, Phys. Lett. B **510**, 107 (2001).
28. R. Alkofer, M. B. Hecht, C. D. Roberts, *et al.*, Phys. Rev. Lett. **87**, 193902 (2001).
29. V. S. Popov, Zh. Éksp. Teor. Fiz. **121**, 1235 (2002) [JETP **94**, 1057 (2002)].

Plasma Physics Reports, Vol. 29, No. 3, 2003, pp. 211–219. Translated from Fizika Plazmy, Vol. 29, No. 3, 2003, pp. 236–245.

LOW-TEMPERATURE PLASMA

Glow Discharge in Singlet Oxygen

N. P. Vagin*, A. A. Ionin*, Yu. M. Klimachev*, I. V. Kochetov, A. P. Napartovich**, D. V. Sinitsyn*, and N. N. Yuryshev***

**Lebedev Physical Institute, Russian Academy of Sciences, Leninskiĭ pr. 53, Moscow, 119991 Russia*

***Troitsk Institute for Innovation and Fusion Research, Troitsk, Moscow oblast, 142190 Russia*

Received June 20, 2002; in final form, September 26, 2002

Abstract—Currently, there is no experimental data on the plasma balance in gas mixtures with a high content of singlet delta oxygen $O_2(^1\Delta_g)$. These data can be obtained by studying the parameters of an electric discharge in singlet oxygen produced by a chemical generator. The $O_2(^1\Delta_g)$ molecules significantly change the kinetics of electrons and negative ions in plasma. Hence, the discharge conditions at low and high $O_2(^1\Delta_g)$ concentrations are very different. Here, the parameters of the positive column of a glow discharge in a gas flow from a chemical singlet-oxygen generator are studied. It is experimentally shown that, at an $O_2(^1\Delta_g)$ concentration of 50% and at pressures of 1.5 and 2 torr, the electric field required to sustain the discharge is considerably lower than in the case when all of the oxygen molecules are in the ground state. A theoretical model of the glow discharge is proposed whose predictions are in good agreement with the experimental data. © *2003 MAIK "Nauka/Interperiodica".*

1. INTRODUCTION

For the last 20 years, significant progress has been achieved in studying and designing chemical oxygen–iodine lasers (COILs) [1, 2]. COILs are widely applied in technology [3] because of the high output power of these lasers and the low radiation loss in optical fibers at the COIL wavelength $\lambda = 1.315$ μm. In the COIL active medium, lasing occurs via the iodine atomic transition from the excited electronic state to the ground state, $I^*(^2P_{1/2}) \longrightarrow I(^2P_{3/2}) + h\nu$. The $I^*(^2P_{1/2})$ excited iodine atoms are produced via energy transfer from the singlet state $O_2(^1\Delta_g)$ of an oxygen molecule, referred to as singlet delta oxygen (SDO):

$$O_2(^1\Delta_g) + I(^2P_{3/2}) \longrightarrow O_2(^3\Sigma) + I^*(^2P_{1/2}).$$

SDO is usually produced in a chemical singlet-oxygen generator (SOG) in the gas–liquid chemical reaction

$$Cl_2 + 2KOH + H_2O_2 \longrightarrow O_2(^1\Delta_g) + 2KCl + 2H_2O.$$

The reaction involves hazardous chemical reagents, which restricts the use of COILs in technological applications.

There is an alternative way of obtaining SDO, namely, producing SDO in an electric discharge (see, e.g., [4]). The advantage of this method for SDO production is the absence of hazardous chemical reagents, the possibility of designing entirely gas-phase oxygen–iodine lasers, and the intensification of the atomic iodine production via the dissociation of I_2 by the $O_2(^1\Sigma_g)$ excited molecules [5]. Information on the production and loss of SDO (as well as oxygen in other electronically excited states) is still poor. In [6], we proposed a new method for investigating these processes, namely, a study of the electric discharge parameters in gas mixtures produced in conventional SOGs. This technique allows one to vary the SDO concentration within a very wide range and to study the effect of the SDO concentration on the discharge parameters. In [6], electric breakdown in an oxygen flow with a high SDO content was investigated at the output of a chemical SOG. It was shown that, the breakdown parameters of oxygen with a high SDO content can be adequately described under the assumption that the dependence of the cross section for ionization of $O_2(^1\Delta_g)$ molecules on the reduced electric field in a discharge has the same shape as the cross section for ionization of oxygen in the ground state, but is shifted as a whole toward the lower energies by an energy equal to the excitation threshold energy 0.98 eV. The high SDO concentration in the gas flow strongly affects the electron balance in a discharge plasma. In [7], the parameters of the longitudinal discharge plasma in an oxygen flow from a chemical SOG were studied. It was shown that the plasma parameters changed substantially in the presence of SDO. However, a reliable interpretation of the experimental data and the acquisition of data on elementary processes were hindered because, at the pressures used, the discharge gap was too short to produce a sufficiently homogeneous plasma. Because of the destruction of negative ions in collisions with $O_2(^1\Delta_g)$ molecules, electron attachment has essentially no effect on the parameters of the positive column. Thus, it is natural to expect a decrease in the electric field in the positive column of a glow discharge as the SDO concentration increases. This paper presents the results of studying the current–voltage characteristic of the positive column of a glow

1063-780X/03/2903-0211$24.00 © 2003 MAIK "Nauka/Interperiodica"

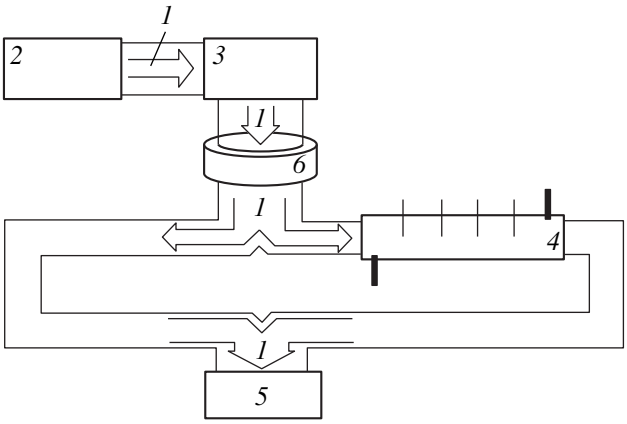

Fig. 1. Block diagram of the experimental facility: (*1*) gas flow, (*2*) gas supply system, (*3*) chemical SOG, (*4*) discharge chamber, (*5*) gas circulation system, and (*6*) water vapor trap.

discharge in an oxygen flow with a high SDO content (~50%) at the output of a conventional chemical SOG.

2. EXPERIMENT

To measure the electric field in a longitudinal glow discharge in SDO, the discharge chamber was placed (Fig. 1) in one of the two gas loop channels of a pulsed COIL pumped by a longitudinal electric discharge [8]. Gas flow *1* in discharge chamber *4* was produced by supplying the gas from system *2* to the chemical SOG *3* located upstream the discharge chamber and pumping-out system *5*. Since aqueous solutions are used to produce SDO, the gas flow from a SOG always contains water vapor, whose amount is determined by the temperature and composition of the SOG working solution. To reduce the water vapor concentration, cooled water vapor trap *6* (ethyl spirit precooled with liquid nitrogen) was set in the gas loop between the SOG and the discharge chamber. At trap temperatures from –60 to –65°C, the water vapor concentration in the gas flow was reduced to a level at which it was possible to ignore the effect of water vapor on the discharge parameters.

The gas was pumped through the system by four VN-1 pumps, providing a gas flow rate of ~80 l/s in the gas loop, which corresponded to a gas flow velocity of ~30 m/s in the discharge chamber. In this case, the time needed for the gas to pass through the discharge zone was ~20 ms. At the entrance to the discharge chamber, the gas was at approximately room temperature. The design and operation of a chemical SOG of the bubbling type are described in detail in papers devoted to COIL studies (see, e.g., [9]).

The discharge chamber was made of Plexiglas and had a length (along the gas flow) of ~60 cm and an inner diameter of 40 mm (Fig. 2). The tungsten electrodes of an IFP-20000 pulsed lamp were used as cathode *2* and anode *3*. The potentials in different regions of the discharge plasma were measured by four needle probes *4*, which were set at a distance of ~100 mm from each other and whose tips were on the chamber axis. The probes (except for their tips) were placed into insulat-

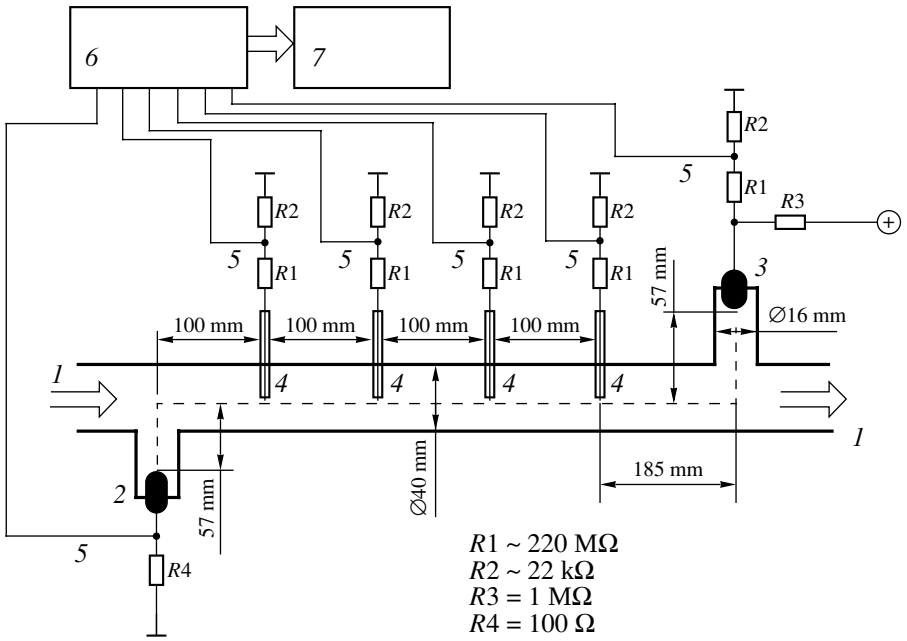

Fig. 2. Schematic of the discharge chamber and diagnostic technique: (*1*) gas flow, (*2*) cathode, (*3*) anode, (*4*) probes, (*5*) measurement channels, (*6*) analog-to-digital data acquisition board, and (*7*) PC.

ing Teflon tubes. The electric signals from dividers *5* (R_1/R_2 = 220 MΩ/22 kΩ) and the current shunt (R_4 = 100 Ω) were fed to LA-4 multichannel digital data acquisition board *6* connected to PC *7*.

Before taking the probe measurements in a discharge in an SDO-containing gas flow, the probe dividers were calibrated and the potential profiles along steady-state discharges in helium and oxygen at different gas pressures and discharge currents were determined (Fig. 3). On analyzing Fig. 3 and taking into account that probe no. 4 resides near the cathode fall region, it was assumed that the region where the potential distribution was uniform (and, consequently, the parameter E/N was constant) was located between probes nos. 1 and 3 (Fig. 2). For this reason, although all four probes were used in the measurements, only the data on the potential drops between the probe nos. 1 and 2 and nos. 2 and 3 were compared with the calculated results.

When performing probe measurements, the voltage and current signals were digitized at a sampling rate of 2 kHz with a total recording time of ~5.5 s. To optimize the relation between the recording time and the sampling rate, the voltage was applied to the discharge gap according to the following procedure. Initially, the output voltage of the power supply was preset such that it was higher than the discharge ignition voltage. At the required gas flow regime, the power supply was switched on; the discharge was ignited; and the discharge current grew to a value determined by the output voltage of the power supply, the ballast resistance (R_3 = 1 MΩ), and the discharge plasma resistance. Then, the power supply voltage was manually increased until the discharge current reached its maximum value (~15 mA); after that, the voltage was decreased and the power supply was switched off.

A typical behavior of the probe voltages, anode voltage, and discharge current during one measurement cycle is shown in Fig. 4.

The probe measurements in the positive column of a dc glow discharge were carried out for both pure oxygen and oxygen with an SDO admixture at total gas pressures of 1.5 and 2.0 torr. For this purpose, the SOG filled with a working solution was blown through with either oxygen (in this case, there was no chemical reaction and the discharge chamber was supplied with pure oxygen) or chlorine (in this case, the chemical reaction proceeded in the SOG and the discharge chamber was supplied with oxygen containing ~50% $O_2(^1\Delta_g)$). For the discharge currents taken from the records similar to that presented in Fig. 4, the potential drops between probe nos. 1 and 2 and nos. 2 and 3 were calculated. The results obtained are shown in Fig. 5.

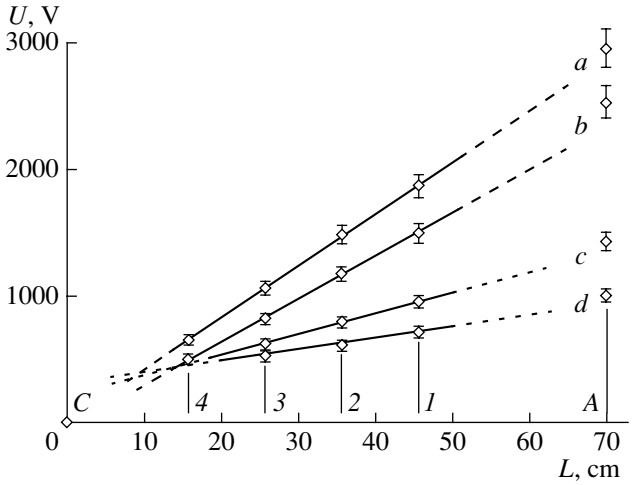

Fig. 3. Longitudinal profiles of the plasma potential in steady-state discharges in (*a*, *b*) oxygen and (*c*, *d*) helium for different gas pressures and discharge currents: (*a*) P = 1.2 torr and I = 2.0 mA, (*b*) P = 0.8 torr and I = 1.1 mA, (*c*) P = 4.4 torr and I = 5.5 mA, and (*d*) P = 1.0 torr and I = 2.4 mA. The positions of the probes along the discharge chamber axis (between anode (*A*) and cathode (*C*)) are marked by *1–4*. The solid lines show the regions where E/N is constant.

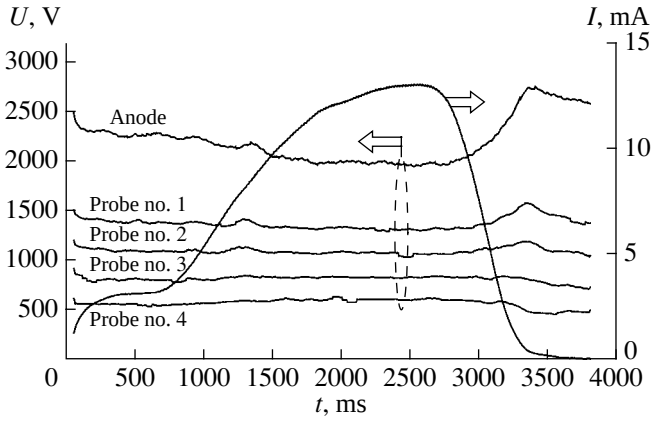

Fig. 4. Typical time evolution of the probe voltages U and discharge current I during one measurement cycle for the $O_2 : O_2(^1\Delta_g) \sim 1 : 1$ gas mixture at P = 1.5 torr.

3. THEORETICAL MODEL

A detailed kinetic model was developed to describe the evolution of the plasma parameters in the gas flowing through the discharge chamber. The preliminary estimates of the plasma parameters showed that, under our experimental conditions, the radial electron density profile in the discharge chamber was to a large extent governed by ambipolar diffusion. The electron and ion transport due to the nonuniformity of the plasma parameters along the glow-discharge positive column could be ignored. The gas flow was also of minor importance.

The elementary processes incorporated in the kinetic scheme are listed in the table. The rate constants for the processes with the participation of electrons were calculated by solving the time-independent Bolt-

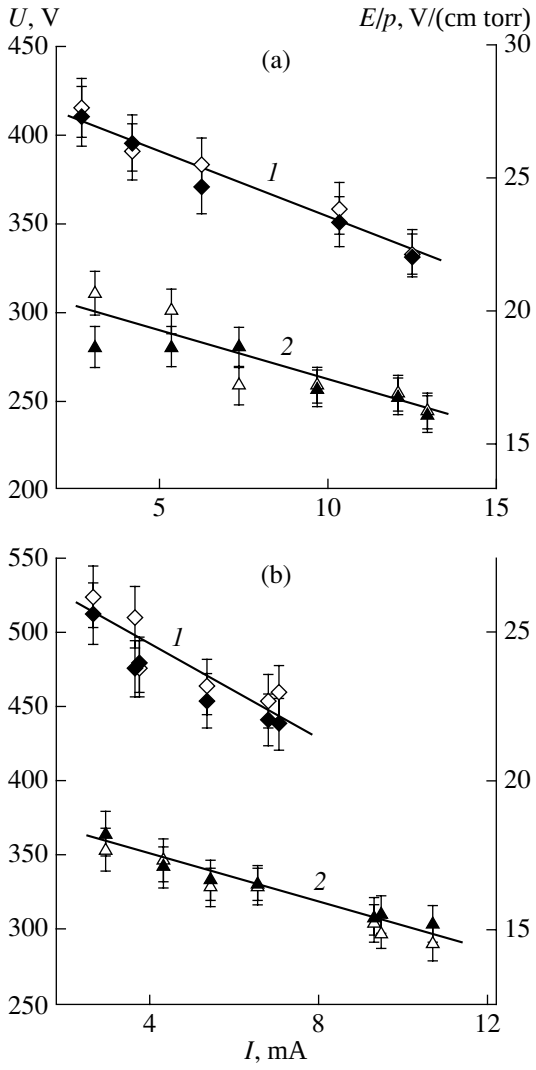

Fig. 5. Current–voltage characteristics of the positive column of a dc discharge in pure oxygen (*1*, ◆, ◇) and the $O_2 : O_2(^1\Delta_g) \sim 1 : 1$ mixture (*2*, ▲, △) for *P* = (a) 1.5 and (b) 2.0 torr. The symbols △ and ◇ show the potential drop between probes nos. 1 and 2, and the symbols ▲ and ◆ show the potential drop between probes nos. 2 and 3.

zmann equation for the electron energy distribution function (EEDF). The time-independent Boltzmann equation was solved numerically in the two-term approximation. For the sake of simplicity, the vibrational levels of an oxygen molecule were combined into one "reservoir," $O_2(v)$. The rate constant for the excitation of the reservoir of vibrational energy, $O_2(v)$, was calculated using the effective excitation cross section

$$\sigma_{\text{eff}}^{v} = \sum v\sigma_v,$$

where v is the number of the vibrational level and σ_v is the cross section for the electron-impact excitation of a molecule to the vibrational level v. When calculating the EEDF, in addition to inelastic processes listed in the table, the elastic scattering of electrons by oxygen molecules in different excited states and oxygen atoms was taken into account. In this model, the excitation of the rotational levels of an oxygen molecule was ignored. Special test calculations showed the applicability of this approximation under the conditions of a self-sustained discharge in oxygen.

The majority of the cross sections incorporated in the model were taken from [10]. The set of the cross sections for the dissociation of an oxygen molecule and its excitation to the electronic states was somewhat modified. In particular, the cross sections for the excitation of an oxygen molecule to the $O_2(A^3\Sigma, c^1\Sigma, C^3\Delta)$ state with a threshold energy of 4.5 eV (process no. 9 from the table) and the dissociation of an oxygen molecule (process no. 13) were taken from [11]. Since the energies of the $A^3\Sigma$, $c^1\Sigma$, and $C^3\Delta$ electronic states of an oxygen molecule are fairly close to each other, they were combined into one effective level, which is referred to as $O_2(4.5)$ below. The modified set of cross sections allowed us to achieve better agreement when modeling the experiments on the excitation to the $O_2(b^1\Sigma_g)$ [12] and $O_2(a^1\Delta_g)$ states in oxygen–argon mixtures [13]. In the table, these two lower states are denoted as $O_2(1.63)$ and $O_2(0.98)$, respectively. The electronically excited states with energies higher than 8.4 eV can result in the dissociation of O_2 molecules with the production of excited $O(^1D)$ atoms (process no. 17). The model incorporates two channels for the ionization of an oxygen molecule from the ground state: the ionization with the production of O_2^+ ions (process no. 21) and the dissociative ionization with the production of O^+ ions (process no. 25). Obviously, the higher the mean electron energy (i.e., the higher the reduced electric field E/N), the larger the role of the latter process.

A distinctive feature of the model is that it allows one to take into account the change in the gas mixture composition as the concentrations of oxygen atoms, ozone molecules, and $O_2(a^1\Delta_g)$ and $O_2(b^1\Sigma_g)$ oxygen metastable molecules in the plasma increase, which is necessary to self-consistently calculate the EEDF. Indeed, under the given conditions, the relative concentrations of the particles produced in the discharge can be as high as ten and even several tens of percents. In this situation, the electron-impact excitation and dissociation of the produced particles begin to play an important role in the total kinetic balance. Apparently, in this case, the set of cross sections should be supplemented with the cross sections for the interaction between electrons and excited particles; i.e., it is necessary to take stepwise processes into account. In our model, the cross sections for stepwise processes were constructed by using the cross sections for the interactions with particles in the ground states. These cross sections were shifted as a whole along the energy axis toward the lower energies by the excitation energy; the shape and the absolute values of the original cross sec-

Elementary processes in an oxygen plasma

No.	Reaction	k_f, cm^3/s, cm^6/s	k_r, cm^3/s, cm^6/s	Reference
1	$O_2 + e \longleftrightarrow O_2(v) + e$	EEDF	EEDF	10
2	$O_2 + e \longleftrightarrow O_2(0.98) + e$	EEDF	EEDF	10
3	$O_2 + e \longleftrightarrow O_2(1.63) + e$	EEDF	EEDF	10
4	$O_2(0.98) + e \longleftrightarrow O_2(1.63) + e$	EEDF	EEDF	10
5	$O_2 + e \longrightarrow O^- + O$	EEDF		15
6	$O_2(v) + e \longrightarrow O^- + O$	EEDF		*)
7	$O_2(0.98) + e \longrightarrow O^- + O$	EEDF		16
8	$O_2(1.63) + e \longrightarrow O^- + O$	EEDF		17
9	$O_2 + e \longleftrightarrow O_2(4.5) + e$	EEDF	EEDF	11
10	$O_2(v) + e \longleftrightarrow O_2(4.5) + e$	EEDF	EEDF	*)
11	$O_2(0.98) + e \longleftrightarrow O_2(4.5) + e$	EEDF	EEDF	*)
12	$O_2(1.63) + e \longleftrightarrow O_2(4.5) + e$	EEDF	EEDF	*)
13	$O_2 + e \longrightarrow O + O + e$	EEDF		11
14	$O_2(v) + e \longrightarrow O + O + e$	EEDF		*)
15	$O_2(0.98) + e \longrightarrow O + O + e$	EEDF		*)
16	$O_2(1.63) + e \longrightarrow O + O + e$	EEDF		*)
17	$O_2 + e \longrightarrow O(^1D) + O + e$	EEDF		10
18	$O_2(v) + e \longrightarrow O(^1D) + O + e$	EEDF		*)
19	$O_2(0.98) + e \longrightarrow O(^1D) + O + e$	EEDF		11
20	$O_2(1.63) + e \longrightarrow O(^1D) + O + e$	EEDF		*)
21	$O_2 + e \longrightarrow O_2^+ + e + e$	EEDF		10
22	$O_2(v) + e \longrightarrow O_2^+ + e + e$	EEDF		*)
23	$O_2(0.98) + e \longrightarrow O_2^+ + e + e$	EEDF		*)
24	$O_2(1.63) + e \longrightarrow O_2^+ + e + e$	EEDF		*)
25	$O_2 + e \longrightarrow O^+ + O + e + e$	EEDF		10
26	$O_2(v) + e \longrightarrow O^+ + O + e + e$	EEDF		*)
27	$O_2(0.98) + e \longrightarrow O^+ + O + e + e$	EEDF		*)
28	$O_2(1.63) + e \longrightarrow O^+ + O + e + e$	EEDF		*)
29	$O_2^+ + e \longrightarrow O + O$	EEDF		14
30	$O + e \longrightarrow O^+ + e + e$	EEDF		10
31	$O(^1D) + e \longrightarrow O^+ + e + e$	EEDF		*)
32	$O_2(v) + M \longrightarrow O_2 + M$	1.0×10^{-13}		Estimate
33	$O_2(4.5) + M \longrightarrow O_2(0.98) + M$	1.0×10^{-13}		18
34	$O_2(4.5) + M \longrightarrow O_2(1.63) + M$	9.0×10^{-13}		18
35	$O + O + M \longrightarrow O_2 + M$	4.8×10^{-33}		18
36	$O + O + M \longrightarrow O_2(0.98) + M$	2.4×10^{-33}		18
37	$O + O + M \longrightarrow O_2(1.63) + M$	1.2×10^{-33}		18
38	$O + O_2 + M \longrightarrow O_3 + M$	6.9×10^{-34}		19
39	$O + O_3 \longrightarrow O_2 + O_2$	4.2×10^{-15}		18
40	$O + O_3 \longrightarrow O_2(0.98) + O_2$	2.8×10^{-15}		18
41	$O + O_3 \longrightarrow O_2(1.63) + O_2$	1.4×10^{-15}		18
42	$O + O(^1D) \longrightarrow O + O$	7.5×10^{-11}		20
43	$O(^1D) + O_2 \longrightarrow O + O_2(1.63)$	3.08×10^{-11}		20
44	$O(^1D) + O_2 \longrightarrow O + O_2$	7.2×10^{-12}		20
45	$O(^1D) + O_3 \longrightarrow O_2 + O + O$	1.2×10^{-10}		18
46	$O(^1D) + O_3 \longrightarrow O_2 + O_2$	1.2×10^{-10}		18
47	$O(^1D) + O_3 \longrightarrow O_2(0.98) + O_2$	1.5×10^{-11}		18
48	$O(^1D) + O_3 \longrightarrow O_2(1.63) + O_2$	7.7×10^{-12}		18
49	$O_2(0.98) + O \longrightarrow O_2 + O$	1.6×10^{-16}		21
50	$O_2(0.98) + O_2 \longrightarrow O_2 + O_2$	2.2×10^{-18}		21
51	$O_2(0.98) + O_3 \longrightarrow O_2 + O_2 + O$	3.8×10^{-15}		21

Table. (Contd.)

No.	Reaction	k_f, cm^3/s, cm^6/s	k_r, cm^3/s, cm^6/s	Reference
52	$O_2(0.98) + O_2(0.98) \longrightarrow O_2(1.63) + O_2$	2.2×10^{-18}		21
53	$O_2(1.63) + O \longrightarrow O_2 + O$	4.0×10^{-14}		22
54	$O_2(1.63) + O \longrightarrow O_2(0.98) + O$	4.0×10^{-14}		19
55	$O_2(1.63) + O_2 \longrightarrow O_2 + O_2$	8.0×10^{-18}		22
56	$O_2(1.63) + O_2 \longrightarrow O_2(0.98) + O_2$	3.2×10^{-17}		19
57	$O_2(1.63) + O_3 \longrightarrow O_2 + O_2 + O$	1.54×10^{-11}		19
58	$O_2(1.63) + O_3 \longrightarrow O_2(0.98) + O_2 + O$	7.0×10^{-12}		19
59	$O_3 + e \longrightarrow O_2 + O + e$	8.8×10^{-10}		Estimate
60	$O_3 + e \longrightarrow O_2(0.98) + O + e$	1.2×10^{-10}		Estimate
61	$O_2 + e + O \longleftrightarrow O_2 + O^-$	1.0×10^{-31}	$f(E/N)$	23, 14
62	$O_2 + e + O_2 \longleftrightarrow O_2^- + O_2$	$f(E/N)$	$f(E/N)$	14
63	$O_3 + e + O_2 \longleftrightarrow O_3^- + O_2$	4.6×10^{-29}	1.0×10^{-14}	14
64	$O_3 + e \longleftrightarrow O^- + O_2$	9.0×10^{-12}	5.0×10^{-15}	24
65	$O^- + O \longrightarrow e + O_2$	1.9×10^{-10}		24
66	$O^- + O_2(0.98) \longrightarrow e + O_3$	3.0×10^{-10}		25
67	$O^- + O_2(1.63) \longrightarrow O + e + O_2$	7.0×10^{-10}		Estimate
68	$O^- + e \longrightarrow O + e + e$	4.0×10^{-8}		Estimate
69	$O^- + O_2 \longleftrightarrow O + O_2^-$	$f(E/N)$	3.3×10^{-10}	14
70	$O^- + O_3 \longleftrightarrow O + O_3^-$	5.3×10^{-10}	1.0×10^{-13}	24
71	$O^- + O_3 \longrightarrow O_2 + O_2 + e$	3.0×10^{-10}		25
72	$O^- + O_2 + O_2 \longrightarrow O_3^- + O_2$	$f(E/N)$		14
73	$O_2^- + O_2(0.98) \longrightarrow O_2 + O_2 + e$	2.0×10^{-10}		23
74	$O_2^- + O_2(1.63) \longrightarrow O_2 + O_2 + e$	3.6×10^{-10}		23
75	$O_2^- + O \longleftrightarrow O_3 + e$	3.0×10^{-10}		25
76	$O_2^- + O_3 \longrightarrow O_3^- + O_2$	4.0×10^{-10}		23
77	$O_3^- + O \longrightarrow O_2 + O_2 + e$	1.0×10^{-13}		25
78	$O_3^- + O \longrightarrow O_2^- + O_2$	3.2×10^{-10}		23
79	$O_3^- + O_3 \longrightarrow O_2 + O_2 + O_2 + e$	1.0×10^{-12}		14
80	$O^+ + O_2 \longrightarrow O_2^+ + O_2$	1.9×10^{-11}		26
81	$O_2^+ + O_2 + O_2 \longleftrightarrow O_4^+ + O_2$	2.4×10^{-30}	1.73×10^{-13}	23
82	$O_4^+ + O_2(0.98) \longrightarrow O_2^+ + O_2 + O_2$	1.0×10^{-10}		23
83	$O_4^+ + O_2(1.63) \longrightarrow O_2^+ + O_2 + O_2$	1.0×10^{-10}		23
84	$O_4^+ + O \longrightarrow O_2^+ + O_3$	3.0×10^{-10}		23
85	$O^- + O_4^+ \longrightarrow O_2 + O_3$	$f(E/N)$		14
86	$O^- + O_2^+ \longrightarrow O + O_2$	$f(E/N)$		14
87	$O_2^- + O_4^+ \longrightarrow O_2 + O_2 + O + O$	$f(E/N)$		14
88	$O_2^- + O_2^+ \longrightarrow O_2 + O_2$	$f(E/N)$		14
89	$O_3^- + O_4^+ \longrightarrow O_2 + O_2 + O_3$	$f(E/N)$		14
90	$O_3^- + O_2^+ \longrightarrow O_3 + O_2$	$f(E/N)$		14
91	$e + O^+ + O_2 \longrightarrow O + O_2$	1.0×10^{-26}		Estimate
92	$e + O_4^+ \longrightarrow O_2 + O_2$	2.2×10^{-7}		23

Note: k_f and k_r are the rate constants of the forward and reverse processes, respectively; EEDF means that the rate constant is calculated by the Boltzmann equation; $f(E/N)$ means that the rate constant is assumed to be a function of E/N; and the asterisks denote the cross sections for stepwise processes obtained by shifting the cross sections for the corresponding transitions from the ground state toward the lower energies by the particle excitation energy.

tions were not changed. The validity of this procedure of finding the cross section for ionization from the $O_2(^1\Delta_g)$ state was proved in [6].

The processes listed in the table are an integral part of the air plasma model described in detail in [14]. The rate constants of some processes with the participation of ions (process nos. 61, 62, 69, 72, 85–90) were tabulated as functions of the reduced electric field E/N (see [14] for details). These data were used to solve a set of time-dependent balance equations for the plasma components, including electrons, positive ions, negative ions, and chemical components (such as O_2, O, O_3, $O_2(v)$, $O_2(0.98)$, $O_2(1.63)$, $O_2(4.5)$, $O(^3P)$, $O(^1D)$, O^+, O_2^+, O_4^+, O^-, O_2^-, and O_3^-). Note that the numbers in parentheses show the energy of the corresponding molecular (atomic) states in eV.

The heating of the gas during its motion was neglected. The discharge was assumed to be fed from a power supply through a ballast resistance such that the voltage drops across the discharge and the ballast resistance were approximately equal to each other.

Two stages could usually be distinguished in the calculated plasma evolution. In the first stage, the plasma parameters changed rapidly (with a characteristic time of ~100 μs), and, in the second stage, they slowly evolved with a characteristic time of about tens of milliseconds. Taking into account that, under our experimental conditions, the gas stayed in the discharge zone for ~20 ms, the time at which the calculated electric current and the discharge voltage became equal their measured values was, for definiteness, set at 16 ms for pure oxygen in the ground state and 2 ms for oxygen with a 50% SDO content. Thus, the time during which the discharge current in mixtures with a high SDO content is established is significantly shorter than that in pure oxygen. This is because the $O_2(^1\Delta_g)$ and O components (which are responsible for detachment in pure oxygen) are produced more slowly in the latter case.

Let us briefly discuss the role of ambipolar diffusion in the plasma balance in the positive column of a glow discharge. To adequately describe the radial density distribution of the plasma components in an oxygen glow discharge, at least three plasma components should be taken into consideration, namely, electrons, positive ions, and negative ions (several positive and negative ion species were usually taken into account). Generally, the diffusion equations for the plasma components cannot be reduced to one equation for ambipolar diffusion; hence, it is impossible to obtain a simple expression for the diffusive losses of charged particles by averaging over the discharge chamber volume. However, under our experimental conditions, attachment and detachment are the most rapid processes in the balance equation for negative ions. Among the attachment processes, dissociative attachment is dominant, which is characteristic of a low-pressure self-sustained discharge. By setting the attachment rate equal to the decay rate of negative ions, one can find that the electron density and the negative ion density are related to each other by the expression $n_n = n_e\nu_a/\nu_d$, where ν_a and ν_d are the attachment and detachment rates, respectively. Assuming that the plasma is quasineutral, the rest of the balance equations for electrons and positive ions can be reduced to the equation of ambipolar diffusion. The next step is to average this equation over the volume and to approximate the diffusion flux toward the wall by the well-known expression corresponding to the Shottky approximation. When there are several positive ion species in the plasma, we also assume that the diffusion fluxes of the different ion species are proportional to each other under different conditions. In this case, by equating the diffusive loss of electrons to the loss of all the positive ion species, one can obtain explicit expressions for the diffusive loss of each ion species. The set of equations obtained was solved numerically together with the equations for the plasma chemical components and the electric-circuit equation.

The effect of electron collisions with $O_2(^1\Delta_g)$ molecules is illustrated in Fig. 6, which shows the fractions of the electron energy lost in different plasma processes as functions of the reduced electric field. (Note that the energy fractions are normalized to the energy acquired by the electrons from the electric field; the energy fractions are plotted on a logarithmic scale; and, for negative energy fractions, their absolute values are shown.) The calculated results for pure oxygen in the ground state are shown in Fig. 6a. It can be seen that the fraction of the electron energy spent on the direct excitation of the $O_2(^1\Delta_g)$ state has a pronounced maximum (0.43 at $E/N = 0.87 \times 10^{-16}$ V cm^2). Figure 6b presents the calculated fractions of the electron energy lost in different plasma processes in a mixture with an ~50% $O_2(^1\Delta_g)$ content, the other excited states being neglected. It is seen that, at low electric fields, the rate of energy transfer from SDO molecules to electrons is ten times higher (1000%) than the rate at which the electrons acquire energy from the electric field [27]. In addition to the processes presented in Fig. 6a, the following processes with the participation of $O_2(^1\Delta_g)$ molecules were taken into account: electron deexcitation, electron attachment, transitions to the higher electronic states, dissociation, and ionization. At low electric fields, the electron energy balance is maintained by the approximate equality between the energy delivered from SDO molecules and the energy spent on the excitation of SDO molecules to the higher energy levels, dissociation, and ionization (curve *10*). Since the potential curves of the ground and singlet electronic states are similar in shape, the cross sections for the transitions from the $O_2(^1\Delta_g)$ state were obtained from the cross sections for the corresponding transitions from the ground state by shifting them toward the lower energies by an energy of 0.98 eV. A comparison between Figs. 6a and 6b shows a drastic change in the electron energy balance. However, at electric fields typical of a self-sustained glow

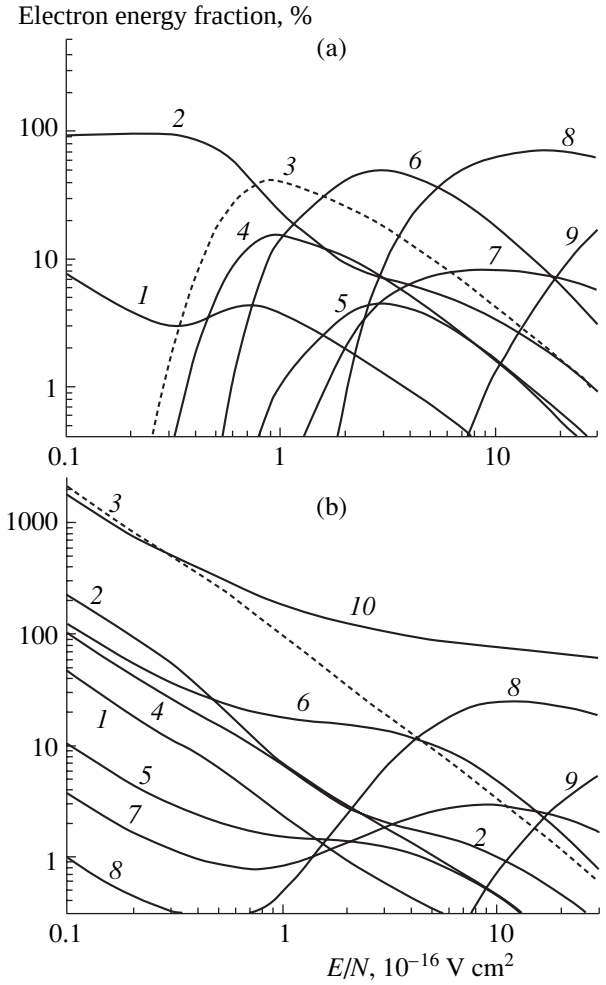

Fig. 6. Fractions of the electron energy lost in different plasma processes in (a) pure O_2 and (b) a mixture with a 50% SDO content: (*1*) elastic losses and the excitation of molecule rotations, (*2*) excitation of molecule vibrations, (*3*) excitation of $O_2(^1\Delta_g)$ (in Fig. 6b, the absolute value of this fraction is shown), (*4*) excitation of $O_2(^1\Sigma_g^+)$, (*5*) attachment, (*6*) excitation of the effective electronic level of O_2^* with a threshold energy of 4.5 eV, (*7*) dissociation into $O(^3P)$ atoms, (*8*) dissociation to $O(^3P)$ and $O(^1D)$ atoms, (*9*) ionization, and (*10*) total excitation from the $O_2(^1\Delta_g)$ state to the higher lying states.

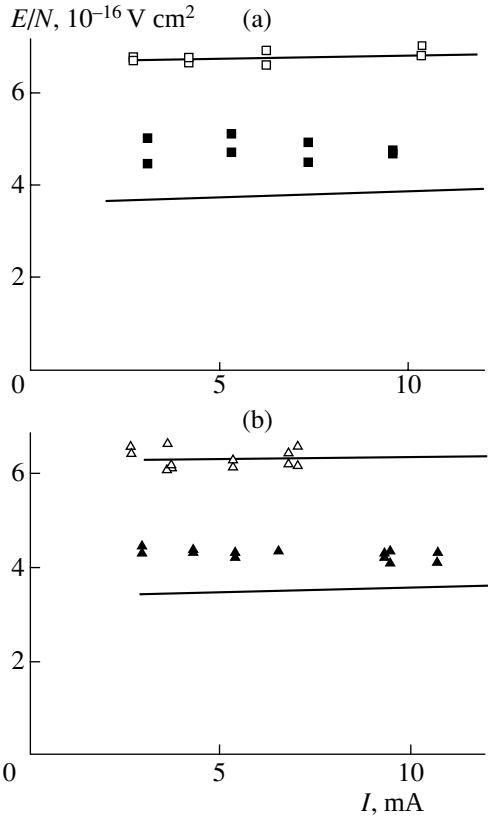

Fig. 7. Measured (symbols) and calculated (solid lines) reduced electric field in an oxygen discharge at pressures of (a) 1.5 and (b) 2 torr for an SDO content of 0 (□, △) and 50% (■, ▲).

discharge (see the next section), the energy flux from SDO molecules to electrons amounts to only about 10% of the power acquired by the electrons from the electric field. For this reason, at reduced electric fields of higher than 6×10^{-16} V cm^2, the electron transport coefficients (the drift velocity and the diffusion coefficient) change only slightly [6].

4. RESULTS AND DISCUSSION

The experiments show that there is a region in the discharge where the electric field is nearly constant. The reduced electric field *E*/*N* in this region was measured as a function of the discharge current for two gas-mixture pressures (1.5 and 2 torr). The results of these measurements are presented in Fig. 5. The average gas temperature in the discharge chamber increases with increasing discharge current. Taking this effect into account, we made a correction for the averaged gas heating (and, consequently, for the reduction in the gas density) and found that the *E*/*N* value remains essentially unchanged as the current increases from 3 to 11 mA (Fig. 7). Figure 7a shows the measured and calculated *E*/*N* values for oxygen at a pressure of 1.5 torr. It can be seen that, in pure oxygen, the calculated and measured reduced electric fields are in good agreement. Here, the reduced electric field is determined by the balance between the production of plasma particles due to ionization and their loss via both attachment (detachment) and ambipolar diffusion. Note that, within a large part of the discharge (along the gas flow), the electron attachment is, to some extent, balanced by detachment in collisions with SDO molecules and oxygen atoms produced in the discharge. However, the densities of these components are not high enough to significantly change the plasma balance. The decrease in the reduced electric field in discharges in an oxygen gas mixture with a 50% $O_2(^1\Delta_g)$ content is due to the much higher detachment rate in collisions with SDO molecules. This

effect turns out to be much greater than the increase in the attachment rate in collisions with SDO molecules. In this case, the total loss of the charged particles is, to a great extent, controlled by the diffusive losses. For an $O_2(^1\Delta_g)$ concentration of ~50%, the calculated decrease in the reduced electric field is much deeper than the measured one. It is not surprising if one takes into account that the available data on the processes with the participation of $O_2(^1\Delta_g)$ molecules are far from complete. A similar situation is observed for gas mixtures at a pressure of 2 torr. It can be seen in Fig. 7b that, for a discharge in pure oxygen at a pressure of 2 torr, the reduced electric field is lower than that at a pressure of 1.5 torr. A similar reduction in E/N with increasing pressure is observed at an SDO concentration of ~50%, although in this case, the scatter in the experimental data is larger than for pure oxygen.

5. CONCLUSION

The parameters of the positive column of a glow discharge in an oxygen flow at the output of a chemical SOG have been studied both experimentally and theoretically. It has been found that the reduced electric field in a discharge in an oxygen mixture with a 50% SDO content is lower than that in unexcited oxygen. A detailed kinetic model describing the parameters of a plasma containing significant amounts of different excited oxygen species has been developed. It is shown that, at low electric fields, the 50% SDO admixture to oxygen strongly affects the electron energy balance. However, for electric fields characteristic of a self-sustained glow discharge, the power transferred to electrons from the SDO molecules amounts to only 10% of the deposited electric power. With the discharge chamber dimensions and gas pressures used in this study, the electric field in the positive column of a glow discharge is determined by the balance between the production of charged particles due to ionization and their loss via both attachment (detachment) in collisions with oxygen molecules and diffusion toward the wall. At high SDO concentrations, the destruction of negative ions in collisions with SDO molecules is of major importance. The theoretical calculations somewhat overestimate the effect of the electric field reduction in an oxygen mixture with a 50% SDO content. Further investigations are required to explain the disagreement between experiment and theory.

ACKNOWLEDGMENTS

This study was supported by the Russian Foundation for Basic Research, project no. 02-02-17452, and the International Science and Technology Center, project no. 2415 P.

REFERENCES

1. W. E. McDermott, N. R. Pchelkin, D. J. Behard, and R. R. Bousek, Appl. Phys. Lett. **32**, 469 (1978).
2. S. Lamberston, Proc. SPIE **4184**, 1 (2001).
3. M. Hallada, S. Seiffert, R. Walter, and J. Vetrovec, Laser Focus World **5**, 205 (2000).
4. E. A. Ogryzlo, in *Singlet Oxygen*, Ed. by H. Wasserman and R. Murray (Academic, New York, 1979).
5. D. King, D. Carroll, J. Laystrom, *et al.*, in *Proceedings of the International Conference LASER-2000*, Ed. by V. Corcoran and T. Corcoran (STS Press, McLean, VA, 2001), p. 265.
6. N. P. Vagin, A. A. Deryugin, A. A. Ionin, *et al.*, Fiz. Plazmy **26**, 299 (2000) [Plasma Phys. Rep. **26**, 278 (2000)].
7. N. P. Vagin, A. A. Ionin, Yu. M. Klimachev, *et al.*, Preprint No. 57 (Lebedev Phys. Inst., Rus. Acad. Sci., Moscow, 2000).
8. N. P. Vagin, V. S. Pazyuk, and N. N. Yuryshev, Kvant. Élektron. (Moscow) **22**, 776 (1995).
9. N. P. Vagin, P. G. Kryukov, and N. N. Yuryshev, Kvant. Élektron. (Moscow) **12**, 1921 (1985).
10. B. Eliasson and U. Kogelschatz, Rep. No. CH-5405 (Brown Boveri Forschungszentrum, Baden, 1986).
11. K. S. Klopovskiĭ and T. V. Rakhimova, private communication (1994).
12. S. A. Lawton and A. V. Phelps, J. Chem. Phys. **69**, 1055 (1978).
13. K. Tachibana and A. V. Phelps, J. Chem. Phys. **75**, 3315 (1981).
14. Yu. S. Akishev, A. A. Deryugin, V. B. Karal'nik, *et al.*, Fiz. Plazmy **20**, 571 (1994) [Plasma Phys. Rep. **20**, 511 (1994)].
15. D. Rapp and P. Englander-Golden, J. Chem. Phys. **43**, 1464 (1965).
16. P. D. Burow, J. Chem. Phys. **59**, 4922 (1973).
17. S. L. Akhmanov, K. S. Klopovskiĭ, A. T. Rakhimov, *et al.*, Available from VINITI, No. 5472-83 (Moscow, 1983).
18. A. I. Zakharov, K. S. Klopovskiĭ, A. P. Osipov, *et al.*, Fiz. Plazmy **14**, 327 (1988) [Sov. J. Plasma Phys. **14**, 191 (1988)].
19. D. L. Baulch, Cox, R. F. Hampson, Jr., *et al.*, J. Phys. Chem. Ref. Data **11**, 327 (1982); **13**, 1259 (1984).
20. V. A. Feoktistov, D. V. Lopaev, K. S. Klopovsky, *et al.*, J. Nucl. Mater. **200**, 309 (1993).
21. M. J. McEwan and L. F. Phillips, *Chemistry of the Atmosphere* (Univ. of Canterbury, Christchurch, 1975).
22. S. Mukkavilli, C. K. Lee, K. Varghese, and L. L. Tavlarides, IEEE Trans. Plasma Sci. **16**, 652 (1988).
23. A. Y. Kostinskii, A. A. Matveev, and V. P. Silakov, Plasma Sources Sci. Technol. **1**, 207 (1992).
24. V. G. Samoĭlovich, V. I. Gibalov, and K. V. Kozlov, *Physical Chemistry of a Barrier Discharge* (Mosk. Gos. Univ., Moscow, 1989).
25. J. I. Steinfeld, S. M. Adler-Golden, and J. W. Gallagher, J. Phys. Chem. Ref. Data **16**, 911 (1987).
26. J. C. Person and D. O. Ham, Radiat. Phys. Chem. **31**, 1 (1988).
27. A. P. Napartovich, A. A. Deryugin, and I. V. Kochetov, J. Phys. D **34**, 1827 (2001).

Translated by N.N. Ustinovskiĭ

Plasma Physics Reports, Vol. 29, No. 3, 2003, pp. 220–225. Translated from Fizika Plazmy, Vol. 29, No. 3, 2003, pp. 246–250.

LOW-TEMPERATURE PLASMA

Evolution of the Channel of a Long Leader in Air after a Sharp Decrease in the Discharge Current

N. L. Aleksandrov*, É. M. Bazelyan, and A. M. Konchakov***

**Moscow Institute of Physics and Technology, Institutskiĭ pr. 9, Dolgoprudnyĭ, Moscow oblast, 141700 Russia*

***Krzhizhanovskiĭ Power Engineering Institute, Leninskiĭ pr. 19, Moscow, 117927 Russia*

Received September 26, 2002

Abstract—The dynamics of the plasma parameters in a given cross section of a long-lived leader channel in air after a jumplike decrease in the discharge current is simulated numerically with the help of a one-dimensional non-steady-state model constructed with allowance for the dynamics of the energy input into the channel, the expansion of the channel, and the nonequilibrium ionization kinetics in the leader plasma. It is shown that, after a decrease in the current, the electric field in the channel, first, rapidly decreases and, then, increases gradually as the gas cools. The higher the energy input into the discharge before the decrease in the current, the longer the time scale on which the electric field increases. The results of simulations of the electric field in the channel agree with the data from the experimental modeling of the actual leader channel by a short spark.

1. INTRODUCTION

In a spark discharge, the leader process gives rise to a plasma channel with a lifetime of up to a few tens of a millisecond. Because of the gas heating, the ionization process in such a channel is maintained in relatively weak electric fields. A leader bridging the discharge gap inevitably initiates a breakdown, i.e., the formation of a highly conducting channel with a descending current–voltage characteristic [1–3]. The longer the leader, the larger the fraction of the applied voltage that drops across the channel and the greater the extent to which the electric field in the leader channel determines the breakdown voltage of the gas gap.

Although the electric field in the leader channel is an important characteristic of the spark breakdown, it has not yet been measured directly even in discharges in air, which is the most thoroughly studied gas. The estimates of the electric field that were obtained from indirect measurements differ by tens of times, depending on the experimental conditions [4–8] (see also [3]). The dynamics of the electric field in the leader channel has also received little experimental study. It might be anticipated that, just after the formation of each next part of the channel (with a gas temperature of about 1000 K), the reduced electric field E/N (where N is the density of neutral particles) in it is close to the critical value 10^{-15} V cm^2, at which the impact ionization rate in air is equal to the rate of electron attachment to O_2 molecules [3]. Thus, the electric field at atmospheric pressure is estimated to be $E \approx 10$ kV/cm. The experimental data on very long (150–200 m) spark channels [9, 10] provide convincing evidence that the mean electric fields in a leader channel are far weaker, $E < 200$–250 V/cm, which is several tens of times less than the electric fields at the very beginning of the leader process.

In theoretical models known in the literature [1, 11–14], it is assumed that the electrons in the plasma of the leader channel are produced predominantly through electron-impact ionization of molecules and that the two main effects of the gas heating are the electron detachment from negative ions and an increase in the reduced electric field E/N in the channel because of a decrease in N at constant pressure. However, under these assumptions, the electric field E in a leader channel heated to about 6000 K [3, 6, 13] cannot be weaker than 1 kV/cm, which is four to five times stronger than in experiments [9, 10]. Some models of the leader channel, namely, those in which the electric conductivity of air is determined under the assumption of a local thermodynamic equilibrium of the plasma [15, 16], make it possible to estimate the plasma parameters in long-lived parts of the channel where the electric field is weak. However, these models are certainly inapplicable for describing the evolution of the channel from an initial nonequilibrium state, in which the electric field is intrinsically fairly strong, to a final equilibrium state.

A kinetic model that adequately describes the processes of the production and loss of the electrons over the entire nonequilibrium leader channel in air was constructed in [17]. Based on this model, it was shown that gas heating leads to a substantial decrease in the reduced electric field E/N because the appearance of additional ionization mechanisms in a heated air (the electron-impact ionization of NO molecules with a low ionization energy and the associative ionization in collisions between O and N atoms) causes the plasma conductivity to increase. However, in [17], the analysis was carried out by using a zero-dimensional model. A one-

1063-780X/03/2903-0220$24.00

dimensional model of the leader channel in air was developed in [18], where it was used to self-consistently calculate the dynamics of the parameters of a leader plasma throughout the entire history of the discharge in a long air gap—from the very beginning of breakdown to the quasi-equilibrium state. The results of calculations of the electric field in the channel were found to agree well with the data from experimental modeling of a long leader by a spark discharge in a short gap. According to the model calculations of [18], the evolution of the plasma in a given cross section of a long leader proceeds in two stages. During the first stage (with a duration of about 10 μs), the gas is rapidly heated to a temperature of about 6000 K, the electron density increases abruptly because of the onset of the associative ionization reactions involving O and N atoms, and, as a consequence, the electric field in the channel decreases by one order of magnitude or more. During the second stage, the gas gradually cools down in the axial region of the channel and heats up at the periphery due to molecular heat conduction. The channel expands and its conductivity increases despite a decrease in the plasma density in the axial region. As a result, at a constant current, the electric field continues to decrease gradually to a level typical of arc discharges.

In [18], the development of a leader channel was studied under the assumption that the discharge current was constant. This assumption is, on the whole, quite natural; however, the so-called flash form of the development of the leader, accompanied by an abrupt change in the current flowing through the channel, is often observed in experiments [6]. That is why the study of the plasma behavior in the leader channel when the discharge current changes in a jumplike manner is of practical interest. Also, in order to check the extent to which the models of the leader process are adequate, it might be useful to compare the theoretical results with the measurement data from the available experiments. This subject was studied experimentally in [11] (see also [3]) by modeling the channel of a long leader by a short arc discharge. The goal of the present paper is to exploit the model developed in [18] to calculate the behavior of the parameters of a leader channel after a sharp decrease in the discharge current for the experimental conditions of [11]. Another goal is to clarify the main processes that govern the evolution of the leader plasma under the same conditions.

2. MODEL FOR THE DEVELOPMENT OF A LEADER CHANNEL

The one-dimensional model used here was described in detail in [18], where it was found to fit well with the data from measurements of the mean electric field in a leader channel at a constant discharge current [11]. The model makes it possible to follow the evolution of the plasma parameters in a certain cross section of a leader channel during the second stage of the leader process, when the channel gradually cools down and expands after its rapid heating has come to an end. In the model, the radial variations of the plasma parameters are taken into account, whereas much smaller longitudinal gradients are neglected. The model ignores electron diffusion (which, under the conditions adopted here, is far slower than the internal processes) and the processes involving negative ions (which is justified for $T > 1000$ K [13, 17]). The main processes determining the electron density are assumed to be the electron-impact ionization of neutral particles; the associative ionization in collisions between O and N atoms,

$$\mathrm{N} + \mathrm{O} \longrightarrow e + \mathrm{NO}^+; \tag{1}$$

and the reverse process—the dissociative recombination of electrons with NO^+ ions. The densities of neutral particles are assumed to be equal to their thermodynamically equilibrium values.

Without allowance for evolutionary processes occurring on short time scales (shorter than 30 μs), the electron balance can be described by the quasi-steady-state equation [18]

$$k_i n_e N + k_{ia} N_\mathrm{O} N_\mathrm{N} - k_{ei} n_e^2 = 0, \tag{2}$$

where n_e is the electron density; N_O and N_N are the densities of O and N atoms; k_{ia} are the rate constants of associative ionization reaction (1); k_{ei} is the rate constant of a reverse process: the electron–ion dissociative recombination reaction involving an NO^+ ion; and the ionization rate constant k_i is averaged over the main neutral components of the gas (O_2, N_2, and NO molecules and O and N atoms in the excited and ground states).

The non-steady-state hydrodynamic model in question was constructed in the isobaric approximation, which gives a correct description of a leader because many experiments provide evidence for the subsonic radial expansion of the leader channel in air at discharge currents of about 1 A, typical of the initial phase of the process (see, e.g., [3, 13]).

The set of model equations includes the heat conduction equation

$$c_p \frac{\partial T}{\partial t} = jE + \frac{1}{r}\frac{\partial}{\partial r}\left(r\lambda\frac{\partial T}{\partial r}\right); \tag{3}$$

the quasi-steady-state equation (2) for the electron density balance; and the following condition on the electric current I in the channel, which serves as an input parameter of the problem:

$$I = 2\pi\int_0^\infty jr\,dr. \tag{4}$$

Here, r is the radial coordinate, c_p is the specific heat at constant pressure, λ is the thermal conductivity, $j = en_e w$ is the current density, e is the charge of an electron, n_e is the electron density, and w is the electron drift velocity.

The current I is usually assumed to be constant because it is determined by the ionization processes in the streamer zone (rather than by the conductivity of the part of the leader channel under consideration) and thus is actually an external parameter for this part of the channel.

In the range of E/N values of interest to us, the energy acquired by the electrons in the electric field is transferred to the electronic and vibrational degrees of freedom of the molecules (primarily, N_2 molecules). On time scales $t > 30$ μs, the internal energy of the molecules is fully converted into heat; hence, in what follows, it is assumed that all the electron energy goes into heating the gas.

According to [18], the plasma conductivity at $T >$ 6000 K becomes so high and the electric field becomes so weak (at a constant discharge current) that the electron density is close to its equilibrium value. Under these conditions, the kinetic description of the electrons becomes more complicated because additional processes (such as three-body electron–ion recombination) come into play. However, these conditions can be described without referring to the kinetic description. For this reason, Eq. (2) was not solved; instead, the electric conductivity of the plasma at $T > 6000$ K was assumed to be equal to its thermally equilibrium value, which was taken from the experimental data of [19].

The values of $c_p(T)$ and the composition of the neutral component of the heated air were taken from the results of the hydrodynamic calculations performed in [20–22], and the values of $\lambda(T)$ were taken from the experimental data available in the literature [23]. The values of $k_i(E/N, T)$ and $w(E/N, T)$ were determined by numerically solving the Boltzmann equation for the electrons in the familiar two-term approximation (in which only the first two terms in the expansion of the electron distribution function in spherical functions are taken into account). The rate constants $k_{ei}(E/N, T)$ and $k_{ia}(T)$ were taken by analogy with [17].

The boundary and initial conditions have the form

$$\frac{\partial T(t, r = 0)}{\partial r} = 0,$$

$$T(t, r = \infty) = T_\infty,$$

$$E/N\ (t = 0, r = 0) = 10^{-15}\ \text{V cm}^2.$$

The initial profiles $T(t = 0, r)$ and $n_e(t = 0, r)$ were modeled by step functions (this corresponds to uniform distributions over a channel of radius r_0). Most of the calculations were carried out for $T_\infty = 300$ K, $T_0 = 1000$ K, and $r_0 = 0.03$ cm. The initial conditions approximately correspond to the part of the leader channel that had just been formed. At $t = 0$, the density n_0 was determined from condition (4). The gas density N was found from the condition of a constant pressure, which was assumed to be atmospheric in all calculations.

3. CALCULATED RESULTS AND DISCUSSION

Numerical calculations were carried out for the conditions of the experiments of [11], in which the channel of a long leader was modeled by a spark channel between two rod electrodes in a 7-cm-long air gap. The experiments were arranged so as to make the inherent capacitance of the electrodes and of the other components of the electric circuit as small as possible in order for the energy stored in the capacitors and released in the spark channel after bridging the discharge gap to not have any significant effect on the properties of the leader plasma. As a result of small inherent capacitance and high internal resistance of the generator, the discharge current across the channel remained essentially unchanged during the development of the spark, at the instant of bridging, and for a subsequent time of 1–2 ms. Such a spark was considered to be a physical model of a part of a long leader at a fixed current.

We experimentally investigated the relaxation dynamics of the electric field in the leader channel after a jumplike decrease in the discharge current. This decrease can be approximated by the following dependence: $I(t) = I_1$ at $t < \tau$ and $I(t) = I_2$ at $t > \tau$. The investigations were carried out for $I_1 = 4.4$ A; $I_2 = 0.8$ A; and $\tau = 40$, 210, and 375 μs. We also investigated the case of lower discharge currents: $I_1 = 0.9$ A, $I_2 = 0.15$ A, and $\tau = 740$ μs.

Figure 1 shows how the electric field in a spark channel changes with time under the above conditions. The electric field was determined as the ratio of the voltage drop across the channel to the channel length. After a sharp decrease in the current, the electric field in the channel, first, decreases rapidly (because the thermal conductivity remains at its initial level by virtue of the inertial character of the thermal regime under consideration) and, then, increases gradually as the gas cools. The rate at which the field increases depends strongly on the energy deposited in the channel in the preceding stages of the leader. The lower the current in the channel before the pulse was partly cut off and the shorter the time during which the current flew through the channel, the faster the rate at which the electric field increases to the level it was before the cutoff.

Figure 1 also shows the theoretical results from the corresponding calculation of the electric field with the help of the model described in the previous section. The theoretical model is seen to qualitatively reflect all of the main regular features of the increase in the electric field in the channel after a jumplike decrease in the electric current.

In order to clarify the main processes that govern the dynamics of the channel parameters, Figs. 2–4 present the calculated time evolutions of the gas temperature and electron density at the channel axis and of the so-called thermal radius R, which is defined as a radius at

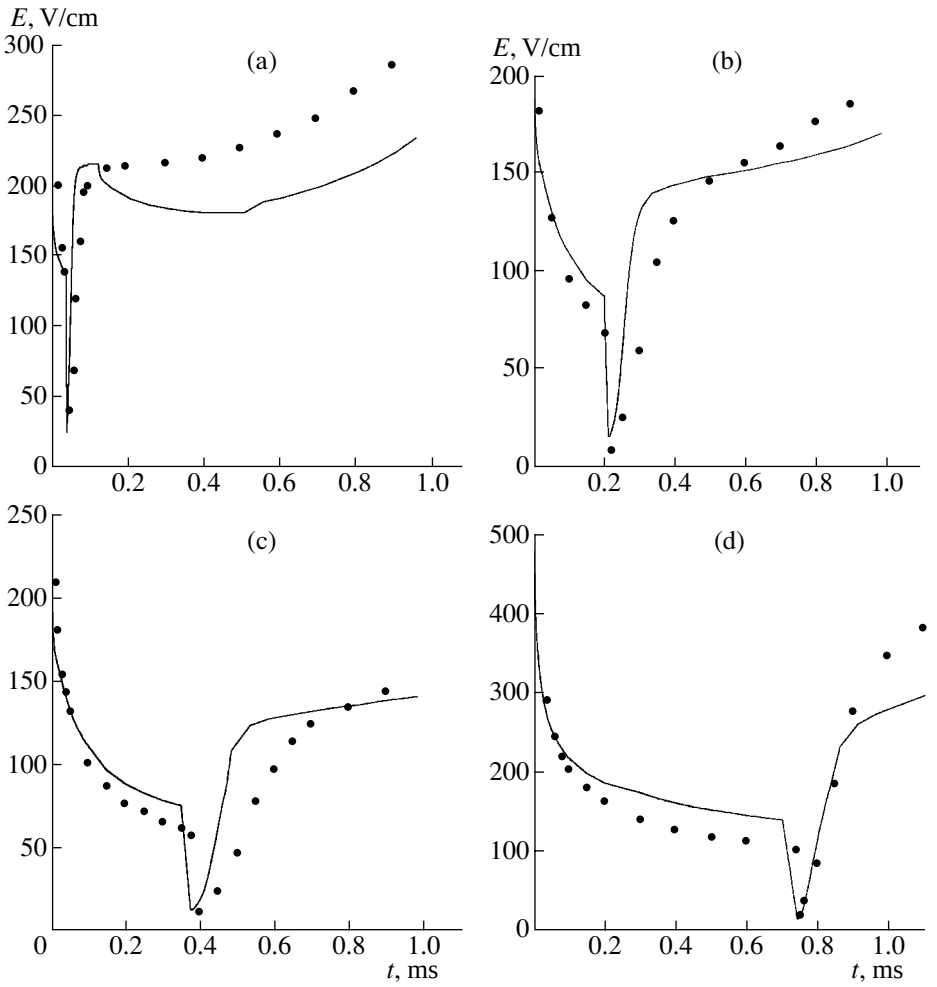

Fig. 1. Time evolutions of the electric field in the leader channel at different discharge currents for (a) $I_1 = 4.4$ A, $I_2 = 0.8$ A, and $\tau = 40$ μs; (b) $I_1 = 4.4$ A, $I_2 = 0.8$ A, and $\tau = 210$ μs; (c) $I_1 = 4.4$ A, $I_2 = 0.8$ A, and $\tau = 375$ μs; and (d) $I_1 = 0.9$ A, $I_2 = 0.15$ A, and $\tau = 740$ μs. The points represent the experimental data of [11], and the solid curves are the calculated results.

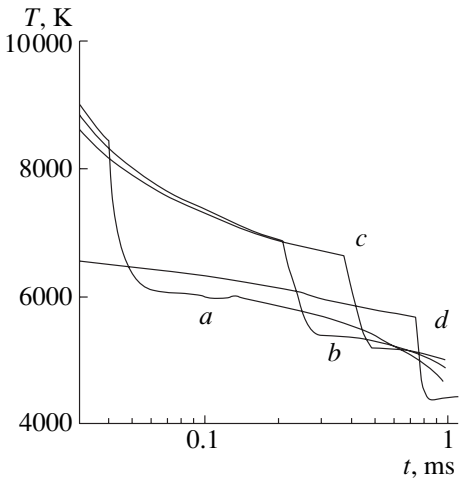

Fig. 2. Time evolutions of the gas temperature at the axis of the leader channel at different discharge currents. Curves *a*, *b*, *c*, and *d* correspond to the parameters of plots (a), (b) (c), (d) in Fig. 1.

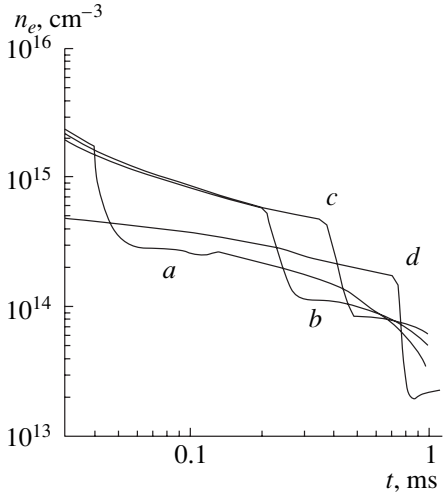

Fig. 3. Time evolutions of the electron density at the axis of the leader channel at different discharge currents. The notation is the same as in Fig. 2.

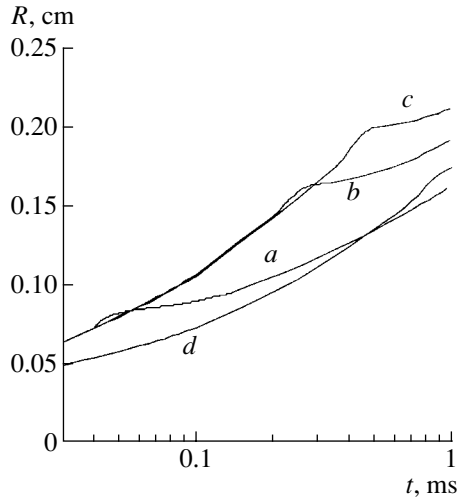

Fig. 4. Time evolutions of the thermal radius of the leader channel at different discharge currents. The notation is the same as in Fig. 2.

which the gas temperature is one-half of the central temperature:

$$T(r = R) = T(r = 0)/2.$$

The field in the channel is described by the expression $E = I/(\sigma S)$, where σ is the averaged (over the cross section of the channel) electric conductivity of the plasma and S is the cross-sectional area of the channel. As the discharge current decreases, the electric field also decreases, because the conductivity and the channel radius both respond relatively slowly to any changes in the parameters of the system. Under the conditions adopted here, the electron density is determined primarily by the gas temperature; this is especially true for the temperature range $T > 6000$ K, in which the conductivity is equal to its equilibrium value, and is roughly true for lower temperatures [down to a temperature of 4500 K, at which the main ionization mechanism is associative ionization reaction (1)]. Consequently, after a jumplike decrease in the current and the resulting drop in the energy deposition in the channel, a decrease in the electron density follows a decrease in the gas temperature (Figs. 2, 3). The relaxation time of the gas temperature is determined by the time during which the channel is cooled by heat conduction; this cooling time is on the order of R^2/χ, where χ is the thermal diffusivity. Since χ is weakly dependent on the gas temperature, the cooling time of the channel is determined largely by its thermal radius. In turn, the higher the energy input into the channel, the larger the thermal radius (this is also evidenced by Fig. 4). It is this circumstance that explains the experimentally measured and theoretically calculated shapes of the dependence of the characteristic time scale of variations of the plasma channel parameters on the deposited energy after a sharp decrease in the discharge current.

4. CONCLUSION

We have carried out a numerical modeling of the time evolution of the plasma parameters in a given cross section of a long-lived leader channel in air after a sharp decrease in the current flowing through the channel. The calculated dynamics of the electric field agrees well with the data from experimental modeling of an actual leader channel by a short spark. It is shown that the relaxation time of the plasma parameters after a jumplike decrease in the current depends on the energy deposition in the channel, which is determined by both the time during which the discharge is maintained and the discharge current. The higher the energy deposition, the slower the relaxation of the plasma parameters. The main mechanism by which the channel relaxes is the gas cooling by collisional heat conduction, the governing parameter being the thermal radius of the channel at the time at which the discharge current decreases. The wider the channel, the longer the time during which it cools.

ACKNOWLEDGMENTS

This study was supported by the Russian Foundation for Basic Research, project no. 00-02-17399.

REFERENCES

1. J. M. Meek and J. D. Craggs, *Electrical Breakdown in Gases* (Wiley, New York, 1987).
2. Yu. P. Raizer, *Gas Discharge Physics* (Nauka, Moscow, 1987; Springer-Verlag, Berlin, 1991).
3. E. M. Bazelyan and Yu. P. Raizer, *Spark Discharge* (MFTI, Moscow, 1997; CRC, Boca Raton, 1998).
4. I. S. Stekol'nikov, Izv. Akad. Nauk SSSR, Otd. Tekh. Nauk **5**, 133 (1957).
5. V. P. Larionov, Élektrichestvo, No. 8, 72 (1961).
6. Les Renardieres Group, Electra **53**, 3 (1977).
7. E. M. Bazelyan, V. I. Levitov, and A. Z. Ponizovsky, in *Proceedings of the 3rd International Symposium on High Voltage Engineering, Milan, 1979*, p. 1.
8. R. T. Waters, IEE Proc. A **128**, 319 (1981).
9. E. I. Anisimov, O. V. Bogdanov, A. S. Gayvoronskii, *et al.*, Élektrichestvo, No. 11, 55 (1988).
10. A. S. Gayvoronskii and A. G. Ovsjannikov, in *Proceedings of the 9th International Conference on Atmospheric Electricity, St. Petersburg, 1992*, p. 792.
11. E. M. Bazelyan and I. M. Razhanskiĭ, *Spark Discharge in Air* (Nauka, Novosibirsk, 1988).
12. J. N. Ross, B. Jones, and R. T. Waters, Electra **53**, 85 (1977).
13. I. Gallimberti, J. Phys. (Paris) **40**, 193 (1979).
14. A. Bondiou and I. Gallimberti, J. Phys. D **27**, 1252 (1994).
15. Yu. N. Vershinin and I. M. Razhanskiĭ, Élektrichestvo, No. 6, 46 (1976).
16. I. M. Razhanskiĭ, Izv. Sib. Otd. Akad. Nauk SSSR, Ser. Tekh. Nauk, No. 3, 41 (1976).

17. N. L. Aleksandrov, E. M. Bazelyan, I. V. Kochetov, and N. A. Dyatko, J. Phys. D **30**, 1616 (1997).

18. N. L. Aleksandrov, E. M. Bazelyan, and A. M. Konchakov, Fiz. Plazmy **27**, 928 (2001) [Plasma Phys. Rep. **27**, 875 (2001)].

19. E. I. Asinovskiĭ, A. V. Kirillin, and V. L. Nizovskiĭ, *Stabilized Electric Arcs and Their Application in Thermal Physics Experiments* (Nauka, Moscow, 1992).

20. A. S. Predvoditelev, E. V. Stupochenko, A. S. Pleshanov, *et al.*, *Tables of Thermodynamical Functions of Air (for Temperatures from 200 to 6000 K and Pressures from 0.00001 to 10 atm.)* (Vych. Tsentr Akad. Nauk SSSR, Moscow, 1962).

21. *Tables of Thermodynamical Functions of Air for Temperatures from 6000 to 12000 K and Pressures from 0.001 to 1000 atm.*, Ed. by A. S. Predvoditelev (Izd. Akad. Nauk SSSR, Moscow, 1957).

22. N. L. Aleksandrov and E. M. Bazelyan, J. Phys. D **31**, 1343 (1998).

23. *Physics and Technology of Low-Temperature Plasma*, Ed. by S. V. Dresvin (Atomizdat, Moscow, 1972).

24. E. M. Bazelyan and Yu. P. Raizer, *Lightning Physics and Lightning Protection* (IOP, Bristol, 2001; Nauka, Moscow, 2001).

Translated by G.V. Shepekina

Plasma Physics Reports, Vol. 29, No. 3, 2003, pp. 226–230. Translated from Fizika Plazmy, Vol. 29, No. 3, 2003, pp. 251–255.

LOW-TEMPERATURE PLASMA

Gas Temperature in the Plasma of a Low-Pressure Electrode Microwave Discharge in Hydrogen

Yu. A. Lebedev and M. V. Mokeev

Topchiev Institute of Petrochemical Synthesis, Russian Academy of Sciences, Leninskiĭ pr. 29, Moscow, 119991 Russia

Received May 20, 2002; in final form, September 26, 2002

Abstract—The gas temperature in an electrode microwave discharge in hydrogen at pressures of 1–8 torr and input powers of 20–90 W is determined from the relative intensities of the rotational lines of the electronically excited molecules of the Fulcher α system of molecular hydrogen. It is found that the gas temperature in the discharge is no higher than 800 K over the entire range of the experimental conditions under study. For this reason, plasma resonance cannot be regarded as a factor determining the physical processes in the discharge over the entire pressure range. Since the discharge unit is a nonuniform gas-dynamic system (the gas is fed through a small hole into a chamber of limited size), there is a possibility of generating vortex flows that intensively mix the gas. This results in a uniform distribution of the gas temperature throughout the entire volume of the spherical plasma structure produced in the experiment. *© 2003 MAIK "Nauka/Interperiodica".*

Electrode microwave discharges with a plasma size smaller than the size of the discharge chamber are a good example of the plasma structure formation [1, 2]. A molecular-gas discharge consists of a thin electrode sheath and a surrounding luminous spherical region, separated from the dark external space by a sharp boundary. The plasma parameters and physical processes in these discharges have been studied rather poorly.

The gas temperature is an important parameter determining both the characteristic features of the interaction of the electromagnetic field with the plasma (this interaction is governed, to a large extent, by the temperature-dependent ratio ν/ω, where ν is the effective electron collision frequency and ω is the circular frequency of the electromagnetic field) and the kinetics of the plasma processes.

The experiments were carried out with a hydrogen discharge at pressures of 1–8 torr, input powers of 20–90 W (the absorbed power being 2–12 W), and a microwave frequency of 2.45 GHz. The discharge chamber was a metal cylinder 8.5 cm in diameter with an antenna inserted through its end via a vacuum joint (see [1, 2] for details). The antenna (a cylindrical stainless-steel tube 6 mm in diameter) was a part of a coaxial-to-waveguide converter, which was adjusted with the help of a short-circuiting piston. The gas was fed through a 3-mm-diameter channel located in the upper cover of the discharge chamber. The chamber was pumped out through a hole in the lower cover.

The discharge was ignited around the antenna (the exciting electrode). The discharge dimensions were much smaller than the chamber diameter and the distance to the chamber lower end. The space-resolved measurements were performed in a gas flow. The output power of the microwave generator, operating at a frequency of 2.45 GHz, was up to 170 W. The discharge emission was output from the discharge chamber through a window on its side wall. A spectral range of 400–800 nm was investigated with the help of an MDR-23 monochromator. An FEU-79 photomultiplier was used as the emission detector.

The gas temperature was determined from the relative intensities of the rotational lines of the electronically excited molecules of the Fulcher α system of molecular hydrogen [3] (The $H_2(d^3\Pi_u \longrightarrow a^3\Sigma_g^+)$ transition). Strictly speaking, the Fulcher α system determines the rotational temperature of the upper excited state $d^3\Pi_u$ of molecular hydrogen. The gas temperature was calculated from the intensity of the Q branch of the diagonal band of the Fulcher α system (the vibrational quantum numbers of the upper and lower states are $V' = V'' = 2$). The rotational temperature was calculated assuming a Boltzmann molecule distribution over the rotational levels of the upper state:

$$\ln\left(\frac{I_{J'\to J''}}{\nu_{J'\to J''}^4 S_{J',J''}}\right) = -\frac{hc}{kT_{\mathrm{rot}}^*}F(J') + \mathrm{const}, \qquad (1)$$

where $I_{J'\to J''}$ is the intensity of the emission corresponding to a transition between the rotational levels of the vibrationally excited electronic states of molecules, $\nu_{J'\to J''}$ is the frequency of this transition, $S_{J',J''}$ is the Hönl–London factor, and $F(J')$ is the rotational energy of the upper state. The temperature was determined from the slope of the linear function $\ln(I_{J'\to J''}/(\nu_{J'\to J''}^4 S_{J'J''}))$ versus

1063-780X/03/2903-0226$24.00 © 2003 MAIK "Nauka/Interperiodica"

$F(J')$. The rotational temperature of the ground state was calculated by the formula

$$T_{\text{rot}}^{0} = T_{\text{rot}}^{*}\frac{B^{0}}{B'}, \quad (2)$$

where B^0 and B' are the rotational constants of the ground and excited states, respectively. The rotational temperature of the ground state was assumed to be equal to the gas temperature.

Some remarks should be made concerning the applicability of formula (2). It can be use only if the $H_2(d^3\Pi_u)$ state is quenched via a radiative transition to the ground state and the collisions with atoms and molecules can be neglected. Estimates show that, e.g., at a pressure of 100 torr and temperature of 3000 K, formula (2) is applicable when the quenching constant satisfies the inequality $k_q \ll 10^{-11}$ cm^3 s^{-1} [4]. Otherwise, the temperatures of the excited and ground states are equal. In [4], based on experimental data, a conclusion was drawn about the decisive role of quenching collisions. In [5], the data about the quenching constant $H_2(d^3\Pi_u)$ ($k_q \approx 10^{-9}$ cm^3 s^{-1}) were presented and it was found that, under the experimental conditions (at a pressure of up to 4.5 torr and a gas temperature of ≈1300 K), the quenching rate is comparable with the radiative deexcitation rate ($\nu_{em} \approx 4 \times 10^7$ s^{-1}). However, it was also shown that a 20-fold pressure variation (from 25 to 500 Pa) does not influence the distribution of the excited molecules over the rotational levels and only slightly affects their rotational temperature. This allows us to conclude that, for molecular densities in the ground state of up to $[H_2] \approx 4 \times 10^{16}$ cm^{-3}, collisions can be neglected. In [6], the gas temperature was measured simultaneously from the Fulcher spectrum and the Doppler broadening of the spectral lines. According to formula (2), at a pressure of 0.5 torr and a gas temperature of ~600 K, the rotational temperature $H_2(d^3\Pi_u)$ is half as large as the neutral-gas temperature. At a pressure of 1 torr, the temperature ratio is $T_{\text{gas}}/T_{\text{rot}}^{*} \approx 1.7$. The authors estimate the characteristic rate of the collisional relaxation of the rotational states to be $\nu_{\text{coll}}/p = 8 \times 10^6$ s^{-1} torr^{-1}. Thus, at a pressure of 1 torr, the inequality $\nu_{\text{coll}} \ll \nu_{em}$ holds. Evidently, the collisional deexcitation must be taken into account at molecular densities in the ground state of higher than ~10^{17} cm^{-3}; thus, under our experimental conditions, the gas temperature can be estimated by formula (2).

The experiments demonstrate that the assumption of a Boltzmann molecule distribution over the rotational levels is valid and that the dependence of $\ln(I_{\nu'\to\nu''}/(\nu_{\nu'\to\nu''}^4 S_{J'J''}))$ on $F(J')$ is well fit by a straight line. According to the data available in the literature and the results of our measurements, the $Q(2–2)$ band gives a temperature that is closest to the mean value determined from several bands or even using different methods [7]. The error, i.e., the deviation of the function $\ln(I_{\nu'\to\nu''}/(\nu_{\nu'\to\nu''}^4 S_{J'J''})) \sim F(J')$ from a straight line, is also minimum in this case.

The measurements show that the gas temperature in the electrode sheath is slightly higher than that in the surrounding spherical region. In the power and pressure ranges under study, the neutral gas temperature in a hydrogen discharge amounts to 550–800 K. The temperature gradually increases with increasing pressure and input power (see Fig. 1). (We note that the absorbed power is proportional to the input power.)

This result allows us to find out the processes responsible for the existence of the discharge. One of these processes may be energy absorption in the plasma resonance region. Calculations show [8] that the role of this mechanism decreases as the ratio ν/ω increases; at pressures of 3–4 torr, the field in the plasma resonance region increases only slightly and the change in the radial profile of the field near the electrode is only determined by the electrodynamic properties of the system. Since discharges with the same shape and structure also exist at high pressures, these results testify that gas heating does not provide conditions under which the resonance mechanism could be responsible for the discharge formation over the entire pressure range. As was noted above, taking into account the collisional quenching of the $H_2(d^3\Pi_u)$ states, which were used to determine the gas temperature, can only decrease the measured temperature value and, consequently, can only decrease the role of the resonance electron heating within the pressure range under study.

Figure 2 shows the radial profiles of the gas temperature at a pressure of 1 torr and an input power of 90 W. It can be seen that the temperature is almost uniform over the entire luminous region of the discharge.

The almost uniform distribution of the gas temperature over the entire emitting region of the discharge may be attributed to the gas dynamics of the system. The influence of the gas flow on the features of an electrode microwave discharge was demonstrated in the experiments of [2, 9], in which the gas was fed through an electrode channel. In this case, when the distance to the lower end of the chamber was shorter than the plasma size, luminous vortexes caused by the reflection of the plasma flow from the chamber wall were observed near the chamber end. When the distance to the lower end of the chamber was longer than the plasma size, a slightly diverging luminous plasma flow propagating to a distance much longer than the plasma size was observed. The gas flow also affects the results of the measurements of the plasma density near the electrode. The higher the gas flow rate, the stronger this influence. The reason is that the plasma near the gas-dynamic channel is depleted of charged particles due to the appearance of an additional channel for the loss of charged particles that are carried away by the gas flow, whose velocity exceeds the ambipolar diffusion veloc-

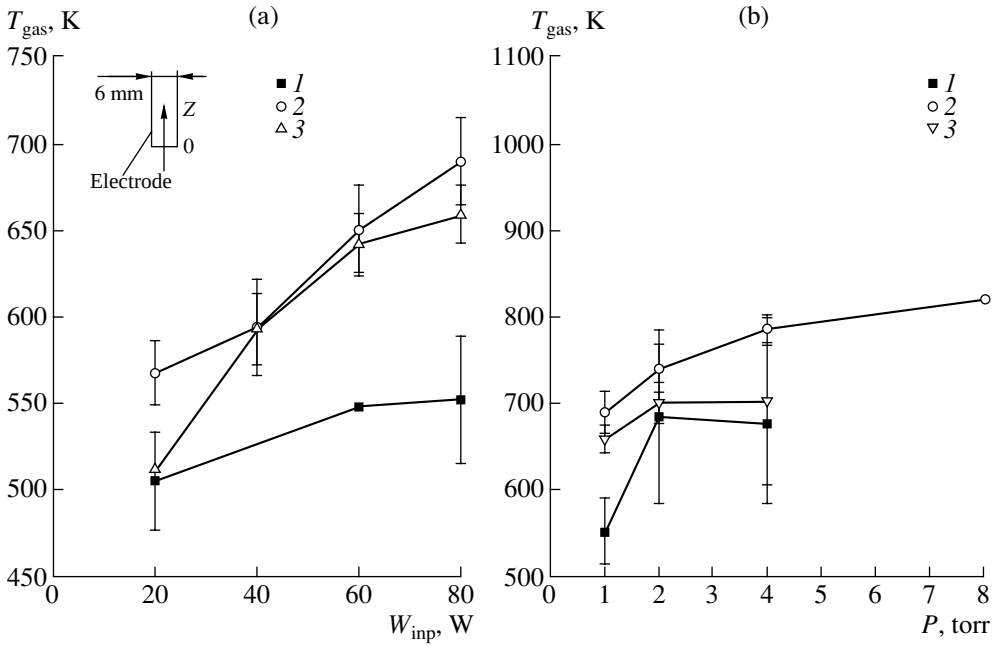

Fig. 1. Gas temperature in an electrode microwave discharge in the H_2 + 5% Ar mixture as a function of (a) input power at a pressure of 1 torr and (b) pressure at an input power of 80 W (*1*) in the spherical discharge region and in the thin electrode sheath (*2*) 0.5 mm below the electrode end and (*3*) 0.6 mm above the end. The *z*-axis is directed along the electrode axis.

ity. This effect was observed at gas flow rates higher than 100 sccm.

We also performed experiments with a dusty plasma. Solid grains with a mean diameter of 5 μm (the largest diameter being 100 μm) were introduced into the gas flow, and their trajectories in the plasma were observed with the help of a ribbon laser beam [10]. Experiments carried out with and without pumping-out show that the pumping-out strongly affects the grain motion. This is because the pumping-out produces turbulent gas flows: when the pumping-out is turned on, the fast stochastic motion of the grains is observed instead of their vertical fall. It can be assumed that the gas temperature is equalized by these flows, which mix the gas in the discharge chamber and make impossible the appearance of a typical diffuse distribution of the gas temperature. Let us make some estimates.

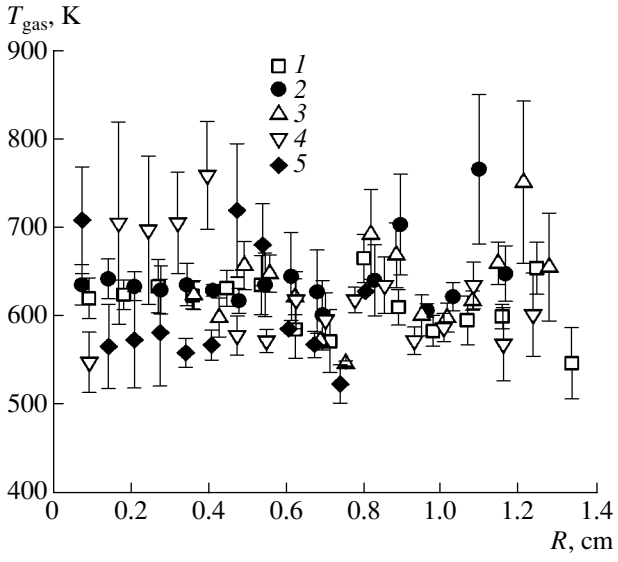

Fig. 2. Radial profile of the neutral-gas temperature in a hydrogen discharge at a pressure of 1 torr and an input power of 90 W in different cross sections of the discharge: z = (*1*) –1.5, (*2*) –1.0, (*3*) 0.5, (*4*) –3.5, and (*5*) –7.5 mm. The z coordinate is counted from the electrode end.

The gas flow rate is 5 l/min. The hole through which the gas is fed is ~3 mm in diameter. Accordingly, the gas velocity near the hole is equal to $v_{hole} \approx 5000/(\pi(0.3/2)^2(60) \approx 10^4$ cm/s. Visually, the dust grains, which were observed with the help of a TV camera, moved very fast across the viewing field. For estimate, we take the viewing field of the camera to be 10 cm and the visual time delay to be 1/30 s; then, we obtain $v_{pass} = 10 \times 30 = 300$ cm/s. The gas flow velocity v in the discharge chamber is lower than v_{hole} and higher than v_{pass}. Let us estimate the ratio between the heat transferred by heat conduction and that transferred by the gas flow (we ignore the heat transfer by charged and active plasma particles).

The heat conductivity $K = u\lambda\rho c_v/3$ is equal to the energy transferred through a unit area per unit time at a temperature gradient of $(dT/dx) = 1$ [11]. Here, u is the mean particle velocity, λ is the mean free path, ρ is the mass density, and c_v is the specific heat. Accordingly,

the heat flux through a unit area is equal to $W_K = u\lambda\rho c_v(dT/dx)/3$.

In a time of $t = 1$ s, the flow travels the distance $\Delta x = vt$. The temperature difference at this distance is $\Delta T \approx (dT/dx)\Delta x = (dT/dx)v$. The volume of the gas passing through the surface with an area of $S = 1$ cm^2 per one second is vtS, and the gas mass is $m = v\rho$. The heat transferred by the gas flow is $W_v = mc_v\Delta T = v^2\rho c_v(dT/dx)$. The ratio between the heat transferred by heat conduction and that transferred by the gas flow is $W_K/W_v = u\lambda/(3v^2)$. For hydrogen at a pressure of 1 torr and temperature of 0°C (under our experimental conditions, the temperature is ~300°C), we have $u = 1.69 \times 10^5$ cm/s and $\lambda = 8.41 \times 10^{-3}$ cm [12]. The upper estimate (for a minimum flow velocity of $v = 300$ cm/s) is $W_K/W_v \approx 0.01 \ll 1$. Thus, under our experimental conditions, the heat transfer in the plasma is governed by the gas flows.

Let us estimate the possible temperature gradients in the plasma. Passing over to the molar heat $c_{v\text{mol}} \approx 5R = 5 \times 8.31$ J/(K mol) and the molar density $\rho_{\text{mol}} \approx 1/(760 \times 2 \times 22400) \approx 3 \times 10^{-8}$ mol/cm^3 at a pressure of 1 torr and temperature of 600 K, we obtain $W_v = 0.1(dT/dx)$. In calculating the upper estimate of the temperature gradient, for W_v, we substitute the total deposited power divided by one-half of the discharge surface area, because heat is transferred by the gas flow in one direction (through the discharge): $W/S \approx 10/(2\pi R^3/3) \approx 1.5$ W/cm^2 (the radius of the glow region is assumed to be $R \approx 1.5$ cm). Then, we obtain $(dT/dx)_{\max} = 10W_v \approx 15$ K/cm. We note that the error of the temperature measurements is larger than 15 K.

In principle, the gas-temperature gradients might be fairly high near the electrode, where a bright luminous sheath is observed, if the most heat was liberated there. However, the sheath is adjacent to the metal electrode, which ensures efficient heat removal. For estimates, we assume that one-third of the discharge power is released in the sheath (the experiments show that about one third of the radiation energy is emitted from this sheath). Then, we have $(dT/dx)_{\max} \approx 3.3W/S_{\text{sh}} \approx 90$ K, where S_{sh} is the sheath area. Thus, the maximum gradient is no higher than 90 K/cm. This is true for a narrow region (2 to 5 mm thick) near the electrode; i.e., the temperature difference $(dT/dx)_{\max}\Delta x$ is 20–50 K.

It is clear that, the above considerations are valid not only for a minimum pressure of 1 torr and maximum power of 90 W, but over the entire pressure and power ranges under study.

Hence, we arrive at the conclusion that the heat transfer in the gas is mainly determined by the gas flows produced by pumping-out and, thus, the distribution of the gas temperature cannot be notably nonuniform. The neutral gas is heated almost uniformly throughout the entire chamber.

The existence of gas flows in the chamber was additionally confirmed by the observations of a high-pressure (20–30 torr) argon discharge with the help of a TV camera. In this case, the discharge consisted of plasma filaments originating at the electrode end. We observed a rather fast stochastic motion of the filaments (with a frame frequency of 1/25 s, we could not trace the filament motion in detail). This fact also testifies to the large role of the gas flows produced by the pumping-out of the discharge chamber. We note that the plasma filaments observed in an argon discharge in a uniform coaxial system at pressures of 40–80 torr moved much more slowly [13]. Hence, such fast stochastic motion of the plasma filaments in an electrode discharge in a nonuniform gasdynamic system is due to gas flows and cannot be caused by the plasma processes.

CONCLUSION

In an electrode microwave discharge in hydrogen, the gas temperature does not exceed 800 K over the entire range of the experimental conditions under study. This allows us to conclude that plasma resonance cannot be regarded as a factor determining the physical processes in the discharge over the entire pressure range. Since the discharge unit is a nonuniform gasdynamic system (the gas is fed through a small hole into a chamber of limited size), there is a possibility of generating vortex flows that intensively mix the gas. This results in a uniform distribution of the gas temperature throughout the entire volume of the spherical plasma structure produced in the experiment.

ACKNOWLEDGMENTS

We thank V.M. Torchinskiĭ and M.Yu. Pustyl'nik for providing us with the diagnostic equipment and assisting in experiments with a dusty plasma. This work was supported in part by the Russian Foundation for Basic Research, project no. 02-02-16021.

REFERENCES

1. Yu. A. Lebedev and M. V. Mokeev, Fiz. Plazmy **27**, 443 (2001) [Plasma Phys. Rep. **27**, 418 (2001)].
2. Yu. A. Lebedev, M. V. Mokeev, A. V. Tatarinov, and I. L. Epstein, in *Proceedings of the IV International Workshop on Microwave Discharges: Fundamentals and Applications, Zvenigorod, 2001* (Yanus-K, Moscow, 2001), p. 187.
3. Qing Zhou, D. K. Otorbaev, G. J. H. Brussaard, *et al.*, J. Appl. Phys. **80**, 1312 (1996).
4. S. I. Gritsinin, I. A. Kossyi, N. I. Malykh, *et al.*, J. Phys. D **31**, 2942 (1998).
5. S. A. Astashkevich, M. Käning, E. Käning, *et al.*, J. Quant. Spectrosc. Radiat. Transf. **56**, 725 (1996).
6. L. Tomasini, A. Rousseau, G. Gousset, and P. Leprince, J. Phys. D **29**, 1006 (1996).

7. N. Lang, M. Kalatchev, M. Käning, *et al.*, in *Frontiers in Low-Temperature Plasma Diagnostics III, Saillon, 1999* (Centre de Recherches en Physique des Plasmas, Ecole Polytechnique Federale de Lausanne, Lausanne, 1999), p. 253.
8. Yu. A. Lebedev, A.V. Tatarinov, and I. L. Epstein, Plasma Sources Sci. Technol. **11**, 146 (2002).
9. L. Bardos and Yu. A. Lebedev, Teplofiz. Vys. Temp. **38**, 552 (2000) [High Temp. **38**, 528 (2000)].
10. V. I. Molotkov, A. P. Nefedov, M. Yu. Pustyl'nik, *et al.*, Pis'ma Zh. Éksp. Teor. Fiz. **71**, 152 (2000) [JETP Lett. **71**, 102 (2000)].
11. B. M. Yavorskiĭ and A. A. Detlaf, *Handbook of Physics* (Nauka, Moscow, 1974).
12. Yu. P. Raizer, *Physics of Gas Discharge* (Nauka, Moscow, 1987; Springer-Verlag, Berlin, 1991).
13. E. Räuchle, in *Proceedings of the III International Workshop on Microwave Discharges: Fundamentals and Applications, Abbaye Royale de Fontevraud, 1997*; J. Phys. IV (France) **8**, Pr7-99 (1998).

Translated by N.F. Larionova

Plasma Physics Reports, Vol. 29, No. 3, 2003, pp. 231–234. Translated from Fizika Plazmy, Vol. 29, No. 3, 2003, pp. 256–260.

LOW-TEMPERATURE PLASMA

Efficient Generation of Negative Hydrogen Ions in a Low-Voltage Cesium–Hydrogen Discharge

F. G. Baksht, L. I. Elizarov, V. G. Ivanov, S. I. Kon'kov, N. K. Mitrofanov, and S. M. Shkol'nik

Ioffe Physicotechnical Institute, Russian Academy of Sciences, Politekhnicheskaya ul. 26, St. Petersburg, 194021 Russia

Received June 27, 2002

Abstract—The possibility of achieving the high density of negative hydrogen ions N_{H^-} in a low-voltage cesium–hydrogen discharge is investigated. The N_{H^-} density is determined experimentally from the absorption of laser radiation due to the photodetachment of electrons from H^- ions. The discharge plasma is investigated by the probe technique. The populations of the excited states of Cs atoms are determined from their emission intensities. With an input power of $W \approx (15–25)$ W/cm^2 in the discharge, densities of $N_{H^-} \sim (10^{12}–10^{13})$ cm^{-3} are achieved. The self-consistent calculations of the plasma parameters in the discharge gap agree well with the experimental results. The absorption of laser radiation due to the photoionization of Cs atoms is investigated. It is shown that the role of this absorption mechanism is negligible. © *2003 MAIK "Nauka/Interperiodica".*

1. Negative hydrogen ions are used in acceleration techniques, controlled nuclear fusion, plasma technologies, etc. At present, H^- ions are usually produced in volume plasma sources via the dissociative attachment (DA) of thermal electrons to vibrationally excited H_2 molecules, which are primarily in the ground electronic state $X'\Sigma_g^+(v)$.

This paper is devoted to the generation of H^- ions in a plasma of a cesium–hydrogen discharge. We study a low-voltage (LV) modification of this discharge—an LV arc with a heated cathode. The discharge voltage U is chosen such that the cathode potential drop φ_1 is not high enough to excite the lower dissociation term $b^3\Sigma_u^+$ of an H_2 molecule directly by the cathode electron beam (the voltage needed to excite this term from the ground state $X'\Sigma_g^+(v = 0)$ is equal to $U_1 \approx 8.8$ V). At these φ_1 values, both the direct dissociation of molecules by electron impact and the processes of electronic excitation followed by the stepwise ionization of molecular or atomic hydrogen in an LV discharge are excluded. As a result, the density of atomic hydrogen in an LV cesium–hydrogen discharge is relatively low and only Cs atoms are ionized. The degree of ionization of Cs is controlled by choosing the proper Cs concentration and by heating the plasma electrons to the required temperature T_e. The small (as compared to high-voltage discharges) content of atomic hydrogen in the LV-discharge plasma substantially enhances the vibrational pumping of H_2 molecules, which is necessary for the DA generation of H^- ions. The reason is that the constants of v–t exchange between vibrationally excited H_2 molecules and H atoms [1] are three orders of magnitude higher than the corresponding constants for pure molecular hydrogen [2].

The theory of such a discharge was developed in [3–5]. The first experimental studies [6–10] showed that the plasma parameters required for intense H^- generation were actually achieved in these discharges. In [11], the density N_{H^-} of negative hydrogen ions was measured experimentally from the absorption of laser radiation due to the photodetachment of electrons from H^- ions. It was shown that the H^- density measured with this technique near the cathode was close to the N_{H^-} density calculated under the assumption that the plasma in the gap was uniform.

In this paper, we focus on two problems. First, a detailed comparison between theory and experiment is performed using the typical regimes of an LV cesium–hydrogen discharge as an example. The experiment is compared with the exact local values of the density $N_{H^-}(x)$ calculated by numerically solving the full set of equations [5] describing the discharge (rather than with the calculated average densities N_{H^-}). Second, we consider the problem of the populations N_k of the highly excited states of Cs atoms ($k = 7P, 6D, \ldots$), because the photoionization of these states can also contribute to the absorption of laser radiation. The populations of these states are not only calculated numerically (as in [11]), but also determined experimentally. The measured and calculated populations $N_k(x)$ are compared to each other. It is shown that the absorption of laser radi-

1063-780X/03/2903-0231$24.00

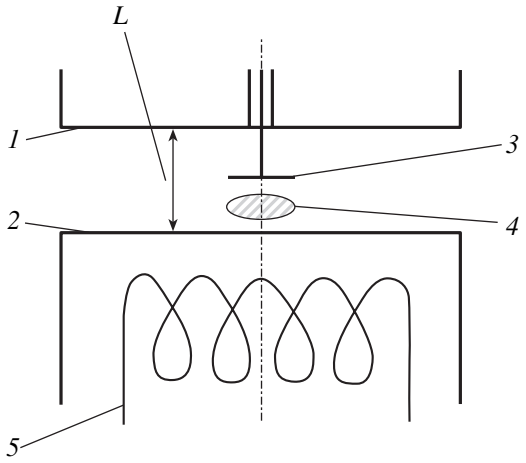

Fig. 1. Schematic of the experimental diode: (*1*) anode, (*2*) cathode, (*3*) probe, (*4*) cross section of the laser beam, and (*5*) heater.

ation due to photoionization from these states is insignificant.

2. Figure 1 shows a schematic of the experiment. The measurements were performed in a diode with plane-parallel electrodes separated by a gap of length $L = 3$ mm. The electrodes were the ends of cylinders with diameters $D = 12$ mm; the side surfaces of the cylinders were insulated with BeO ceramic. The emitter was a platinum foil attached by spot welding to the end of the molybdenum cylinder. A 0.1-mm-diameter cylindrical probe made from gold-plated tungsten was inserted into the gap through a hole in the center of the anode; the axis of the 2-mm-long probe was parallel to the electrode surfaces. The probe measured the electron temperature T_e, electron density n_e, and plasma potential φ in the center of the gap ($x = L/2$). The gap-averaged populations of the excited states of Cs atoms was determined from the intensities of the corresponding lines.

The density N_{H^-} was determined from the absorption of laser radiation due to the photodetachment of electrons from H^- ions. A cw semiconductor laser with a power $P \simeq 0.1$ W generated radiation in the band $\Delta\lambda \sim 2$ nm with the maximum intensity near $\lambda_0 = 816$ nm ($h\nu_0 = 1.52$ eV). The wavelength λ_0 falls into a rather flat maximum of the ionization cross section for an H^- ion ($\sigma_0 = 4 \times 10^{-17}$ cm^{-2} [12]). This radiation can easily be filtered from the discharge emission because this wavelength falls into a fairly wide "window" in the Cs emission spectrum. The laser radiation was divided into a reference and probing beams. The probing beam was focused so that the beam cross section in the gap was elliptical. The 1-mm-long major semiaxis was parallel to the electrodes, and the 0.35-mm-long minor semiaxis was perpendicular to the electrodes. The difference signal between the reference and probing beams was amplified by a differential amplifier and was then recorded with a special circuit [13]. With this circuit, we achieved a sensitivity of the measurements of the relative absorption of laser radiation of no worse than 10^{-5}. The experimental device and the measurement technique are described in more detail in [11].

To compare the experiment with the theory, we used the discharge modes with a relatively dense plasma ($p_{H_2}L \geq 1$ torr mm). In this case, as a rule, the interaction of $H_2(v)$ molecules with the electrode surfaces only slightly affects the vibrational distribution function (VDF) in the plasma bulk and, thus, the VDF does not depend on the unknown probabilities of the vibrational deactivation of molecules on cesium-coated surfaces. When solving the set of equations describing the discharge, the electron temperature $T_e(L/2)$ measured by a probe located in the center of the gap was specified as an entry parameter. The distributions of the other plasma parameters in the gap were calculated by solving the set of transport equations with the corresponding boundary conditions [5]. The VDF of a molecule in the ground state $X'\Sigma_g^+(v)$ and the densities N_k of the excited Cs atoms were calculated at every point x of the gap from the equations of electronic–vibrational kinetics [4]; these equations were solved self-consistently with the transport equations. A particular problem is how to specify the parameter $N_{Cs}^{(0)} = \langle N_{Cs}(x) + N_{Cs^+}(x) \rangle$ [5], which is equal to the total cesium density averaged over the discharge gap. Due to the diffusion of Cs through the feeding line of the experimental device (see, e.g., [6]) and because of the gas-temperature variations in the cell, the averaged density $N_{Cs}^{(0)}$ can be much lower than the equilibrium cesium density $N_{Cs}(T_{Cs})$ immediately above the liquid cesium surface (here, T_{Cs} is the Cs liquid-phase temperature). Since $N_{Cs}^{(0)}$ is difficult to calculate, the $N_{Cs}^{(0)}$ value was determined from the condition that the calculated and measured densities $N_{Cs^+}(L/2)$ of cesium ions should coincide in the center of the gap, where the probe is located. Under our experimental conditions, we have $N_{Cs^+} \approx n_e$.

3. Figures 2 and 3 present the experimental results and their comparison with theory. Figure 2 shows the measured density N_{H^-} near the cathode (*1*) for two values of the hydrogen pressure p_{H_2} and close values of the discharge current density j. The horizontal bars indicate the spatial resolution, which is determined by the transverse dimensions of the laser beam. Solid curves show the calculated profiles of the density $N_{H^-}(x)$ and some other plasma parameters along the gap, including the cesium neutral density $N_{Cs}(x)$ and the temperature $T_g(x)$ of the neutral gas and Cs^+ ions. The figure also shows the calculated values of potential

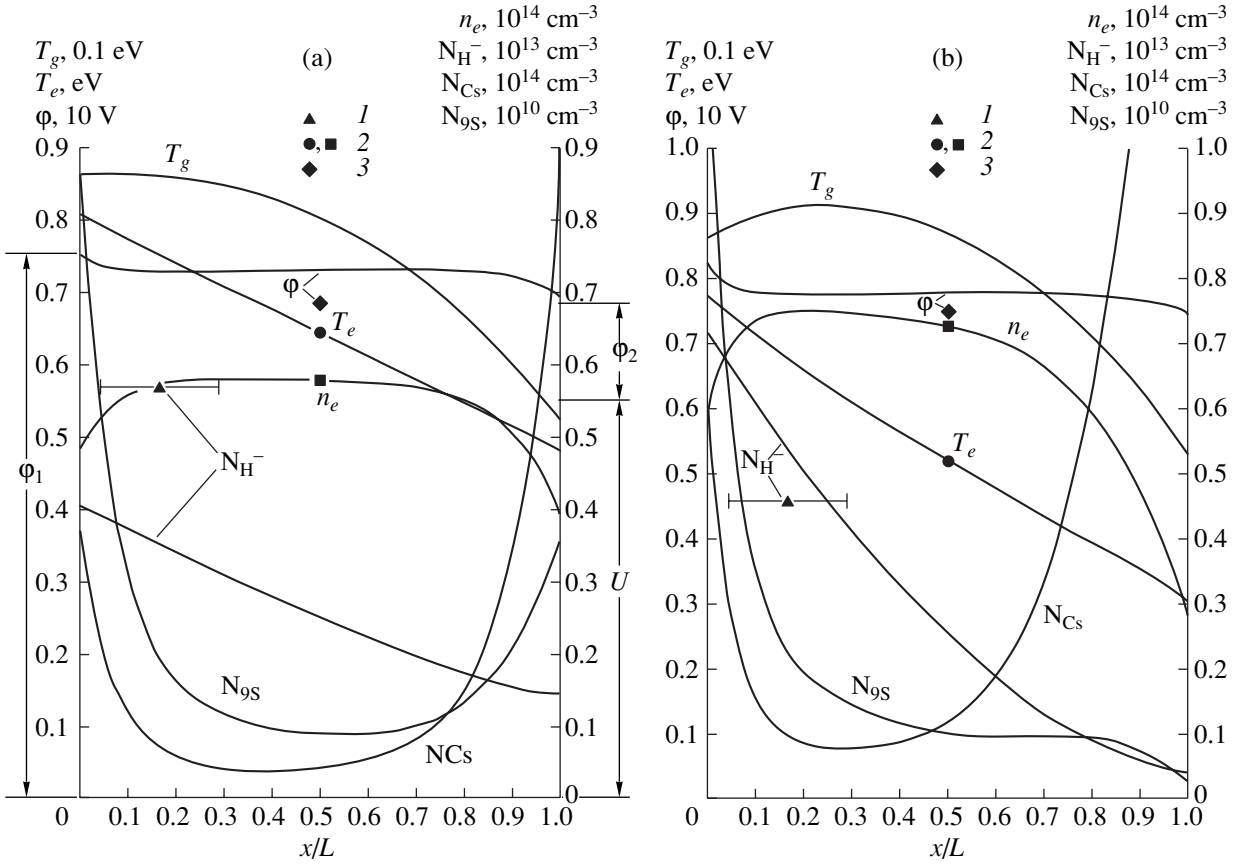

Fig. 2. Density of negative hydrogen ions and some other parameters of the plasma of a low-voltage cesium–hydrogen discharge: (*1*) the N_{H^-} density measured from the absorption of laser radiation near the cathode and (*2*) the electron temperature and density and (*3*) plasma potential measured by an electric probe in the center of the gap for (a) p_{H_2} = 1 torr, j = 3.2 A/cm^2, and U = 4.5 V and (b) p_{H_2} = 2 torr, j = 3.7 A/cm^2, and U = 7 V. The solid curves show the calculated profiles of the plasma parameters in the gap at (a) p_{H_2} = 1 torr, $N_{Cs}^{(0)} = 0.75 \times 10^{14}$ cm^{-3}, U = 5.44 V, φ_1 = 7.5 V, and φ_2 = 1.44 V and (b) p_{H_2} = 2 torr, $N_{Cs}^{(0)} = 10^{14}$ cm^{-3}, U = 6.71 V, φ_1 = 8.2 V, and φ_2 = 0.73 V.

drops φ_1 and φ_2 across the cathode and anode sheaths and the calculated discharge voltage U. It can be seen in Fig. 2 that, at relatively small input powers of $W \approx$ (15–25) W/cm^2, a rather high H^- density of $N_{H^-} \sim (10^{12}$–$10^{13})$ cm^{-3} is achieved in the plasma.

Figure 2 also illustrates a typical longitudinal distribution of the populations $N_k(x)$ of the highly excited Cs states that can be ionized by laser radiation. As an example, the figure shows the distribution of the population $N_{9S}(x)$ of the 9*S* state. This distribution is highly nonuniform, which is explained by the fact that the $N_{Cs}(x)$ and $T_e(x)$ distributions are nonuniform. At a relatively low hydrogen pressure ($p_{H_2} \le 1$ torr), when the T_e temperature drop across the gap is relatively small, the $N_{9S}(x)$ distribution is similar to the $N_{Cs}(x)$ distribution and has maxima near the electrodes, where the Cs neutral density is relatively high (Fig. 2a). At a higher hydrogen pressure ($p_{H_2} \ge 2$ torr), when the T_e temperature drop across the gap is large and the temperature T_e near the anode is low, the maximum of the density $N_{9S}(x)$ near the anode disappears (Fig. 2b).

The ionization of the highly excited Cs states (from 7*P* and higher) can cause significant troubles for the diagnostics of the H^- ions by the absorption of laser radiation with λ_0 = 816 nm. Figure 3 shows the gap-averaged populations $\langle N_k(x) \rangle$ of several highly excited Cs states for one of the investigated discharge regimes. The populations were measured from the spectrum of plasma emission (6*P*–9*S*, 5*D*–7*F*, 5*D*–8*F*, 6*P*–7*D*, 5*D*–6*F*, and 5*D*–5*F* transitions). The figure also shows the corresponding values of $\langle N_k(x) \rangle$ calculated self-consistently by the procedure described in [4, 5]. It can be seen that, although the calculated values are always somewhat higher than the experimental ones, the difference between them is small. The experiment confirms

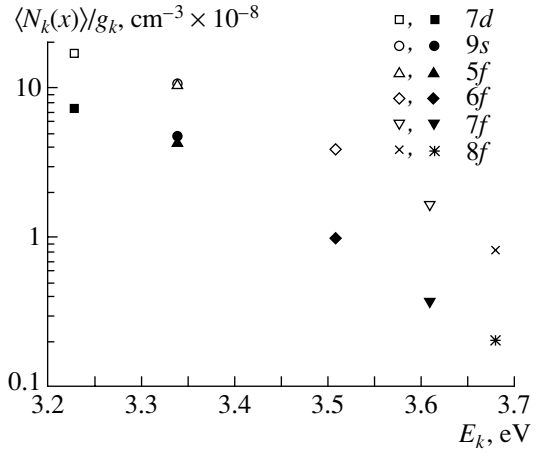

Fig. 3. Gap-averaged densities ⟨$N_k(x)$⟩ of the excited Cs atoms, divided by the statistic weights g_k of the excited states, for the discharge parameters p_{H_2} = 1 torr, j = 2 A/cm^2, U = 7 V, $T_e(L/2)$ = 0.7 eV, and $n_e(L/2) = 5 \times 10^{13}$ cm^{-3} (the calculated value of $N_{Cs}^{(0)}$ is equal to 0.64×10^{14} cm^{-3}). The closed symbols show the experimental data, and the open symbols show the calculated results.

that, in the approximation of a quasi-continuous spectrum, the values of N_k/g_k for highly excited Cs states are only determined by the excitation energy E_k of the corresponding state (see [4, 11] for details]). As a result, both in theory and experiment, the values of N_k/g_k are the same for the 9*S* and 5*F* states, for which the excitation energies are E_k = 4.137 eV and 4.146 eV, respectively [14]. This fact makes it possible to accurately calculate the photoabsorption of laser radiation due to the photoionization of cesium. In the examples presented in Figs. 2a and 2b, the calculated relative contributions to the photoabsorption due to cesium photoionization (the photoionization cross sections were taken from [15]) amount to $\Delta P/P_0 \approx 0.9 \times 10^{-6}$ and 1.1×10^{-6}, respectively. These values, which correspond to the calculated absorption of laser radiation due to cesium photoionization at the center of the ellipsoidal laser beam (see Fig. 1), are two orders of magnitude lower than the measured values (2.3×10^{-4} and 2×10^{-4}, respectively) of relative photoabsorption. The small absorption due to cesium photoionization is also confirmed by the calculations of [11], which were performed under the assumption that the plasma in the gap is uniform.

Thus, the experiment has demonstrated the possibility of an efficient volume generation of H^- ions in the plasma of an LV cesium–hydrogen discharge. With an input power of $W \approx$ (15–25) W/cm^2 in the discharge, densities of $N_{H^-} \sim (10^{12}$–$10^{13})$ cm^{-3} have been achieved. Calculations have shown that these N_{H^-} values are not limiting and can be raised by increasing the electron temperature T_e. This can be achieved, e.g., by increasing the emission current j_S from the plane cathode or by using a hollow-cathode cesium–hydrogen discharge.

ACKNOWLEDGMENTS

This study was performed with the support of the St. Petersburg Scientific Center of the Russian Academy of Sciences for 2002.

REFERENCES

1. E. Garcia and A. Lagana, Chem. Phys. Lett. **123**, 365 (1986).
2. J. H. Kiefer, J. Chem. Phys. **57**, 1938 (1972).
3. F. G. Baksht and V. G. Ivanov, Pis'ma Zh. Tekh. Fiz. **12**, 672 (1986) [Sov. Tech. Phys. Lett. **12**, 278 (1986)].
4. F. G. Baksht, L. I. Elizarov, V. G. Ivanov, and V. G. Yur'ev, Fiz. Plazmy **14**, 91 (1988) [Sov. J. Plasma Phys. **14**, 56 (1988)].
5. F. G. Baksht, L. I. Elizarov, and V. G. Ivanov, Fiz. Plazmy **16**, 854 (1990) [Sov. J. Plasma Phys. **16**, 497 (1990)].
6. F. G. Baksht, G. A. Dyuzhev, L. I. Elizarov, *et al.*, Zh. Tekh. Fiz. **62** (9), 148 (1992) [Sov. Phys. Tech. Phys. **37**, 959 (1992)].
7. F. G. Baksht, G. A. Dyuzhev, L. I. Elizarov, *et al.*, Pis'ma Zh. Tekh. Fiz. **19** (22), 39 (1993) [Tech. Phys. Lett. **19**, 716 (1993)].
8. F. G. Baksht, V. G. Ivanov, A. G. Nikitin, and S. M. Shkol'nik, Pis'ma Zh. Tekh. Fiz. **20** (22), 84 (1994) [Tech. Phys. Lett. **20**, 927 (1994)].
9. F. G. Baksht, V. G. Ivanov, A. N. Kostin, *et al.*, Zh. Tekh. Fiz. **65** (8), 186 (1995) [Tech. Phys. **40**, 851 (1995)].
10. A. G. Nikitin and S. M. Shkol'nik, Zh. Tekh. Fiz. **67** (1), 125 (1997) [Tech. Phys. **42**, 110 (1997)].
11. F. G. Baksht, V. G. Ivanov, S. I. Kon'kov, and S. M. Shkol'nik, Zh. Tekh. Fiz. **71** (8), 17 (2001) [Tech. Phys. **46**, 946 (2001)].
12. H. Massey, *Negative Ions* (Cambridge Univ. Press, London, 1976; Mir, Moscow, 1979).
13. Yu. A. Barinov and S. I. Kon'kov, Prib. Tekh. Éksp., No. 2, 60 (2001).
14. *Physical Quantities: Handbook*, Ed. by I. S. Grigor'ev and E. Z. Meĭlikhov (Énergoatomizdat, Moscow, 1991).
15. J. Lahiri and S. T. Manson, Phys. Rev. A **33**, 3151 (1986).

Translated by N.F. Larionova

Plasma Physics Reports, Vol. 29, No. 3, 2003, pp. 235–250. Translated from Fizika Plazmy, Vol. 29, No. 3, 2003, pp. 261–276.

THE 30th ANNIVERSARY OF SPT OPERATION IN SPACE

2001 was anniversary for the plasma physics community. In May 1951, active investigations on controlled nuclear fusion with magnetic plasma confinement began in the USSR and the USA. By the end of the second decade of these investigations, a tokamak toroidal system was developed at the Kurchatov Institute. Now, this system underlies the International Experimental Thermonuclear Reactor (ITER) project. However, another achievement of the Kurchatov institute, also related to plasma physics, is less known. This is the successful development of the idea proposed by A.I. Morozov—a small-size stationary plasma thruster (SPT) with a relatively low thrust, which is, however, sufficient for controlling a space vehicle under conditions of microgravity. Thirty years ago, at the end of 1971, such a thruster installed on a Meteor satellite of mass about 2 t lifted this satellite by 15 km in one week. This made it possible to maintain a space vehicle in an orbit for a long time, to adjust its orbit, to orient its solar batteries, etc. Moreover, at present, a flight of a spacecraft to Mars is being prepared with the purpose of delivering soil from its satellite Phobos. It is planned that the motion of this spacecraft outside the gravitational field of the planets will be controlled with an SPT.

On December 25, 2001, a symposium devoted to the thirtieth anniversary of SPT operation in space was held at the Institute of Nuclear Fusion of the Russian Research Centre Kurchatov Institute. Some of the reports presented at this symposium are published in this issue.

Editorial Board

The Conceptual Development of Stationary Plasma Thrusters

A. I. Morozov

Nuclear Fusion Institute, Russian Research Centre Kurchatov Institute, pl. Kurchatova 1, Moscow, 123182 Russia

Received May 23, 2002; in final form, September 25, 2002

Abstract—The history of the development of the concept of the stationary plasma thruster is described. The data obtained indicate the possibility of creating extended (over a distance substantially longer than the Debye radius) electric fields in a fully ionized plasma with a relatively high electron temperature ($T_e > 10$ eV) and a conductivity close to the classical one. Based on these results, a number of fundamentally new plasma-dynamic systems were proposed; in particular, the principles of plasma optics were formulated and verified experimentally. In the course of these investigations, new physical processes, such as the formation of the distribution function of the electrons in their collisions with the wall and the effect of the near-wall conductivity, were discovered. The structure of the Debye layer for the case in which the coefficient of the secondary electron emission of a dielectric wall is larger than unity was investigated. © *2003 MAIK "Nauka/Interperiodica"*.

1. INTRODUCTION

1. As L.A. Artsymovich said, plasma physics is faced, among others, with three great problems:

(i) controlled nuclear fusion,

(ii) MHD generators capable of substantially increasing the efficiency of thermoelectric power stations, and

(iii) space plasma thrusters.

The first section of this paper is devoted to the development of stationary plasma thrusters, which have operated for thirty years on 30 satellites and have proved to be quite adequate for the current problems of astronautics. The second section outlines the importance of the physical results obtained in the course of the development of stationary plasma thrusters (SPTs) for the general problems of plasma dynamics and various practical applications.

2. On December 29, 1971, the satellite *Meteor-18*, equipped with an ÉOL electric propulsion system (EPS) with SPTs (Fig. 1), was launched into orbit. The SPTs and the ÉOL model were developed at the Kurchatov Institute of Atomic Energy, and the flight EPS, which satisfied all the requirements of space technology, was developed at the Fakel Experimental and Design Bureau (EDB) (Kaliningrad).

The tests were successful [1]. Since that time, the Fakel EDB has supplied various satellites with SPT-based EPSs. In fact, the launching of the ÉOL system with SPTs marked the beginning of the practical use of electric propulsion engines.

1063-780X/03/2903-0235$24.00 © 2003 MAIK "Nauka/Interperiodica"

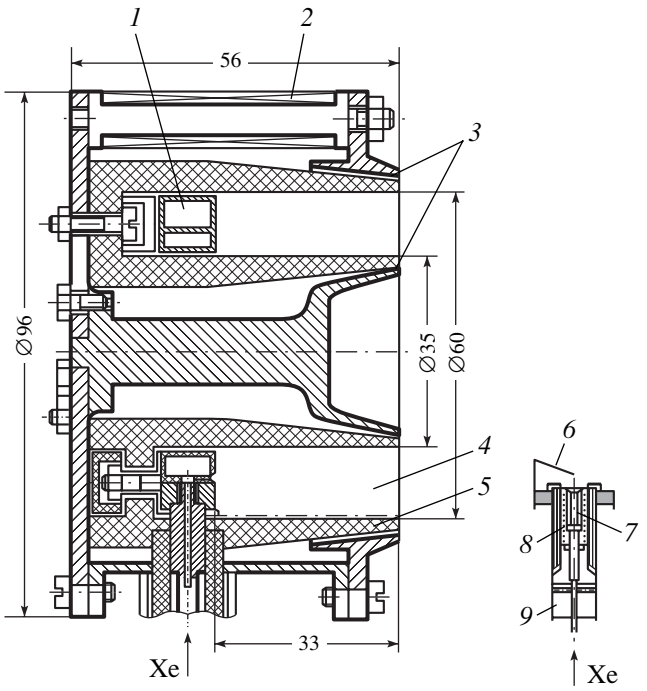

Fig. 1. Schematic diagram of the first ÉOL-SPT with an electric-discharge cathode: (*1*) anode, (*2*) magnetic coils, (*3*) magnet poles, (*4*) acceleration channel, (*5*) insulator, (*6*) ignition electrode, (*7*) emitter made from LaB_6, (*8*) preheater, and (*9*) cathode case.

The necessity of switching to electric engines is quite evident. It follows from the Tsiolkovsky formula, which relates the starting (initial) mass M_0 of a rocket with its final mass (payload):

$$M = M_0 e^{-\frac{v}{u}},$$

where u is the material exhaust velocity from the engine and v is the so-called characteristic expedition velocity, i.e., the velocity that a rocket might acquire if it were not affected by other forces and moved along a straight line and if the engine operated as during an actual expedition. For example, in the case of a Moon flight with a landing and return mission, the characteristic velocity is $v \sim 23$ km/s. At the same time, the gas exhaust velocity from Saturn engines installed on the Saturn–Apollo rocket complex, which got astronauts to the Moon and back, was ~3 km/s. Because of the large difference between the characteristic and exhaust velocities, the starting mass of the complex was 2900 t, whereas the command module returning with the astronauts weighed 5 t.

Clearly, it is necessary to increase the exhaust velocity. Among thermochemical engines, oxygen–hydrogen engines provide the highest flow velocity (~4.5 km/s), which, however, is too low for long-range flights.

The switching to engines with high exhaust velocities requires external energy sources. In space, energy (solar or nuclear) is cheaper than mass; hence, such a change is justified. The energy cost of the thrust (W/N) increases in proportion to the exhaust velocity; consequently, for every expedition, there is an optimal exhaust velocity at which the total mass of the working material and the energy system is minimal. At present, the optimal exhaust velocities are 15–30 km/s for most of the tasks, and it is SPTs that cover this range.

3. My first paper on the problem of plasma acceleration (in particular, electric propulsion) was published in 1957 [2]. In that paper, a rail-type accelerator and an induction accelerator of plasma rings were described for the first time. In addition, that paper revealed the role of the volume Hall electric field in plasma acceleration, which was especially important for further research.

The second step in my work on electric propulsion was stimulated by a boom in this field caused by the progress in space research. In July 1959, Artsimovich, the head of the Plasma Research Department of the Institute of Atomic Energy[1] gathered his collaborators involved in the problem of the generation of ion and plasma flows and suggested that they to draw more attention to the problem of electric propulsion. Soon, four approaches to the problem and the leaders responsible for them were determined. These approaches were based on pulsed guns (A.M. Andrianov); Penning ions sources (P.M. Morozov); ion magnetrons, originally used by M.S. Ioffe to fill a mirror confinement system (A.V. Zharinov); and, finally, an original scheme of a stationary magnetoplasma analog of a gasdynamic nozzle (A.I. Morozov).

The general principle of operation of this analog is as follows. It was proposed that, in a coaxial system of two profiled electrodes, the current (as a matter of course, this current was assumed to flow approximately in the radial direction) will produce a magnetic-pressure gradient, which will cause the acceleration of the plasma generated from a gas admitted at the entrance to the system. In such a system, the Alfvén velocity[2] plays the role of acoustic velocity; as a result, at large Reynolds numbers, the flow velocity at the exit from the system should be on the order of

$$u \approx \sqrt{2}\, C_{A0},$$

where C_{A0} is the Alfvén velocity corresponding to the parameters at the exit of the system.

It should be remembered that this was the time of euphoria aroused by the progress in space research; thus, the main aim of electric propulsion research was considered to be the creation of an engine for manned expedition to Mars. Engines with a power of 10 MW, a thrust of 100 N, and an exhaust velocity of 100 km/s were thought about. For this reason, the above scheme

[1] Presently, the Nuclear Fusion Institute at the Russian Research Centre Kurchatov Institute.

[2] More precisely, it is the fast magnetosonic velocity; however, thermal effects are assumed to be unimportant.

was appreciated by Artsimovich, and he insisted that I organize a working group and, under the guidance of G.Ya. Shchepkin, verify the idea of a stationary coaxial "quasi-nozzle." The test device was put into operation in February 1960. The device provided the necessary quasi-steady currents and voltages for 2–5 ms. However, the result turned out to differ from that predicted by an elementary theory because of the unfavorable Hall effect. It became clear that it was not an easy matter to achieve the predicted operating regime of the quasi-nozzle in its original version. In three to four years, we gained a clearer understanding of the nozzle operation after creating a theory of two-component ideal plasma flows and after discovering the effects of the magnetic insulation of the anode, current crisis, compression flows, etc. However, it was only about thirty years later that, due to the joint effort of scientists from the Kurchatov Institute of Atomic Energy, Kharkov Institute of Physics and Technology, Troitsk Institute for Innovation and Fusion Research, Institute of Applied Mathematics, etc., we managed to make the nozzle work as was predicted by the simple model; moreover, we had to increase the power of the device to above one gigawatt. This powerful machine was named KSPU [3].

As time elapsed, the difficulties related to the quasi-nozzle operation became more evident, and the hope for great energetics rapidly waned. We had to search for new approaches to the electric-propulsion problem. Ultimately, this search led us to the SPT.

The work on the SPT at the Kurchatov Institute progressed in close cooperation with other institutions. The Kurchatov Institute organized an interdepartmental electric propulsion seminar, which operated for ten years. Regular All-Union conferences on plasma accelerators also considerably contributed to the progress in this new field of physics and technology.

In this paper, the focus is primarily on the studies that were performed with my immediate participation. The results obtained by other teams are reported elsewhere (see, e.g., [4, 5]). The operation of SPTs and similar systems is described in detail in reviews [6, 7].

2. CREATION OF THE SPT

A chronological description of the fairly intricate work on optimizing the SPT design and technology together with the research of the physical processes in the SPT would be very involved. For this reason, we will describe these two lines of investigation separately.

2.1. Physical Backgrounds

By early 1962, it became clear that there was no hope for high-power space energetics, and we had to turn our attention toward engines with powers of several hundreds of watts (at best, several kilowatts). Furthermore, we had to direct our efforts to engines with a relatively low exhaust velocity of $u \le 25$ km/s. All this disagreed with the original Mars-oriented concept. Moreover, there was already a confirmation of the validity of new requirements, specifically, an engine created by A.M. Andrianov for the position control system for the *Zond-2* interplanetary vehicle constructed at the experimental and design bureau headed by S.P. Korolev. The parameters of this engine were moderate: the energy released in one pulse was ~57 J, the exhaust velocity was ~2–5 km/s, the pulse duration was $\sim 10^{-3}$ ns, and the repetition rate was ~1 Hz. In 1963, the *Zond-2* vehicle with this propulsion system was put into interplanetary flight, during which it maintained the vehicle orientation for ~1 h.

Thus, it was necessary to radically change the main direction of research in our laboratory.

Naturally, the question arose as to what we should create. At first, there was no doubt that this thruster should be stationary. Pulsed thrusters are appropriate for controlling the vehicle orientation; however, it is unlikely that they will be competitive with stationary thrusters when dealing with the orbit correction, all the more so, in the case of long-term flights, when so-called march propulsion systems are required. Second, it was also clear that, in the above power range (~100–1000 W), it was necessary to use external magnetic fields (rather than the self-field as in the quasi-nozzle) in order for the system to operate in the low-current (~1–10 A) regime.

Along with these general considerations, there were also some physical aspects; namely, it was necessary that the drift of electrons in the system be closed, otherwise emitters ensuring currents of several tens of amperes would be required. In addition, the closed drift clearly demonstrated its advantages in experiments [8, 9]. However, all this was already in Zharinov's proposal, according to which an ion magnetron could be transformed into a thruster by using an annular channel with a unidirectional ion flow [9]. It was assumed that, in this case, the process would not change dramatically; the potential jump would occur over a distance of no longer than the electron Larmor radius; and the normal velocity regimes would remain high-voltage ($U_p \ge 2$ kV), as in magnetrons.

These specific features of Zharinov's scheme seemed to me disadvantageous. The narrow acceleration gap was dangerous because of the possible breakdowns, and the high voltage (even with the use of the highest Z elements, e.g., lead) resulted in exhaust velocities of ≥44 km/s.

For this reason, it was proposed to create a thruster an electric field distributed along the accelerating channel. This suggestion was met with the negative reaction of experts in gas discharge physics. They definitely stated that this experiment would be preposterous. The argument was that, for the forty years after Townsend

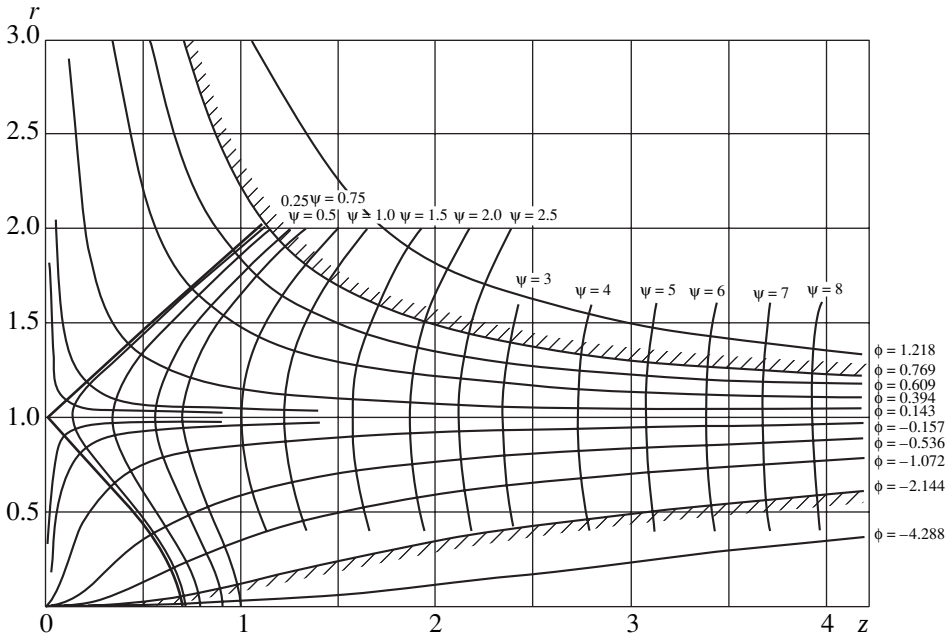

Fig. 2. Magnetic configuration of first SPT models: $\phi_m = z\ln r$ is the magnetic field potential, and $\psi = \frac{z^2}{2} + \frac{r^2}{4} - \frac{r^2}{2}\ln r$ is the flux function.

derived the formula for the classical conductivity across a magnetic field,

$$\sigma_\perp = \frac{\sigma_0}{1 + (\omega_e\tau_e)^2} \quad (1)$$

(where σ_0 is the plasma conductivity in the absence of a magnetic field, ω_e is the electron cyclotron frequency, and τ_e^{-1} is the effective electron collision frequency), an $\omega_e\tau_e$ value of no higher than several units had been achieved in experiments, whereas the proposed thruster required a Hall parameter value on the order of 1000 and higher. Of course, the opponents cited again and again the Bohm formula, which, if valid, doomed our work to failure (as well as all the problem of controlled fusion with magnetic confinement). Of great importance for those of us with Shchepkin was the fact that our leaders, Artsymovich and Leontovich, said nothing against our suggestion.

2.2. The Work Began

In the second half of 1962, a scheme of the thruster model was passed to the design office of our department to develop a thruster design.

Unfortunately, a schematic of the model from that time did not survive; however, we saved the results of calculations of the magnetic configuration used in this model (Fig. 2). The first model was similar to the latter E-1 model, which became a "base" one for a long time; however, there was one important distinction. In the first model, the channel walls were assembled from nonmagnetic rings with dielectric spacers in order to ensure the distribution of the electric field along the channel. The rings should be connected to a divider. In the E-1 model, the insulator was continuous (see below).

The model created can be described as follows. The physical basis of both this model and the subsequent ones was an axisymmetric magnetic field that increased from zero (more precisely, from a very small value) deep in the channel to its maximum value at the exit. This choice (which, at first glance, might appear to be strange) of the magnetic configuration is easily explained. The point is that I was well aware of the fundamental fact of the equipotentialization of magnetic field lines in a plasma at $T_e \longrightarrow 0$, which is described by the expression

$$\Phi(\mathbf{x}) = \Phi(\gamma), \quad (2)$$

where γ is the index of a magnetic field line.

In view of this fact, it was reasonable to make the magnetic field lines (and, thus, the equipotential surfaces) convex in the direction opposite to the channel exit. Due to such a curvature of the equipotential surfaces, the ions produced in the channel should be focused toward the middle of the channel, thus reducing the wall erosion. A gas distributor, which also acted as an anode, was located in the region where the magnetic field was close to zero. In the first experiments, the vacuum chamber served as a cathode. Thus, we arrived

at a scheme with an axisymmetric channel, a quasiradial magnetic field, and a longitudinal electric field. The magnitude of the magnetic field was chosen such that the ion Larmor radius ρ_i was much larger and the electron Larmor radius ρ_e was much smaller than the channel length L:

$$\rho_i \geq L \geq \rho_e. \tag{3}$$

We thereby ensured the closed drift of electrons. It was assumed that the processes in the channel would proceed as follows. Neutral atoms arriving from the gas distributor are ionized in the rotating electron cloud. The ions, being almost insensitive to the magnetic field, are accelerated and leave the SPT channel with an energy

$$\varepsilon = e\Phi_*, \tag{4}$$

where Φ_* is the potential at the point where the ion is produced. In turn, the electrons somehow force their way through the magnetic field to the anode; pass through the electric circuit; and fall through the emitting cathode into the accelerated ion flow, thus neutralizing it. Downstream from the ionization region, the current in the channel, where the electrons are strongly magnetized, should be carried predominantly by the ions. Therefore, we have

$$J_d \approx \frac{e}{M}\dot{m} = J_{\dot{m}}, \tag{5}$$

where $\dot{m}$ is the mass flow rate of the working material, M is the ion mass, e is the ion charge, and $J_{\dot{m}}$ is the mass flow rate expressed in the current units.

The question as to the mechanisms for the electron transport from the ionization region to the anode remained open. Estimates showed that a significant role in this process may be played by electron–neutral collisions and the electron precipitation onto wall rings; we also hoped for the beneficial effect of noise.

The voltage was chosen to be on the order of several hundred volts, and the discharge current should have been about several tens of amperes. The discharge was initiated by a high-voltage inductor placed near the exit from the channel.

Then, the day of the first test came. This was at the end of 1972. Due to the presence of the inductor, the discharge was easily ignited, and, very soon, we discovered two important phenomena. First, arcs were generated on the walls of the vacuum chamber during the discharge. This indicated that an electron source was required at the cathode potential to maintain a stable discharge in the channel. Second, it turned out that the discharge was essentially insensitive to the variations in the potential distribution over the rings and operated even if the rings were switched off. This was very important and allowed us to substantially modify the accelerator. Instead of the sectioned wall, we used an appropriate-size insulator made of insulation porcelain. However, as before, the discharge was ignited by the inductor. Furthermore, the discharge could be initiated only at voltages on the order of several hundred volts and ceased at lower voltages, depending on the presence (or absence) of wall arcs.

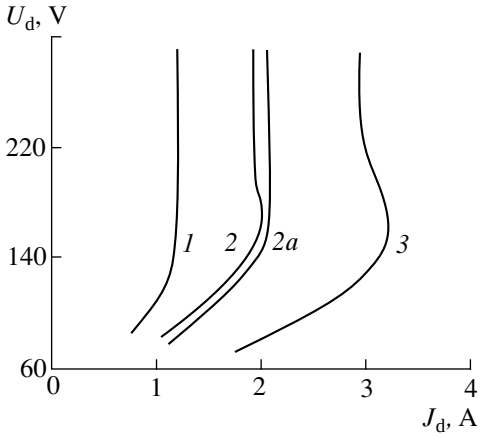

Fig. 3. Typical current–voltage characteristics of the SPT discharge for the optimal magnetic field and different mass flow rates of the working material: $\dot{m}$ = (*1*) 1, (*2*) 2, and (*3*) 3 mg/s. Curve *2a* shows the current–voltage characteristic for $\dot{m}$ = 2 mg/s and nonoptimal magnetic field.

The most important result of the experiments performed with the first model was that the conductivity turned out to be much lower than the Bohm conductivity. Thus, it became clear that the chosen way was not a dead-end.

Subsequent experiments under steady-state operating conditions made it possible to confirm the dependence of the discharge current J_d on the mass flow rate $\dot{m}$. A typical current-voltage characteristic had two distinct segments (Fig. 3): a horizontal one for $J_d < J_{\dot{m}} = \frac{e}{M}\dot{m}$ and a vertical one for $J_d > J_{\dot{m}}$, which corresponded to formula (5). New information was provided by thrust measurements. Initially, the thrust was measured with the help of a pendulum, specifically, a light copper disk hung on two threads and a ruler with which the disk deviation was measured. The results of these measurements agreed satisfactorily with the formula

$$F = \dot{m}V_m \sim \dot{m}\sqrt{\frac{eU_d}{M}} \sim \dot{m}\sqrt{U_d}. \tag{6}$$

Probe measurements showed that the extension of the region where the electric field high was strong was much greater than the electron Larmor radius ρ_e and, all the more, greater than the Debye radius r_D.

These results puzzled our opponents. They, however, recovered rapidly and began to contend that all this might be explained by the fact that the experiments were conducted in a vacuum chamber that had active

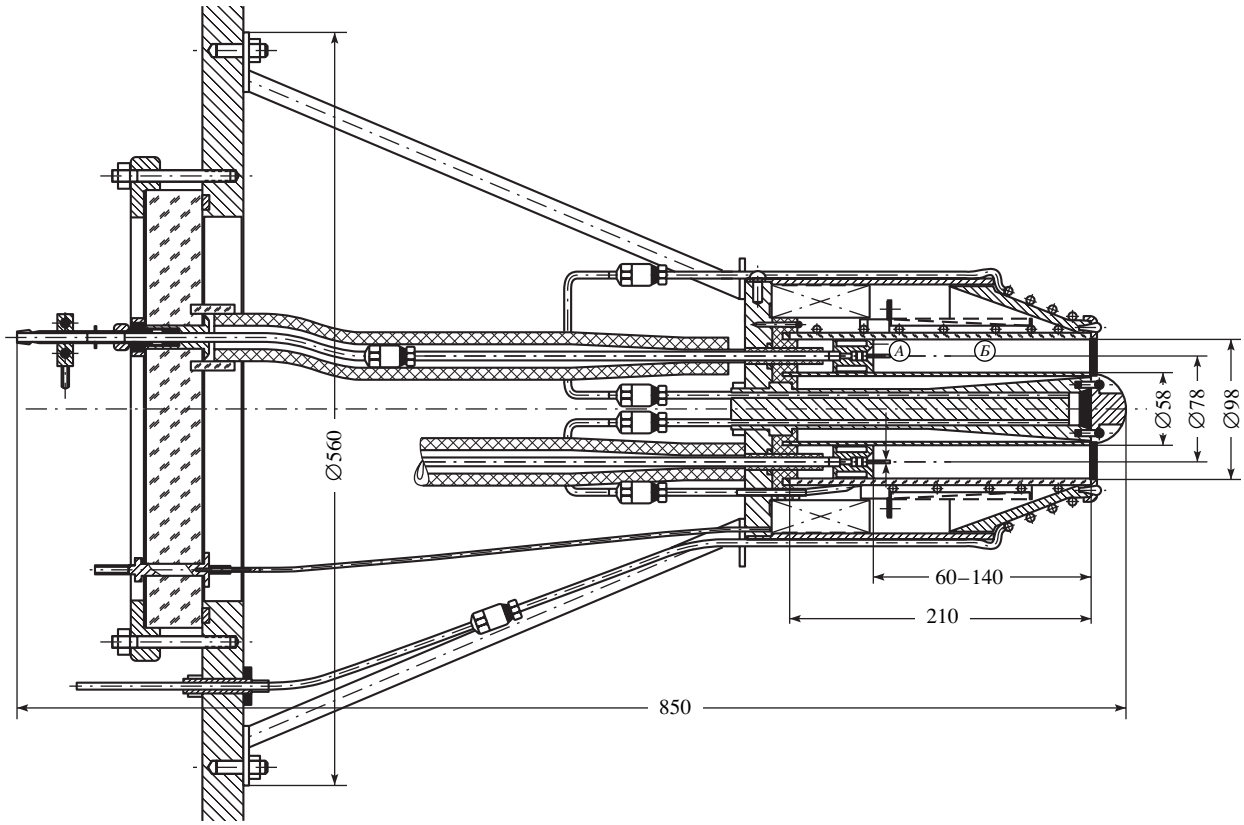

Fig. 4. Schematic diagram of the E-1 SPT.

walls (the main argument was that arcs did arise on them), whereas in space, where these artifacts would disappear, all would be as predicted by the classic Bohm formula.

In the meantime, our work continued. The accelerator demonstrated stable operation and justified our hopes. After we began to make the accelerator walls from continuous heat-resistant insulator, the choice of the insulator material became a very important problem, because it turned out that its composition had a profound effect on the thruster operation. After a series of tests, we decided in favor of quartz. Quartz insulators were used as the basic ones until 1968.

The second problem to be solved was the creation of an emitting cathode that would prevent arcs on the chamber walls and provide the ignition of a discharge in the accelerator. Such a gas-discharge facility with a LaB_6 thermal emitter was created by B.N. Markov in 1963.[3] The presence of a gas discharge in the cathode was necessary to create a plasma bridge along which electrons could freely move between the emitter and the jet. In the end of 1963, the accelerator had only one serious disadvantage—a low efficiency of ~20–30%. Since a typical power at which we examined the models was on the order of 5 kW, the accelerator needed water cooling. This did not embarrass us, because there were good reasons to hope that we should finally succeed in increasing the efficiency and radiative cooling would be sufficient. This, indeed, was the case.

In 1964, we designed and manufactured the E-1 model accelerator (the letter E signified the electric mechanism for ion acceleration). The sketch of this model is presented in Fig. 4. We carried out a wide range of physical studies with the E-1 accelerator; some of them will be described below.

At the end of 1968, we created the first radiative-cooled accelerator model that, unlike the previous model, did not overheat at a power of ~1 kW. At the same time, we began to use boron-containing ceramics (ABN, boron–silicon compounds, etc.); as a result, the efficiency increased to 45%.

It became clear that, for further progress, the elaborated scheme of the thruster should be tested in space. The part of this stage of research that was directly concerned with the Kurchatov Institute will be described in the next section, and the work that was performed at the Fakel EDB and the All-Union Scientific and Research Institute of Electromechanics (VNIIEM) and was

[3] Markov made an important contribution to the creation of ion sources for the electromagnetic separation of isotopes and a multicharged-ion source for the production of transuraniums in Dubna.

related to the operation of the first SPTs in space is considered in [4].

The activity related to space flights began at the end of 1969 and continued up to the end of 1971. At that time, I supervised the scientific research on creating the flight model of an electric propulsion system at the Fakel EDB. When I became free from this responsibility, we prolonged the physical investigations and optimization of the thruster at the Kurchatov Institute. In 1972–1973, one of the most important modifications made to the SPT design was the application of narrow poles. This increases the thruster efficiency to 50% with allowance for the expenditure of the mass and energy in the compensator cathode [1].

After that, the Kurchatov Institute practically stopped the work concerned with the engineering problems of the thruster, and attention was focused on the applications of SPTs in technology and the creation of accelerators with radically new parameters (see the last section of this paper). As for the running tasks concerned with SPTs, the work on their improvement and implementation was primarily performed at the Fakel EDB. Great assistance in this work was offered by the Moscow Aviation Institute. The main result of this cooperation was the achievement of a service lifetime of ~5000 h in the SPT-M models and a service lifetime of >9000 h in the M-100 model. These models are described in more detail in [4]. However, in spite of the high reliability, small weight, and other advantageous parameters of these thrusters, the efficiency remained at a level of ≤50% (as for the first thrusters) with allowance for the facts that the mass expenditure in the cathode was only ~0.1 of that in the main channel and that a very low power of ~0.5% was spent to supply the magnetic system connected in series to the main discharge. Besides, the thruster jet was highly divergent: about 90% of the ions were ejected within an angle of ±45°. An external manifestation of this fact was the presence of a sort of "spoke" (i.e., a very extended crossover) on the system axis.

The situation changed radically in the early 1990s, when the SEP firm (France) offered me and A.I. Bugrova—the head of the Plasma Laboratory at the Moscow Institute of Radioengineering, Electronics, and Automation (MIREA)—to create a fundamentally new SPT model and provided the financial support for this work. Such a thruster was created [6, 7]. It possesses two specific features (Fig. 5). First, there is a buffer volume, which ensures the uniform admission of the working material into the channel and where the working material is partially ionized, which also favors to the better organization of the process in the channel.

The second feature consists in a very careful adjustment of the channel length and the magnetic field profile. The necessity of such an adjustment is explained by the contradictory requirements on the field. On the one hand, the field must suppress the electron transport along the channel in order to decrease the through electron current from the cathode to anode; on the other hand, the magnetic field between the ionization region and the anode must allow the electrons produced by ionization to rapidly leave the discharge. In addition, the magnetic field must provide a profile of the equipotential surfaces such that the ion flow is pressed from the channel walls. The results obtained at the MIREA turned out to be very impressive. The efficiency of a thruster with the same dimensions as the M-70 model increased almost to 75% without allowance for the mass expenditure in the cathode and to ~68% with allowance for this expenditure. At the same time, the flow divergence was radically reduced (to a level of ≤±10°). The high efficiency allowed this model to operate at a power of up to 2 kW, whereas the limiting power of the conventional M-70 thruster was ~1 kW. This SPT was called the Aton SPT [10]. The shape of the Aton SPT jet depends on the coil currents; in particular, the jet can be cylindrical without any kind of spoke. When viewing from the exit side, it is clearly seen that the ion flow is well separated from the walls.

Note, however, that such an isolation of the ion flow from the walls requires fairly good vacuum conditions.

2.3. Problem of the Interaction of an SPT with the Vacuum Chamber

When testing the high-efficiency Aton SPT at MIREA, we unexpectedly faced the nontrivial problem of the interaction of an SPT with the vacuum chamber [6, 7, 11] (Fig. 6). This problem stems from the fact that the ions leaving the SPT usually have energies of ~200–300 eV. At such energies, the sputtering factor of the target (the plate receiving the flow) is usually about 0.2–0.5. Hence, there are two (instead of one) sources of fast particles inside the vacuum chamber. The experiments carried out at MIREA showed that the thruster actively draws in the sputtered particles (more precisely, the negative ions arriving from the target surface), which poison the working surfaces of the channel because of the change in the secondary electron yield $\sigma(\varepsilon)$. In the conventional models (ÉOL, M-70, and M-100), this adverse effect is eliminated, because a fraction of the accelerated ion flow falls onto the channel walls and cleans them. In the case of the Aton SPT, MIREA has already invented rather efficient methods for lowering the wall pollution. It can be expected that all the advantages of the Aton SPT will be demonstrated in space, where pollution of this kind is absent.

3. CREATION OF THE TEST MODEL OF THE ÉOL PROPULSION SYSTEM AT THE KURCHATOV INSTITUTE

By 1969, our plasma thrusters stood out against electric propulsion systems developed in other institutions. Let us list the typical parameters of our thrusters at that time [1]. The energy cost of the thrust was γ = 180–200 W/g at a thrust efficiency of η_F = 35–45%, and

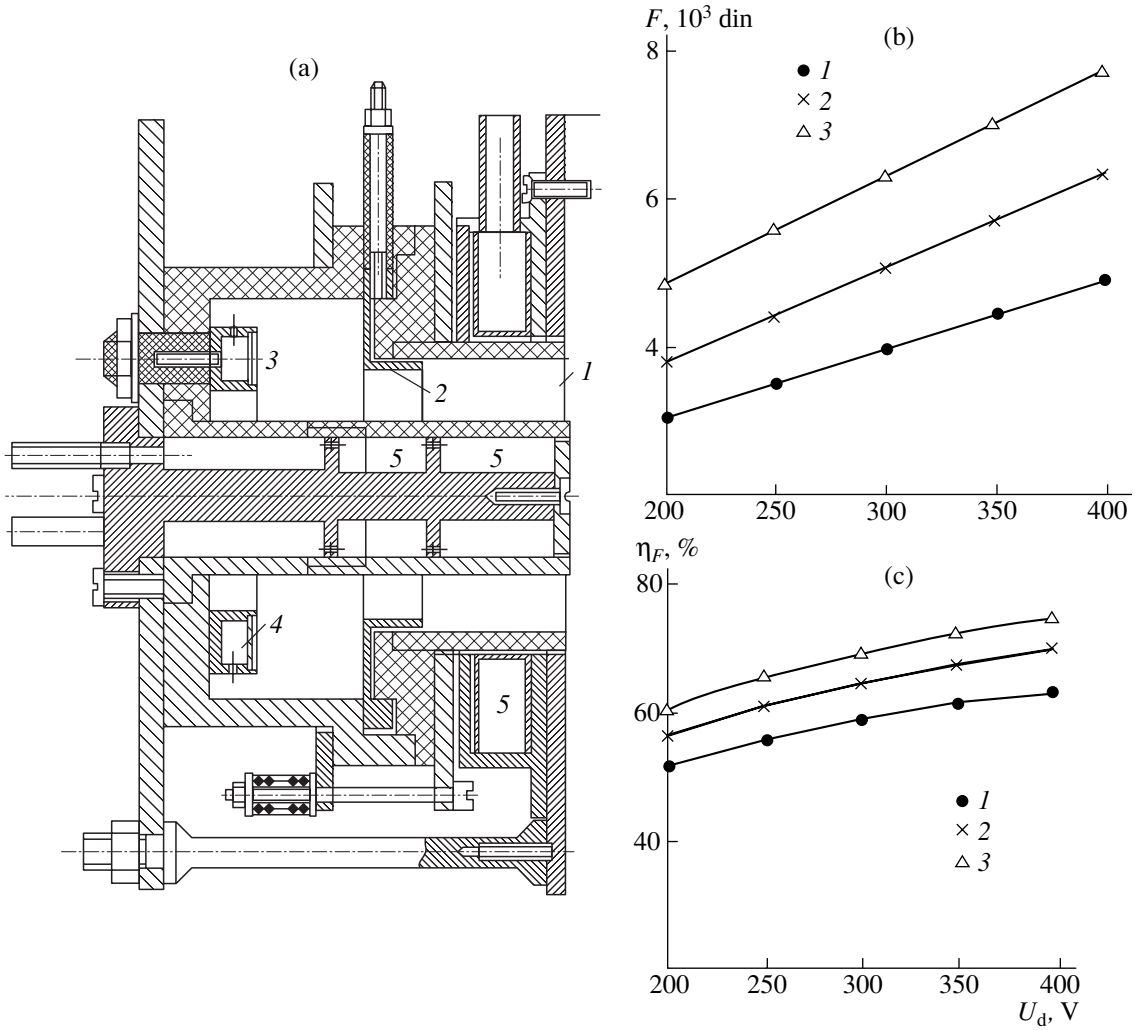

Fig. 5. (a) Schematic diagram of the Aton SPT: (*1*) acceleration channel, (*2*) anode, (*3*) buffer volume, (*4*) gas distributor, and (*5*) magnetic coils; (b) the thrust and (c) efficiency of the Aton SPT as functions of the discharge voltage for different xenon mass flow rates $\dot{m}$ = (*1*) 2, (*2*) 2.5, and (*3*) 3 mg/s.

the exhaust velocity was 10–18 km/s. Based on a 200-h test conducted at a power of $P \approx 5$ kW, the thruster service lifetime at a power of ~1 kW was estimated to be ~1000–1500 h.

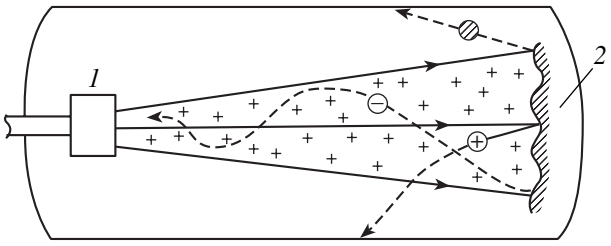

Fig. 6. Scheme illustrating the influence of the positive potential of the SPT jet on the positive secondary ions ejected from the receiving plate (target) in a vacuum chamber and the trapping of the negative ions in the SPT channel: (*1*) SPT and (*2*) target.

Note that the thrusters operated at relatively low voltages (~200–300 V) and low magnetic fields (H ~ 150–200 Oe). The working material was xenon (a noble gas convenient in every respect). The critical temperature of xenon is equal to t_{ct} = 289.7 K, and the corresponding pressure and mass density are 58.4 kg/cm^2 and 1.1 cm^{-3}, respectively. Under these conditions, it became necessary to carry out a space test of the accelerator, because the laboratory studies had exhausted all of their possibilities. In connection with this, in the beginning of 1969, A.P. Aleksandrov, Director of the Kurchatov Institute, spent much effort to organize such a test.

For this purpose, he gathered a group of the leading designers of space systems and asked them to install a propulsion system with our thruster at a satellite. However, all of them refused for one or another reason.

Then, Aleksandrov gathered another group of leading designers. At last, A.G. Iosif'yan, the chief designer of the *Meteor* meteorological satellites, agreed to install an SPT at his satellite. In December 1969, we received from the VNIIEM a performance specification for designing a full-scale model of a propulsion system that was called ÉOL. That time, the thrusters that we invented were given the name "stationary plasma thrusters," which became known later by the acronym SPT. This name was explained by the fact that there was no other stationary thrusters that time. According the performance specification, we had only six months (until the middle of May 1970) to design an SPT operating at a power of ~400 W (which significantly exceeded the powers of the previous models) with a radiative cooling and a proper compensator cathode, as well as the other units ensuring the autonomous operation of the propulsion system. These were an onboard electric supply system with an output voltage of 24 V, a thruster control system, and a system for the storage and supply of the working gas (xenon). The propulsion system would ensure a thrust of 2 g for 100 h, and its total mass would be no larger than 16 kg. This work was assigned to a small group of ten to twelve specialists of our laboratory. Of course, we had to invite experts from other institutions to take part in designing the supply and control systems. However, the main goal was to design the ÉOL-SPT and the compensator cathode. A vibration-proof thruster scheme was proposed by Yu.A. Sharov (Fig. 1). This scheme, which became a basic one, was then reproduced in many papers. A thruster made according to this scheme was hung on a three-filament torsion balance and thoroughly investigated. First, it was powered from the power and gas supply systems on the stand, and then it was tested as a part of an autonomous propulsion system. This propulsion system was connected with the "outer world" only by a 24-V electrical pathway and a system cable.

In this paper, there is no sense in talking about the lack of coordination that often occurred, but was finally overcome. A particular series of studies was devoted to the creation of a compact and efficient compensator cathode. This cathode is shown schematically in Fig. 1. Its heart was an emitter—a cylinder made from LaB_6 with an axial hole, which was connected to a metal tube for admitting xenon. The tube was simultaneously used to apply a negative discharge potential to the emitter. The emitter was surrounded by a preheating spiral; heat shields; and a case, which had an insulator to mount the electrode igniting the discharge. A high voltage (from a separate source providing a voltage higher than the main discharge voltage) was applied between this electrode and the emitter and was then switched off after the main discharge was ignited. In order to simplify the supply circuit and to ensure stable ignition, the magnetic coils were connected in series to the main discharge. The thruster was activated as follows. First, the cathode heater was switched on. In about one minute, the heater heated the hexaboride emitter to the required temperature. Then, valves were opened, and xenon began to flow into the thruster channel and the compensator cathode. After that, a voltage was applied between the anode and the compensator cathode, and, finally, a voltage pulse was applied to the igniting electrode. One pulse was usually sufficient for the discharge to be initiated in the thruster channel and, accordingly, for the magnetic field to increase. Then, the cathode heater was switched off, and the hexaboride cylinder was heated by the discharge that occurred between this cylinder and the SPT jet, which had the positive (~12 V) potential.

By the end of March, the short-term tests of the ÉOL propulsion system were finished. During the remaining one and a half months, we conducted a lifetime test and prepared the documentation. All of the bottlenecks were cleared up rather soon, and the required parameters were attained. The only unit that still remained unfinished was the compensator cathode, in which, after 50–70 h of operation, the discharge advanced into the gas pipeline. It was decided to eliminate this defect at the Fakel EDB, and this was done there.

It should be noted that the specialists from the Faklel EDB (K.P. Kozubskii, B.A. Arkhipov, and others) actively participated in the tests carried out at the Kurchatov Institute and gained our experience. We also maintained close contacts with Yu.P. Rylov, Yu.V. Trifonov, and V.P. Khodnenko from VNIIEME.

In the middle of May 1970, the test model of the ÉOL EPS with a detailed description of the work performed was sent to the Fakel EDB, where the work on creating the flight model of an electric propulsion system was continued for nearly one and a half years [2]. During that time, the scientists from our laboratory worked there for several months. I was the official supervisor of this work at the Fakel EDB.

On December 29, 1971, the ÉOL propulsion system was launched on the *Meteor* satellite into space. The space tests are described in [1].

4. SCIENTIFIC RESULTS OF THE WORK ON DESIGNING AND INVESTIGATING THE SPT

In the previous section, the accent was put on the engineering aspects of creating plasma thrusters for spacecrafts. Now, we dwell on the contribution that these investigations made in fundamental physics. Here, we only briefly discuss the results obtained because most of them were already described in original papers and reviews.

1. First of all, a novel type of electric-discharge plasmodynamic system was created, which made it possible to generate multiampere ion flows of various materials with particle energies in the range from ~50 eV to 1 keV and higher. This range (50–1000 eV) at currents of several amperes was unattainable for the conventional devices—plasmatrons and ion sources.

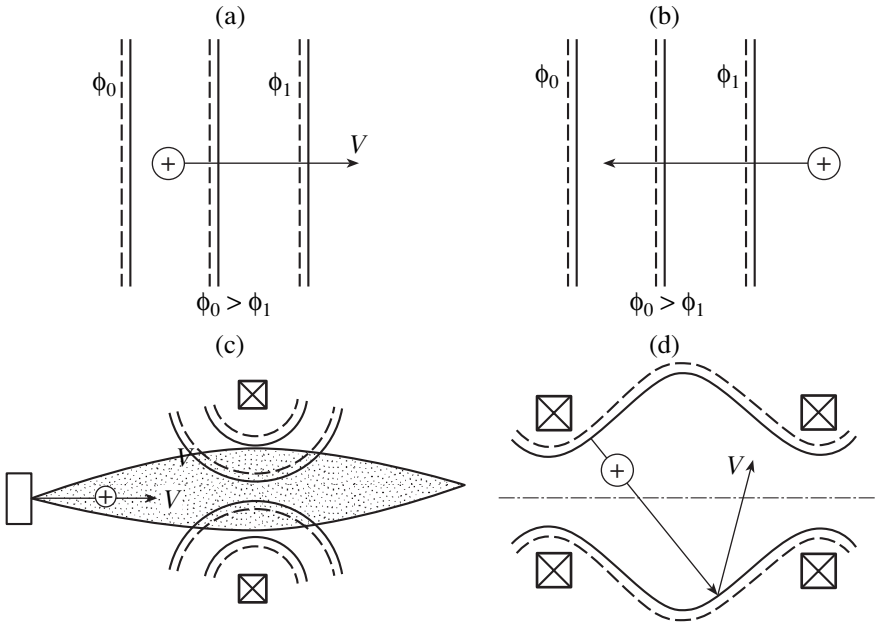

Fig. 7. Types of magnetoelectric systems with a poloidal field (closed drift): (a) plasma accelerators, (b) plasma recuperators (ion decelerators), (c) plasma optics systems, and (d) magnetoelectric confinement systems.

2. The direct experiments demonstrated the high efficiency of employing the equipotentialization of the magnetic field lines in the plasma, i.e., the dependence described by the formula

$$\Phi_T \equiv \phi - \frac{1}{e}\int \frac{dp(n)}{n} = \Phi_T(\gamma), \qquad (7)$$

where p is the plasma pressure, n is the electron density, γ is the index of the magnetic field line, and Φ_T is the so-called "thermalized" potential [for $T_e \longrightarrow 0$, we obtain formula (2)].

The studies performed laid the foundation for the approach in which the magnetic field lines in the plasma are regarded as "electronic–magnetic" electrodes that allow one to produce different reliefs of the electric potential and, consequently, different plasmodynamic systems.

Figure 7 schematically shows four classes of such systems with poloidal fields. The solid lines denote the magnetic field lines, and the dashed lines show the equipotential surfaces at $T_e \longrightarrow 0$. The ions are assumed to be weakly magnetized. Plot (a) presents accelerators of the SPT type, plot (b) corresponds to recuperators (designed by V.A. Obukhov and his colleagues at the Moscow Aviation Institute and the Moscow Institute for Physics and Technology), plot (c) corresponds to plasma optics systems (i.e., systems for focusing high-current particle flows by electric and magnetic fields), and plot (d) presents systems that provide the electrostatic confinement of ions and the magnetic confinement of electrons. Particular principles of the realization of these systems will be outlined in the next paragraph. It is evident from here that the investigations of SPTs allow one to better understand the role of the equipotentialization of the magnetic field lines when designing plasmodynamic systems.

3. The fundamental result of the studies performed was the demonstration of the possibility of producing plasmodynamic systems with stable volume electrostatic configurations and $\Delta\Phi \geq T_e$ and the formulation of a criterion for macroscopic stability (at least, for systems of the SPT type).

In the modern SPTs, the parameter $\omega_e\tau_e$ is

$$\omega_e\tau_e \sim 3000,$$

which is three orders of magnitude higher than the Bohm barrier. For axisymmetric systems, the above criterion for macroscopic stability can be written in the compact form

$$\frac{dW}{d\Phi_T} > 0, \qquad (8)$$

where

$$W(\psi) = \int \frac{ndl}{H} \qquad (9)$$

is the so-called "loading" of a magnetic field line and $\Phi_T(\psi)$ is thermalized potential (7). Initially, this criterion was written in the form [12]

$$(\mathbf{v}\cdot\nabla)\frac{H}{n} > 0 \qquad (10a)$$

or in the approximate form

$$(\mathbf{v} \cdot \nabla)H > 0. \quad (10b)$$

This condition of a positive gradient of H is realized in all of the modern versions of plasma accelerators with poloidal fields, i.e., with a closed electron drift [in both SPTs and thrusters with an anode layer (TALs)]. This condition was verified many times in experiments.

The above three fundamental results were obtained theoretically by the author and verified in the experiments carried out at the Kurchatov Institute in the laboratory headed by Shchepkin and Morozov and later in other laboratories. These results opened a way for physical studies and for the development of various technological facilities. We note, however, that along with the above results, a number of another very important (although less general) results were obtained in the course of SPT studies. All the results discussed below (except for the anomalous insulator erosion, discovered at the Fakel EDB [13]) were revealed and studied in the experiments carried out at MIREA in the laboratory headed by Bugrova. These phenomena were analyzed theoretically by the author together with Bugrova and V.V. Savel'ev.

It should be emphasized that it is the achievements described below that enabled us to construct realistic models of the processes occurring in the SPT.

4.1. Electron Distribution Function in the SPT Channel

The studies of the current–voltage characteristics measured by Burgova in the SPT channel by oriented probes showed that the electron distribution function (EDF) was essentially non-Maxwellian [6, 7, 14]. The EDF can be represented as a sum of the three distribution functions shown in Fig. 8. In the electron generation regions (the ionization region and the region where electrons enter the channel from the compensator cathode), these distributions are superimposed to form a curve with a single maximum. Away from these regions, these distributions become separated. In this case, only the magnitudes of the partial distribution functions vary, with their shapes changing only slightly. Such an EDF structure is related to the fact that the magnetic field lines terminate at the channel walls; to the presence of an electric field along the channel; and to the potential difference along the magnetic field lines, because the density of the ion flow and, accordingly, the potential value are maximum in the middle of the gap separating the walls. As a result, low-energy electrons do not reach the walls. Their distribution function decreases linearly with energy. Probe measurements showed that, between the generation regions of these electrons, the low-energy component drifts (rotates) as a single entity. The group of electrons that have the distribution function in the form of a parabola consists of electrons that undergo elastic reflections from the walls. These are runaway electrons, which move toward the anode almost without a loss of energy.

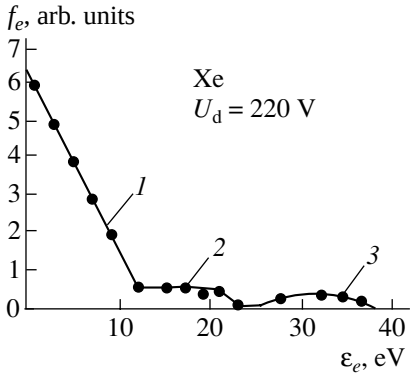

Fig. 8. Distribution functions of three groups of electrons in the SPT channel: (*1*) low-energy (forbidden) electrons, (*2*) intermediate electrons, and (*3*) high-energy (runaway) electrons.

As a result, their energy grows continuously, although the density decreases, because some electrons lose their energy in collisions with the walls. Finally, there is an intermediate group of electrons that fall onto the wall and undergo inelastic collisions. This group is responsible for the near-wall conductivity (see below). It can be seen from here that, in the SPT, we have a specific discharge in which the EDF is mainly determined by electron collisions with the walls, rather than by electron–electron collisions, which lead to thermalization.

4.2. Near-Wall Conductivity Across the Magnetic Field

In the SPT, we also observe a specific type of neoclassical conductivity [6, 7, 15, 16]. This is a result of the electron collisions with the wall and the related decrease in the electron drift velocity. Being scattered by either inevitable microscopic inhomogeneities or macroscopic structures, electrons change their azimuthal velocity and move toward the anode. It is now clear that this type of conductivity prevails in the SPT. This conductivity was identified experimentally from a certain peculiarity, specifically, the fact that the electron current in the channel is spatially modulated in the radial direction (Fig. 9). Note that the modulations allow us to find the distribution function of the reflected electrons over the longitudinal (along the magnetic field) velocity component (see below). For the near-wall conductivity to operate efficiently, the secondary electron yield σ should be on the order of unity; consequently, it is the intermediate group of electrons that are responsible for the near-wall conductivity. The near-wall conductivity was predicted in 1968 [15] and was observed experimentally in 1976 by Bugrova *et al.* [16].

4.3. Debye Layers at a Secondary Electron Yield of $\sigma \geq 1$

The electron temperature in the SPT is fairly high ($T_e \geq 10$–20 eV); hence, for a number of dielectrics, we

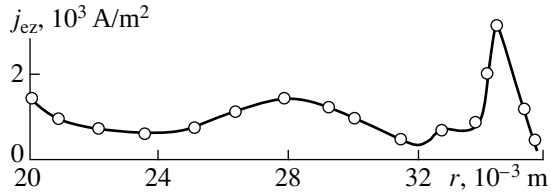

Fig. 9. Measured radial profile of the z component of the current density in the channel of an SPT operating with xenon at $\dot{m}$ = 3 mg/s and U_d = 250 V.

have $\sigma(\varepsilon) \geq 1$. It is reasonable to assume that, in this case, something must happen with the Debye layers, because the well-known relationship

$$j_{in} = (1-\sigma)e^{\frac{-U_D}{kT_e}} j_{en},$$

(where U_D is the potential drop across the Debye layer) apparently becomes invalid. The above-mentioned possibility of determining the distribution function of the reflected electrons from the specific current profile in the channel (Fig. 9) indicates that the Debye layer undergoes radical rearrangement and can even disappear at all. The subsequent studies of microwave noise performed by K.P. Kupriyanov also showed that, most likely, the disruption of these layers is quasi-periodic in character [6, 7, 17]. Important information about the behavior of the Debye layers at $\sigma \geq 1$ was obtained from computer simulations, which showed that, in this case, the wall layer transforms into an extended structure oscillating in space and time (Fig. 10) [7, 18].

4.4. Anomalous Erosion of the Insulator

In the course of a long-term ($t \geq 2000$ h) test carried out at the Fakel EDB in the early 1990s, a new, previously unknown form of erosion of the channel walls under the action of the plasma flow was discovered [6, 7, 13]. Before, it was known that the parts of insulators located immediately near the exit from the channel underwent ion sputtering, which was accompanied by the formation of a specific "pike-tongue" structure oriented across the flow. However, in the course of long-term operation, the insulator profile "accommodates" to the ion-flow structure due to ion sputtering, in which case the ion sputtering weakens and the character of erosion changes radically (Fig. 11): specifically, grooves oriented along the ion flow and separated by the distance equal to the cycloid length (or the double Larmor radius) appear and grow. This clearly indicates the great role of the electron component in this erosion mechanism. However, no complete model of this phenomenon has been proposed yet.

4.5. The SPT Discharge Scaling

In the SPTs that are employed in propulsion systems, xenon is used as the working material. However, this gas is rather expensive; in addition, for a number of

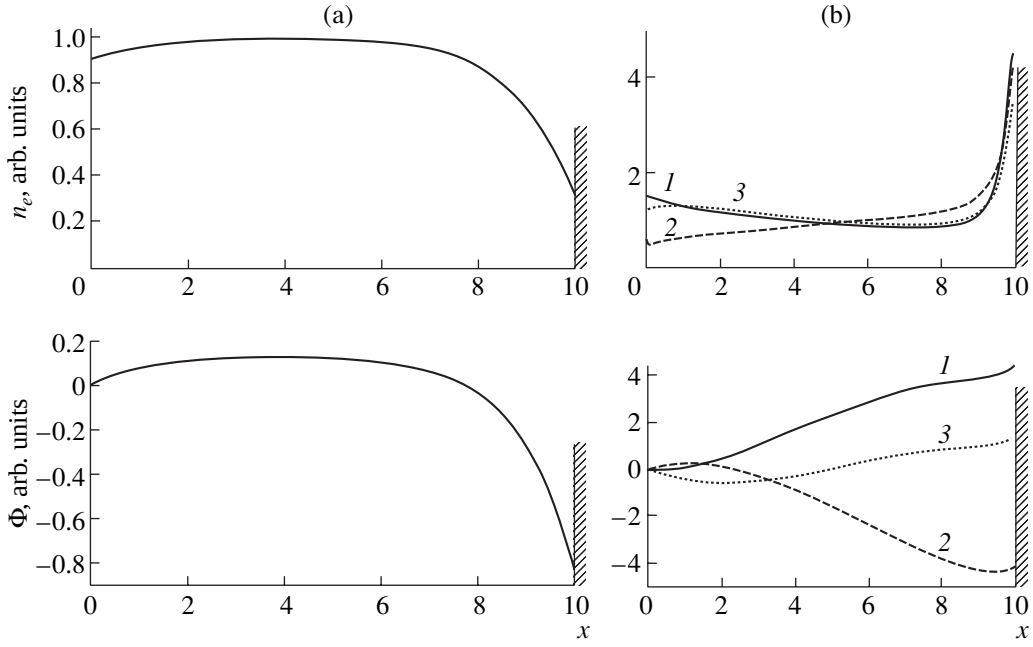

Fig. 10. Computed distributions of the parameters in the Debye layer at (a) $\sigma(T_e) \ll 1$ and (b) $\sigma(T_e) > 1$; curves *1*, *2*, and *3* show the distributions of the electron density and electric potential at different times during one oscillation period.

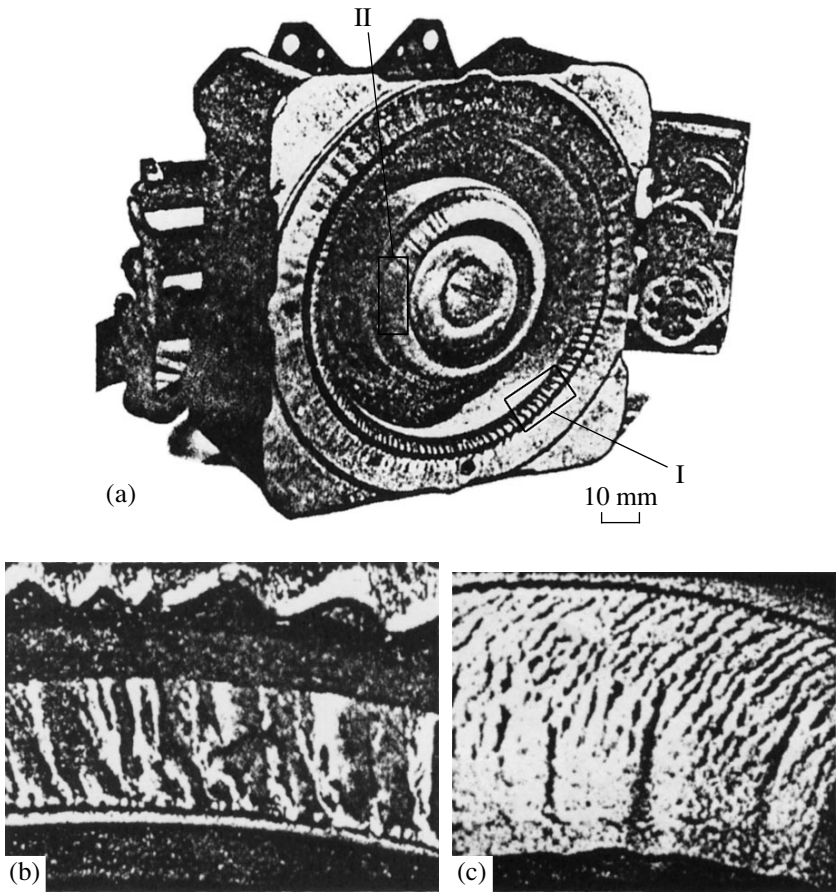

Fig. 11. Erosion of the M-100 SPT after a 5000-h lifetime test: (a) a general view of the thruster, (b) an enlarged photo of fragment I of the outer insulator, and (c) an enlarged photo of fragment II of the inner insulator.

problems, it is required to produce flows of other materials. In 1974, Morozov and Melikov [19] established a scaling law for the SPT discharge, which was later refined with the participation of Bugrova and N.A. Maslennikov [20] (see also [6, 7]). This law contends that, to within a factor on the order of unity for all of the working materials, the steady-state operating regime is established at the same material mass flow rate per unit length of the SPT channel in the azimuthal direction. This finding was confirmed for the first time by A.K. Vinogradov for various working materials (from hydrogen to xenon). For example, the small-sized Aton SPT with a channel diameter of 70 mm can operate with xenon, thus providing an ion current of ~2 A, and also with hydrogen, providing a current of up to ~120 A. Note that here we do not discuss the problem of thermal load.

Above, we have outlined the observed effects that are of general importance (not only for SPTs). For the sake of completeness, we additionally note some more particular studies, such as the study of oscillations over a wide frequency range from 1 kHz to several gigahertz and the spectral studies of the processes occurring in the channel. Extensive methodical work has been done on studying the specific nature of probe measurements under SPT conditions. Computer simulations of the processes in the SPT channel [6, 7, 21] also are of great importance.

4.6. Experiments Beyond the Scope of the Particular Problem of the SPT

As can be seen from the aforesaid, the possibility of controlling the electric field in a plasma opens the way for a wide scope of activity. Unfortunately, being restricted by the scope of this paper, I cannot describe in detail what was done not only theoretically, but also experimentally in this field. Therefore, we only list the main points.

(i) In 1976–1977, an SPT model with a channel diameter of 300 mm and a power of ~30 kW was designed at the Kurchatov Institute. A remarkable property of this model was a high efficiency of 70%. The model efficiently operated with radiative cooling. Later, similar models were created at the Fakel EDB.

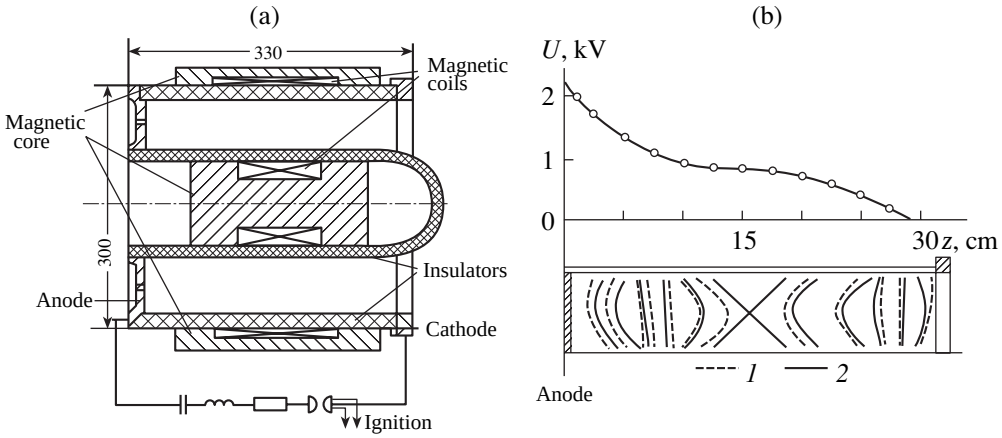

Fig. 12. (a) Schematic diagram of a two-lens accelerator and (b) the topograms of the measured equipotential surfaces and magnetic field lines for $L = 0.7$ mH, $C = 3 \times 10^{-3}$ F, and $R = 11\ \Omega$.

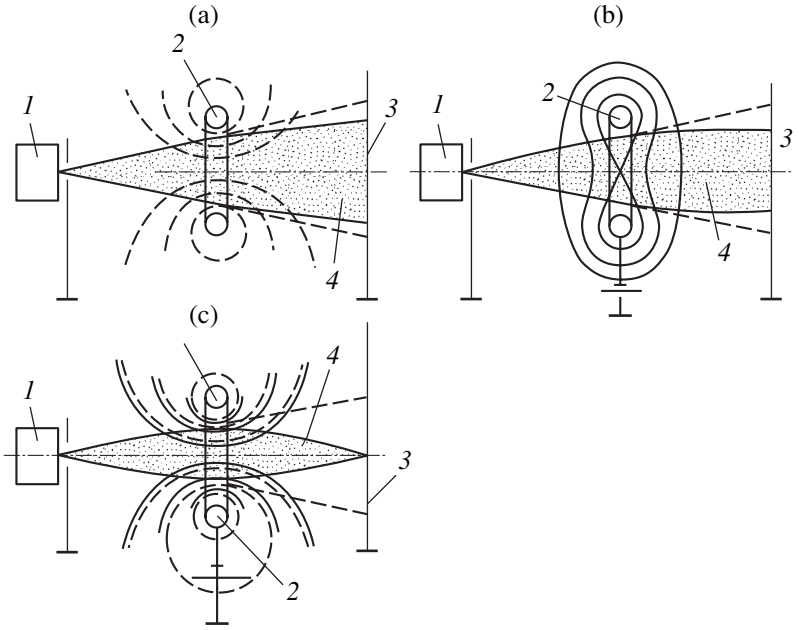

Fig. 13. Structures of the fields of (a) a magnetic lens, (b) an electrostatic vacuum lens, and (c) an electrostatic plasma lens: (*1*) ion source, (*2*) lens, (*3*) receiving screen, and (*4*) beam.

(ii) Naturally, a question arises as to the limiting power and, accordingly, the thrust of the ion flows that can be generated in SPTs. Unfortunately, the SPT model described above was not tested at high powers. However, in the laboratory headed by Shchepkin and Morozov, the so-called "two-lens" accelerator was designed (Fig. 12), which operated with hydrogen in the quasi-steady regime (the duration of the working pulse was ~10 ms) at a discharge voltage of ~5 kV and current of ~5000 A [22]. The exhaust velocity estimated by formulas (3) and (4) was ~10^8 cm/s, and the thrust delivered by the accelerator during the pulse was $F \sim 5$ kg.

(iii) As was mentioned above in connection with the schemes presented in Fig. 7, the equipotentialization of the magnetic field lines allows one to create not only accelerators, but also other types of plasmodynamic systems. Thus, Demitrov and Obukhov [23] created a unit allowing one to control the energy of quasineutral flows; this unit has found application in a number of technological systems. Here, we will not discuss magnetoelectric confinement systems proposed by

O.A. Lavrent'ev and G.I. Budker; electrostatic plasma confinement systems [24]; and galatheas [25], investigated by Bugrova and her colleagues. To date, a fair number of papers devoted to all these systems have been published.

Finally, we dwell on the scheme presented in Fig. 7d and describe the so-called "plasma lens" [7, 26], which was the first plasma-optics device realized experimentally [7, 27, 28].

The main element of this lens is a simple ring (coil) (Fig. 13). This is a simple lens, which is well known in classical particle (e.g., electron) optics. If an electric potential with respect to the ion source is applied to the conducting shell of the ring, then the equipotential surfaces of the electric field in vacuum will be shaped as in Fig. 13b. For a low-density (with a negligibly small volume charge) ion beam, the focal length of the lens is equal to

$$F_E = \frac{128}{3\pi}\frac{\varepsilon^2}{(eU_0)^2}R;$$

where ε and e are the energy and charge of an ion, R is the ring radius, and U_0 is the maximum potential at the ring axis. The quadratic dependence of F on the charge indicates that the lens is a converging one irrespective of the sign of the particle charge. If a quasineutral ion beam passes through the lens and the Debye radius satisfies the inequality $r_D \ll R$, than the core ions are insensitive to the ring; i.e., no focusing occurs.

If the voltage is switched off and the coil current is switched on (Fig. 13a), then the focal length is equal to

$$F_H = \frac{64}{3\pi^3}Mc \cdot 4\frac{\varepsilon}{(eJ)^2}R.$$

This lens is also converging; it can also focus quasineutral ion flows because the magnetic field penetrates into the plasma.

Let us return to a low-density ion flow. If we simultaneously switch on the coil and apply an electric potential to the shell, then the focal length F_{EH} is determined by the well-known formula

$$\frac{1}{F_{EH}} = \frac{1}{F_H} + \frac{1}{F_E}.$$

For argon ions with an energy of 10 keV at a focusing voltage of U_0 = 1 kV, number of ampere-turns of $J_0 = 10^3$ A, and radius of R = 5 cm, we obtain

$$F_E \approx 50 \text{ m}, \quad F_H \approx 300 \text{ m}.$$

Now, let us do the last step and increase the ion current from several microamperes to several milliamperes (in this case, the beam becomes quasineutral). We can see that the focal length of the plasma lens at the same values of U_0, J, and ε decreases to $F_H \approx 25$ cm. This lens can be converging or diverging. All this is a result of the equipotentialization of the magnetic field lines (Fig. 13c), i.e., of a complete rearrangement of the structure of the equipotential surfaces. It can be easily seen that now we have

$$F_{pl} = \frac{R}{2}\frac{\varepsilon}{eU}.$$

To conclude, we emphasize that the equipotentialization principle makes it possible to create a variety of high-current particle-optics systems: lenses, separators, energy analyzers, etc.

REFERENCES

1. L. A. Artsimovich, I. M. Andronov,[4] A. I. Morozov, *et al.*, Kosm. Issled. **12** (3), 451 (1974).
2. A. I. Morozov, Zh. Éksp. Teor. Fiz. **32**, 305 (1957) [Sov. Phys. JETP **5**, 215 (1957)].
3. A. I. Morozov, *Encyclopedia of Low-Temperature Plasma* (Nauka, Moscow, 2000), p. 482.
4. K. P. Kozubskiĭ, V. N. Murashko, Yu. P. Rylov, *et al.*, Fiz. Plazmy **29**, 251 (2003) [Plasma Phys. Rep. **29**, 251 (2003)].
5. V. N. Oraevsky, Yu. Ya. Ruzhin, V. S. Dokukin, and A. I. Morozov, Fiz. Plazmy **29**, 293 (2003) [Plasma Phys. Rep. **29**, 267 (2003)].
6. A. I. Morozov and V. V. Savelyev, Rev. Plasma Phys. **21**, 203 (2000).
7. A. I. Morozov, *Encyclopedia of Low-Temperature Plasma* (Nauka, Moscow, 2000), p. 444.
8. E. E. Yushmanov, *Plasma Physics and the Problem of Controlled Nuclear Fusion*, Ed. by M. A. Leontovich (Akad. Nauk SSSR, Moscow, 1958), Vol. 4, p. 235.
9. S. D. Grishin, V. S. Erofeev, and A. V. Zharinov, *Plasma Accelarators*, Ed. by L. A. Artsimovich (Mashinostroenie, Moscow, 1975), p. 54.
10. A. I. Morozov, A. I. Bugrova, A. V. Desyatskov, *et al.*, Fiz. Plazmy **23**, 635 (1997) [Plasma Phys. Rep. **23**, 587 (1997)].
11. A. I. Bugrova, A. S. Lipatov, and A. I. Morozov, Fiz. Plazmy **21**, 650 (1995) [Plasma Phys. Rep. **21**, 614 (1995)].
12. A. I. Morozov, Yu. V. Esipchuk, A. M. Kapulkin, *et al.*, Zh. Tekh. Fiz. **42**, 612 (1972) [Sov. Phys. Tech. Phys. **17**, 482 (1972)].
13. B. A. Arkhipov, R. Yu. Gnizdor, N. A. Maslennikov, *et al.*, Fiz. Plazmy **18**, 1241 (1992) [Sov. J. Plasma Phys. **18**, 641 (1992)].
14. A. I. Bugrova, A. V. Desyatskov, and A. I. Morozov, Fiz. Plazmy **18**, 963 (1992) [Sov. J. Plasma Phys. **18**, 501 (1992)].
15. A. I. Morozov, Prikl. Mekh. Tekh. Fiz. **3**, 19 (1968).
16. A. I. Bugrova, A. I. Morozov, and V. K. Kharchevnikov, Fiz. Plazmy **18**, 963 (1992) [Sov. J. Plasma Phys. **18**, 501 (1992)].
17. K. P. Kirdyashev and A. I. Morozov, Fiz. Plazmy **25**, 326 (1999) [Plasma Phys. Rep. **25**, 293 (1999)].
18. A. I. Morozov and V. V. Savel'ev, Fiz. Plazmy **28**, 1103 (2002) [Plasma Phys. Rep. **28**, 1017 (2002)].

[4] The pseudonym of A.G. Iosif'yan.

19. A. I. Morozov and I. V. Melikov, Zh. Tekh. Fiz. **44**, 544 (1974) [Sov. Phys. Tech. Phys. **19**, 340 (1974)].

20. A. I. Bugrova, N. A. Maslennikov, and A. I. Morozov, Zh. Tekh. Fiz. **61**, 45 (1991).

21. A. I. Morozov and V. V. Savel'ev, Fiz. Plazmy **21**, 970 (1995) [Plasma Phys. Rep. **21**, 917 (1995)].

22. I. P. Zubkov, A. Ya. Kislov, and A. I. Morozov, Zh. Tekh. Fiz. **40**, 2301 (1970) [Sov. Phys. Tech. Phys. **15**, 1796 (1971)].

23. S. K. Demitrov and V. A. Obukhov, *Ion Injectors and Plasma Accelerators*, Ed. by A. I. Morozov and N. N. Semashko (Énergoatomizdat, Moscow, 1990), p. 193.

24. V. V. Zhukov, A. I. Morozov, and G. Ya. Shchepkin, Pis'ma Zh. Éksp. Teor. Fiz. **9**, 24 (1969) [JETP Lett. **9**, 14 (1969)].

25. A. I. Morozov and V. V. Savel'ev, Usp. Fiz. Nauk **168**, 1153 (1998) [Phys. Usp. **41**, 1049 (1998)].

26. V. V. Zhukov, A. I. Morozov, and G. Ya. Shchepkin, Pis'ma Zh. Éksp. Teor. Fiz. **9**, 24 (1969) [JETP Lett. **9**, 14 (1969)].

27. A. I. Morozov, Dokl. Akad. Nauk SSSR **163**, 1363 (1965) [Sov. Phys. Dokl. **10**, 775 (1965)].

28. A. I. Morozov and S. V. Lebedev, in *Reviews of Plasma Physics*, Ed. by M. A. Leontovich (Atomizdat, Moscow, 1974; Consultants Bureau, New York, 1980), Vol. 8.

Translated by N.F. Larionova

Plasma Physics Reports, Vol. 29, No. 3, 2003, pp. 251–266. Translated from Fizika Plazmy, Vol. 29, No. 3, 2003, pp. 277–292.

THE 30th ANNIVERSARY OF SPT OPERATION IN SPACE

Stationary Plasma Thrusters Operate in Space

K. N. Kozubskiĭ*, V. M. Murashko*, Yu. P. Rylov, Yu. V. Trifonov**, V. P. Khodnenko**, V. Kim***, G. A. Popov***, and V. A. Obukhov*****

**Fakel Experimental and Design Bureau, Moskovskiĭ pr. 181, Kaliningrad, 236001 Russia*

***All-Russia Scientific and Research Institute of Electromechanics, P.B. 496, Glavpochtamt, Moscow, 101000 Russia*

****Research Institute of Applied Mechanics and Electrodynamics of the Moscow Aviation Institute, P.B. 43, Leningradskoe sh. 5, Moscow, 125080 Russia*

Received May 23, 2002; in final form, September 25, 2002

Abstract—The first ÉOL-1 flight propulsion system with a stationary plasma thruster created at the Fakel Experimental and Design Bureau (EDB) on the basis of an experimental thruster designed and tested at the Kurchatov Institute of Atomic Energy is described. Subsequent versions of the ÉOL-type systems designed at the Fakel EDB using M-70, M-100, and other thrusters are reviewed. The current state of work on stationary plasma thrusters in the world is analyzed. The Phobos-Grunt project, whose aim is to deliver soil samples from Phobos and which implies the use of stationary plasma thrusters, is discussed. © *2003 MAIK "Nauka/Interperiodica".*

1. INTRODUCTION

In connection with the thirtieth anniversary of the first use of a stationary plasma thruster (SPT) in space, a symposium devoted to the history of the creation and development of the SPT was held on December 25, 2002, at the Nuclear Fusion Institute of the Russian Research Centre Kurchatov Institute.

This paper presents a review of the following reports made at this symposium:

(i) *Creation and Tests of the First Space Propulsion Systems with SPTs* by K.N. Kozubskiĭ;

(ii) *Tests of the ÉOL Electric Propulsion System on the Meteor Satellite and the Beginning of the Wide Application of SPTs in Space Technology* by Yu.P. Rylov, Yu.V. Trifonov, and V.P. Khodnenko;

(iii) *Creation of Propulsion Systems at the Fakel Experimental and Design Bureau: from ÉOL-1 to SPT-140* by V.M. Murashko;

(iv) *Development of SPTs in Other Countries* by V. Kim; and

(v) *SPTs on the Phobos-Grunt Spacecraft* by G.A. Popov.

2. CREATION AND TESTS OF THE FIRST SPACE PROPULSION SYSTEMS WITH SPTs

In 1968, it was decided to design an SPT-based orbit-control propulsion system for the *Meteor* meteorological satellites. An experimental model of the propulsion system with an SPT was successfully developed and tested at the Kurchatov Institute [1]. This activity marked the beginning of the creation of space electric propulsion systems (EPS) with Morozov's thrusters, which were first tested in space thirty years ago and have been successfully operated on satellites up to the present [2].

The first test orbit-control EPS ÉOL-1 with SPTs was created at the Fakel Experimental and Design Bureau (EDB), which was headed by R.K. Snarskiĭ. By that time, an experimental base for the development and tests of electric propulsion thrusters (EPTs) had been created at the Fakel EDB. The personnel of the EDB had an experience of successful collaboration with the other EDBs engaged in space technology and with physicists from the Kurchatov Institute during the creation of the Globus experimental propulsion system with pulsed plasma thrusters.

Below, we list the basic parameters of the first space EPSs with xenon SPTs created at the Fakel EDB and their subsystems—the products of new space technology.

2.1. Design of the First Space SPTs

An R-60 flight SPT was developed based on an experimental model created at the Kurchatov Institute [1].

The general view of the R-60 thruster is shown in Fig. 1a, and its design is presented in Fig. 1b. The thruster included the following components:

(i) discharge chamber *1* with an annular channel (with an outer diameter of 60 mm) made from a high-temperature ceramic and capable of withstanding high mechanical loads during the launching;

(ii) gas-distributor anode *2*, which ensured the uniform (to within 1%) admission of xenon into the thruster working channel and which was placed inside the discharge chamber; and

1063-780X/03/2903-0251$24.00 © 2003 MAIK "Nauka/Interperiodica"

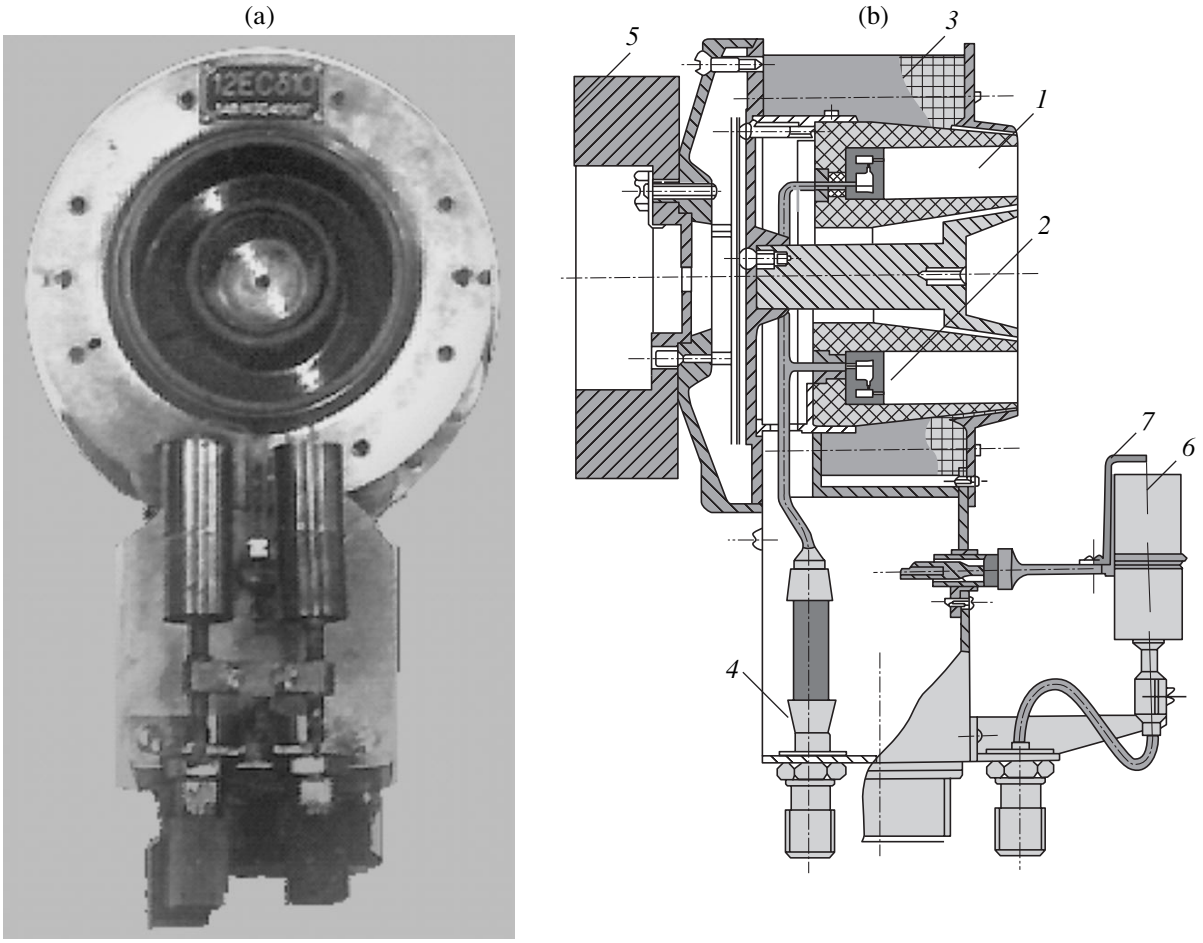

Fig. 1. (a) General view and (b) design of the R-60 SPT of the ÉOL-1 EPS: (*1*) discharge chamber, (*2*) gas-distributor anode, (*3*) magnetic system, (*4*) high-voltage lead-in, (*5*) mounting holder, (*6*) cathode compensator, and (*7*) ignition electrode.

(iii) magnetic system *3* with eight outer heat-resistant magnetization coils, producing the radial magnetic field in the acceleration channel.

The electric strength of the thruster was provided by high-voltage metal–ceramic intakes *4* for admitting xenon into the gas-distributor anode and cathode compensators and by the shielding of the current-carrying components from the action of the surrounding low-temperature plasma.

The thruster design met the requirements for the SPT adjustment on a spacecraft. The position of the thrust vector with respect to the mounting plane was determined accurate to 15 angular minutes. When mounting the thruster on the spacecraft, its holder *5* was updated taking into account the results of determining the thrust vector and the actual location of the spacecraft's center of mass.

The most heat-loaded element of the SPT was the gas-discharge cathode compensator, which served as a negative electrode in the SPT discharge circuit and as a neutralizer of the space charge of the accelerated ions at the SPT exit. Two xenon cathode compensators *6* were used to ensure the reliability of space experiments. The thruster was activated by ignition electrode *7* placed at the SPT exit.

Figure 2 shows the designs of the cathodes of (a) the SPT experimental model and (b) the R-60 and M-60 flight thrusters. The cathodes had hollow lanthanum-hexaboride thermal emitter *1*, which was inserted into gas-admitting pipe *2*. High-temperature heater *3* was used to preheat the thermal emitter. Heat screens *4* provided the cathode operation when the heater was switched off. The cathode design features ensuring the lifetime requirements are considered below.

The M-60 and M-50 SPTs were intended for the ÉOL-2 and ÉOL-3 orbit-control propulsion systems. The characteristic design feature of these thrusters is an elevated gradient of the magnetic field in the working channel; for this purpose, the width of the magnetic-system poles was reduced according the recommendations of the physicists from the Kurchatov Institute. In these SPTs, the magnetization coils were connected in series to the main discharge circuit. The outer diameter

of the thruster working channel was taken to be a scaling SPT parameter. The main design features of the M-60, M-50, and R-60 SPTs were then used when developing new types of SPTs.

2.2. Electric Characteristics of the SPT

When constructing the test model, the following main parameters were adopted for the R-60 thruster: the discharge voltage was 160 V, the discharge current was 2.5 A, and the xenon mass flow rate was 2.5 mg/s. Typical current–voltage characteristics of the thruster are shown in Fig. 3.

To reduce the noise level during the discharge, a matching element was introduced into the discharge circuit of the thruster. For the R-60 thruster, this was a 10-mH inductance, and, for the M-60 and M-50 thrusters, the inductance was supplemented with a parallel-connected resistance of 100 Ω.

The R-60 thruster was activated after preheating the cathode emitter for 50 s to a temperature of 1500°C with the help of a 200-W radiation heater. Simultaneously with the switching-on of the heater, a voltage was applied between the anode and cathode of the thruster and xenon was admitted into the anode and cathode. To activate the thruster, the ignition electrode of the cathode compensator was connected to the anode voltage source through a 300-Ω resistor, which ensured an ignition current of 0.5 A at a voltage of 150–190 V. To improve conditions for the discharge ignition, the source of the magnetization current was triggered with a fast electronic switch after the discharge current reached a value of 0.5–0.8 A. After the discharge was ignited, the triggering circuits of the heater and the ignition electrode were switched off and the cathode working temperature was maintained by the potential difference between the emitter and the plasma outflowing from the thruster.

2.3. Lifetime Characteristics of the First SPTs. Operation in Space

The prescribed service lifetime of the R-60 thruster was 100 h, which was sufficient for the first space tests of the SPT. For the discharge chamber, such a lifetime was guaranteed by the excess thickness of the discharge chamber walls in the region where it underwent erosion under the action of the accelerated ions.

As was noted in [1], the first cathodes operated for 20–40 h; then, the discharge penetrated into the input cavity of the cathode and the tubular cathode holder was destroyed. This disadvantage was eliminated by using a cathode emitter with a T-shaped channel (Fig. 2a). Later, the cathode compensators of the M-60 thruster were equipped with a special getter for xenon purification (Fig. 2b). Direct tests confirmed that the cathode service lifetime increased to no less than 2000 h. One of the cathodes of the M-60 thruster successfully operated in space for 600 h.

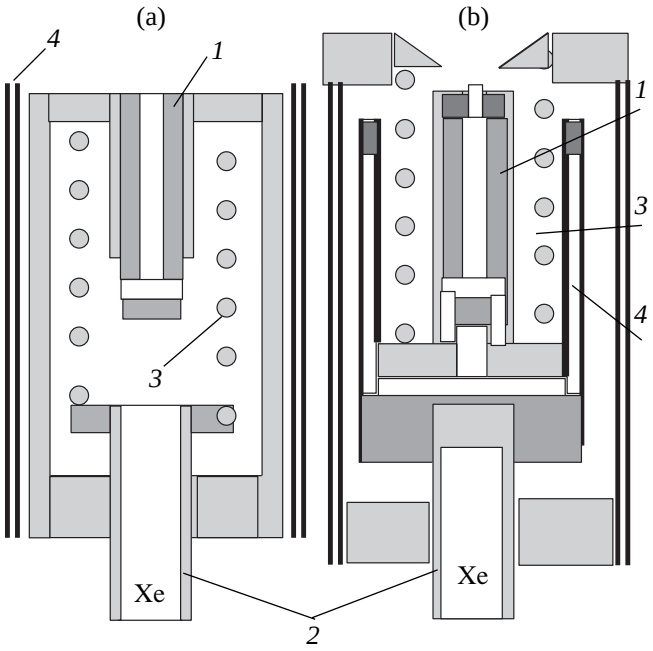

Fig. 2. Schematics of the compensator cathodes of (a) the SPT experimental model and (b) the R-60 and M-60 flight thrusters: (*1*) thermal emitter, (*2*) gas-admitting pipe, (*3*) heater, and (*4*) heat screens.

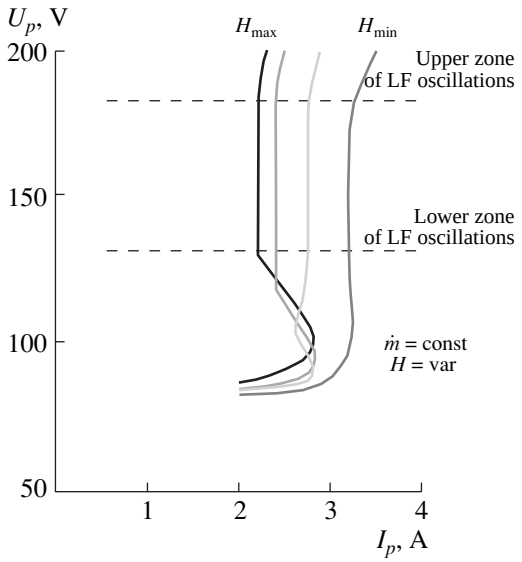

Fig. 3. The current–voltage characteristics of the R-60 SPT.

In the course of ground tests, an insignificant drift of the parameters within the specification limits was observed. This drift was caused by the deposition of a coating on the walls of the discharge chamber, in particular, because of the presence of a residual vapor of organic compounds and because of the sputtering of the chamber walls; i.e., the test conditions inadequately simulated space conditions. The expected change in the parameters under space conditions was 5–10%. Hence,

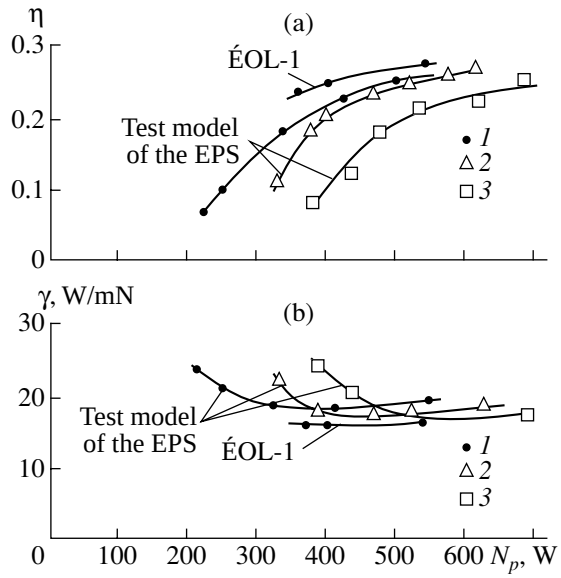

Fig. 4. Thrust characteristics of the first SPTs: (a) efficiency and (b) energy cost of thrust for $\dot{m}$ = (*1*) 2, (*2*) 2.5, and (*3*) 3 mg/s.

space tests were necessary not only to demonstrate the operability of the SPTs in space, but also to verify whether the laboratory tests adequately simulated space conditions.

The thrust and energy characteristics of the first flight models of the SPT are shown in Fig. 4. It can be seen from the figure that the parameters of the flight models exceeded the parameters of the original experimental model. The ÉOL-1 EPS units are illustrated in Fig. 5.

The qualification and acceptance tests of the R-60 thrusters, being a part of the ÉOL EPS, confirmed that their characteristics satisfied the requirements for the first SPT tests in space.

In the course of creating the M-60 and M-50 thrusters, the lifetime and thrust characteristics were achieved that satisfied the requirements for a precise orbit adjustment of the *Meteor* and *Meteor-Priroda* satellites over a long period of time.

The M-60 thruster was also used as an efficient ion source in astrophysical experiments under the Porcupine program [2].

2.4. Concluding Remarks

The creation and tests of the first space EPSs with SPTs became possible due to the successful collaboration of many institutions.

Thus, the power supply and management subsystems for these EPSs were elaborated by designers from the Zarya EDB (Moscow) and the Sukhumi Institute for Physics and Technology. The first flight models of the engine management systems for the SPT-based EPSs were created by designers from the Zarya EDB under the guidance of E. Shashkov and L. Novoselov.

The xenon storage and feeding subsystems were elaborated at the Fakel EDB. The use of xenon as a working gas, which was proposed by scientists from the Kurchatov Institute more than thirty years ago, turned out to be very advantageous.

A great contribution in the design and ground tests of the first space SPTs was made by the designers and engineers from the Fakel EDB: G. Komarov, Yu. Gorbachev, B. Arkhipov, É. Besedin, V. Stoyanov, Yu. Kondakov, V. Podol'skiĭ, V. Linnik, L. Luzev, M. Vasil'ev, and F. Sivagin. The complex tests and laboratory operation of the first SPT-based EPS, as well as their fueling with xenon, were performed by B. Merzlyakov, G. Razumikin, V. Mezhuev, and M. Loginov. The first space tests of the SPT were performed with the direct participation of R. Snarskiĭ, K. Kozubskiĭ, B. Merzlyakov, and Yu. Kondakov.

The integration of the ÉOL EPS in the *Meteor* satellite was provided by the engineers Yu. Rylov, Yu. Trifonov, N. Furdak, and V. Khodnenko from the All-Union Scientific and Research Institute of Electromechanics (VNIIEM).

At all of the stages of creation of the first space SPTs, close cooperation was maintained with the scientists Yu. Esiptchuk, G. Tilinin, Yu. Sharov, and Yu. Levchenko from the Kurchatov Institute, working under the guidance of A. Morozov and G. Shchepkin.

3. TESTS OF THE ÉOL EPS ON THE *Meteor* SATELLITE AND THE BEGINNING OF THE WIDE APPLICATION OF SPTS IN SPACE TECHNOLOGY

On December 29, 1971, the Soviet satellite *Meteor-18*, equipped with Morozov's SPTs, was launched into orbit.

Ion thrusters had previously been tested in space, but the SPT tests were performed for the first time. In the space tests of the SPT-based EPS, besides the specialists from the VNIIEM, the designers and engineers from the Fakel and Zarya EDBs and the scientists from the Kurchatov Institute, Moscow Aviation Institute, and other institutions took part.

The *Meteor* satellites, which were a part of a space hydrometeorological system consisting of two to three satellites, combined all of the properties required for the EPS tests and applications, namely, precise triaxial attitude control, a rather high power system, and long operation time.

Based on the *Meteor* satellite, in the late 1960s, work began at VNIIEM on the development of a *Meteor-Priroda* satellite intended for both the investigation of the Earth's natural resources and environmental monitoring. This satellite was to perform a regular detailed survey of small regions of the Earth's surface

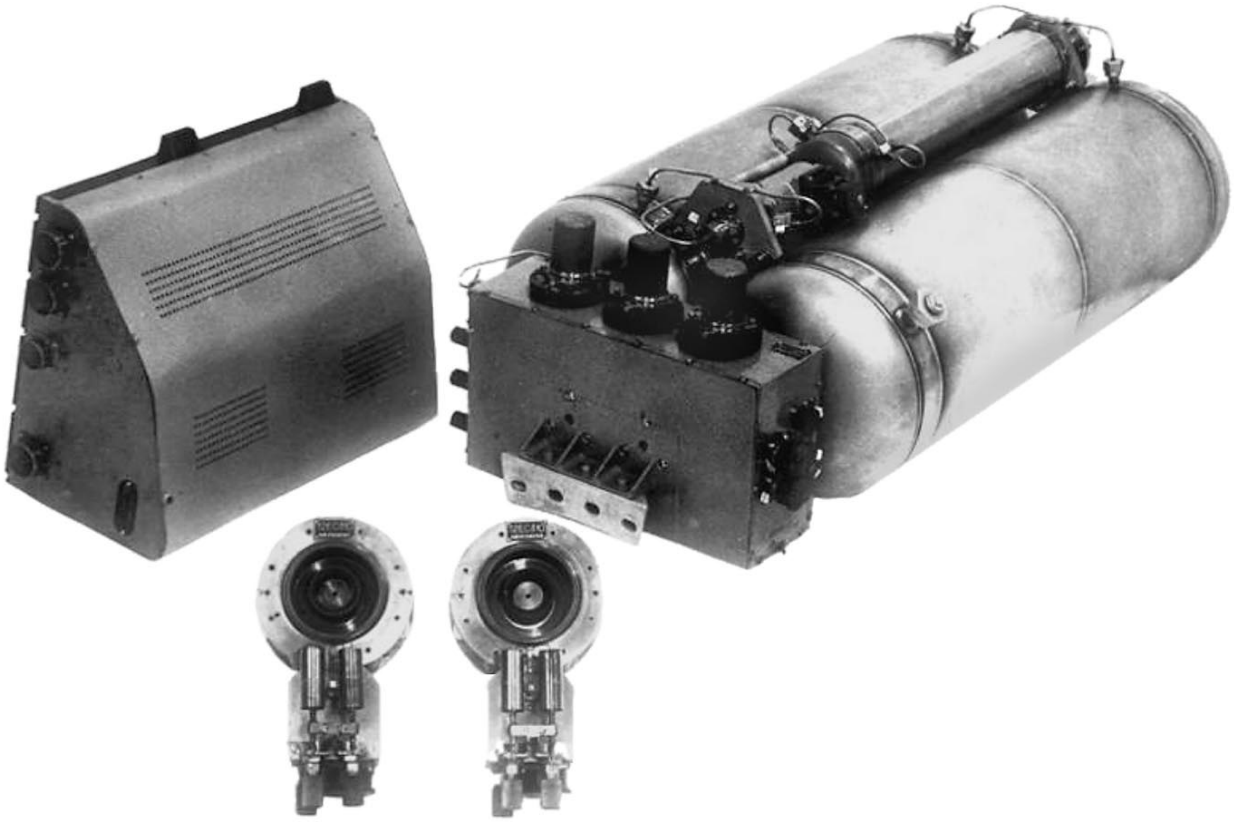

Fig. 5. Units of the ÉOL-1 EPS.

with a resolution of 20–30 m. For this purpose, it was necessary to precisely control the orbit parameters and, first of all, to place the satellite in special orbits stabilized in time and longitude: latitude-stabilized orbits, solar-synchronized orbits, etc.

The main goals of flight tests were the following:

(i) to test the EPS operability and determine the SPT characteristic under space conditions,

(ii) to measure the SPT thrust by different methods,

(iii) to test the compatibility of the EPS with the other satellite systems and study the effect of EPS operation on the reception of radio commands from Earth,

(iv) to perform long-term tests of the SPT-based EPS with the purpose of changing the orbital parameters (up to the transition to quasi-synchronous orbit), and

(v) to elaborate the procedure of controlling the operation of the SPT-based EPS under flight conditions and confirm that these propulsion systems can be used in the orbit- and attitude-control systems of space vehicles.

3.1. ÉOLs Operate in Space

The general view of the *Meteor* satellite with the ÉOL-1 EPS is illustrated in Fig. 6. The satellite had a hermetic container, which provided the conditions appropriate for the operation of the electronic equipment inside it. The location of the satellite was determined using onboard systems for the orbit radiocontrol.

The thruster units (TU-1 and TU-2) were oriented in the forward and backward directions with respect to the satellite motion, and the thrust vectors could be deflected by angles of 5°05′ and 4°15′, respectively. This allowed the thruster to produce a small (~2×10^{-3} Nm) pitch moment and made it possible to measure and monitor the thrust by its action on the attitude-control system of the satellite; at the same time, the thrust was almost entirely utilized to perform an orbit correction maneuver.

The gas storage and feeding system (SFS) of the EPS was installed outside the satellite instrument module and was covered with a sealed heat shield to ensure a normal heat regime. The thruster units were connected to the SFS through pipelines.

The system for transforming the parameters of the EPS power supply was placed inside the above hermetic container.

The space tests were conducted in three stages.

In the first stage, each thruster unit was switched on for a short (~1.5 min) time by the main and reserve channels[1] in the radio-visibility zone. In the telemeter-

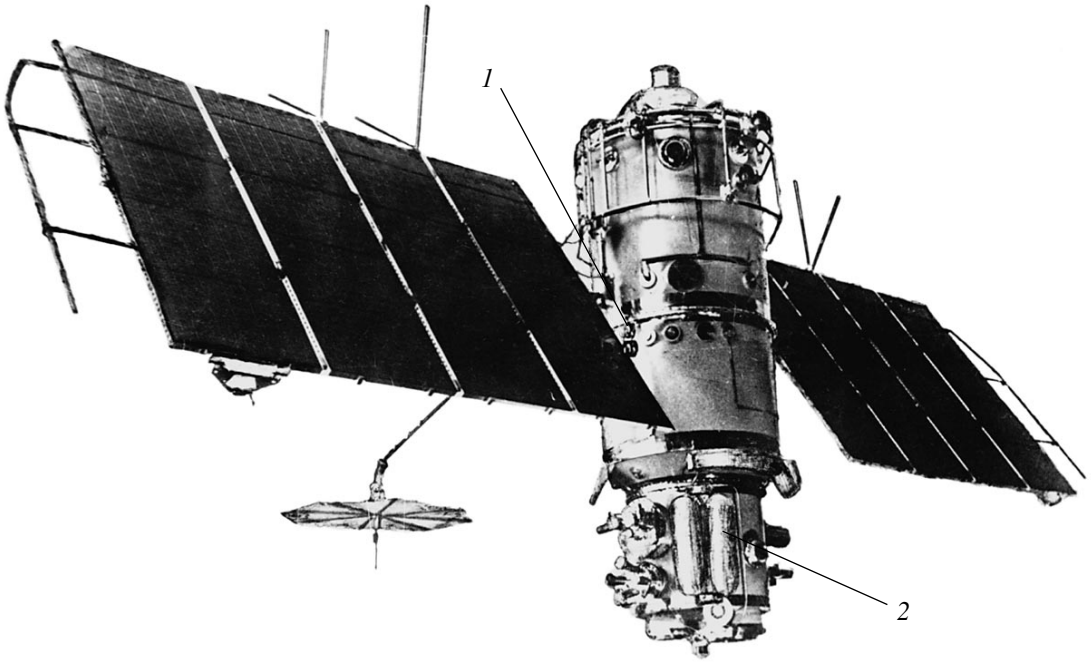

Fig. 6. *Meteor* satellite with the ÉOL-1 EPS: (*1*) SPT and (*2*) balloons with xenon.

ing regime, the following parameters were controlled: the discharge current I_p, the discharge voltage U_p, and the flywheel rotation velocity n. The EPS operability was assessed from these parameters. Simultaneously, a test was performed for transmitting commands from the Earth to the satellite radio equipment during the SPT operation.

In the second stage, the SPT thrust was measured. The TU-1 unit was switched on by the main and reserve channels during one orbit around the Earth, whereas the TU-2 unit was switched on by the reserve channel during two orbits. The thrust value was determined from the results of trajectory measurements (i.e., from the change in the orbital parameters), as well as from the measurements of the thrust action on the satellite attitude-control system.

The third stage included the long-term operation of the EPS for 170 h (from February 14 to February 22, 1972) in a shadowless orbit. During this period, the orbit was raised by 17 km and the *Meteor* satellite was placed in an orbit close to a quasi-synchronous one; i.e., the satellite began to pass the equator every day at the same longitude (with a period of 14 orbits). As a result, a strict tracing schedule was ensured, the survey of the Earth surface in given synoptic periods became better, and the gridding accuracy improved. In the third stage, the SPT thrust was also measured from the change in the orbital parameters.

[1] The channels differed in the cathode compensators.

Altogether, the ÉOL-1 EPS operated for more than 180 h and produced a total momentum of ~11.7 kNs. The tests yielded a number of important results concerning the compatibility of the ÉOL-1 EPS with the other satellite systems:

(i) During the EPS operation, the characteristics of the power system (solar and accumulator batteries) were within the normal range.

(ii) During the long-term EPS operation, the electromagnetic attitude-control system reliably compensated for the perturbing moments. The tests confirmed the good compatibility of the SPT magnetic system and the sensitive element of the electromagnetic system (a DSGK-61 magnetometer).

(iii) An analysis of the transmission of radio commands to the service and scientific equipment during the EPS operation showed that, in the frequency range 40–45 MHz, the noise produced by the SPT did not disrupt the radio contact between the satellite and the ground station.

The change in the satellite effective reflecting surface for electromagnetic waves during the EPS operation was estimated with the help of a radar. In the meter wavelength range, a nearly tenfold increase in the effective reflecting surface was observed.

The successful tests of the ÉOL-1 EPS laid the foundation for a wide application of SPTs in systems for the precise adjustment of the satellite orbital parameters.

Further, over a period of ten years, the ÉOL-2 and ÉOL-3 correcting SPT-based EPSs were efficiently used to correct the orbits of satellites of the same type

Table 1. Main characteristics of the SPT-based ÉOL EPSs

Type	ÉOL-1	ÉOL-2	ÉOL-3
Thrust, mN	16–19	15–21	22–25
Power consumption, W	420–440	380–400	400–450
Total produced thrust impulse, kN s	11.7	39	8.7
Number of switchings	≤15	≤273	≤180
Specific impulse, s	$(7.9–9.8) \times 10^5$	$(8.7–9.2) \times 10^2$	$(1–1.2) \times 10^3$
Discharge current, A	1.90–2.1	1.82–2.1	1.9–2.15
Discharge voltage, V	170–188	161–172	175–185

as the *Meteor* and the *Meteor-Priroda* satellites. Table 1 presents the main parameters of the ÉOL EPSs

During the flight tests performed in 1974–1976, the fundamental problems of the SPT operation in space were solved.

In the next stage (1977–1983), a method was elaborated for optimizing (with respect to the time and energy consumption) the correction maneuvers with the purpose of placing a satellite in a rational orbit. In this case, the total operation time of the ÉOL EPSs amounted to 1000 h for a group of six satellites. There were practically no failures in the EPS operation, and the EPSs remained able to operate during the entire satellite service lifetime.

3.2. Study of the SPT–Satellite–Magnetosphere System

During the first space tests of the SPTs, a very important problem was the compatibility of an SPT with a satellite. In order to solve this problem, a broad range of studies was performed, including physical research. In view of its completeness and thoroughness, there are still no analogs of this research in the world. Below, we outline the main results of these studies.

(i) Mass-spectrometric measurements of the satellite environment at an altitude of 900 km during the SPT operation showed that the density of the surrounding plasma increased to 10^5 cm^{-3}, the energy of ions bombarding the satellite surface increased to 30 eV, and the satellite potential decreased to –10 V.

(ii) When studying the SPT jet, it was found that the jet plasma density and the ion energy near the satellite depended substantially on the direction of the jet with respect to the geomagnetic field.

(iii) The noise produced by the SPT and the electromagnetic fields in the surrounding space were measured with the help of special antennas and an electromagnetic analyzer. The analyzer detected the presence of low-frequency electromagnetic oscillations in the range 5–20 kHz with a field intensity of 0.1 V/m during the operation of the cathode compensator. When a discharge was excited, high-frequency oscillations with an amplitude of 0.005 V/m were generated in the electron cyclotron frequency range 0.8–1.5 MHz. When dipole antennas placed at the solar-battery (SB) panels fell into the plasma jet, the noise level at a frequency of 40 MHz increased from 10 to 20–30 mV.

(iv) The measurements of the perturbing moments acting on the satellite when the SPT plasma jet partially fell onto the SB panels showed that the moments could attain 0.007 Nm and depended on the relative positions of the SPT and SB.

(v) No substantial degradation of the SB was observed after the SPT had operated during several hundred hours.

On the whole, the creation, study, and operation of satellites with EPSs provided great experience and laid the foundation for the employment of SPTs in space technology.

4. CREATION OF THE PROPULSION SYSTEMS AT THE FAKEL EDB: FROM ÉOL-1 TO SPT-140

For most of the current problems, the range of the SPT exhaust velocities have a number of advantages. Among these problems, of particular importance is that of placing a satellite at the working point in geostationary orbit and stabilizing its position in this orbit.

Because of the high cost of launching satellites into geostationary orbit ($30000–40000 per 1 kg of payload), it is very important to increase their efficiency and service lifetime. As to the Russian geostationary satellites, the challenge was to prolong the satellite service lifetime from 2–3 to 5–10 years and, where possible, up to 15 years. Such a considerable prolongation of the service lifetime was impossible without developing a novel propulsion system for placing a geostationary satellite at the working point and stabilizing it there, because the available (even if promising) chemical jet engines required very large fuel reserves. Morozov's SPT, whose specific impulse[2] exceeds the specific impulse of chemical engines by a factor of 5 and higher,

[2] The specific impulse is $J_s = U/g$, where U is the exhaust velocity from the engine and g is the free fall acceleration on the Earth's surface.

Table 2. Characteristics of the post-ÉOL thrusters

	SPT-50	SPT-70	SPT-100	SPT-140	PPS-1350
Power, W	325	660	1350	5000	1500
Voltage, V	175	300	300	400	350
Thrust, mH	25	40	85	330	90
Service lifetime, h	2500	≥3000	≥9000	≥7200 (expected)	≥5000
Mass, kg	0.8	1.2	3.5	8	3.6
Note	Four SPTs worked in space (1978)	68 SPTs worked in space since 1982	48 SPTs worked in space at Russian satellites	Qualification tests are being conducted	Designed in cooperation with SNECMA. Qualification tests have been completed

allow this problem to be solved. For this reason, from the early 1970s, the development of SPT-based propulsion systems began at the Fakel EDB.

For thirty years, the Fakel EDB has produced and maintained the flight SPT-based EPSs, which were successfully used to adjust the orbits of *Meteor* and *Meteor-Priroda* satellites in the 1970s and have successfully been employed on *Kosmos* and *Luch* satellites since 1982 and *Gals* and *Ékspress* satellites since 1994.

To develop thrusters and propulsion systems intended for use as space-qualified hardware, it was necessary, first of all, to solve the following problems:

(i) to study the feasibility of the long SPT service lifetime, find methods for ensuring this lifetime, and develop a physicotechnical base for designing SPTs;

(ii) to elaborate the basic design principles appropriate for constructing flight models of SPTs and SPT-based EPSs;

(iii) to elaborate a methodical basis and create a test base for the detailed on-the-ground development of thrusters and propulsion systems; and

(iv) to elaborate the principles of using EPSs at spacecrafts and carry out flight experiments with thrusters and EPSs in space (including operation onboard serial satellites).

The Fakel EDB (in cooperation with other scientific and industrial institutions) has performed the entire design and manufacturing cycle—from the choice of the parameters of a new SPT model to the delivery of an SPT-based propulsion system and the control over its operation in space.

Much attention has been given to the maintenance of the reliable SPT operation during the entire service lifetime. The lifetime tests are the most laborious and expensive; e.g., for SPT-100, such a test lasted for 9000 h of the operation time. Note that, in practice, this time is accumulated with pauses; consequently, the test should also be conducted with pauses. As a results, the lifetime test of a model can take several years.

One can get an idea of the cost of the lifetime test, if we say that 1 m^3 of xenon weighs about 5 kg and costs about \$10000, whereas the consumption of xenon during the test of a thruster with a power of ~1 kW is ~15 g per hour.

Clearly, such tests are accompanied by unexpected findings. For example, a new form of erosion was discovered in the early 1960s at the Fakel EDB [1]. It was found that, in this case, in spite of the substantial erosion of the insulator and the poles of the magnetic system, the thrust characteristics of the M-70 and M-100 SPTs changed only slightly.

4.1. Serial SPTs Already Designed and Being Designed at the Fakel EDB

Serial SPTs used as a base for creating propulsion systems at the Fakel EDB are listed in Table 2.

In this models, 95% of the plasma jet falls within an angle of ±45°. Along with these thrusters, which have worked or will work in space in the nearest future, there are a number of models that are presently in different design stages: SPT-25 (100 W, 5.8 mN), SPT-35 (200 W, 12 mN), SPT-200 (11 kW, 490 mN), and SPT-290 (≤30 kW, ≤1.5 N). The exhaust velocities attain 30 km/s in the latter two models and are ≤10 km/s in first two models.

The SPT-50, SPT-70, and SPT-100 thrusters were included into the orbit-control systems and successfully operated on many Russian satellites. It can be seen from Table 3 that SPTs have been used on satellites produced at the leading space-rocket enterprises and firms. It should be emphasized that, with the use of an SPT, the service lifetime of *Gals* and *Ékspress* satellites was prolonged from two–three years to five–seven years and the service lifetime of the *Ékspress-A*, *SESAT*, and *Ékspress-AM* satellites was prolonged to ten years. Due to the prolonged service lifetime, the higher technical–economical efficiency, as well as the higher efficiency of performing the satellite missions, was achieved.

The SPT-based EPSs designed at the Fakel EDB were first launched into geostationary orbit in May 1982. The M-70 thrusters were used to adjust the orbits of *Kosmos* satellites. Up to the present, 60 M-70 SPTs

Table 3. SPTs in space

Satellite	Thruster type	Cathode type	Launching date	Operation, h/number of SPTs
Near-Earth orbit, orbit correction maneuvers				
Meteor-Priroda	SPT-50	KÉ-2	March 1977	100/24
Meteor-Priroda	SPT-50	KÉ-2	May 1978	130/12
Plazma	SPT-70	KÉ-5	February 1987	152/6
Plazma	SPT-70	KÉ-5	July 1987	80/6
Geostationary orbit, final positioning and station holding of the satellite				
Kosmos	SPT-70	KÉ-5	May 1982	261/4
Kosmos	SPT-70	KÉ-5	March 1984	223/4
Louch	SPT-70	KÉ-5	October 1985	52/4
Kosmos	SPT-70	KÉ-5	April 1986	301/4
Kosmos	SPT-70	KÉ-5	October 1987	272/4
Louch	SPT-70	KÉ-5	November 1987	828/4
Kosmos	SPT-70	KÉ-5	August 1988	560/4
*Louch**	SPT-70	KÉ-5	December 1989	496/4
Kosmos	SPT-70	KÉ-5	July 1990	90/4
Kosmos	SPT-70	KÉ-5	November 1991	189/4
*Gals**	SPT-YuO	KN-3	January 1994	1766/8
*Kosmos**	SPT-70	KÉ-5	September 1994	357/4
*Ekspress**	SPT-YuO	KN-3	October 1994	1890/8
*Louch**	SPT-70	KÉ-5	December 1994	421/4
*Kosmos**	SPT-70	KÉ-5	August 1995	91/4
*Kosmos**	SPT-70	KÉ-5	October 1995	91/4
*Gals-2**	SPT-YuO	KN-3	November 1995	1920/8
*Ékspress-2**	SPT-YuO	KN-3	September 1996	984/8
Kupon	SPT-70	KÉ-5	November 1997	174/4
*Yamal-100**	SPT-70	KÉ-5	September 1999	708/8
*Ékspress-A**	SPT-YuO	KN-3B	March 2000	12/8
Ékspress-AM	SPT-YuO	KN-3B	2002	/8
*SESAT**	SPT-100	KN-3B	April 2000	25/8
*Kosmos**	SPT-70	KÉ-5	July 2000	70/4
Ruslan-MM	SPT-100 or SPT-140	KN-3B, KN-15	2003	Four SPT-100s or two SPT-140s
Yakhta	SPT-100	KN-3B	2003	/4
Yamal-200	SPT-100	KN-3B	2003	/8
Ékspress-1000	SPT-70	KÉ-5	2003	/4
Ékspress-2000	SPT-100	KN-3B	2003	/8
Phobos-Grunt	SPT-100 or SPT-140	KN-3B, KN-15	2004–2005	Nine SPT-100s or three SPT-140s
Scheduled application of SPTs on US and French satellites				
Omega	SPT-100	KN-3B	2003	/4
Stentor	SPT-100	KN-3B	2002	/4
Astra-IK	SPT-100	KN-3B	2002	/4
Inmarsat	SPT-100	KN-3B	2003	/8
Intelsat-X	SPT-100	KN-3B	Delivery in November 2000	/4
Telstar-8	SPT-100	KN-3B	Delivery in 2000	/4
LS-2020	SPT-140	KN-15	2005	/4
Ipstar-II	SPT-100	KN-3B	2002	/8
Eurostar	SPT-100	KN-3B	2002	/8
Spacebus-4000	SPT-100	KN-3B	Delivery in February 2001	/4
Intelsat	SPT-100	KN-3B	Delivery in April 2001	/4
Spacebus-4000	SPT-100	KN-3B	Delivery in June 2001	/4
Intelsat-X	SPT-100	KN-3B	Delivery in June 2001	/4
Intelsat-X	SPT-100	KN-3B	Delivery in September 2001	/4

* Satellite is operating.

have operated at various satellites. The total operation time of the M-70 SPTs at satellites is longer than 3700 h.

A new stage of the SPT application began with the launching of *Gals* and *Ékspress* satellites into geostationary orbit. The orbits of these satellites are corrected not only along the longitude (in the East–West direction), but also along the inclination (in the North–South direction).

In 1994–1996, two *Gals* and two *Ékspress* satellites were launched into a geostationary orbit. By June 2000, the total operation time of the 32 SPT-100 thrusters on these satellites reached 7300 h.

On September 6, 1999, a *Yamal-100* satellite was launched into a geostationary orbit. By the time at which *Yamal-100* was placed at a given point in the geostationary orbit, 50 maneuvers had been performed to correct the orbit, which needed more than 500 switchings, and none of the EPSs installed on the satellites had failed. By June 2001, the total operation time of eight thrust modules of the *Yamal-100* satellite was 1323 h and the number of switchings was 2189.

On the whole, experience gained during the flight tests and the long-term space operation on 32 satellites confirms the high efficiency and reliability of the SPT-based EPSs developed at the Fakel EDB. The operation of EPSs with SPT-70 and SPT-100 thrusters is well compatible with the spacecraft systems and does not have any adverse effect on them.

Among the electric propulsion thrusters with a specific impulse of 1000–2500 s, the service lifetime of the SPT-100 thruster exceeds 9000 h. A considerable service lifetime was also demonstrated by the PPS-1350 French–Russian thruster, designed relying on the results of the Fakel EDB and created with its participation. Currently, other SPTs developed in different countries have operated less than 2500 h. In view of this fact, some firms, such as Space Systems/Loral (USA) and Alcatel (France), order SPTs produced at the Fakel EDB. Thus, it is planned to launch a *Stentor* geostationary satellite in 2002–2003, which has been designed by Alcatel by request of the French Space Agency (CNES) and provided with two SPT-100 thrusters created at the Fakel EDB; an *Astra-1K* French geostationary commercial satellite, designed by Alcatel and provided with four SPT-100 thrusters; and *Omega* and *Telstar* American commercial satellites designed at Space Systems/Loral with four SPT-100 thrusters on each of them. It is also planned to use SPTs designed at the Fakel EDB at other satellites, in particular, in constellations of satellites (such as a *Skybridge* constellation) (see Table 3).

4.2. Outlook for Further Improvement of the Characteristics of SPTs Designed at the Fakel EDB

To enhance the thrust efficiency, increase the service lifetime, reduce the jet divergence, and enhance the SPT capability, the Fakel EDB (together with other institutions involved in scientific cooperation) have performed the following studies and engineering works:

(i) Methods were elaborated for increasing the SPT thrust efficiency by 5–7% and for reducing the divergence half-angle of 95% of the ion flow from 45°–47° to 30°–32° by using a thruster scheme with conducting inserts near the exit of the discharge chamber.

(ii) A novel thruster scheme with an improved magnetic system was designed. This system allows one to increase the thrust efficiency from 53–55% to 60–62% at a discharge voltage of 300 V, i.e., to increase the thrust efficiency by nearly 7–9%. An experimental model of an SPT-140 thruster has been developed based on this scheme.

(iii) The layout of the so-called hinged system for controlling the deflection of the thrust vector from the axis within ±5° was designed. With this system, thrusters can be used to control not only the motion of the satellite center of mass, but also its orientation, which substantially simplifies the satellite attitude-control system.

(iv) The processes occurring at the cathodes and anodes and in the electrode regions of various types of plasma sources were studied.

(v) Cathodes that do not need preliminary heating, which allow one to substantially shorten the thruster start time, and also cathodes for high-power SPTs were designed.

(vi) Small-sized SPTs capable of efficiently operating at powers of 100 W were designed, which makes it possible to use SPT-based EPSs at small-sized satellites.

(vii) SPTs were designed that are capable of operating at discharge voltages as high as 1000 V and provide a specific impulse as high as 3000 s.

5. GEOGRAPHY OF THE CURRENT WORKS ON SPTs

5.1. Brief Historical Review

The first works on plasma accelerators with closed electron drift and an extended acceleration region (in the USSR, these accelerators were later given the name SPT) began in the early 1960s almost simultaneously in the USSR and the USA. In the USSR, the studies on the SPT were performed at the Kurchatov Institute under the leadership of Morozov.

As early as the late 1960s, necessary experience was gained for the practical use of SPTs at satellites. The first SPT space tests were successfully carried out in 1972 [1]. In view of this success, the Fakel EDB was

charged with developing efficient flight SPTs and applying them to space technology. This problem was solved in cooperation with the Kurchatov Institute, VNIIEM, MAI, the Central Institute of Aviation Motorbuilding, the State Institute of Applied Chemistry, and other institutions.

A valuable contribution to the physical research and modeling of the processes occurring in the SPT and to the development of novel methods for enhancing the thruster efficiency in the last 15–20 years has been made by Moscow State University; the Moscow Institute of Radioengineering, Electronics, and Automation (MIREA); the Research Institute of Applied Mechanics and Electrodynamics of the MAI (RIAME MAI); and the Keldysh Institute of Applied Mathematics. A number of studies have been performed at the Keldysh Research Center (KRC).

In the USA, the work on thrusters that can be called the SPT analogs began in the early 1960s. These analogs were called Hall ion thrusters (HIT), or simply Hall thrusters. By the mid-1960s, the laboratory models of thrusters had been created and the characteristics of thrusters operating with inert gases and cesium had been studied [3, 4]. In particular, a thrust efficiency of $\eta \approx 0.2$–0.3 was obtained at a specific impulse of 1000–2000 s. Based on the studies of oscillations in the thruster acceleration channel, it was concluded that the main cause of the relatively low efficiency is that, due to plasma oscillations, a substantial fraction of the total current in the channel is carried by electrons [3]. By the early 1970s, the work on SPTs in the USA was practically stopped.

The loss of interest in HITs may be explained by two factors:

(i) the considerable success in the development of classical ion thrusters by the early 1970s and

(ii) the doubts of western experts as to whether it is possible to reduce the through electron current and to increase the HIT thrust efficiency.

The physical basis of the successful work at the Kurchatov Institute was the criterion found by Morozov for the stability of a discharge against the most dangerous azimuthally asymmetric mode. This criterion implies a sufficiently rapid increase in the magnetic field from the anode toward the exit from the channel.

Interest in HITs (more precisely, SPTs) rapidly increased in the early 1990s. By that time, the SPT thrust efficiency reached a rather high level; SPT-based EPSs were successfully used in Russia to insert satellites into geostationary orbit and to stabilize them at the working point; and it was realized that most of the current EPS problems can be successfully solved by using thrusters with exhaust velocities of 10–30 km/s, which were provided by SPTs.

As a result, SPTs are now extensively studied in many countries; the current status of this studies will be considered in the next section.

We emphasize that, in the USA, interest arose not only toward SPTs, but also in thrusters with an anode layer (TALs), proposed by A.V. Zharinov, and toward Russian studies on high-current lithium plasma thrusters.

5.2. Assessment and Qualification of Russian SPTs. Design and Application of the SPT-based Propulsion Systems

The relevant investigations were carried out at the NASA Glenn Research Center (GRC) and the NASA Jet Propulsion Laboratory (JPL) and also in Russia under contracts with US institutions and firms.

The US institutions and firms interested in the evaluation of thrusters (including both the development and full-scale tests) were NASA, the US Air Force, the Ballistic Missile Defense Organization (BMDO) of the Department of Defense of the USA [5], and the Space Systems/Loral (SS/L) and Space Power Inc. (SPI) firms. In particular, the BMDO elaborated the NEP STP and other spacecraft projects for the demonstration of the novel technology of space flights with the use of nuclear and promising solar power systems and SPT- and TAL-based EPSs.

In 1992, the SS/L firm in cooperation with the Fakel EDB and the RIAME MAI founded the International Space Technology, Inc. (ISTI) joint venture for the development and delivery of Fakel's SPTs and SPT-based EPSs to western firms producing satellites. In 1994, ISTI accepted the Atlantic Research Corporation and the Societe Europeennee de Propulsion (SEP) (now, a subdivision of the SNECMA Moteurs firm).

To realize the goals of the ISTI, a qualification test for the compliance of the SPT-100 thruster with the requirements of the western standards adopted in the USA and Europe was successfully passed [2]. In recent years, in addition to the tests at the Fakel EDB, a series of tests of SPT-140s were performed at the GRC, the JPL, and the Aerospace Corporation.

The SPI firm in cooperation with the KRC designed an SPT-based propulsion systems [6]. Now, experts from the SPI, which has entered the firm Pratt Whitney, are working on SPTs with a power of up to 10 kW.

In Europe, the main work on SPTs is conducted by the SNECMA firm [7]. This firm first designed its own SPT (in cooperation with the MIREA). After it joined the ISTI, the SNECMA in cooperation with the Fakel EDB developed under the ISTI program a PPS-1350 thruster with a power of 1.5 kW; now, the qualification tests of this thruster are coming to an end. At present, the SNECMA, supported by the French Space Agency (CNES), have begun to design a thruster with an elevated power of ~4–6 kW.

A technological geostationary *Stentor* satellite equipped with two SPT-100 thrusters and two PPS-1350 thrusters and a commercial *Astra-IK* satellite of

Table 4. New types of SPTs

Country	Firm, institution	Thruster power, kW	Exhaust velocity, km/s	Current status of work
USA	General Dynamics	2–4	10–20	Engineering models
	Busek	0.2–6	10–25	Experimental models
	Pratt Whitney under the support of TRW	0.1–10	10–25	Experimental and engineering models
	Glenn Center	up to 50	10–30	Experimental models
France	SNECMA	1.5	17	Flight models
		4–6	10–25	Experimental models
	MMS (now Astrium)	2–6	10–25	Experimental and engineering models
Japan	Tokio and Osaka Universities	0.1–0.5	10–20	Laboratory models

the Alcatel firm with four SPT-100 thrusters are to be launched in 2002 [7].

We note that the Matra Marconi Space (MMS, nowadays Astrium) firm provided the financial support of the work at the KRC on designing an SPT version other than that patented by the Fakel EDB and the ISTI. As a result, the ROS-99, ROS-2000, and other SPTs were designed and tested [8]. At present, this work (including the design of SPTs with an elevated power of 2–6 kW) is being continued under the partial support of the European Space Agency.

5.3. Development of Alternative SPT Versions

In the USA, the investigations on SPTs were initiated at higher education institutes (such as the Massachusetts Institute of Technology) and in the SPI and Busek firms under the financial support of NASA, the Air Force, BMDO, and other state financing funds. After the Busek firm obtained promising results, they were bought by a larger firm Primex, which later entered General Dynamics.

Obviously, this technology will also evolve in a similar way in Japan, where the investigations on SPTs are now carried out only at universities.

In France, the investigations on SPTs began simultaneously in two powerful firms: SNECMA and MMS.

At present, there are three great western firms that intend to design, produce, and sell their own SPTs: SNECMA, MMS, and General Dynamics.

Characterizing the situation as a whole, we can conclude that the SPT technology is now used throughout the world. The characteristics of a number of SPTs under development are given in Table 4.

5.4. Directions of Research on SPTs in the World

The particular interest and financial support of the state organizations (NASA, the Air Force, and BMDO in the USA; CNES in France; and the Ministry of Science in Japan), as well as of the commercial firms (SS/L, TRW, General Dynamics, and Busek in the USA and Alcatel, Astrium, and SNECMA in Europe) stimulated extensive research on SPTs.

In addition to large test benches in the NASA, Air Force, and Aerospace Corporation laboratories and in commercial firms, there are test benches in universities, such as a test bench at the University of Michigan (the inside diameter of the vacuum chamber is about 6 m). In these benches, modern diagnostics and powerful computers are widely used. We only mention laser diagnostics for the direct measurements of the ion and atom velocities in the acceleration channel and in the thruster jet and systems for time-resolved measurements of the intensity of atomic and ionic optical radiation from different points inside the acceleration channel with a microsecond time resolution and fair spatial resolution. These measurements have already yielded a number of qualitatively new results, such as the spatiotemporal structure of fluctuations in the ion and neutral densities in the channel and the thruster jet.

The use of powerful computers allows one to perform the statistical modeling of the time-dependent plasma dynamics with the kinetic description of ions, electrons, and atoms in axisymmetric or three-dimensional geometry. Although some questions as to the relevance of such a modeling still remain unanswered, we can expect considerable progress in this direction too.

6. EMPLOYMENT OF AN SPT-BASED EPS IN THE PHOBOS-GRUNT PROJECT

So far, we have discussed the use of SPTs for Earth-orbital flights, including launchings into geostationary orbit. However, not only future SPTs, but also the available SPT-100 and SPT-140 thrusters can make flights to the planets and asteroids much more efficient. Here, we will describe the project of a spacecraft flight with SPTs to Phobos. One can say that this will be the flight of a "little comet" with a plasma tail. This raises many questions (which are, in essence, physical) as to how the

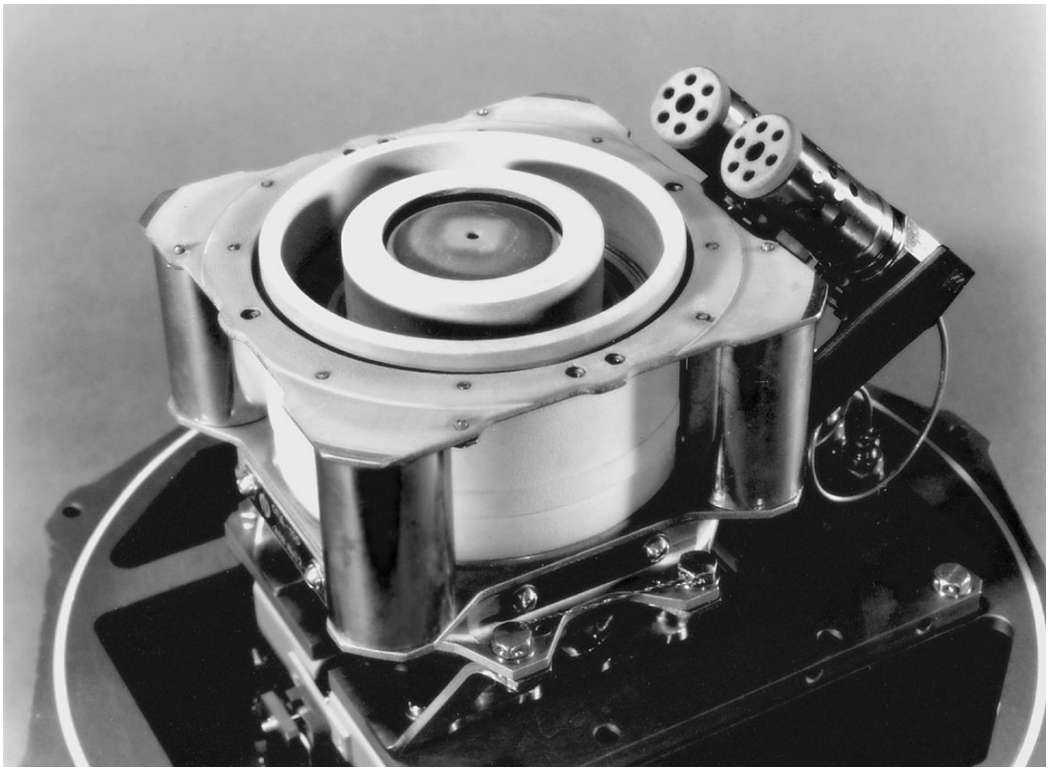

Fig. 7. M-100 SPT.

operating SPTs influence the spacecraft systems, how the plasma tail influences radiocommunication, etc.

The project is being developed under the Russian space program. The flight of a spacecraft to Phobos is scheduled for 2007–2010 [9]. The main objective of the project is to return a soil sample from the surface of Phobos. The scientific goal of the project consists in studying the fundamental problems of the formation of the solar system in the initial stages of its evolution [10]. The implementation of the project implies the use of a *Soyuz* medium-lift launch vehicle. The transport of the spacecraft from Earth's orbit into that of Mars should be realized by a three-stage rocket system consisting of a liquid engine (LE) of the *Fregat* upper stage, an EPS with solar batteries, and a deceleration LE with a relatively low (50 kg) thrust. In the Earth's orbit, the EPS will be powered by a solar power system (SPS) with a power of $N_0 = 7.5$ kW, of which 6.5 kW is the EPS power consumption. The total corrective thrust impulse of the solar EPS (SEPS) needed to increase the spacecraft velocity by $\Delta V = 3$ km/s is nearly $I_\Sigma = 7$ MN s, and the thruster operation time exceeds $T_t = 10000$ h. The spacecraft mass in the orbit of Mars after the separation of the SEPS must be about $M_f = 1000$ kg. The use of the SEPS nearly doubles the mass efficiency of the orbital injection in comparison with the use of chemical jet propulsion only. This allows one to use a relatively inexpensive *Soyuz* launcher instead of an expensive heavy-lift *Proton* launcher.

In [11], results of designing an SEPS on the basis of the SPT-100 thruster developed at the Fakel EDB are presented.

At present, a new thruster SPT-140 is passing ground development tests. In this paper, we consider a concept of the expedition, taking into account the specific features of the flight with a small thrust provided by SPT-140, and the design of the EPS intended for the *Phobos-Grunt* spacecraft.

6.1. Expedition Scenario

The components and configuration of the spacecraft at different stages of the expedition are shown schematically in Fig. 8 [12]. The launch vehicle puts the spacecraft into an open trajectory with an apogee of 200 km. The LE is switched on for the first time at the apogee in order to launch the spacecraft into a circular orbit with an altitude of 200 km. With the second switching-on of the LE, the spacecraft is placed in an intermediate elliptical orbit with an apogee of $r_\alpha = 46370$ km and a perigee of $r_\pi = 6840$ km. Here, the outboard fuel tanks of the propulsion system are dumped. Then, the LE is switched on for the third time for the spacecraft to leave the Earth's gravisphere with a certain hyperbolic excess of velocity (HEV) V_0. The value and direction of the

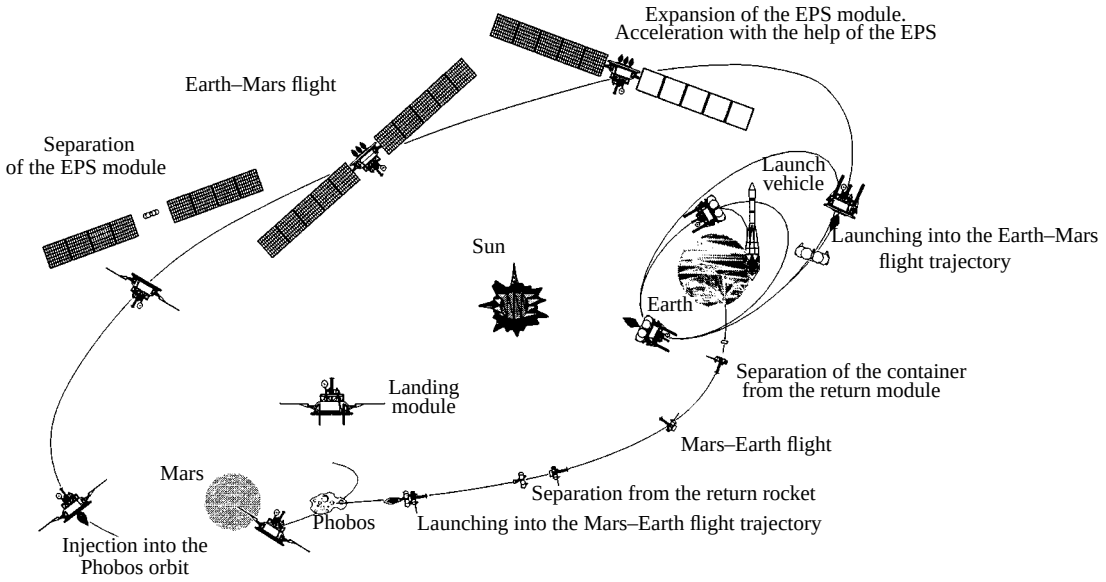

Fig. 8. Scenario of the flight under the Phobos-Grunt project.

HEV are to be chosen by calculating the optimal trajectory at the heliocentric path of the flight realized with the help of the SEPS. As the distance of the spacecraft from the Sun varies, the electric power produced by the SPS varies as $N = N_0/r^{1.7}$, where r is the distance from the spacecraft to the Sun in astronomical units. A decrease in the SPS power due to the action of radiation and ions on the SBs (≈5% per year) should also be taken into account. The basic requirement of the EPS is that, at the beginning of the trajectory of the flight to Mars, the EPS provide a thrust of P = 30–33 g at a power of 6.5 kW and a specific impulse of I = 2100 s. These parameters can be obtained with an EPS on the basis of the SPT-140. The variation in the thrust value according to the available electric power at each point on the spacecraft trajectory is achieved by varying the mass flow rate of the working gas (xenon). The EPS maintains the flight from the Earth's gravisphere to Mars's gravisphere.

When the spacecraft enters Mars's gravisphere, the SEPS is separated. The approach to Phobos and the landing on its surface occur with the help of the third-stage engine.

Without going into details of the program of research on the Phobos surface, we note that, to achieve the goal of the expedition, a soil sample will be taken with the help of a special instrument from a depth of up to 1.5 m and will be placed into a special container. After this part of the scientific program is accomplished, a return launching vehicle will place the spacecraft in a near-Mars orbit, where the scientific program of the expedition will be continued. No later than July 2009, the spacecraft must start toward Earth with the help of the same launching vehicle. The homeward journey, including one or two orbit corrections, will take about a year. When approaching Earth, the spacecraft with the soil samples must overcome the terrestrial atmosphere and land in Russian territory. The mass of the soil sample brought back to Earth will be 200–300 g, whereas the start mass of the *Soyuz* launch vehicle is nearly 200 t.

The requirements to the SEPS are determined from ballistic calculations of the optimal flight trajectory. Some calculated results are listed in Table 5 for relatively short trajectories, although there may also exist more complicated optimal trajectories.

Table 5. Parameters of optimal trajectories for a scheduled start in 2007

T, days	Start date	ΔV, km/s	M_{00}, kg	T_t, days	M_{Xe}, kg	M_f	I_Σ, MN s	Flight finish
480	October 1, 2007	4.107	1888	364.9	306	1582	6.307	–
400	September 21, 2007	3.394	2035	379.6	3216	1714	6.600	October 25, 2008
450	August 30, 2007	2.275	2227	405.7	354	1837	7.297	November 22, 2008
500	August 20, 2007	1.957	2271	422.2	380	1891	7.837	January 1, 2009

In Table 5, which was calculated assuming that the start will be in 2007, we present the optimal start dates and the values of ΔV, the initial mass M_{00} at the moment at which the spacecraft leaves the Earth's gravisphere, the SPT operation time T_t, the total momentum I_Σ given to the spacecraft, M_f, and the xenon mass M_{Xe} corresponding to different flight times T.

The final mass M turns out to be maximum for the flight duration $T > 500$ days. For reasons of completing the scientific program, a flight lasting 550 days was chosen to be the base version.

Figure 9 shows the general view of the *Phobos-Grunt* spacecraft designed at the Lavochkin Science and Production Association. The figure corresponds to the stage at which the spacecraft is already launched into a near-Earth orbit. The EPS uses three SPT-140 thrusters [13].

6.2. Problems of the Interaction of the SPT Plasma Jet with the Spacecraft Systems

The use of an EPS on the *Phobos-Grunt* spacecraft offers a unique opportunity for experimentally studying the complicated processes of the interaction of the SPT jet with the spacecraft systems under the condition of a long-term (more than 500 days) flight. In this case, the spacecraft environment will be affected by neither the operation of other types of thrusters nor the Earth's atmosphere. It is hardly possible to achieve such pure conditions during ground tests. Below, we consider the main factors affecting the spacecraft systems during the operation of the SPT.

(i) The unfavorable force action of the SPT jets is caused by the interaction of the peripheral part of the jet with the spacecraft elements that fall into the ion flow. This action leads to the appearance of perturbing forces and moments. The calculations of the components of the resulting parasitic momentum **F** and moment **M** acquired from the jet show that, even for a power consumption as high as 6.5 kW, the parasitic momentum will not exceed 0.25% of the thrust value along any spacecraft axis and will not significantly affect the flight trajectory. The effect of the perturbing moment will be compensated for by deflecting the SPT thrust vector through turning the gimbal suspension within an angle of 1°.

(ii) Ion sputtering is of minor importance from the standpoint of the mechanical damage of the spacecraft construction elements. It is more important that, due to the sputtering of the surfaces of the spacecraft elements, the sputtered material can be deposited on other elements, thus changing their functional characteristics. At the same time, if the polluted surface is exposed to the action of the jet, then the deposited material can be sputtered again. This can be accompanied by a partial cleaning of the surface. The erosion and deposition rates were calculated for the *Phobos-Grunt* configuration with SPT-140. The anticipated maximum rate of the deposition of the sputtered material amounts to ~3 nm/h. For the estimated thruster operation time, the coating thickness can substantially reduce the transparency of the SB protective glass coating.

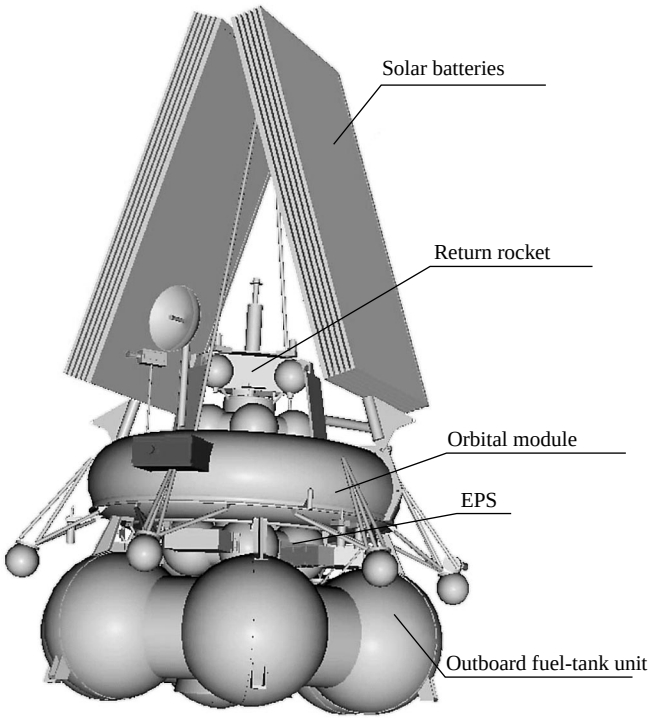

Fig. 9. *Phobos-Grunt* spacecraft.

(iii) The adverse effect of the plasma jet on the radiocommunication during a space flight is caused by the partial reflection and absorption of electromagnetic waves passing through the jet and the high level of noise generated by the jet itself. During a deep-space mission, the mutual orientation of the jet and the directional receiving–transmitting antenna is unfavorable because both of them are directed to the Earth, and the distance to which information should be transmitted attains several astronomical units. Hence, it is impossible to avoid the passage of the transmitted and received radio signals through the plasma jet. The electromagnetic wave spectrum generated by the SPT-100 plasma jet was studied in detail. It was found that the radiation intensity is maximum in the frequency range 1.8–6 GHz and falls rapidly toward higher frequencies. The radio complex of the *Phobos-Grunt* spacecraft will operate at frequencies of ~8 GHz, for which the adverse effect of the jet noise is expected to be insignificant. The data on the ion thruster operation acquired during a long-term flight performed under the American program Deep Space 1 is encouraging. Even in situations where the radio signal passed through the jet of the ion thruster with a power of 0.5–2.5 kW, there were no problems with the passage of radio signals. However,

we note that the problems of the electromagnetic compatibility of the EPS with the spacecraft radio complex are difficult to investigate in ground tests; moreover, techniques for such investigations are still poorly developed. The study of this problem in the course of space mission is of particular importance.

REFERENCES

1. A. I. Morozov, Fiz. Plazmy **29**, 261 (2003) [Plasma Phys. Rep. **29**, 235 (2003)].
2. V. N. Oraevsky, Yu. Ya. Ruzhin, V. S. Dokukin, and A. I. Morozov, Fiz. Plazmy **29**, 293 (2003) [Plasma Phys. Rep. **29**, 267 (2003)].
3. G. S. Janes and R. S. Lowder, Phys. Fluids **9**, 1115 (1966).
4. E. A. Pinsley, C. O. Brown, and C. M. Banas, J. Spacecr. Rockets **1** (5) (1964).
5. L. H. Caveny, D. M. Allen, and G. Herbert, in *Proceedings of the 24th International Electric Propulsion Conference, Moscow, 1995*.
6. N. Britt, in *Proceedings of the 38th Joint Propulsion Conference and Exhibit, Indianapolis, IN, 2002*, Paper AIAA-2002-3559.
7. G. Saccoccia, in *Proceedings of the 38th Joint Propulsion Conference and Exhibit, Indianopolis, IN, 2002*, paper AIAA-20023561.
8. J. M. Stephan, in *Proceedings of the 3rd International Conference on Spacecrafts Propulsion, Cannes, 2000*, p. 81.
9. É. A. Akim, É. M. Galeev, R. S. Kremnev, *et al.*, Izv. Vyssh. Uchebn. Zaved., Estestvennye Nauki, Spetsvypusk, 13 (2001).
10. T. M. Eneev, G. B. Efimov, and V. V. Smirnov, in *Proceedings of the 2nd German–Russian Conference on Electric Propulsion Engines and Their Technical Applications, Moscow, 1993*.
11. V. A. Obukhov, G. A. Popov, V. Kim, *et al.*, in *Proceedings of the IAF Conference, Rio-de-Janeiro, 2000*, paper IAF-0-S.4.05.
12. G. A. Popov, V. A. Obukhov, M. S. Konstantinov, *et al.*, Fundam. Prikl. Probl. Kosmonavtiki, No. 2, 26 (2001).
13. G. A. Popov, V. A. Obukhov, M. S. Konstantinov, *et al.*, in *Proceedings of the IAF Conference, Toulouse, 2001*, paper IAF 01-Q-03.b.05.

Translated by N.F. Larionova

Plasma Physics Reports, Vol. 29, No. 3, 2003, pp. 267–275. Translated from Fizika Plazmy, Vol. 29, No. 3, 2003, pp. 293–301.

THE 30th ANNIVERSARY OF SPT OPERATION IN SPACE

Dynamics of Quasineutral Plasma Beams and the Structure of the Beam-Induced Disturbances in Ionospheric Plasma

V. N. Oraevsky*, Yu. Ya. Ruzhin*, V. S. Dokukin*, and A. I. Morozov**

**Institute of Terrestrial Magnetism, Ionosphere, and Radio-Wave Propagation, Russian Academy of Sciences, Troitsk, Moscow oblast, 142092 Russia*

***Nuclear Fusion Institute, Russian Research Centre Kurchatov Institute, pl. Kurchatova 1, Moscow, 123182 Russia*

Received May 23, 2002; in final form, September 25, 2002

Abstract—Phenomena accompanying the injection of a dense plasma beam from the payload of a rocket into ionospheric plasma are analyzed. The dynamics of both the quasineutral plasma beam and the beam-induced disturbances in the ionospheric plasma are investigated. It is shown that the electric field in the beam has a complicated structure, which leads to the generation of currents in both the beam and the ambient ionospheric plasma. The transverse size of the disturbance zone in the ionospheric plasma is found to greatly exceed the beam diameter. The proposed model of the current closing in the ionospheric plasma agrees well with the experimental data. The xenon beam temperature at moderate distances from the injector is determined by using the plasma shadow theory. It is found that the ion beam temperature is at least four times lower than the plasma temperature in the injection zone. This unexpected result is explained by the adiabatic cooling of the current system. The critical radius beyond which a constant temperature in the beam is established is found to be less than 11 m. © *2003 MAIK "Nauka/Interperiodica"*.

1. INTRODUCTION

In the ECHO, Zarnitza, and ARAKS active experiments, the injection of dense plasma jets was used to neutralize the charge accumulated on a rocket during electron injection. The first experiments with a neutralized fast-ion beam propagating across the geomagnetic field were carried out in 1979 under the Porcupine program [1–3]. In these experiments, Morozov's plasma thruster [4], which showed high performance parameters when operating in space, served as a beam source (plasma generator). It was supposed that, in this case (in contrast to the case of an unbounded plasma flow considered by Chapman and Ferraro [5]), the transverse propagation is sustained due to the generation of the polarization electric field $\mathbf{E}_0 = -(1/c)\mathbf{V}_0 \times \mathbf{B}_0$ in the jet. The experiments showed that the neutralization of the polarization charges with currents flowing in the background ionospheric plasma (the so-called "short-circuit" mechanism) begins to play a dominant role in jet dynamics at beam densities hundred times higher than the ionospheric plasma density. In this case, electrodynamic disturbances with a scale length much larger than the jet diameter are produced in the ionosphere.

2. SYSTEM OF CURRENTS PRODUCED DURING THE QUASI-TRANSVERSE INJECTION OF XENON PLASMA BEAMS INTO THE IONOSPHERIC PLASMA

2.1. Active Experiments Carried Out under the Porcupine Program

In the Porcupine international experiment [2, 3, 6], the distributions of the electric and magnetic fields produced during the injection of a plasma beam into the ionosphere were measured. It was found that the effect of the background plasma was very important—the polarization field turned out to be much lower than E_0 and rapidly decreased with distance. A schematic of the experiment is shown in Fig. 1 [3, 6]. A conical quasineutral xenon plasma jet was injected at altitudes of 190–450 km from an injector separated from the payload of the rocket to the east. The jet diagnostics was installed on the rocket and two separate containers, UCB-1 and UCB-3. The launchings were carried out near midnight (in March 1979) in the auroral zone (Kiruna, Sweden).

The plasma source produced a Xe ion jet with a flux density on the order of 5×10^{17} cm^{-2} s^{-1} (an equivalent current of $I_0 \sim 4$ A), a velocity of $V_0 \sim 17$ km/s (an ion

1063-780X/03/2903-0267$24.00

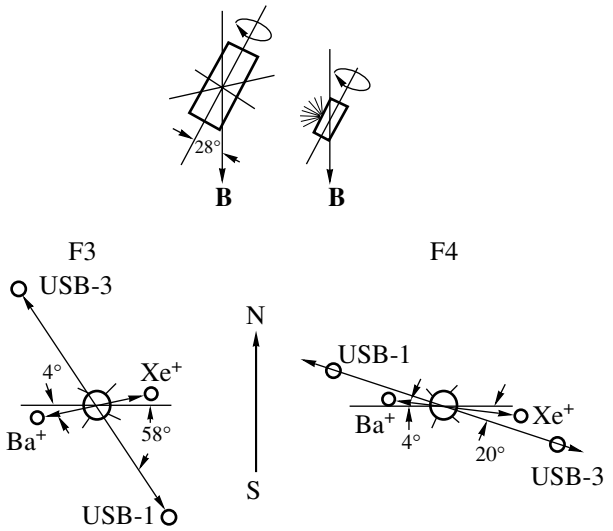

Fig. 1. Sketch of the Porcupine rocket experiment with the injection of a quasineutral plasma beam into the ionosphere.

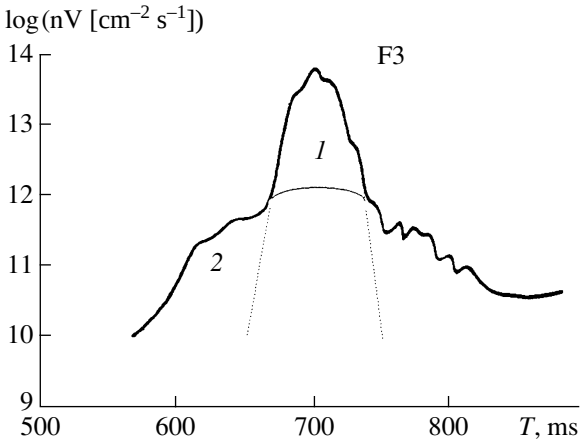

Fig. 2. Transverse profile of the plasma flux density of the beam passing through the rocket as a function of time during one period (281 ms) of the container rotation in flight F3: (*1*) fast and (*2*) thermal components of the plasma flow. The zero time corresponds to a flight time of 121.5 s.

energy of $\varepsilon_0 \sim 200$ eV), and an injection cone half-angle of 30° [4]. The jet was injected transversely to the longitudinal axis of the container, rotating with a period of $T_{inj} = 0.281$ s. Because of the container rotation and the tilt of its axis with respect to the geomagnetic field ($\Delta\alpha \sim 28°$; see Fig. 1), the longitudinal (with respect to the geomagnetic field) component of the plasma jet was directed upward when the jet was injected toward the rocket and downward in the opposite case. In the second flight (F4), the injection began when the container moved apart from the rocket at a distance of 3.7 m. On the rocket, the measurements of the dc and ac electric fields (up to 16 kHz for low-frequency fields and to 12 MHz for high-frequency fields), magnetic field fluctuations (up to 4 kHz), ion and electron fluxes, and electron densities were performed.

During the first flight (F3), the geomagnetic conditions were absolutely quiescent. During flight F4, the geomagnetic field was slightly disturbed; in this case, the background density was $n \sim 3 \times 10^5$ cm^{-3} at an altitude of 190 km and the transverse ionospheric electric field $E_\perp \sim 30$ mV/m was directed nearly southward.

2.2. Determination of the Currents from Magnetic Measurements

By the first recording ($\sim 2.4 \times 10^{-4}$ s), all of the quantities on the rocket (i.e., at a distance of ~4 m from the beam) have already been established. The longitudinal component $B_\parallel$ of the disturbed magnetic field is related to the currents flowing across the geomagnetic field, first of all, to the xenon ion current. Let us consider a purely ion beam and determine its magnetic field. To do this, it is necessary to know the spatial distribution of the ion flux. In the Porcupine experiment, the profile of the Xe ion flux nV was fairly complicated; in the first approximation, it can be regarded as a sum of a narrow and a wide beam. Figure 2 shows a typical distribution of the plasma flux density across the beam, and Fig. 3 shows the maximum plasma flux density on the beam axis, $(nV)_{max}$, as a function of the distance from the injector.

The azimuthal component of the disturbed magnetic field was calculated in [7], where the longitudinal ($B_\parallel$) and transverse ($B_\perp$) components of the magnetic field produced by the ion beam at different times were determined with allowance for the specific orientation of the

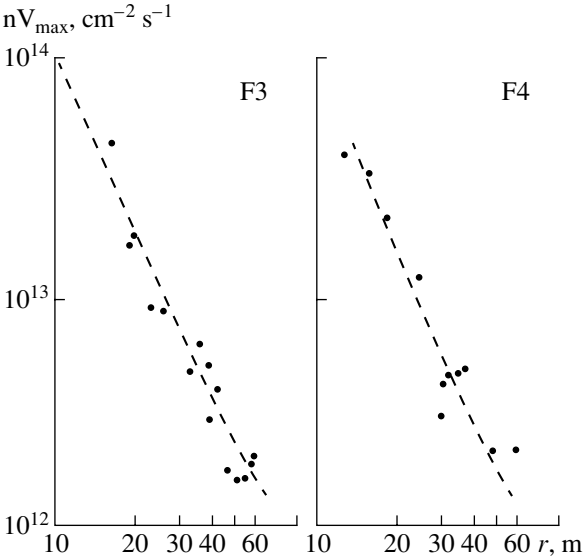

Fig. 3. Maximum plasma flux density (on the beam axis) vs. distance from the injector in flights F3 and F4.

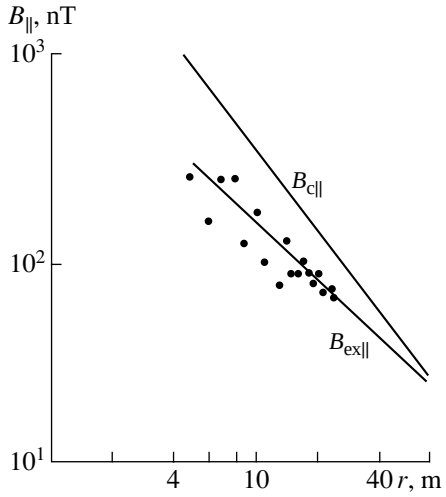

Fig. 4. Comparison between the simulated ($B_{c\parallel}$) and measured ($B_{ex\parallel}$) magnetic field in the beam.

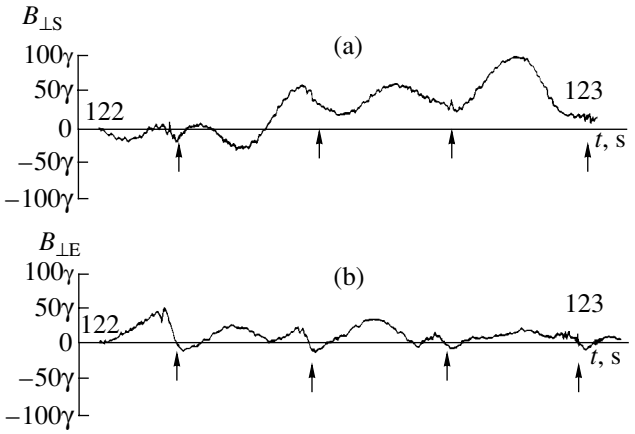

Fig. 5. Disturbances of the (a) southward and (b) eastward components of the magnetic field caused by the longitudinal currents near the injector.

injector, beam, and rocket with respect to the geomagnetic field $\mathbf{B}_0$. Figure 4 shows the amplitudes of the calculated ($B_{c\parallel}$) and measured ($B_{ex\parallel}$) longitudinal components of the disturbed magnetic field as functions of the distance between the injector and a magnetometer placed aboard the rocket for the flight F4. At large distances from the injector, the calculated and measured $B_{c\parallel}$ values are in good agreement, which confirms the validity of the model of the injected ion beam and indicates that, at large distances, the disturbed magnetic field is mainly produced by the xenon ion beam.

Let us consider the longitudinal (with respect to the geomagnetic field) electron spreading during the injection of the plasma jet [8–10]. Near the injector, the electrons move together with the Xe ions due to the produced polarization electric field. This field rapidly decays with distance (see below) and, at a distance of $\approx$23 m from the injector, it is almost zero. For this reason, the injected electrons spread along $\mathbf{B}_0$, thus giving rise to longitudinal currents. These currents are the highest in the region where the polarization field has already substantially decreased, i.e., at a distance of $R^* \sim$ 3–4 m from the injector. To ensure the electron spreading along the magnetic field, the plasma potential near the injector should be negative with respect to its value at infinity. Both the longitudinal electron current and the polarization field sharply decrease with the distance from the injector.

We will assume that all of the longitudinal current is concentrated near the injector (at distances of less than R^* from it), the sum of the inflow currents is equal to the Xe ion current, and no electric charge is accumulated inside this region. The calculated magnetic field disturbances caused by the longitudinal currents are maximum when the injector is oriented southward, which agrees with the experimental data (in Fig. 5, the disturbance of the southward component is seen to be substantially larger than that of the eastward component). It can be seen in Fig. 5b that the magnetic field disturbances are maximum at the moments when the plasma jet arrives at the rocket (at the diagnostic equipment). One can also see fairly high disturbances at the moments (marked with arrows) when the injector "shoots" in the opposite direction. It is the longitudinal currents near the injector that are responsible for these disturbances.

2.3. Analysis of the Electric Fields inside the Injected Beam and at Its Periphery

When analyzing the experimental data, it is convenient to separate different electric field components. Let us represent the electric field as a sum of four components [11]:

$$\mathbf{E} = \mathbf{E}_i + \mathbf{E}_p + \mathbf{E}_b + \mathbf{E}_B. \quad (1)$$

During the first injection (t = 118.56–133 s), the ionospheric field $\mathbf{E}_i$ changed only slightly (being about 30 mV/m) and was directed nearly southward (along the 150° azimuth). The polarization field $\mathbf{E}_p$ was directed transversely to the beam and caused the electrons to drift in the direction of the jet of Xe ions. The beam field $\mathbf{E}_b$ arose due to the different velocities of electrons and ions along the beam and ensured the electron spreading along $\mathbf{B}_0$. This field was directed toward the injector (along the radius). The $\mathbf{E}_B$ field is the Boltzmann one, and, accordingly, its potential is equal to $\varphi = (T_e/e)\ln((n_b/n_0) + 1)$. In contrast to the other components, it decreases along $\mathbf{B}_0$ over a distance on the order of the jet diameter. The radial (beam-aligned) component of this field is maximum at the beam axis, where the azimuthal component is zero. Formulas for the Boltzmann field components were obtained in [11] by substituting the n_b distribution into the expression for φ.

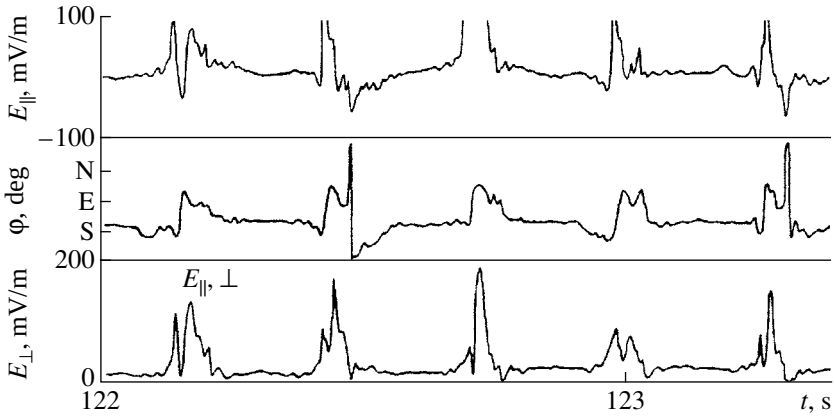

Fig. 6. Polarization electric field corrected for the drift of the beam electrons.

In the Porcupine experiment, the xenon jet consisted mainly of two beams (see Fig. 2). Each beam was characterized by its own Boltzmann and polarization fields. The contribution of the thermal Xe ions to the total field can be ignored because it is significantly smaller than the contribution of these beams.

The $E_\parallel$ and $E_\perp$ components and the $\mathbf{E}_\perp$ orientation are shown in Fig. 6; one of the moments at which the jet maximum passes through the rocket is marked with an arrow. It can be seen that the field $E_\perp$ corresponding to the first maximum is directed nearly southward, whereas the field corresponding to the second maximum is directed 70° counterclockwise with respect to the northward direction. Such a situation is typical as long as there is a polarization field in the jet.

The polarization field in the jet can be estimated using the experimental data on $B_\parallel$ and the calculated longitudinal component of the magnetic field produced by a pure ion beam. The difference between the measured ($B_{ex\parallel}$) and calculated ($B_{c\parallel}$) values is related to the transverse electron current. This current is determined by the drift of the beam electrons with the velocity $\mathbf{V}_e = c[\mathbf{E}_p \times \mathbf{B}_0]/B_0^2$, and the magnetic field produced by the drift electron current is proportional to the polarization field $\mathbf{E}_p$. The proportionality factor K can be found assuming that electrons follow the Xe ion trajectories, i.e., form the same conelike beam. Then, the magnetic field $B_{c\parallel}$ produced by the transverse ion beam is equal to KE_0. Hence, the polarization field in the beam is described by the expression [12]

$$E_p = E_0(1 - B_{ex\parallel}/B_{c\parallel}). \quad (2)$$

The polarization field calculated by formula (2) (see Fig. 7) is ≈600 mV/m at a distance of ≈6 m from the injector. At this distance, the plasma density in the jet is still fairly high ($\approx 1.4 \times 10^8$ cm^{-3}).

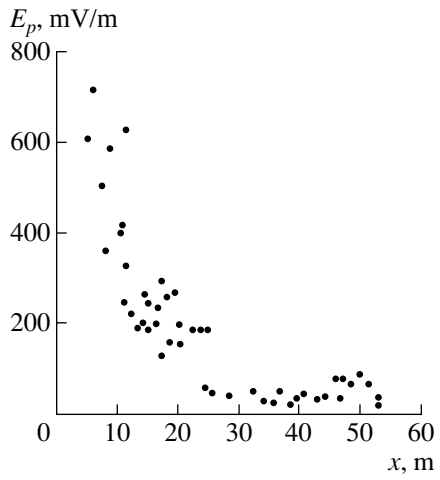

Fig. 7. Decrease in the polarization electric field with the distance from the injector.

The total electric field $E_\perp$ measured with probes in the plane perpendicular to the geomagnetic field at the instant at which the jet maximum passes through the rocket is significantly lower than that shown in Fig. 7. For example, the $E_\perp$ value decreases from 230 mV/m at a distance of 11 m from the injector to a background level of 30 mV/m at $r \sim 23$ m. Thus, the estimate of the polarization field by the data on $E_\perp$ differs greatly from the $\mathbf{E}_p$ value obtained from magnetic measurements. This difference stems from the fact that the field $E_\perp$ is highly localized over the angle φ. The distance between the probes that measured the potential difference between two spatial points was $L = 5$ m, which was larger than the effective diameter $a_\perp$ of the fast component of the beam at distances of up to 23 m from the injector. Hence, the measured electric field $E_\perp = \Delta\varphi/L$ is strongly underestimated as compared to the true value of $E_\perp$ at these distances. However, at $L < a_\perp$, the measured electric field corresponds to the true value of $E_\perp$ [8, 11].

2.4. Model of the System of Currents and Electric Fields

An analysis of the experimental data from [6, 8, 9] enabled us to reconstruct the following system of currents and electric fields (Fig. 8). After injection from the plasma source, the electrons propagate together with the ions due to the drift in the electric field and spread along $\mathbf{B}_0$ (the z-axis), occupying a region with a certain characteristic scale length $L_\parallel$. Within this region, all of the background plasma is involved in convective motion. Far from the source, at the beam front, the background plasma electrons move toward the beam ions, thus providing plasma quasineutrality. Near the source, there are the field $\mathbf{E}_p$, which enables the electron drift in the injection direction x; the field $\mathbf{E}_a$, which arises because the electrons drift more slowly than the jet ions and, as a result, the region near the injector acquires a negative charge; and the Boltzmann field $\mathbf{E}_B$. Near the injector, the beam plasma potential is negative, and, far from the injector, it is positive with respect to its value at infinity. The fields $\mathbf{E}_p$ and $\mathbf{E}_b$ extend over a certain distance along $\mathbf{B}_0$, whereas the φ_B potential decreases over a distance on the order of the beam diameter a. The presence of the $\mathbf{E}_b$ component causes the electrons injected from the source to drift at a certain angle with respect to the ion velocity (in the direction between the directions of the x- and y-axes), so that the longitudinal currents at $y > 0$ turn out to be higher than those at $y < 0$. Except for the region near the beam front, the density of the background ions changes slightly because their drift in the electric field is balanced by the inertial current caused by the inhomogeneity of the electric field.

The set of equations describing the potential distribution is presented in [8–10]. For the background plasma far away from the beam, the continuity equation for current density

$$\nabla \cdot \mathbf{j} = 0 \tag{3}$$

can be rewritten in the form

$$b_{e\parallel}\frac{\partial^2\phi}{\partial z^2} = \frac{c^3 m_i}{eB^3}\left[\frac{\partial}{\partial x}\left(\frac{\partial\phi}{\partial y}\frac{\partial^2\phi}{\partial x^2} - \frac{\partial\phi}{\partial x}\frac{\partial^2\phi}{\partial x\partial y}\right) + \frac{\partial}{\partial y}\left(\frac{\partial\phi}{\partial y}\frac{\partial^2\phi}{\partial x\partial y} - \frac{\partial\phi}{\partial x}\frac{\partial^2\phi}{\partial y^2}\right)\right]. \tag{4}$$

When deriving Eq. (4), it was assumed that the background plasma was only slightly perturbed. The left-hand side of this equation is the divergence of the longitudinal electron flux. The quantity $b_{e\parallel} = e/m_e\nu_{\text{eff}}$ is the electron mobility, and ν_{eff} is the effective electron collision frequency. The right-hand side is the divergence of the transverse ion flow, which is related to the inertial drift as

$$j_1 = \frac{c^2 n m_i}{B^3}[(\mathbf{V}\cdot\nabla)\mathbf{V}\times\mathbf{B}], \tag{5}$$

where $V = -c\dfrac{[\nabla\phi\times\mathbf{B}]}{B^2}$.

Equation (4) holds if

$$\lambda_e \gg L_\parallel, \quad \rho_{ci} \gg a, \tag{6}$$

where λ_e is the electron mean free path and ρ_{ci} is the ionospheric ion cyclotron radius.

Estimates (see below) show that conditions (6) are satisfied at distances L_* longer than several meters from the source. Equation (4) can be solved numerically. At $x > a$, the dependences of the potential and currents on the parameters and the distance along the jet are as follows:

$$\frac{E_\perp}{E_0} \sim \frac{E_p}{E_0} \sim \frac{E_b}{E_0} \sim \frac{A^2\nu_{\text{eff}}a^4}{V_0}\frac{m_e}{m_i}\frac{1}{x^3}, \tag{7}$$

$$\frac{L_\parallel}{a} \sim \frac{\omega_{ce}}{\nu_{\text{eff}}}\frac{x^3}{Aa^3}, \tag{8}$$

$$j_\parallel \sim \frac{en_0A^3\nu_{\text{eff}}a^6}{x^5}\frac{m_e}{m_i}, \tag{9}$$

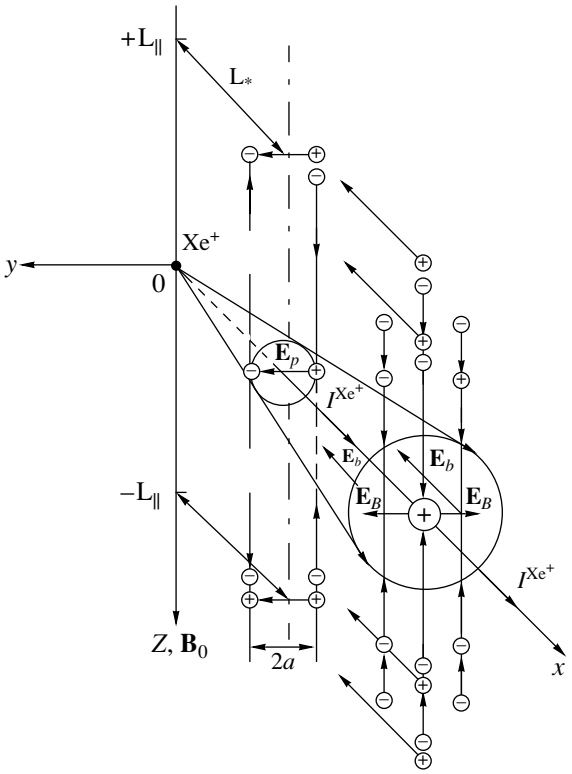

Fig. 8. System of currents and electric fields in the plasma beam and the ambient plasma.

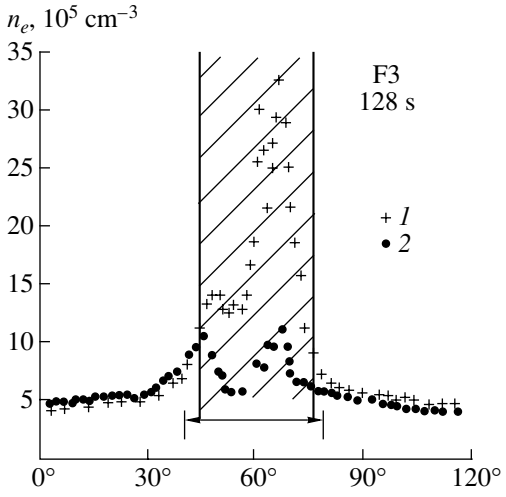

Fig. 9. Transverse profiles of the beam during its passage through the rocket: (*1*) at the shadow edge and (*2*) near the shadow center.

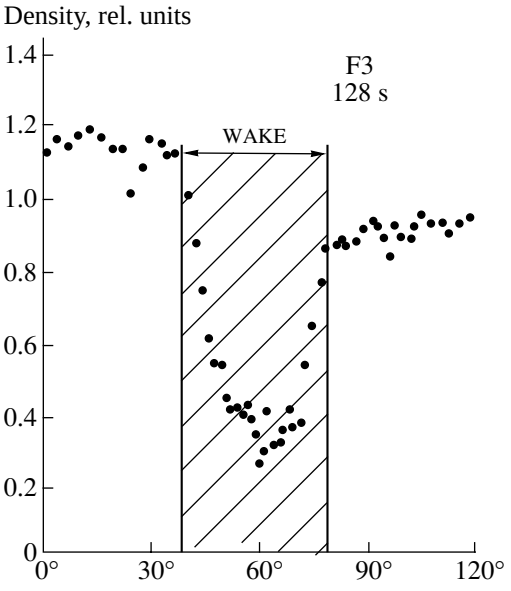

Fig. 10. Normalized profile of the beam plasma density behind the rocket and the effective trace (shadow) size.

where $A = n_b/n_0$ at $x = 0$, a is the initial beam diameter, m_i is the ionospheric ion mass, and ω_{ce} is the electron cyclotron frequency. For an effective electron collision frequency of $\nu_{eff} \sim 10^4$ s^{-1}, $A = 10$, and $a = 1$ m, expressions (7)–(9) are applicable beginning from distances of $x = 3$–4 m. At these distances, we have $E \sim E_0 = 850$ mV/m and $j_\parallel \approx j_b$ (the injected ion current density). At a distance of $x = 20$ m, we have $E = 200$ mV/m, $L_\parallel = 1.3$ km, and $j_\parallel = 10^{-7}$ A/cm^2. These estimates correspond to the above results. It can be seen that the transverse fields and longitudinal currents decrease sharply with distance, which also corresponds to the results of measurements [13–16]. The agreement between the experimental data and theoretical predictions indicates that collective processes (resulting in the effective collision frequency ν_{eff} between electrons and waves) play an important role in the formation of the current system and the electric field distribution in the ionosphere as the plasma jet propagates perpendicular to $\mathbf{B}_0$.

3. SHADOW EFFECT AND ADIABATIC BEAM COOLING

3.1. Determination of the Temperature by the Shadow Effect

In the Porcupine experiment, there were favorable conditions for the point measurements of various parameters inside the beam at different distances from the source. However, the presence of obstacles to the plasma flow led to the formation of a "shadow" region (trace) behind the body being bypassed. The slow rotation of the main diagnostic unit (with a period of $T \approx 1$ s) allowed us to investigate the shadow (trace) region with the help of detectors placed at the arms. In this context, the electron density (with a Langmuir probe), ion flux (with an electrostatic probe), and electric field (with two pairs of crossed arms) measurements (which could allow us to analyze the shadow structure with a good time resolution) could be most successful. However, the data on the electric field appeared to be hardly applicable to quantitative estimates within the near (diamagnetic) zone and an intermediate region (where the current system forms) because the detectors operated mainly in the saturation regime. It was also difficult to use the probe data on the ion flux because the instants of the beam passage coincided very rarely with the proper orientation of the detector toward the trace. Actually, only the Langmuir probe provided undirected density measurements, which can be used to study density variations in the shadow region.

The well-developed theory of the trace [17, 18] allowed us to make definite conclusions [19] about the beam cooling and determine the beam temperature.

3.2. Experimental Results

Figure 9 shows two plasma density profiles measured behind the rocket when the beam passed through it and the Langmuir probe was screened by the main diagnostic unit. The measurements were carried out at the shadow edge (curve *1*) and near the shadow center (curve *2*). The transverse trace dimensions and position of its center can be determined from Fig. 10, which shows the normalized density of the fast component of the beam, N_i/N_0 (where N_0 is the unperturbed plasma density in the beam and N_i is its density in the shadow), corresponding to Fig. 9. The size of the density perturbation is larger than the width of the beam profile in

Fig. 9 but is smaller than the size of the rocket geometrical shadow.

There are at least two reasons for this:

(i) The rocket is not an ideal cylinder. The diagnostic equipment installed on the rocket is partially permeable to the plasma flow; as a result, the effective cross section of the rocket can be smaller than its geometrical size.

(ii) On the other hand, both the shadow size and the degree to which the ion density N_i is perturbed within the shadow region depend on the physical conditions in the plasma flowing around the rocket. The ion temperature is also a very important parameter. The increase in T_i naturally leads to the narrowing of the trace (shadow), because thermal motion promotes the penetration of ions beyond the edge of the geometrical shadow. It is this effect that will be considered below based on the theoretical model of the shadow [15] under the conditions of the Porcupine experiment.

3.3. Theory of a Plasma Jet Flowing around a Cylinder under the Conditions of the Porcupine Experiment

In accordance with [15], we consider a plasma jet incident on an infinite cylinder perpendicular to its axis with a velocity V_0. The jet velocity satisfies the condition $V_i < V_0 < V_e$, where V_i and V_e are the thermal velocities of the jet ions and electrons, respectively. All of the characteristic sizes are assumed to be much smaller than the mean free paths of the jet particles. The cylinder radius $R_0 \gg D$ is assumed to be much larger than the Debye radius $D = (T_e/4\pi e^2 n_e)^{1/2}$ (where e is the electron charge and T_e and N_e are the temperature and density of the jet electrons, respectively). For the ion density behind the cylinder (in the shadow), we have

$$\frac{N_i}{N_0} \approx \frac{\exp[-(V_0^2/V_i^2)\sin\theta_0]}{\sqrt{\pi}(V_0/V_i)\sin\theta_0}, \qquad (10)$$

where θ_0 is the angle with respect to the shadow axis.

3.4. Measurements of the Ion Temperature and Observations of the Beam Cooling

It can be seen from Fig. 10 that the relative density at the symmetry axis of the shadow is minimum (0.2–0.3) at distances of 25–45 m, which corresponds to $\sin\theta_0 = 0.25$. Figure 11 shows the normalized density calculated by formula (10) as a function of the ion temperature. It can be seen that the density at the axis decreases monotonically with decreasing temperature. In the shaded region, the ion thermal velocity varies in the range $V_i/V_0 = 0.25$–0.29, which corresponds to the ion temperature $T_i \le 15$ eV.

The obtained temperature value is the upper limit for the ion temperature in the plasma jet under the conditions of the Porcupine experiment. In all of the measurements, the Langmuir probe never resided exactly on the shadow axis; thus, we failed to determine the true value of the minimum electron density. Hence, the temperature obtained from the measured electron density is higher than the true temperature of the plasma beam. On the other hand, taking into account the complicated shape of the diagnostic unit (the rocket is not a regular cylinder), we can suppose that some fraction of the beam is scattered by the diagnostic equipment toward the shadow center. This will lead to an increase in the electron density at the shadow axis, which, in turn, will result in overestimated values of T_i. The initial temperature of the beam ions near the source was $T_i \sim$ 50 eV [4]. The obtained temperature values are nearly four times lower, which indicates an intense beam cooling it the initial stage of the beam propagation.

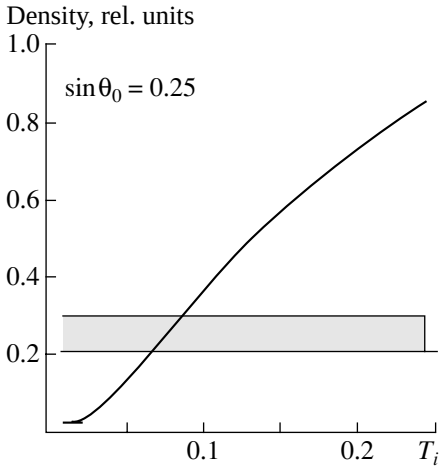

Fig. 11. Calculated normalized beam density in the shadow vs. normalized beam ion temperature (in units of $\langle V_i^2\rangle/V_0^2$). The shaded region corresponds to the range of the beam densities measured in the Porcupine experiment.

3.5. Discussion

A simplest explanation for the cooling of the xenon plasma beam in the Porcupine experiment is to assume the beam is cooled adiabatically during its expansion after injection. Under the assumption that the beam behaves like an ideal gas, the formula for adiabatic expansion gives

$$T_i/T_{i0} = (N_{in}/N_{i0})^{\gamma-1}, \qquad (11)$$

where T_{i0} is the initial beam temperature, N_{in} is the beam density measured at a distance of $r_{in} = 3.75$ m from the plasma source, and N_{i0} is the initial beam density [2]. From Eq. (11), we can find the adiabatic index γ or the critical cooling radius r_c, at which the final ion temperature is reached. It is well known from experi-

ment [3, 6] that the beam density decreases with the distance r from the source as

$$N/N_{in} \approx (r_{in}/r)^2. \quad (12)$$

Hence, the temperature is scaled as

$$T_i/T_{i0} \approx (r_{in}/r)^{2(\gamma-1)}. \quad (13)$$

At a distance of $r_{in}/r \approx 10$, the measured temperature ratio is $T_i/T_{i0} \approx 5$. From here, we obtain $\gamma = 1.32$. To simplify the estimates, we have suggested that the process of adiabatic cooling proceeds from the source to the measurement point. However, the obtained γ value is significantly less than the 5/3 value expected for an expanding unmagnetized gas. Since there is no reason for such a reduction in γ for a xenon plasma beam, then, setting γ equal to 5/3, we can find the limiting distance r_c at which the cooling is over: $r_c \approx 11$ m. This distance is much longer than the radius of the diamagnetic zone, which is estimated [1] to be 3–4 m; i.e., it is less than the size of the zone where the current system forms (<15 m [6]). Thus, under the conditions of the Porcupine experiment, the obtained value of the critical distance for cooling is a reasonable estimate.

During the diamagnetic phase, the plasma beam expands almost without disturbances until it becomes as wide as the diamagnetic cavity. Hence, it is this stage during which the main cooling occurs. On the other hand, a certain fraction of the beam (in the region where the current system forms) behaves like an adiabatically expanding gas, in which electrons can follow ions [6] because of the drift in the crossed polarization electric field $\mathbf{E}_p$ and surrounding magnetic field. Then, the beam electrons are captured by the magnetic field, and the beam expands quite differently from an ideal gas. The above model of the current closing, which relates to this "nonadiabatic" stage, agrees well with the experimental data. The adiabatic cooling comes to an end before this stage, at distances smaller than the size of the zone where the current system forms. Thus, at $r > r_c$, the ion temperature in the beam (jet) will remain unchanged, provided that there is no additional heat sources.

The anticipated collisionless heating should mainly affect the beam electrons and the background plasma ions. Electron heating inside the rotating beam indicates the presence of ion-cyclotron and lower hybrid turbulence in the region occupied by the beam [20, 21]. Urban [22] recorded fast background ions produced during the injection of a xenon beam in the Porcupine experiment. In principle, the heating of the beam ions should hamper the observed cooling. Although the electrons and background ions are accelerated at the expense of the beam energy, this only leads to the deceleration of the beam. It is expected, however, that the beam ions will be slightly heated at the beam edge as long as the beam density is higher than or comparable to the background plasma density. Numerical simulations confirm this conclusion. Similar results were obtained in subsequent experiments [13–16]. The problem of the formation of a diamagnetic cavity [1] during the injection a similar Xe plasma jet was considered in detail in [23] based on the results of the *APEX* satellite project.

4. CONCLUSION

In experiments on the injection of a dense plasma beam from the payload of a rocket, self-consistent electric fields and currents ensuring plasma quasineutrality arise. In the absence of a background plasma, the beam drifts in the crossed fields. In this case, the beam propagates across the magnetic field $\mathbf{B}_0$ with a constant velocity $\mathbf{V}_0$ and the polarization field $\mathbf{E}_p$ arises in the beam plasma. In the presence of a background plasma, the situation is very different. The electron and ion currents flowing, respectively, along and across the magnetic field are generated in the plasma; these currents significantly reduce the polarization field. The electric field persists over a long distance along $\mathbf{B}_0$. The beam electrons do not follow the ions, and an intricate pattern of currents and electric fields is established in the plasma.

By analyzing the results of the plasma density measurements in the trace of an ion beam injected in the course of the Porcupine experiment, it was found that, in the initial stage of the beam expansion, the temperature of the injected quasineutral beam decreased by a factor of almost 4, as if it were an ideal gas. These results are explained based on the assumption of the adiabatic cooling of the beam plasma at distances of $r_c < 11$ m, where the beam current system is formed. This agrees well with the proposed model of the current system produced by the beam in the ambient plasma.

REFERENCES

1. A. A. Galeev, V. S. Dokukin, I. A. Zhulin, *et al.*, *Research on the Problems of Solar–Terrestrial Physics* (IZMIRAN, Moscow, 1977), p. 152.
2. R. Bush, V. S. Dokukin, G. Haerendel, *et al.*, Preprint No. 21 (287) (Inst. of Terrestrial Magnetism, Ionosphere, and Radio-Wave Propagation, Acad. Sci. USSR, Moscow, 1980).
3. G. Haerendel and R. Z. Sagdeev, Adv. Space Res., No. 1, 29 (1981).
4. A. I. Morozov, Yu. V. Esipchuk, G. N. Tilinin, *et al.*, Zh. Tekh. Fiz. **42**, 54 (1972) [Sov. Phys. Tech. Phys. **17**, 38 (1972)].
5. S. Chapman and V. C. A. Ferraro, Terr. Magn. Atmos. Electr. **38**, 79 (1933).
6. B. Hausler, R. A. Treuman, O. H. Bauer, *et al.*, J. Geophys. Res. **91** (A1), 287 (1986).
7. V. Ya. Kapitanov and V. G. Korobeinikov, Preprint No. 37 (570) (Inst. of Terrestrial Magnetism, Ionosphere, and Radio-Wave Propagation, Acad. Sci. USSR, Moscow, 1985).

8. R. Z. Sagdeev, V. N. Oraevsky, E. V. Mishin, *et al.*, *Tess. COSPAR (General Assembly), Toulouse, 1986*, Nos. 1–2.
9. R. Z. Sagdeev, V. N. Oraevsky, E. V. Mishin, *et al.*, Preprint No. 49 (Max-Plank Inst., München, 1986).
10. V. A. Rozhanskiĭ, Fiz. Plazmy **12**, 294 (1986) [Sov. J. Plasma Phys. **12**, 170 (1986)].
11. V. S. Dokukin, G. Haerendel, V. Ya. Kapitanov, *et al.*, in *Proceedings of the XV International Conference on Phenomena in Ionized Gases, Minsk, 1981*, p. 267.
12. V. G. Korobeĭnikov, Preprint No. 29 (643) (Inst. of Terrestrial Magnetism, Ionosphere, and Radio-Wave Propagation, Acad. Sci. USSR, Moscow, 1986).
13. R. L. Kaufmann, Space Sci. Res. **37**, 313 (1984).
14. R. L. Kaufmann, R. L. Arnoldy, T. E. Moore, *et al.*, J. Geophys. Res. **90**, 9595 (1985).
15. T. E. Moore, R. L. Arnoldy, R. L. Kaufmann, *et al.*, J. Geophys. Res. **87**, 7569 (1982).
16. C. W. Roth, M. K. Hudson, and R. L. Lysak, J. Geophys. Res. **88**, 8115 (1983).
17. Ya. L. Al'pert, *Waves and Artificial Bodies in the Near-Earth Plasma* (Nauka, Moscow, 1974).
18. A. V. Gurevich, Planet. Space Sci. **9**, 321 (1962).
19. Yu. Ya. Ruzhin, A. M. Moskalenko, R. A. Treuman, *et al.*, J. Geophys. Res. **92**, 267 (1987).
20. P. M. Kintner and M. C. Kelley, Adv. Space Res. **1**, 41 (1981).
21. D. Jones, Adv. Space Res. **1**, 103 (1981).
22. A. Urban, Planet. Space Sci. **29**, 1353 (1981).
23. A. S. Volokitin, Yu. Ya. Ruzhin, V. G. Korobeĭnikov, *et al.*, Geomagn. Aeron. **40** (3), 133 (2000).

Translated by N.N. Ustinovskiĭ

Plasma Physics Reports, Vol. 29, No. 3, 2003, pp. 276–278. Translated from Fizika Plazmy, Vol. 29, No. 3, 2003, pp. 302–304.

BRIEF COMMUNICATIONS

Comments on the Equilibrium of a Rotating Plasma

V. I. Ilgisonis

Nuclear Fusion Institute, Russian Research Centre Kurchatov Institute, pl. Kurchatova 1, Moscow, Russia

Received October 24, 2002

In a paper by Pustovitov [1], the results obtained in [2] were announced to be erroneous. They are as follows:

(i) By appropriately choosing the profile of the plasma rotation velocity, it is possible to reduce the Shafranov shift of the magnetic surfaces, which is driven by the finite plasma pressure.

(ii) A key role in this effect is played by the profile of the plasma rotation velocity, rather than its absolute value.

(iii) In such regimes with reduced Shafranov shift, the higher values of the parameter β may be achieved.

In my opinion, the critical discussion in [1] is largely the result of misunderstanding. This discussion is mainly focused on the equilibrium of the plasma column in the major radius and the *rigid* displacement of the plasma column is considered, whereas paper [2] studies the *differential* shift of the magnetic surfaces inside the plasma column.

Thus, having written the vector equation for plasma equilibrium in the form

$$\frac{\rho v^2}{r}\mathbf{e}_r - \nabla p + \mathbf{j}\times\mathbf{B} = 0, \qquad (1)$$

the author of [1] concluded that it is the absolute value of the rotation velocity that plays a dominant role in the force balance and, moreover, that this role is always negative. Of course, the centrifugal force is always directed outward from the axis of rotation. However, when the plasma equilibrium in the major radius is ensured by an Ampére's force of the proper strength, the role of rotation is not so simple. The radial pressure distribution can be determined from the radial component of Eq. (1): the pressure becomes dependent on the radius and the way in which it depends is governed by the plasma rotation. This dependence should also be taken into account in the remaining components of Eq. (1), where it appears just inside the derivatives. For example, the equation for the Shafranov shift Δ has the form

$$\left(\frac{J^2}{a}\Delta'\right)' = -\frac{J^2}{aR} - \frac{2a^2}{R}\left(p + \frac{\rho v^2}{2}\right)', \qquad (2)$$

where a is the magnetic surface label (minor radius) and the prime denotes the derivative with respect to a. Integrating Eq. (2) twice, it is possible to obtain the expression for the shift $\Delta|_0^a$ of any of the magnetic surfaces with respect to the magnetic axis. Clearly, adding a constant to the kinetic energy of rotation does not change the expression; it is in this sense that the absolute value of the rotation velocity is considered to be less important than its profile. A simple analytic example given in the Appendix clearly demonstrates that the rotation can indeed reduce this shift. In contrast to the definite statement of the author of [1], this example shows that, in complete accord with the qualitative conclusions reached in [2], the local increase in rotation velocity in the central region of the column may produce a global effect—a decrease in the absolute value of $\Delta|_0^{a_b}$.

The quantity $\Delta|_0^{a_b}$ describes the displacement of the plasma column center with respect to the boundary magnetic surface ($a = a_b$), which may be *fixed*, e.g., by the conducting wall or by choosing the proper position of the magnetic separatrix. In such a situation, an increase in the plasma pressure leads merely to the deformation of the magnetic surfaces in the axial region; in turn, the reduction of this deformation allows the attainable β value to be increased. Note that, although, in the expression for the ellipticity, a combination of the derivatives of the pressure and of the kinetic energy of rotation with respect to a is somewhat different (see [2]), the resulting effect may be also favorable (a decrease in the ellipticity). The equation for the ellipticity is difficult to integrate analytically; however, the numerical calculations carried out in [3] with no expansion in the inverse aspect ratio justify the possibility of reducing the Shafranov shift without increasing the higher moments. Note that examples of how the problem of the maximum attainable β is treated in formulations other than that used in [1] are known in the literature; among these is the problem referring to a tokamak with frozen-in fluxes [3], which is, in principle, free from restrictions on β.

Hence, the conclusions reached in [1] regarding the negative effect of plasma rotation are only valid for a particular formulation of the problem, and are not of universal applicability.

1063-780X/03/2903-0276$24.00

APPENDIX

Let us consider the model radial profiles of the plasma pressure and toroidal magnetic field,

$$p = p_0 + (p_b - p_0)x^\lambda, \tag{3}$$

$$B_t^2 = B_0^2(1 + \mu x^\lambda) \tag{4}$$

in a tokamak with nearly circular cross sections of the magnetic surfaces and with a large aspect ratio $R/a_b \gg 1$, where a_b is the radius of the plasma boundary and R is the tokamak major radius. Here, we have introduced the dimensionless variable $x = a/a_b$. The plasma pressures at the axis of the plasma column and at the plasma boundary are denoted by p_0 and p_b, respectively. Let the kinetic energy of plasma rotation E at the center ($a = 0$) and at the boundary ($a = a_b$) be equal to E_0 and E_b, respectively, and, at $0 < a < a_b$, be described by the profile

$$E = \frac{\rho v^2}{2} = E_b + (1 - x^\gamma)(E_0 - E_b + E_1 x^\alpha), \tag{5}$$

where the powers α and γ are positive. In the lowest order in the expansion parameter a_b/R, the toroidal current J in Eq. (2) obeys the equation

$$JJ' = -a^2\left(p + \frac{B_t^2}{2}\right)'. \tag{6}$$

We easily integrate Eqs. (2) and (6) to obtain

$$J^2 = a_b^2 B_{p_b}^2 x^{\lambda+2}, \tag{7}$$

$$\Delta|_0^a = \Delta_J + \Delta_p + \Delta_E, \tag{8}$$

where

$$\Delta_J = -\frac{a_b^2}{R}\frac{x^2}{2(\lambda+2)}, \tag{9}$$

$$\Delta_p = -\frac{a_b^2}{R}\frac{\lambda(p_0 - p_b)}{(\lambda+2)B_{p_b}^2}, \tag{10}$$

$$\Delta_E = \frac{a_b^2}{R}\left(\frac{2E_1}{B_{p_b}^2}\left(\frac{\alpha x^{\alpha+2-\lambda}}{(\alpha+2)(\alpha+2-\lambda)} - \frac{(\alpha+\gamma)x^{\alpha+\gamma+2-\lambda}}{(\alpha+\gamma+2)(\alpha+\gamma+2-\lambda)}\right) + \frac{2\gamma}{\gamma+2}\frac{E_b - E_0}{B_{p_b}^2}\frac{x^{\gamma+2-\lambda}}{\gamma+2-\lambda}\right). \tag{11}$$

Formula (7), in which

$$B_{p_b}^2 = \frac{\lambda}{\lambda+2}(2(p_0 - p_b) - \mu B_0^2), \tag{12}$$

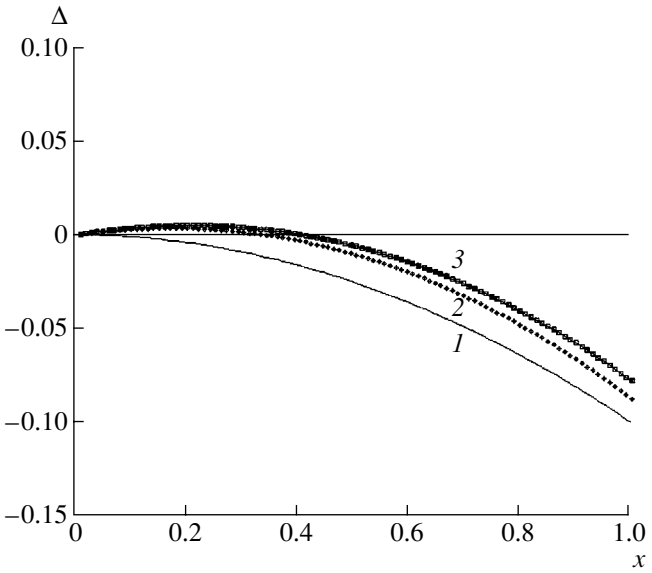

Fig. 1. Radial profiles of the terms in the expression for the shift in the case of a parabolic pressure profile with $\lambda = 2$: (*1*) $\Delta_p(x)$, (*2*) $\Delta_p(x) + \Delta_E(x)$ at $E_b - E_0 = 0$, and (*3*) $\Delta_p(x) + \Delta_E(x)$ at $(E_b - E_0)/E_1 = 0.2$.

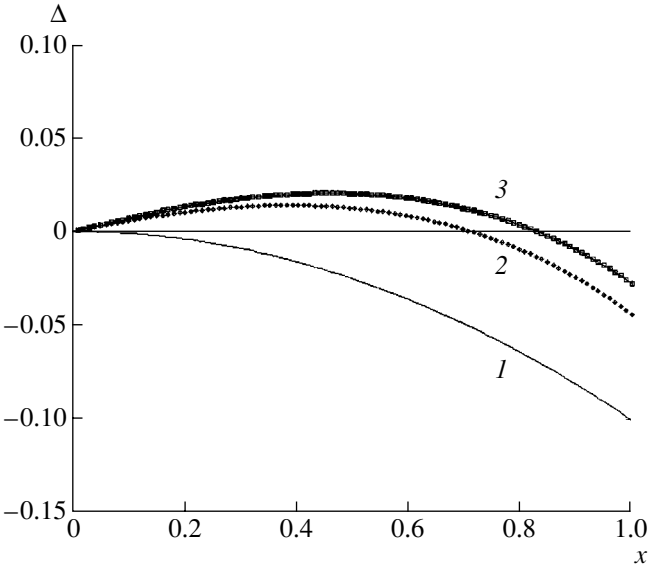

Fig. 2. The same as in Fig. 1, but for a pressure profile with $\lambda = 4$.

is simply the Bennett relation

$$\bar{p} - p + \frac{\overline{B_t^2} - B_t^2}{2} = \frac{B_p^2}{2}, \tag{13}$$

which is also valid for a toroidally rotating plasma. Formulas (8)–(11) determine the shift of any of the magnetic surfaces with respect to the magnetic axis. The quantities Δ_J, Δ_p, and Δ_E are related to the plasma cur-

rent, plasma pressure, and plasma rotation, respectively.

First, we consider the simplest case $p_b = 0$ and $E_0 = E_b = 0$. For certain relationships between α, γ, and λ, the quantity Δ_E is positive; hence, in formula (8), it can compete with the negative term Δ_p associated with the plasma pressure. Increasing γ and decreasing α produces a beneficial effect. As follows from Eq. (5), it is these parameters that characterize the *profile* of the plasma rotation velocity. In Figs. 1 and 2, curves *1* give the dependence $\Delta_p(x)$, which is the pressure-produced shift of the magnetic surfaces in a nonrotating plasma, and curves *2* display the dependence $(\Delta_p + \Delta_E)(x)$ for a plasma rotating at a subsonic speed.[1] That the rotation velocity profile is especially important is clear from formula (11) and also follows directly from Eq. (2), which contains the derivative of the kinetic energy rather than its absolute value.

The figures show that, in a rotating plasma, the absolute value of $\Delta|_0^a$ can decrease over the entire plasma column, up to the plasma boundary $x = 1$. This effect takes place not only for a class of radially increasing profiles of the plasma pressure (as was erroneously concluded in [1]), but also for a wider class of pressure profiles described by formula (3). However, a parabolic pressure profile with $\lambda = 2$, which is a traditional subject of investigations, is least convenient for our purposes; that is why in the paper [5] cited by the author of [1] the effect is small. Any other profile with $\lambda > 2$ in class (3) provides a more clear demonstration of the effect in question (cf. Fig. 1, Fig. 2).

It is also necessary to draw attention to the following important circumstance that was not taken into consideration in [1]. It has been shown experimentally (see, e.g., [6]) that the plasma rotation velocity at the boundary magnetic surface can be nonzero, and the same is true for the plasma pressure ($p_b \neq 0$). If the quantity $E_b - E_0$ is positive, then the last term on the right-hand side of formula (8) may also have a favorable effect (see Figs. 1, 2, curves *3*), while the unfavorable factor $p_0 - p_b$ may remain unchanged as the mean β value increases.

Thus, the example presented provides a clear evidence in support of the effect whose existence was denied in [1].

[1] In the figures, the quantity Δ is normalized to a_b^2/R; the rotation parameters are, for definiteness, chosen to be $\alpha = \gamma = \lambda - 0.9$; and the plasma pressure averaged over the plasma column and the parameters E_1 and $E_b - E_0$ (all normalized to $B_{p_b}^2/2$) are equal to 0.2, 0.15, and 0.03, respectively.

REFERENCES

1. V. D. Pustovitov, Fiz. Plazmy **29**, 124 (2003) [Plasma Phys. Rep. **29**, 105 (2003)].
2. V. I. Ilgisonis and Yu. I. Pozdnyakov, Pis'ma Zh. Éksp. Teor. Fiz. **71**, 454 (2000) [JETP Lett. **71**, 314 (2000)].
3. V. I. Ilgisonis, Plasma Phys. Controlled Fusion **43**, 1255 (2001).
4. R. A. Dory and Y.-K. M. Peng, Nucl. Fusion **17**, 21 (1977).
5. B. J. Green and H. P. Zehrfeld, Nucl. Fusion **13**, 750 (1973).
6. M. J. Schaffer, B. D. Bray, J. A. Boedo, *et al.*, Phys. Plasmas **8**, 2118 (2001).

Translated by O.E. Khadin